Design and Geometrically Nonlinear Analysis of Rigid Origami Structure with Multiple Degrees of Freedom

Kentaro Hayakawa

2023

Contents

List of Figures

List of Tables

Chapter 1

Introduction

1.1 Background of research

1.1.1 Origami in academic field

Origami is a kind of art and pastime creating a two-dimensional or a three-dimensional objects by folding a sheet of paper. Origami is originally a Japanese word but recently internationally used. A word "origami" is decomposed into two words "ori" meaning "folding" and "kami" ("gami" is a conjugation of it) meaning "paper". In this study, "origami" is used as both a countable and uncountable noun. When it is used as a countable noun, it denotes the individual objects formed by folding a sheet of paper or a thin object. On the other hand, when it is used as an uncountable noun, it refers to the concept of origami as the art and the methodology. In Japan, origami has been widely practiced through the ages, and a huge number of books have been published for introducing techniques of origami. It should be noted that a book titled *Secret Fold Techniques of Connected Cranes* has been published in 1797 which explains various methods of constructing a paper crane and connected cranes [1]. There also exists English literature on the folding patterns and methods of traditional and modern origami [2].

Origami has also attracted attention of researchers and engineers because of its mathematical and physical properties. In the field of computational geometry, origami forms an academic field referred to as *computational origami*, and the properties attributed to the operation of folding are studied from the perspectives of geometry and computational theory [1, 3, 4]. An origami in this field is often regarded as an abstract object which does not have thickness. Although origami has been popular among people as the art and pastime for a long time, there are many mathematical open problems, e.g., about *foldability*; an origami can be folded or not by a specified operation. On the other hand, kinematics and statics of origami have also widely been studied as *structural origami* [5] or *engineering origami* [6] for engineering applications in the fields of mechanical, civil, and architectural engineering. An origami is often treated as a mechanism which can be deformed without external loads or a shell structure which has a corrugated shape. In this field, thickness and material property of an origami may or may not be incorporated. Origami's nonlinear

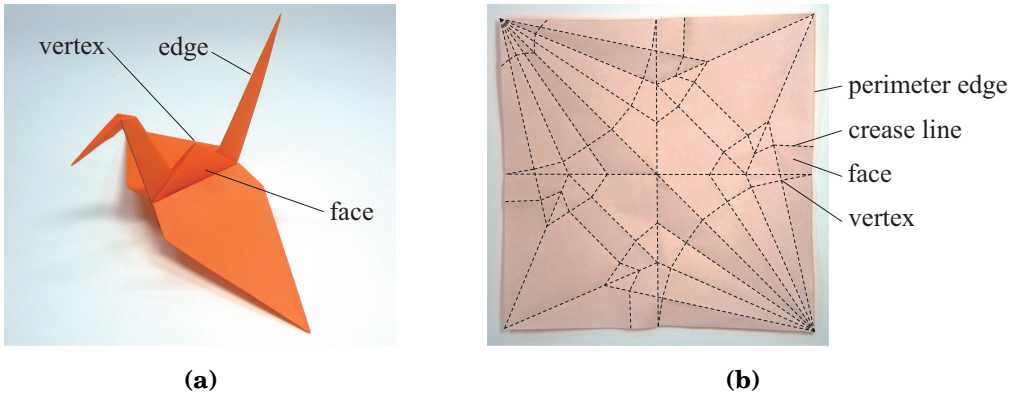

Figure 1.1: Orizuru (paper crane, folded by Kentaro Hayakawa); (a) Three-dimensional form, (b) Crease pattern.

continuous folding motions have wide potential for application to deployable and morphing structures. Its mechanical properties of the whole structure, such as the load bearing capacity and deformation characteristics resulting from folding, have also been studied to realize high-performance structures. These origami's properties have been applied to a variety of purposes; e.g., solar panels mounted on artificial satellites [7], foldable and portable shelters [8, 9], crushable structures for energy absorption [10, 11], medical devices used in human bodies [12], and metamaterials which have unique mechanical properties; e.g., bistability [13] and tunable Poisson's ratio [14]. Origami can improve the efficiency of manufacturing and assembly processes and also can realize the materials with novel physical properties.

Origami's properties are also actively studied for architectural design and engineering. In practice, origami has been applied to the design of building envelopes to realize characteristic shapes consisting of faces and edges [15]. The kinematics of origami is also applied to a retractable roof and a temporal shelter. However, the mechanical and kinematic properties of origami are still not fully understood, and there are few practical examples that take full advantage of the characteristics of origami; the folding motion and unique mechanical properties. In the academic field, the International Association for Shell and Spatial structures (IASS) has organized a research group on origami in Working Group 15 [16], and various research papers and presentations have been produced on the potential applications of origami in architecture.

1.1.2 Nomenclature of origami

An origami is often regarded as a polyhedral surface in the two- or three-dimensional space, and a surface formed by an origami is referred to as an *origami surface* in this study. It is assumed that an origami basically consists of *vertices*, *faces*, and *edges* as shown in Fig. 1.1 after the structure of a mesh used in the field of geometry. A vertex is a point where two or more edges joins. A face is a flat surface bounded by several edges. An edge is a line segment

(a) **(b)**

Figure 1.2: Mountain and Valley fold crease lines; (a) Mountain fold, (b) Valley fold.

classified into a *crease line* between two faces or a *perimeter edge* on the boundary. Further classification of edges is provided in Chapters 2 and 3 for form generation and kinematic analysis, however, it is not explained in this section. Only flat faces and straight edges are considered in this study although there is a concept of *curved-folding* origami [17] where faces and crease lines are curved.

A pair of adjacent faces can relatively rotate about a crease line between them. According to the relative position between a crease line and the faces adjacent to it, the crease line is referred to as the *mountain fold* crease line represented by a red chain line in Fig. 1.2(a) or the *valley fold* crease line by a red dotted line in Fig. 1.2(b). Viewing from the front side of an origami, a mountain fold crease line is above the adjacent faces, and a valley fold crease line is below the adjacent faces as shown in Fig. 1.2. Combination of the connectivity, length, and direction of the crease lines of an origami is referred to as the *crease pattern*. A *folding angle* of a crease line is defined as a supplementary angle of a dihedral angle between the faces adjacent to the crease line. When the faces adjacent to a crease line are on the same plane and do not overlap with each other, a folding angle of the crease line is equal to 0, and when the faces are coplanar and overlap with each other, a folding angle is equal to π. If necessary, the sign of each folding angle is defined in accordance with the arrangement of mountain and valley; folding angle of a mountain/valley fold crease line is negative/positive. An origami is at an *unfolded* state and at a *flat-folded* state especially when all the folding angles are equal to 0 and $\pm\pi$, respectively. Other states are referred as *partially folded* state or simply *folded* state. The shape of origami or the diagram of the crease lines in the unfolded state is referred to as the *development diagram*.

1.1.3 Rigid origami

Rigid origami, which is the main subject of this study, can be folded and unfolded without in-plane or out-of-plane deformation of its faces. The folding mechanism of a rigid origami is called a *rigid-foldable* mechanism and determined only by its crease pattern; i.e., its deformation mechanism is independent of its material properties. Therefore, a rigid origami is often regarded as a mechanism consisting of rigid panels connected by hinges. A rigid-foldable mechanism is very suitable for engineering applications and has been applied to a deployable structure consisting of stiff panels [18] and kinematics modeling of a robot [19]. It also has been utilized in the fields of architecture and civil engineering; e.g., the movable

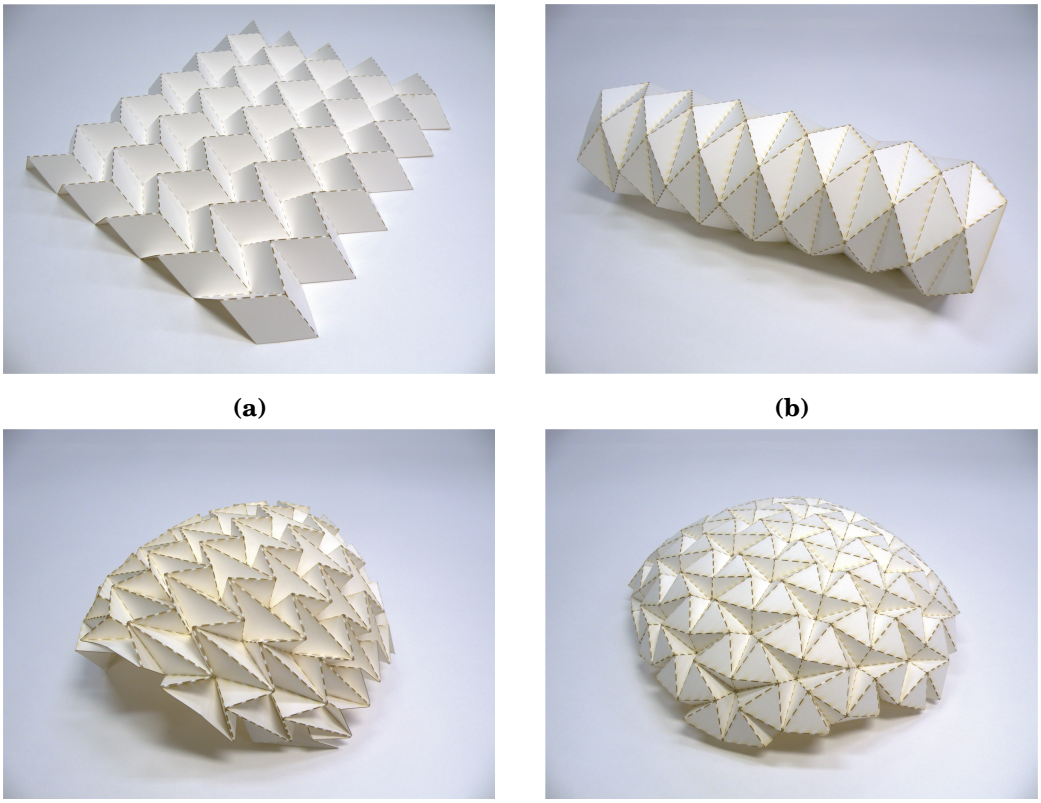

Figure 1.3: Rigid-foldable crease patterns (folded by Kentaro Hayakawa); (a) Miura-ori, (b) Yoshimura pattern, (c) Waterbomb tessellation, (d) Resch's pattern.

sunshade of *Al Bahr Towers* in the UAE and *Rolling Bridge* in the UK which can be rolled up [20]. In addition, rigid origami can contribute to developing new construction methods of building roofs and facades with distinctive shapes like the Panta-dome by Kawaguchi [21].

There are some known and well studied crease patterns such as *Miura-ori*, *Yoshimura-pattern*, *waterbomb tessellation*, and *Recsh's pattern* as shown in Fig. 1.3. However, the rigid-foldability of a non-regular crease pattern is not trivial, and many studies have been done for the investigation of the properties of a rigid-foldable mechanism and the form generation of rigid origami. Various techniques from mathematics and structural engineering are utilized for research on rigid origami. The rigid-foldability of quadrilateral mesh has been investigated with respect to the integrability theory in the field of mathematics [22] and the infinitesimal mechanism in the field of structural engineering [23]. Tachi [24] has proposed a method for simulating a folding process of an input crease pattern based on the projection to the constraint space. A design method of rigid origami based on the Bayesian topology optimization has been proposed by Shende *et al.* [25]. Graph theory of mathematics is utilized for rigidity analysis based on the theory of combinatorial rigidity [26]. The method for assigning the mountain or valley fold to each crease line based on graph theory and mixed-integer linear programming has been proposed by Chen *et al.* [27].

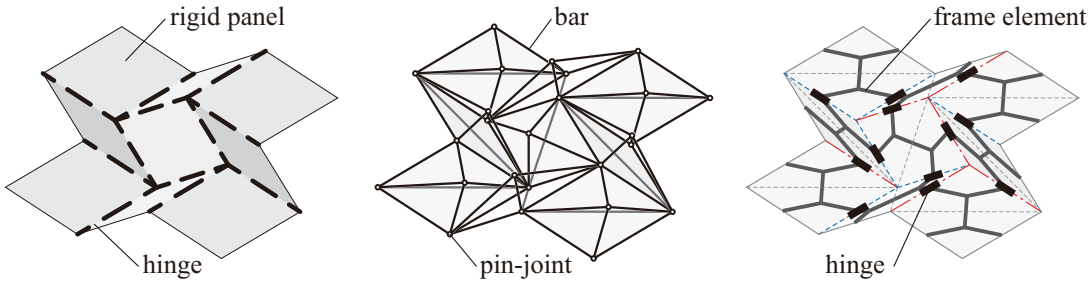

Figure 1.4: Numerical models of rigid origami; (a) Rotational hinge model, (b) Truss model, (c) Frame model.

1.2 Objectives and methods

In this study, methods for design and analysis of a rigid origami are proposed mainly for the architectural purposes. In order to apply rigid origami to the architectural design and construction methods, it is important to be able to generate a crease pattern that realizes a shape required by the designer and a deformation mechanism that takes into account the efficiency and safety of construction. Therefore, a method is developed to approximate a target curved surface using a rigid origami with a small number of crease lines and a small deformation degrees of freedom, which contributes to the constructability. Proposed method generates a crease pattern that can realize a curved surface from a flat state by a rigid-folding motion for the application to roof structures and building envelopes. In addition, it is also necessary to sufficiently understand the complex deformation path to apply the rigid-folding mechanism to the construction method. When applying a rigid origami to building structures, it is important to consider the external loads and the stability of equilibrium although the deformation mechanism of a rigid origami is determined by geometrical conditions. Then, a method is proposed to analyze the deformation path of a rigid origami determined by the equilibrium of forces under geometric conditions. A numerical model referred to as the *frame model* [28–31] is developed as a model with properties suitable for the above purposes and is used throughout this study. The detailed objectives and methods of this study are outlined below, and the further background and objectives are given in the corresponding chapters.

To manipulate a rigid origami on a computer program, it is important to develop a numerical model suitable for representing the configuration and the kinematics of a rigid origami. Research that focuses on the mathematical properties of rigid origami requires a simple and accurate model to represent the folding state. By contrast, for engineering applications, it is preferable to use models that can easily adapt existing methods in mechanics and structural engineering and that can represent physical properties. For the first purpose, a rotational hinge model (folding angle model) shown in Fig. 1.4(a) is often used, which represents a folding state of a rigid origami only by the folding angles of crease

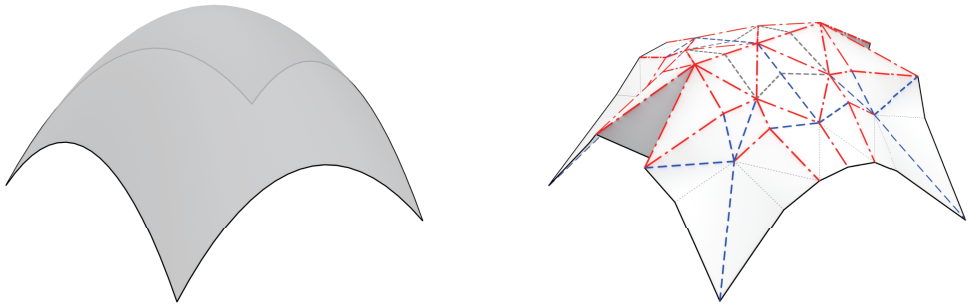

(a) (b)

Figure 1.5: Image of the form generation of a rigid origami; (a) Target surface, (b) Generated origami surface.

lines [24,32,33]. This model is suitable for dealing with rigid origami in an abstract manner. However, it is difficult to intuitively comprehend the shape of the origami since the positions of the vertices are not explicitly expressed in the methods using the rotational hinge model. Therefore, if the positions of vertices need to be referred to, updated, and constrained in the study of a rigid origami such as form generation, the rotational hinge model has a disadvantage. On the other hand, for the second purpose, a truss model (bar and hinge model) shown in Fig. 1.4(b) is often used. It represents a rigid origami by an assembly of pin-jointed bars in a truss model, where the nodal coordinates are the variables [34–37]. When this model is used, the existing methods for the analysis of truss structures can be utilized for the analysis of a rigid origami. However, if a rigid origami has a face with more than three edges, the structure of the model tends to be complicated to constrain the in-plane and out of plane deformation of the face.

To overcome the difficulty of the models described above, a numerical model referred to as the frame model [28–31] shown in Fig. 1.4(c) is developed and used, which is constructed based on the theory used in the partially rigid frames [38–40]. It consists of rigid frame elements connected by hinges corresponding to crease lines of an origami and has an advantage of being able to represent a rigid origami with a simpler configuration for the purpose of this study than the existing numerical models such as the rotational hinge models and the truss models. Further explanations of the models are provided in Chapter 2.

In order for rigid origami to be applicable to the architectural design, the shape of a rigid origami needs to be manipulated to fulfill the designer's requirements while satisfying the strict geometric constraints for rigid-foldability, and only directly using well-known crease patterns such as the Miura-ori pattern shown in Fig. 1.3 limits the range of designs for structures utilizing a rigid origami. Therefore, the development of methods for generating rigid-foldable crease patterns is essential for the engineering applications of a rigid origami. As explained in Chapter 3, there are various methods which generalize and extend the existing well-known crease patterns [41–45] and generate a new rigid-foldable crease pattern [23, 46–50].

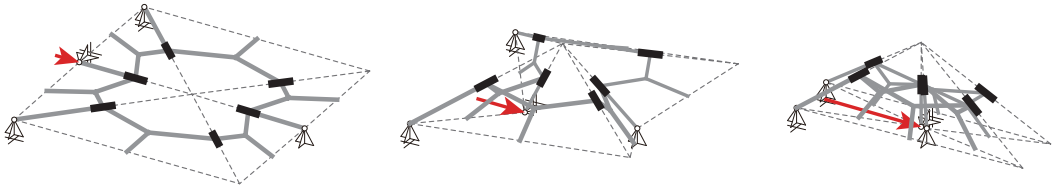

Figure 1.6: Image of the equilibrium path analysis of a rigid origami.

In this study, a form generation method of a rigid origami is proposed for further enhancing the flexibility of the design of a rigid origami. A curved surface defined as the Bézier surface [51] is approximated by a rigid origami with or without cuts which can be developed to a plane [28–30, 52] as shown in Fig. 1.5. The crease pattern is generated from the triangulated target surface; the proposed method does not rely on the typical crease pattern such as Miura-ori. The optimization approach is utilized to minimize the approximation error under the condition so that the origami surface is developable to a plane. Developability conditions of the origami surface and approximation error functions between the target surface and the origami surface are formulated by using the geometric properties of polyhedral surfaces such as Gaussian curvature. In the process of form generation, crease lines of the origami surface are sequentially fixed (removed) to reduce the degrees of freedom of the rigid-folding mechanism. The faces adjacent to a fixed crease line are combined into a single flat face, and the face with more than three edges is generated. The crease lines to be fixed are selected by the criteria reflecting the infinitesimal mechanism of the rigid origami, which help to prevent the crease lines to be locked and to be unable to rotate during the deployment process. The proposed method can approximate the target surface with a simple rigid origami with few crease lines and small folding angles, which has not often been seen in previous studies.

Analysis of the deformation path of a rigid origami is also important to realize a structure utilizing the concept of rigid origami which can be folded/unfolded safely and efficiently. In the previous studies, mainly two types of deformation path analysis of a rigid origami are preformed, which are the pure mechanism analysis [24,32] and the structural analysis with respect to the equilibrium of the structure [34,53,54]. The former analysis can trace the exact rigid-folding deformation path without deformation of the faces by using the rotational hinge model while boundary conditions such as constraints on the positions of vertices are not incorporated, and the physical implications of the deformation path, such as the equilibrium of force, are not considered. The latter analysis mainly traces the *equilibrium path* which is a sequence of equilibrium states under external loads or forced displacements assuming small rotational stiffness of crease lines and/or elastic deformation of the faces of a rigid origami. The truss model is often used in this analysis by allowing the deformation of bars, and the exact rigid-folding deformation path may not be obtained. At present, few studies have been conducted to clarify the relationship between the results of the analysis from a pure mechanism perspective and the results of the analysis from a equilibrium perspective while it is important to understand the foldability [55] of a crease pattern and for

the prototyping of the deployable structure using a rigid-fold mechanism.

Therefore, in this study, methods of equilibrium path analysis and stability analysis of an equilibrium state are developed for a rigid origami to be folded/unfolded in the exact rigid-folding motion. The equilibrium state of a frame model with the external loads applied to the nodes is investigated by assuming the small rotational stiffness proportional to the length of each crease line. The total potential energy is defined with respect to the strain energy of the springs introduced in the hinges and the external work by the nodal loads, and it is minimized to obtain an equilibrium state under the compatibility conditions so that the displacements of the nodes and the members are compatible. An equilibrium path is traced by the incremental loading analysis as shown in Fig. 1.6, and the bifurcations of the equilibrium path is investigated in the numerical examples. The relationship between the deformation mechanism obtained from geometric constraints and the deformation modes obtained in terms of the equilibrium of forces is also numerically investigated, which has not often been investigated in previous studies.

1.3 Thesis structure

This thesis consists of six chapters including this chapter for the introduction. The following chapters are organized as follows. Chapter 2 provides the explanations of the numerical models used in the previous studies and this study. The structure of the frame model used in this study is described and the method for the analysis of the infinitesimal mechanism is provided based on the method for partially rigid frames [38–40]. By extending the formulation of the geometric constraint equations in Ref. [40], variables are newly selected and the constraint equations are reconstructed so that the calculation for the form generation and the deformation path analysis proposed in this study to be simplified. A form generation method of a rigid origami is proposed in Chapter 3, and the case studies of the form generation is shown in Chapter 4. The method proposed in Chapter 3 is the summary of the methods proposed in Refs. [28–30, 52]. The result of the infinitesimal mechanism analysis described in Chapter 2 is utilized to define the selection criteria of the crease lines to be fixed in the process of form generation. Effectiveness of the approximation error functions and the selection criteria of the crease lines are numerically confirmed by the examples shown in Chapter 4. The proposed method improves design flexibility of a rigid origami by approximating the target curved surface without depending on the well-known crease patterns. In addition, by generating a rigid origami structure with a small degrees of freedom of deformation mechanism, the proposed method contributes to realize structures which can be efficiently and safely folded and developed. In Chapter 5, equilibrium path and stability analysis of a rigid origami is explained, which is proposed in Ref. [31]. The total potential energy is minimized under the compatibility conditions formulated in Chapter 2. Equilibrium paths of the waterbomb pattern are traced, and the several deformation paths for different boundary conditions are obtained. The proposed method can be used to obtain a deformation path that simultaneously achieves an exact rigid-folding motion and an equi-

librium of forces. Chapter 6 concludes this thesis. It provides the summaries of the above chapters and the remarks on the results of the numerical examples of the form generation and the equilibrium path analysis.

1.4 Published works included in the thesis

This thesis is the collection of several published papers by the author and co-authors, and detailed information and supplementary materials of these papers are provided. The correspondence between the published papers and the chapters in this thesis is summarized as follows:

Chapter 2

K. Hayakawa and M. Ohsaki, Form generation of rigid origami for approximation of a curved surface based on mechanical property of partially rigid frames, *International Journal of Solids and Structures*, Vol. 216, pp.182–199, May 2021.

K. Hayakawa and M. Ohsaki, Equilibrium path and stability analysis of rigid origami using energy minimization of frame model, *Frontiers in Built Environment*, Vol. 8, Aug. 2022.

Chapter 3

K. Hayakawa and M. Ohsaki, Form generation of rigid origami for approximation of a curved surface based on mechanical property of partially rigid frames, *International Journal of Solids and Structures*, Vol. 216, pp.182–199, May 2021.

K. Hayakawa, Y. Maruyama, A. Adachi, and M. Ohsaki, Approximation of curved surface by rigid origami with cutting lines, *Journal of Architecture and Planning (Transactions of AIJ)*, Vol. 87, No. 801, pp. 2288–2297, Nov. 2022 (in Japanese).

Chapter 5

K. Hayakawa and M. Ohsaki, Equilibrium path and stability analysis of rigid origami using energy minimization of frame model, *Frontiers in Built Environment*, Vol. 8, Aug. 2022.

Chapter 2

Frame model for kinematic analysis and form generation of rigid origami

In this chapter, several numerical models for the kinematic analysis and the form generation of the rigid origami proposed in the previous studies are briefly reviewed, and the configuration of the frame model [28–31] used in this study is introduced. The frame model is a numerical model based on the theory used in the partially rigid frames [38–40]. The analysis method is also presented for the infinitesimal mechanism of the frame model utilizing the formulations of partially rigid frames.

2.1 Numerical models of rigid origami

While geometry plays an important role in the form generation of an origami, mechanics and kinematics are also important for understanding folding properties and applying them to engineering application. Even if each face is assumed to be rigid, the deformation properties of an origami are complicated, and it is important to use an appropriate numerical model suitable for the form generation and the kinematic analysis.

In the study of a rigid origami, a rotational hinge model shown in Fig. 2.1(a) and a truss model (bar and hinge model) shown in Fig. 2.1(b) are often used. In the rotational hinge model, a folding state of a rigid origami is represented only by the folding angles of the crease lines, and this helps us to express the folding state in a simple form [24, 32, 33]. The compatibility constraints on the folding angles which is used as variables are formulated so that the loop around each inner vertex and each hole formed by the origami faces is appropriately closed under the assumption of the rigidity of each face. This approach is also used for the analysis of linkages [56, 57]. *Rigid Origami Simulator* [58] developed by Tachi [24] is a software that can trace an exact folded shape without deformation of faces by successively solving the linearized constraints on the folding angles. Since only the angles between the crease lines and the fold angles are considered in the rotational hinge model,

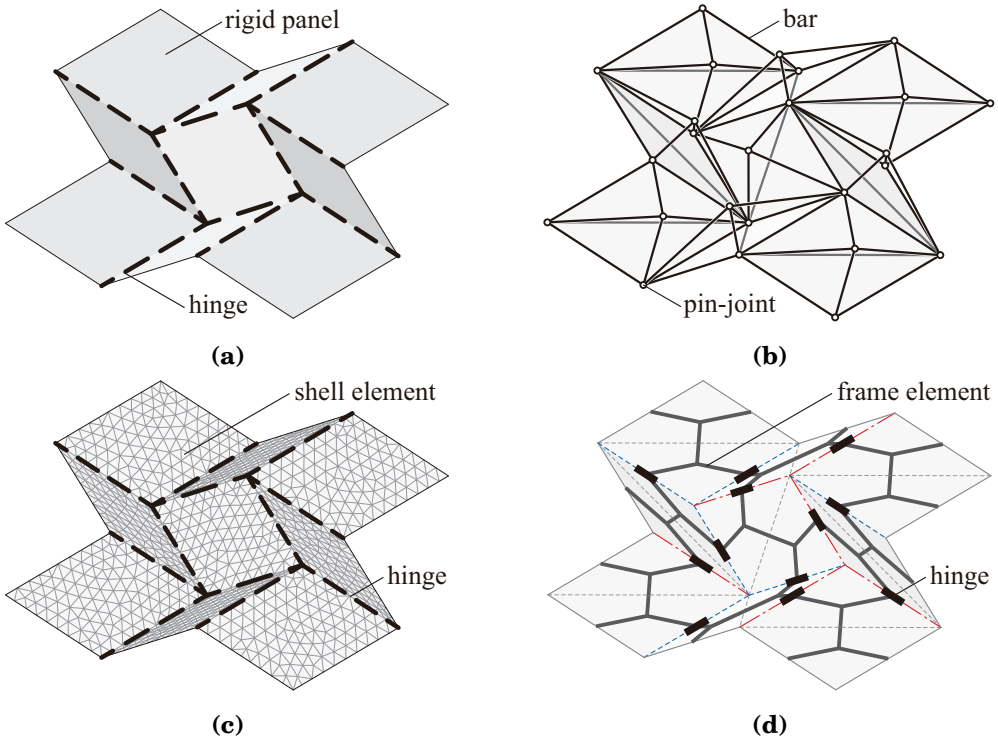

Figure 2.1: Numerical models representing a Miura-ori pattern (Partly reshown, see Chapter 1); (a) Rotational hinge model, (b) Truss model, (c) FE model, (d) Frame model and assignment of mountain and valley.

the positions of vertices should be computed from the complicated nonlinear equations of these angles to obtain the actual shape of the rigid origami. Therefore, the rotational hinge model has a disadvantage for the form generation and the kinematic analysis where the positions of vertices are often referred to, updated, and constrained.

On the other hand, a rigid origami is represented by an assembly of pin-jointed bars in a truss model, where the nodal coordinates are the variables [34–37]. Since the nodes of the truss model are located at the vertices of the origami, it is easy to incorporate the constraints on the nodal positions and displacements. In addition, the equilibrium with nodal loads are easily considered in the deformation path analysis. Therefore, it is often used for the analysis of the equilibrium path under the external loads or the forced displacements; e.g., *MERLIN2* [59] by Liu and Paulino [53] and *Origami Simulator* [60] by Ghassaei *et. al.* [54], and they are also used within the form generation process. The rigidity of each face can be guaranteed by simply placing the rigid bars along the edges for the rigid origami with only triangular faces. However, to constrain the in-plane and out of plane deformation of faces with more than three edges, it is necessary to constrain the relative nodal displacements [34, 35] or to introduce diagonal bars and construct a bar-joint structure in a three-dimensional manner [36, 37], which tends to make the model complicated.

The conventional FE methods are also often used for the elastic and plastic deformation

analysis of rigid origami [10, 61]. Shell elements are usually used in a finite element (FE) model of a rigid origami to model the origami faces, and the crease lines are represented by hinge elements or narrow shell elements with small bending stiffness as shown in Fig. 2.1(c) They are suited to the analysis of detailed mechanical properties of rigid origami, such as local deformation. However, their computational cost is often high and not suited to the large scale analysis and the form generation where the analysis should be carried out repeatedly.

To overcome the difficulty in a rotational hinge model, a truss model, and an FE model as mentioned above, a frame model shown in Fig. 2.1(d) has been proposed by Hayakawa and Ohsaki [28–31] based on the concept of a partially rigid frame [38–40]. Frame members are connected by hinges whose axes are parallel to the crease lines, and rigidly connected on the faces. Details of the configuration of a frame model are explained in Section 2.2. A frame model is used for the form generation and the kinematic analysis with the assumption that the faces of a rigid origami is completely rigid, and the exact rigid-fold path can be obtained. A frame model has an advantage of being able to represent a rigid origami with a simpler configuration than a rotational hinge model and a truss model. Analysis with boundary conditions can be easily performed compared to a rotational hinge model since the nodal coordinates are variables in the frame model. In addition, there is no need to constrain nodal displacements or arrange members three-dimensionally, as is the case with a truss model, to constrain the deformation of faces with more than three edges since each face is composed of multiple rigidly-joined frame elements. The structure of the frame model can be represented directly using beam elements and hinges implemented in general FEA software, and the kinematic analysis can be easily performed with FEA software without using special software.

2.2 Structure of frame model

2.2.1 Components of frame model

A frame model is a kind of partially rigid frame [38–40] representing a rigid origami mechanism [28–31]. Figure 2.2 shows an example of Miura-ori modeled by a frame model. A frame model consists of *nodes*, *members* (frame elements), and *hinges*. The basic structure of a frame model is shown by gray bold lines in Fig. 2.2(a) which represents a shape of the rigid origami. The face with more than three edges is divided into some triangles by the *dividing edges*. The crease lines and the dividing edges are collectively referred to as the *inner edges*. In addition, the inner edges and perimeter edges are collectively referred to as the *origami edges* or simply the *edges* in this study. Although cuts along the edges are also introduced in Chapter 3, they are not considered in this chapter for simplicity. Note that the edges constituting the cuts are treated the same as the inner edges in the formulation of constraints considered in Section 2.2.2. Nodes are located at the center points of origami edges and at the barycenters of triangular faces. As shown by gray in Fig. 2.2(b), two members are connected to the node on a crease line, and a member is connected to

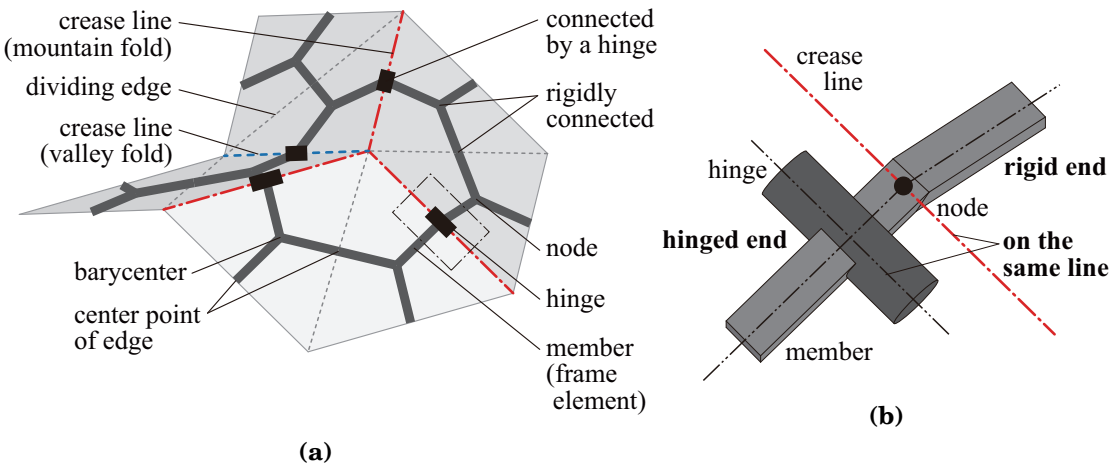

Figure 2.2: Configuration of a frame model representing a Miura-ori pattern; (a) Overall view, (b) Enlarged view of the region surrounded by the dotted lines in the overall view.

the node rigidly and another member is connected to the node via a hinge. In this study, the member end connected to a node rigidly is called the *rigid end*, and the member end connected via a hinge is called the *hinged end*. The axis of each hinge coincides with the corresponding crease line. Note that a member axis is not necessarily perpendicular to the origami edge where the node to which its end connects is located, and a hinge axis is not necessarily perpendicular to the axis of the member connected to it.

The nodal coordinates are used to represent the coordinates of the origami vertices, and they are treated as the design variables in the form generation method proposed in Chapter 3. The number of nodes in a frame model is generally larger than the number of vertices of the corresponding origami surface, and if all nodal coordinates are given arbitrarily, the vertex coordinates cannot be determined consistently. Therefore, the constraint equations satisfied by the nodal coordinates are formulated in Section 2.2.2 on the basis that the origami faces are divided into triangles and the nodes are located at the center points of edges and at the barycenters of triangular faces. Furthermore, a method is shown for extracting a sufficient number of independent nodal coordinates from the constraint equations to represent the vertex coordinates. On the other hand, in the analysis of deformation mechanism of the frame model, the displacements of nodes and members and the increments of the rotation angles of hinges are treated as independent variables. The geometric constraint equations referred to as the *compatibility equations* are formulated with respect to these variables based on the formulation by Watada and Ohsaki [40] which considers the finite translational and rotational displacement. While the hinge rotation angle increments are not included in the formulation in Ref. [40], they are included in the independent variables to simplify the calculation of the stiffness matrix of the frame model used in Chapters 3 and 5. Therefore, the compatibility equations for the hinge rotation angle increments are added to the formulation in Ref. [40].

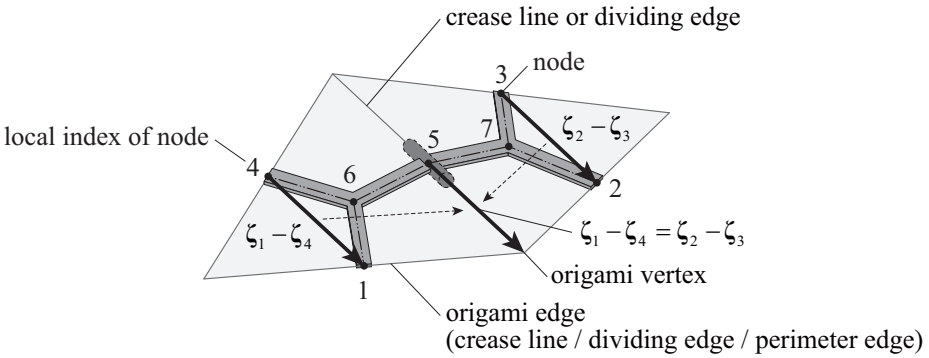

Figure 2.3: Local indices of nodes on the triangular faces adjacent to the crease line or the dividing edge where node 5 is located.

2.2.2 Independent nodal coordinates

In the form generation method, the nodal coordinates of a frame model are used as the design variables. However, the number of those variables is much larger than that required to determine the positions of vertices of the corresponding origami surface. Therefore, in the form generation of rigid origami, the number of variables are reduced by considering the geometric constraints for a consistent representation of the origami shape, and only the independent nodal coordinates are treated as variables. In the following, the constraint equations which nodal coordinates satisfy are formulated assuming that the nodes are always located at the center points of edges and the barycenters of faces, and a method is shown to identify the independent nodal coordinates using the constraint equations. The consistency equations are first formulated locally, and extended to the global expression for the entire origami surface.

Let $\boldsymbol{\zeta}_1, \ldots, \boldsymbol{\zeta}_7 \in \mathbb{R}^3$ denote the position vectors of nodes 1–7 shown in Fig. 2.3 where the indices of nodes are the local indices defined at the adjacent triangular faces. Since the nodes on the edges are located at the center points of the edges, $\boldsymbol{\zeta}_1 - \boldsymbol{\zeta}_4$ and $\boldsymbol{\zeta}_2 - \boldsymbol{\zeta}_3$ should be equal to the vector parallel to the edge where node 5 is located as shown in Fig. 2.3, and $\boldsymbol{\zeta}_1, \ldots, \boldsymbol{\zeta}_4$ satisfy the following consistency equations

$$\boldsymbol{\zeta}_1 - \boldsymbol{\zeta}_4 = \boldsymbol{\zeta}_2 - \boldsymbol{\zeta}_3 \tag{2.1}$$

Equation (2.1) is rewritten by using a 3×21 matrix and a 21-dimestional vector as follows:

$$\begin{bmatrix} \mathbf{I}_3 & -\mathbf{I}_3 & \mathbf{I}_3 & -\mathbf{I}_3 & \mathbf{O}_3 & \mathbf{O}_3 & \mathbf{O}_3 \end{bmatrix} \begin{pmatrix} \boldsymbol{\zeta}_1 \\ \boldsymbol{\zeta}_2 \\ \boldsymbol{\zeta}_3 \\ \boldsymbol{\zeta}_4 \\ \boldsymbol{\zeta}_5 \\ \boldsymbol{\zeta}_6 \\ \boldsymbol{\zeta}_7 \end{pmatrix} = \mathbf{0} \tag{2.2}$$

where $\mathbf{I}_n$ and $\mathbf{O}_n$ are the $n \times n$ identity matrix and the $n \times n$ zero matrix, respectively. Note

that the edge where node 5 is located is a crease line or a dividing edge. The member connecting nodes 5 and 6 and the member connecting nodes 5 and 7 are connected via a hinge if the edge where node 5 is located is a crease line and the members are rigidly connected if the edge is a dividing edge. In addition, since the nodes on the faces are located at the barycenters of the faces, the position vectors of the nodes satisfy the following consistency equations:

$$\boldsymbol{\zeta}_6 = \frac{\boldsymbol{\zeta}_1 + \boldsymbol{\zeta}_4 + \boldsymbol{\zeta}_5}{3} \tag{2.3}$$

$$\boldsymbol{\zeta}_7 = \frac{\boldsymbol{\zeta}_2 + \boldsymbol{\zeta}_3 + \boldsymbol{\zeta}_5}{3} \tag{2.4}$$

Equations (2.3) and (2.4) are rewritten for each face by using 3×21 matrices and a 21-dimestional vector as follows:

$$\begin{bmatrix} \frac{1}{3}\mathbf{I}_3 & \mathbf{O}_3 & \mathbf{O}_3 & \frac{1}{3}\mathbf{I}_3 & \frac{1}{3}\mathbf{I}_3 & -\mathbf{I}_3 & \mathbf{O}_3 \end{bmatrix} \begin{pmatrix} \boldsymbol{\zeta}_1 \\ \boldsymbol{\zeta}_2 \\ \boldsymbol{\zeta}_3 \\ \boldsymbol{\zeta}_4 \\ \boldsymbol{\zeta}_5 \\ \boldsymbol{\zeta}_6 \\ \boldsymbol{\zeta}_7 \end{pmatrix} = \mathbf{0} \tag{2.5}$$

$$\begin{bmatrix} \mathbf{O}_3 & \frac{1}{3}\mathbf{I}_3 & \frac{1}{3}\mathbf{I}_3 & \mathbf{O}_3 & \frac{1}{3}\mathbf{I}_3 & \mathbf{O}_3 & -\mathbf{I}_3 \end{bmatrix} \begin{pmatrix} \boldsymbol{\zeta}_1 \\ \boldsymbol{\zeta}_2 \\ \boldsymbol{\zeta}_3 \\ \boldsymbol{\zeta}_4 \\ \boldsymbol{\zeta}_5 \\ \boldsymbol{\zeta}_6 \\ \boldsymbol{\zeta}_7 \end{pmatrix} = \mathbf{0} \tag{2.6}$$

Here, let N_E, N_Ein, and N_F denote the number of edges, inner edges, and triangular faces of the origami surface, respectively. Then, the number of nodes of the frame model is calculated as $N_\mathrm{N} = N_\mathrm{E} + N_\mathrm{F}$. The position vectors of nodes are assembled into a vector for all nodes as $\mathbf{Z} = (\boldsymbol{\zeta}_1^\mathsf{T}, \ldots, \boldsymbol{\zeta}_{N_\mathrm{N}}^\mathsf{T})^\mathsf{T} \in \mathbb{R}^{3n_\mathrm{N}}$. Then, the *edge consistency matrix* $\mathbf{C}_\mathrm{E} \in \mathbb{R}^{3N_\mathrm{Ein} \times 3N_\mathrm{N}}$ is defined by extending and assembling the coefficient matrix in the left-hand side of Eq. (2.2) for all the inner edges and all the nodes, and the consistency equation at the inner edges for the entire origami surface is written as follows:

$$\mathbf{C}_\mathrm{E}\mathbf{Z} = \mathbf{0} \tag{2.7}$$

In the same way, the *face consistency matrix* $\mathbf{C}_\mathrm{F} \in \mathbb{R}^{3N_\mathrm{F} \times 3N_\mathrm{N}}$ is defined by extending and assembling the coefficient matrices in the left-hand sides of Eqs. (2.5) and (2.6) for all the faces and all the nodes, and the consistency equation at the faces for the entire origami surface is written as follows:

$$\mathbf{C}_\mathrm{F}\mathbf{Z} = \mathbf{0} \tag{2.8}$$

Therefore, the linear constraints for the consistent representation of the origami surface by the nodal coordinates of the frame model can be summarized as follows:

$$\begin{bmatrix} \mathbf{C}_\mathrm{E} \\ \mathbf{C}_\mathrm{F} \end{bmatrix} \mathbf{Z} = \mathbf{C}_\mathrm{N}\mathbf{Z} = \mathbf{0} \tag{2.9}$$

In this study, $\mathbf{C}_\mathrm{N} \in \mathbb{R}^{3(N_\mathrm{Ein}+N_\mathrm{F})\times 3N_\mathrm{N}}$ is referred to as the *node consistency matrix*.

The independent components of $\mathbf{Z}$ satisfying the consistency equation (2.9) are identified by a method utilizing the reduced row-echelon form (RREF) [62] of the node consistency matrix $\mathbf{C}_\mathrm{N}$. Details of the method is explained in Appendix A. The columns of the RREF of a matrix can be classified into pivot and non-pivot columns, and let $\mathbf{Z}_\mathrm{pivot} \in \mathbb{R}^{\mathrm{rank}(\mathbf{C}_\mathrm{N})}$ and $\mathbf{Z}_\mathrm{free} \in \mathbb{R}^{3N_\mathrm{N}-\mathrm{rank}(\mathbf{C}_\mathrm{N})}$ denote the vectors whose components are those of $\mathbf{Z}$ corresponding to the pivot and non-pivot columns of the RREF of $\mathbf{C}_\mathrm{N}$. Then, defining $\mathbf{C}_\mathrm{free} \in \mathbb{R}^{\mathrm{rank}(\mathbf{C}_\mathrm{N})\times(3N_\mathrm{N}-\mathrm{rank}(\mathbf{C}_\mathrm{N}))}$ as the matrix which is the assemblage of the components of the RREF of $\mathbf{C}_\mathrm{N}$ in the non-zero rows and the non-pivot columns, Eq. (2.9) is equivalent to the following equation:

$$\begin{bmatrix} \mathbf{I}_{\mathrm{rank}(\mathbf{C}_\mathrm{N})} & \mathbf{C}_\mathrm{free} \end{bmatrix} \begin{pmatrix} \mathbf{Z}_\mathrm{pivot} \\ \mathbf{Z}_\mathrm{free} \end{pmatrix} = \mathbf{Z}_\mathrm{pivot} + \mathbf{C}_\mathrm{free}\mathbf{Z}_\mathrm{free} = \mathbf{0} \tag{2.10}$$

Therefore, the vectors of independent and dependent nodal coordinates of the frame model can be identified as $\mathbf{Z}_\mathrm{pivot}$ and $\mathbf{Z}_\mathrm{free}$, respectively. Note that the number of independent coordinates is $N_\mathrm{free} = 3N_\mathrm{N} - \mathrm{rank}(\mathbf{C}_\mathrm{N})$. The vector of the dependent nodal coordinates satisfying Eq. (2.9) is calculated from the RREF of $\mathbf{C}_\mathrm{N}$ as follows:

$$\mathbf{Z}_\mathrm{pivot} = -\mathbf{C}_\mathrm{free}\mathbf{Z}_\mathrm{free} \tag{2.11}$$

In addition, the vector of all the nodal coordinates $\mathbf{Z}$ can be written as the rearrangement of the components of $\mathbf{Z}_\mathrm{pivot}$ and $\mathbf{Z}_\mathrm{free}$ as follows:

$$\mathbf{Z} = \mathbf{C}_\mathrm{O} \begin{pmatrix} \mathbf{Z}_\mathrm{pivot} \\ \mathbf{Z}_\mathrm{free} \end{pmatrix} \tag{2.12}$$

where, $\mathbf{C}_\mathrm{O} \in \mathbb{R}^{3N_\mathrm{N}\times 3N_\mathrm{N}}$ is a matrix representing the rearrangement of the components from $(\mathbf{Z}_\mathrm{pivot}^\mathsf{T}, \mathbf{Z}_\mathrm{free}^\mathsf{T})^\mathsf{T}$ to $\mathbf{Z}$, whose (i,j) component is 1 if the i-th component of $\mathbf{Z}$ corresponds to the j-th component of $(\mathbf{Z}_\mathrm{pivot}^\mathsf{T}, \mathbf{Z}_\mathrm{free}^\mathsf{T})^\mathsf{T}$; and otherwise 0. Substituting Eq. (2.11) to (2.12), $\mathbf{Z}$ satisfying Eq. (2.9) can be calculated form the independent nodal coordinates as follows:

$$\begin{aligned} \mathbf{Z} &= \mathbf{C}_\mathrm{A}\mathbf{Z}_\mathrm{free} \\ \mathbf{C}_\mathrm{A} &= \mathbf{C}_\mathrm{O} \begin{bmatrix} -\mathbf{C}_\mathrm{free} \\ \mathbf{I}_{N_\mathrm{free}} \end{bmatrix} \in \mathbb{R}^{3N_\mathrm{N}\times N_\mathrm{free}} \end{aligned} \tag{2.13}$$

The example of a single inner vertex origami surface is shown in Appendix B.

The positions of the origami vertices are also determined by the independent nodal coordinates $\mathbf{Z}_\mathrm{free}$ if Eq. (2.9) is satisfied. First, the linear constraint equations are formulated for the position vectors of a single inner vertex and the nodes around it. Let M_F denote the

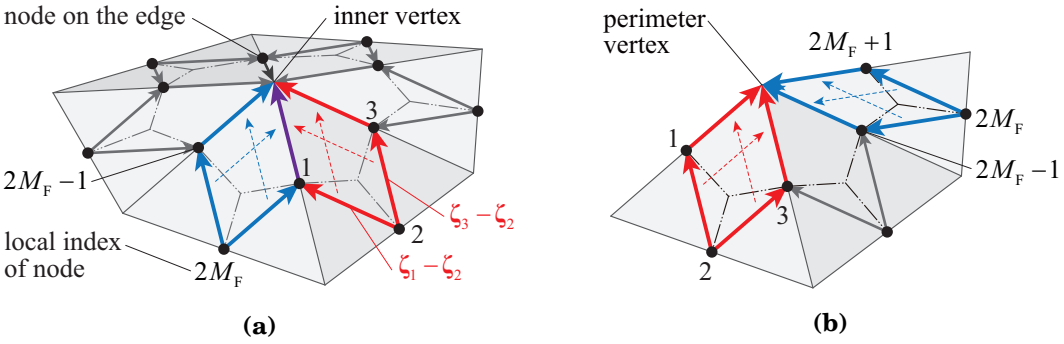

Figure 2.4: Local indices of nodes around an origami vertex; (a) Inner vertex, (b) Perimeter vertex.

number of faces around to an inner vertex to be considered. The local indices of $2M_F$ nodes on the edges are arranged in counterclockwise as shown in Fig. 2.4(a). The position vector $\boldsymbol{\xi}$ of the center vertex in Fig. 2.4(a) can be expressed in M_F different ways using the position vectors of nodes $\boldsymbol{\zeta}_1,\ldots,\boldsymbol{\zeta}_{2M_F}$ as follows:

$$\begin{cases} \boldsymbol{\xi} = \boldsymbol{\zeta}_1 - \boldsymbol{\zeta}_2 + \boldsymbol{\zeta}_3 \\ \quad \vdots \\ \boldsymbol{\xi} = \boldsymbol{\zeta}_{2M_F-1} - \boldsymbol{\zeta}_{2M_F} + \boldsymbol{\zeta}_1 \end{cases} \tag{2.14}$$

where the subscripts of position vectors of nodes are the local indices of nodes on the edges. Then, M_F equations in Eq. (2.14) can be combined into a vector equation as follows:

$$\begin{bmatrix} \mathbf{I}_3 \\ \vdots \\ \mathbf{I}_3 \end{bmatrix} \boldsymbol{\xi} = \begin{bmatrix} \mathbf{I}_3 & -\mathbf{I}_3 & \mathbf{I}_3 & \cdots & \mathbf{O}_3 & \mathbf{O}_3 \\ \vdots & \vdots & \vdots & \ddots & \vdots & \vdots \\ \mathbf{I}_3 & \mathbf{O}_3 & \mathbf{O}_3 & \cdots & \mathbf{I}_3 & -\mathbf{I}_3 \end{bmatrix} \begin{pmatrix} \boldsymbol{\zeta}_1 \\ \boldsymbol{\zeta}_2 \\ \boldsymbol{\zeta}_3 \\ \vdots \\ \boldsymbol{\zeta}_{2M_F-1} \\ \boldsymbol{\zeta}_{2M_F} \end{pmatrix} \tag{2.15}$$

where the coefficient matrix of $\boldsymbol{\xi}$ in the left-hand side of Eq. (2.15) is a $3M_F \times 3$ matrix consisting of M_F identity matrices stacked in the row direction and the coefficient matrix of the assemblage of the position vectors of nodes in the right-hand side of Eq. (2.15) is a $3M_F \times 6M_F$ matrix. Here, the Moore-Penrose inverse [63] of the coefficient matrix of $\boldsymbol{\xi}$ in the left-hand side of Eq. (2.15) can be calculated as the transpose of $\mathbf{E}_{M_F}$ divided by M_F, and the following equation holds:

$$\frac{1}{M_F} \begin{bmatrix} \mathbf{I}_3 & \cdots & \mathbf{I}_3 \end{bmatrix} \begin{bmatrix} \mathbf{I}_3 \\ \vdots \\ \mathbf{I}_3 \end{bmatrix} = \mathbf{I}_3 \tag{2.16}$$

Therefore, Eq. (2.15) can be solved for $\boldsymbol{\xi}$ as follows:

$$\boldsymbol{\xi} = \frac{1}{M_\mathrm{F}} \begin{bmatrix} 2\mathbf{I}_3 & -\mathbf{I}_3 & 2\mathbf{I}_3 & \cdots & 2\mathbf{I}_3 & -\mathbf{I}_3 \end{bmatrix} \begin{pmatrix} \boldsymbol{\zeta}_1 \\ \boldsymbol{\zeta}_2 \\ \boldsymbol{\zeta}_3 \\ \vdots \\ \boldsymbol{\zeta}_{2M_\mathrm{F}-1} \\ \boldsymbol{\zeta}_{2M_\mathrm{F}} \end{pmatrix} \tag{2.17}$$

where coefficient matrix of the assemblage of the position vectors of nodes in the right-hand side of Eq. (2.19) is a $3 \times 6M_\mathrm{F}$ matrix. Note that if the nodal coordinates satisfy Eq. (2.9), $M_\mathrm{F} - 1$ of the M_F equations in Eq. (2.14) are equivalent to Eq. (2.7), and Eq. (2.17) is equivalent to one of the M_F equations in Eq. (2.14). On the other hand, if the nodal coordinates do not satisfy Eq. (2.9) and have some errors, the number of independent equations among the $3M_\mathrm{F}$ equations in Eq. (2.14) is not necessarily three, and Eq. (2.17) represents the average position of the considered vertex calculated from M_F different forms in Eq. (2.14). This situation arises other than for form generation; e.g., the large-deformation analysis of the frame model carried out using general finite element analysis software where the members are represented by the elastic beam elements and their deformation is allowed. Because of the property of the Moore-Penrose inverse, $\boldsymbol{\xi}$ obtained from Eq. (2.17) is the position vector of the considered vertex with the minimum error.

In case of a single perimeter vertex shown in Fig 2.4(b), the position vector $\boldsymbol{\xi}$ of the center vertex in Fig. 2.4(b) can also be expressed in M_F different ways using the position vectors of nodes $\boldsymbol{\zeta}_1, \ldots, \boldsymbol{\zeta}_{2M_\mathrm{F}+1}$ as follows:

$$\begin{cases} \boldsymbol{\xi} = \boldsymbol{\zeta}_1 - \boldsymbol{\zeta}_2 + \boldsymbol{\zeta}_3 \\ \quad \vdots \\ \boldsymbol{\xi} = \boldsymbol{\zeta}_{2M_\mathrm{F}-1} - \boldsymbol{\zeta}_{2M_\mathrm{F}} + \boldsymbol{\zeta}_{2M_\mathrm{F}+1} \end{cases} \tag{2.18}$$

The difference between Eqs. (2.14) and (2.18) is that $\boldsymbol{\zeta}_1$ in the last equation of Eq. (2.14) is replaced with $\boldsymbol{\zeta}_{2M_\mathrm{F}+1}$ in Eq. (2.18). In a similar manner as Eq. (2.17), Eq. (2.18) can be solved for $\boldsymbol{\xi}$ as follows:

$$\boldsymbol{\xi} = \frac{1}{M_\mathrm{F}} \begin{bmatrix} \mathbf{I}_3 & -\mathbf{I}_3 & 2\mathbf{I}_3 & \cdots & 2\mathbf{I}_3 & -\mathbf{I}_3 & \mathbf{I}_3 \end{bmatrix} \begin{pmatrix} \boldsymbol{\zeta}_1 \\ \boldsymbol{\zeta}_2 \\ \boldsymbol{\zeta}_3 \\ \vdots \\ \boldsymbol{\zeta}_{2M_\mathrm{F}-1} \\ \boldsymbol{\zeta}_{2M_\mathrm{F}} \\ \boldsymbol{\zeta}_{2M_\mathrm{F}+1} \end{pmatrix} \tag{2.19}$$

where coefficient matrix of the assemblage of the position vectors of nodes in the right-hand side of Eq. (2.19) is a $3 \times (6M_\mathrm{F} + 3)$ matrix.

Let N_V and $\boldsymbol{\Xi} \in \mathbb{R}^{3N_V}$ denote the number of origami vertices and a vector which is an assemblage of the position vectors of vertices for all the vertices. A $3N_V \times 3N_N$ matrix $\mathbf{C}_V$ is defined by extending and assembling the coefficient matrices of the assemblages of the position vectors of nodes in the right-hand side of Eqs. (2.17) and (2.19) for all the vertices and nodes, and then, $\boldsymbol{\Xi}$ can be calculated from the vector of the nodal coordinates $\mathbf{Z}$ as follows:

$$\boldsymbol{\Xi} = \mathbf{C}_V \mathbf{Z} \tag{2.20}$$

For the calculation of $\mathbf{C}_V$ for a single inner vertex origami surface, see Appendix B. Furthermore, if $\mathbf{Z}$ satisfies Eq. (2.9), substitution of $\mathbf{Z}$ in Eq. (2.13) into Eq. (2.20) leads to expression of $\boldsymbol{\Xi}$ by the vector of the independent nodal coordinates $\mathbf{Z}_{\text{free}} \in \mathbb{R}^{N_{\text{free}}}$ as follows:

$$\boldsymbol{\Xi} = \mathbf{C}_V \mathbf{C}_A \mathbf{Z}_{\text{free}} \tag{2.21}$$

In order for $\boldsymbol{\Xi}$ to be uniquely determined from $\mathbf{Z}_{\text{free}}$ by Eq. (2.21), the following equation needs to hold:

$$\text{rank}(\mathbf{C}_V \mathbf{C}_A) = 3N_V \tag{2.22}$$

Here, $\text{rank}(\mathbf{C}_V \mathbf{C}_A)$ satisfies the following inequality:

$$\text{rank}(\mathbf{C}_V \mathbf{C}_A) \leq \min(3N_V, N_{\text{free}}) \tag{2.23}$$

According to Eqs. (2.22) and (2.23), N_V and N_{free} should satisfy the following inequality:

$$N_{\text{free}} \geq 3N_V \tag{2.24}$$

On the other hand, $\mathbf{Z}_{\text{free}}$ is always uniquely determined from $\boldsymbol{\Xi}$ by the construction of the frame model. Therefore, there exists a row full-rank matrix $\mathbf{C}_{VN} \in \mathbb{R}^{N_{\text{free}} \times 3N_V}$; i.e., $\text{rank}(\mathbf{C}_{VN}) = N_{\text{free}}$, which satisfies the following equation:

$$\mathbf{Z}_{\text{free}} = \mathbf{C}_{VN} \boldsymbol{\Xi} \tag{2.25}$$

Since $\mathbf{C}_{VN}$ is row full-rank, the following inequality holds:

$$\text{rank}(\mathbf{C}_{VN}) = N_{\text{free}} \leq 3N_V \tag{2.26}$$

According to Eqs. (2.24) and (2.26), it can be concluded that $N_{\text{free}} = 3N_V$; i.e., the number of independent nodal coordinates is equal to the number of coordinates of all the vertices.

2.3 Infinitesimal rigid-folding mechanism of frame model

In this section, formulation of the compatibility equations of a frame model in the finite displacement are first presented for the analysis of the infinitesimal mechanism of a frame model. The compatibility equations are formulated with respect to the generalized displacements including translational and rotational displacements of nodes and members and increments of rotation angles of hinges [31, 40, 64]. Then the infinitesimal rigid-folding mechanism is investigated based on the method presented in Ref. [40].

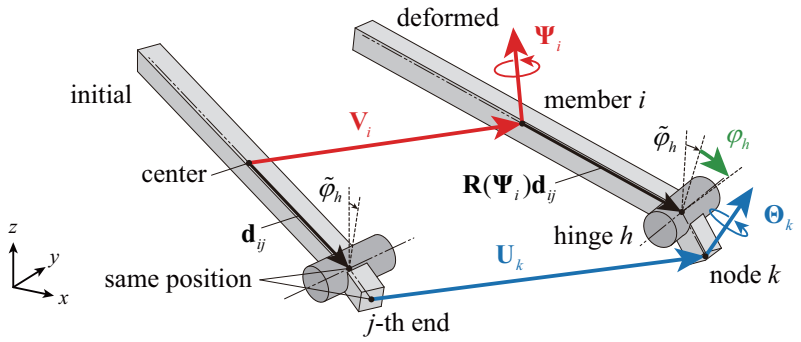

Figure 2.5: Displacements of member i and node k and increment of the rotation angle of hinge h of a frame model.

2.3.1 Compatibility condition at the rigid end

Let N_{M}, N_{N}, and N_{H} denote the number of members, nodes, and hinges, respectively. As shown in Fig. 2.5, the translation vectors of the center point of member i $(=1,\ldots,n_{\mathrm{M}})$ and node k $(=1,\ldots,n_{\mathrm{N}})$ in the global coordinate system (x,y,z) are represented by $\mathbf{V}_i = (V_i^{(1)},V_i^{(2)},V_i^{(3)})^{\mathsf{T}}$ and $\mathbf{U}_k = (U_k^{(1)},U_k^{(2)},U_k^{(3)})^{\mathsf{T}} \in \mathbb{R}^3$, respectively. The rotation vectors are also represented by $\boldsymbol{\Psi}_i = (\Psi_i^{(1)},\Psi_i^{(2)},\Psi_i^{(3)})^{\mathsf{T}}$ and $\boldsymbol{\Theta}_k = (\Theta_k^{(1)},\Theta_k^{(2)},\Theta_k^{(3)})^{\mathsf{T}} \in \mathbb{R}^3$, respectively. The direction and the norm of a rotation vector represent the rotation axis and the rotation angle, respectively. Here, the Rodrigues' rotation matrix $\mathbf{R}(\boldsymbol{\Psi}_i)$ with respect to the rotation vector $\boldsymbol{\Psi}_i$ is defined as follows [64]:

$$\mathbf{R}(\boldsymbol{\Psi}_i) = \cos(\|\boldsymbol{\Psi}_i\|)\mathbf{I}_3 + \frac{1}{\|\boldsymbol{\Psi}_i\|^2}\{1-\cos(\|\boldsymbol{\Psi}_i\|)\}\boldsymbol{\Psi}_i\boldsymbol{\Psi}_i{}^{\mathsf{T}} + \frac{1}{\|\boldsymbol{\Psi}_i\|}\sin(\|\boldsymbol{\Psi}_i\|)[\boldsymbol{\Psi}_i]_\times \tag{2.27}$$

where $\mathbf{I}_3 \in \mathbb{R}^3$ is the 3×3 identity matrix and $[\boldsymbol{\Psi}_i]_\times$ represents the cross-product matrix with respect to $\boldsymbol{\Psi}_i$, which is defined as follows:

$$[\boldsymbol{\Psi}_i]_\times = \begin{bmatrix} 0 & -\Psi_i^{(3)} & \Psi_i^{(2)} \\ \Psi_i^{(3)} & 0 & -\Psi_i^{(1)} \\ -\Psi_i^{(2)} & \Psi_i^{(1)} & 0 \end{bmatrix}$$

The detailed calculation of Eq. (2.27) is shown in Appendix C. Let $\mathbf{d}_{ij} \in \mathbb{R}^3$ denote the vector directing from the center point of member i to the j-th end $(j=1,2)$ of member i at the initial undeformed state as shown in Fig. 2.5. Then, the vector obtained by rotating $\mathbf{d}_{ij}$ with member i is to be $\mathbf{R}(\boldsymbol{\Psi}_i)\mathbf{d}_{ij}$. When j-th end of member i is connected to node k, the following equation holds since the translation of the j-th end of member i and the translation of node k are the same:

$$\begin{aligned} &\mathbf{U}_k = -\mathbf{d}_{ij} + \mathbf{V}_i + \mathbf{R}(\boldsymbol{\Psi}_i)\mathbf{d}_{ij} \\ \Leftrightarrow &\mathbf{U}_k - \mathbf{V}_i - \{\mathbf{R}(\boldsymbol{\Psi}_i) - \mathbf{I}_3\}\mathbf{d}_{ij} = \mathbf{0} \end{aligned} \tag{2.28}$$

In addition, if member i is rigidly connected to node k, the rotation of member i is equal to the rotation of node k, and the following equation holds:

$$\boldsymbol{\Theta}_k - \boldsymbol{\Psi}_i = \mathbf{0} \tag{2.29}$$

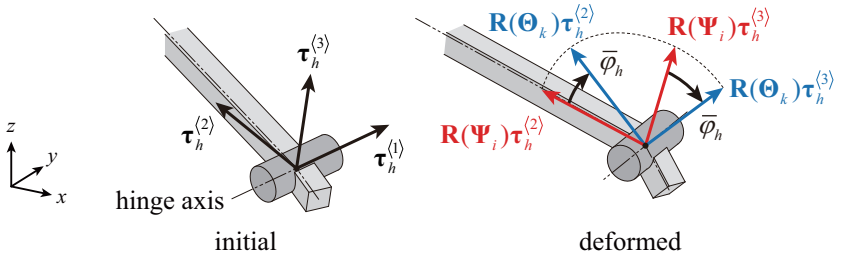

Figure 2.6: Reference frame of hinge h and its rotation with member i and node k

2.3.2 Compatibility condition at the hinged end

As shown in Fig. 2.6, the reference frame of hinge h $(=1,\ldots,N_{\mathrm{H}})$ in the initial undeformed state is defined by the three unit vectors $\boldsymbol{\tau}_h^{\langle l\rangle} \in \mathbb{R}^3$ $(l=1,2,3)$. The unit vector $\boldsymbol{\tau}_h^{\langle 1\rangle}$ is parallel to the rotation axis of hinge h at the initial state in the global coordinate system (x,y,z), and $\boldsymbol{\tau}_h^{\langle 2\rangle}$ and $\boldsymbol{\tau}_h^{\langle 3\rangle}$ are defined as the unit vectors satisfying the following equations:

$$\begin{aligned}\boldsymbol{\tau}_h^{\langle 1\rangle} \times \boldsymbol{\tau}_h^{\langle 2\rangle} &= \boldsymbol{\tau}_h^{\langle 3\rangle}\\ \boldsymbol{\tau}_h^{\langle 2\rangle} \times \boldsymbol{\tau}_h^{\langle 3\rangle} &= \boldsymbol{\tau}_h^{\langle 1\rangle}\end{aligned}$$

Consider the case where the j-th end of member i is connected to node k via hinge h. As in the case of a rigid end, the translation between the center point of member i and node k need to satisfy Eq. (2.28). Since the relative rotation of member i and node k is allowed only around the rotation axis of hinge h, the vector obtained by rotating $\boldsymbol{\tau}_h^{\langle 1\rangle}$ with member i must be perpendicular to the vectors obtained by rotating $\boldsymbol{\tau}_h^{\langle 2\rangle}$ and $\boldsymbol{\tau}_h^{\langle 3\rangle}$ with node k, and the rotation vectors of member i and node k need to satisfy the following equations:

$$\begin{aligned}\left(\mathbf{R}(\boldsymbol{\Psi}_i)\boldsymbol{\tau}_h^{\langle 1\rangle}\right)\cdot\left(\mathbf{R}(\boldsymbol{\Theta}_k)\boldsymbol{\tau}_h^{\langle 2\rangle}\right) &= 0\\ \left(\mathbf{R}(\boldsymbol{\Psi}_i)\boldsymbol{\tau}_h^{\langle 1\rangle}\right)\cdot\left(\mathbf{R}(\boldsymbol{\Theta}_k)\boldsymbol{\tau}_h^{\langle 3\rangle}\right) &= 0\end{aligned} \tag{2.30}$$

As shown in Fig. 2.5, the increment of the rotation angle of hinge h from the initial state to the deformed state is denoted by $\varphi_h \in \mathbb{R}$. The direction of the rotation; i.e., the sign of φ_h, obeys right-hand screw rule along vector $\boldsymbol{\tau}_h^{\langle 1\rangle}$. Note that the hinge rotation angle at the initial state is not necessarily equal to zero, and the residual angle $\bar{\varphi}_h \in \mathbb{R}$ at the initial state may exist. In this study, φ_h is treated as an independent variable although it is not in Ref. [40] and calculated from the displacements of the node and the center point of the member. This simplifies the calculation presented in the following; e.g., prediction of the existence of a locked crease line in the form generation process in Chapter 3 and calculation of the total potential energy and its derivatives for the equilibrium path analysis in Chapter 5 . Assuming that Eq. (2.30) holds and $\mathbf{R}(\boldsymbol{\Psi}_i)\boldsymbol{\tau}_h^{\langle 1\rangle}$ and $\mathbf{R}(\boldsymbol{\Theta}_k)\boldsymbol{\tau}_h^{\langle 1\rangle}$ always coincide during the deformation process, the ideal value of φ_h denoted by $\bar{\varphi}_h$ and shown in Fig. 2.6 can be determined from the following equations:

$$\sin\bar{\varphi}_h = \left(\mathbf{R}(\boldsymbol{\Psi}_i)\boldsymbol{\tau}_h^{\langle 3\rangle}\right)\cdot\left(\mathbf{R}(\boldsymbol{\Theta}_k)\boldsymbol{\tau}_h^{\langle 2\rangle}\right) = -\left(\mathbf{R}(\boldsymbol{\Psi}_i)\boldsymbol{\tau}_h^{\langle 2\rangle}\right)\cdot\left(\mathbf{R}(\boldsymbol{\Theta}_k)\boldsymbol{\tau}_h^{\langle 3\rangle}\right) \tag{2.31}$$

$$\cos\bar{\varphi}_h = \left(\mathbf{R}(\boldsymbol{\Psi}_i)\boldsymbol{\tau}_h^{\langle 2\rangle}\right)\cdot\left(\mathbf{R}(\boldsymbol{\Theta}_k)\boldsymbol{\tau}_h^{\langle 2\rangle}\right) = \left(\mathbf{R}(\boldsymbol{\Psi}_i)\boldsymbol{\tau}_h^{\langle 3\rangle}\right)\cdot\left(\mathbf{R}(\boldsymbol{\Theta}_k)\boldsymbol{\tau}_h^{\langle 3\rangle}\right) \tag{2.32}$$

Therefore, assuming that φ_h satisfies $|\varphi_h - \bar{\varphi}_h| < 2\pi$ throughout the deformation process, the compatibility equation for φ_h is written as follows [64]:

$$\begin{aligned}
&\sin(\varphi_h - \bar{\varphi}_h) = 0 \\
\Leftrightarrow\ &\left\{\left(\mathbf{R}(\boldsymbol{\Psi}_i)\boldsymbol{\tau}_h^{\langle 2\rangle}\right)\cdot\left(\mathbf{R}(\boldsymbol{\Theta}_k)\boldsymbol{\tau}_h^{\langle 2\rangle}\right)\right\}\sin\varphi_h + \left\{\left(\mathbf{R}(\boldsymbol{\Psi}_i)\boldsymbol{\tau}_h^{\langle 2\rangle}\right)\cdot\left(\mathbf{R}(\boldsymbol{\Theta}_k)\boldsymbol{\tau}_h^{\langle 3\rangle}\right)\right\}\cos\varphi_h = 0 \\
\Leftrightarrow\ &\left(\mathbf{R}(\boldsymbol{\Psi}_i)\boldsymbol{\tau}_h^{\langle 2\rangle}\right)\cdot\left\{\sin\varphi_h\left(\mathbf{R}(\boldsymbol{\Theta}_k)\boldsymbol{\tau}_h^{\langle 2\rangle}\right) + \cos\varphi_h\left(\mathbf{R}(\boldsymbol{\Theta}_k)\boldsymbol{\tau}_h^{\langle 3\rangle}\right)\right\} = 0
\end{aligned} \tag{2.33}$$

For the simple expression of the compatibility equations at a hinge end, the functions of $\boldsymbol{\Psi}_i$, $\boldsymbol{\Theta}_k$, and φ_h denote by $\Phi_{ij}^{(l)}(\boldsymbol{\Psi}_i, \boldsymbol{\Theta}_k, \varphi_h)$ $(l = 1,2,3)$ are defined to represent the left-hand sides of Eqs. (2.30) and (2.33) as follows:

$$\begin{aligned}
\Phi_{ij}^{(1)}(\boldsymbol{\Psi}_i, \boldsymbol{\Theta}_k, \varphi_h) &= \left(\mathbf{R}(\boldsymbol{\Psi}_i)\boldsymbol{\tau}_h^{\langle 1\rangle}\right)\cdot\left(\mathbf{R}(\boldsymbol{\Theta}_k)\boldsymbol{\tau}_h^{\langle 2\rangle}\right) \\
\Phi_{ij}^{(2)}(\boldsymbol{\Psi}_i, \boldsymbol{\Theta}_k, \varphi_h) &= \left(\mathbf{R}(\boldsymbol{\Psi}_i)\boldsymbol{\tau}_h^{\langle 1\rangle}\right)\cdot\left(\mathbf{R}(\boldsymbol{\Theta}_k)\boldsymbol{\tau}_h^{\langle 3\rangle}\right) \\
\Phi_{ij}^{(3)}(\boldsymbol{\Psi}_i, \boldsymbol{\Theta}_k, \varphi_h) &= \left(\mathbf{R}(\boldsymbol{\Psi}_i)\boldsymbol{\tau}_h^{\langle 2\rangle}\right)\cdot\left\{\sin\varphi_h\left(\mathbf{R}(\boldsymbol{\Theta}_k)\boldsymbol{\tau}_h^{\langle 2\rangle}\right) + \cos\varphi_h\left(\mathbf{R}(\boldsymbol{\Theta}_k)\boldsymbol{\tau}_h^{\langle 3\rangle}\right)\right\}
\end{aligned} \tag{2.34}$$

When the j-th end of member i is connected to node k via hinge h, the compatibility equations (2.30) and (2.33) satisfied by the rotations of member i and node k and the increment of the rotation angle of hinge h can be combined into a vector form as follows [31]:

$$\boldsymbol{\Phi}_{ij}(\boldsymbol{\Psi}_i, \boldsymbol{\Theta}_k, \varphi_h) = \begin{pmatrix} \Phi_{ij}^{(1)}(\boldsymbol{\Psi}_i, \boldsymbol{\Theta}_k, \varphi_h) \\ \Phi_{ij}^{(2)}(\boldsymbol{\Psi}_i, \boldsymbol{\Theta}_k, \varphi_h) \\ \Phi_{ij}^{(3)}(\boldsymbol{\Psi}_i, \boldsymbol{\Theta}_k, \varphi_h) \end{pmatrix} = \mathbf{0} \tag{2.35}$$

2.3.3 Compatibility equations for the entire structure

The compatibility equations for the entire structure of the frame model are formulated by summarizing the compatibility equations formulated in Sections 2.3.1 and 2.3.2. Let N_{B} denote the number of fixed degrees of freedom of the nodal displacements. The assemblage of the nodal displacements $\mathbf{U}_k$ and $\boldsymbol{\Theta}_k$ for all nodes that are not constrained and the assemblage of the member displacements $\mathbf{V}_i$ and $\boldsymbol{\Psi}_i$ for all members are represented by $\mathbf{U} \in \mathbb{R}^{6N_{\mathrm{N}}-N_{\mathrm{B}}}$ and $\mathbf{V} \in \mathbb{R}^{6N_{\mathrm{M}}}$, respectively. In addition, the vector consisting of φ_h, which is the increment of the rotation angle of the hinge, is denoted by $\boldsymbol{\varphi} \in \mathbb{R}^{N_{\mathrm{H}}}$. Then, the generalized displacement vector is defined as $\mathbf{W} = (\mathbf{U}^{\mathsf{T}}, \mathbf{V}^{\mathsf{T}}, \boldsymbol{\varphi}^{\mathsf{T}})^{\mathsf{T}} \in \mathbb{R}^{N_{\mathrm{W}}}$ where the number of components of $\mathbf{W}$ is calculated as $N_{\mathrm{W}} = 6N_{\mathrm{N}} - N_{\mathrm{B}} + 6N_{\mathrm{M}} + N_{\mathrm{H}}$. Note again that although $\boldsymbol{\varphi}$ is not included in the generalized displacement vector in the formulation of [40], it is included in this study to simplify the formulations described in Chapters 3 and 5. When the j-th end of member i is connected to node k rigidly or via hinge h, translational and rotational incompatibility vectors represented by $\Delta\mathbf{U}_{ij}$ and $\Delta\boldsymbol{\Theta}_{ij} \in \mathbb{R}^3$, respectively, are defined as the violations of Eqs. (2.28), (2.29), and (2.35) as follows:

$$\Delta\mathbf{U}_{ij} = \mathbf{U}_k - \mathbf{V}_i - (\mathbf{R}(\boldsymbol{\Psi}_i) - \mathbf{I}_3)\mathbf{r}_{ij} \tag{2.36}$$

$$\Delta\boldsymbol{\Theta}_{ij} = \begin{cases} \boldsymbol{\Theta}_k - \boldsymbol{\Psi}_i & \text{(Rigidly connected)} \\ \boldsymbol{\Phi}_{ij}(\boldsymbol{\Psi}_i, \boldsymbol{\Theta}_k, \varphi_h) & \text{(Connected by hinge } h \text{)} \end{cases} \tag{2.37}$$

It is assumed that the components of fixed nodal displacements are equal to 0 in Eqs. (2.36) and (2.37). The translational and rotational incompatibility vectors $\Delta\mathbf{U}_{ij}$ and $\Delta\boldsymbol{\Theta}_{ij}$ are combined into the *incompatibility vector* $\mathbf{G}(\mathbf{W}) \in \mathbb{R}^{N_\mathrm{G}}$ as the nonlinear function of the generalized displacement vector $\mathbf{W}$. Accordingly, the compatibility equations are represented as follows:

$$\mathbf{G}(\mathbf{W}) = \mathbf{0} \tag{2.38}$$

Since the compatibility equations should be satisfied at all member ends, the number of components of $\mathbf{G}(\mathbf{W})$ is $N_\mathrm{G} = 12N_\mathrm{M}$.

2.3.4 Derivation of first-order infinitesimal mechanism

The series expansion of the incompatibility vector $\mathbf{G}(\mathbf{W})$ with respect to $\mathbf{W}$ is written as follows:

$$\mathbf{G}(\mathbf{W}) = \mathbf{G}(\mathbf{0}) + \frac{d\mathbf{G}(\mathbf{0})}{d\mathbf{W}}\mathbf{W} + \cdots \tag{2.39}$$

where $d\mathbf{G}(\mathbf{W})/d\mathbf{W}$ is a $N_\mathrm{G} \times N_\mathrm{W}$ matrix whose (i,j) component is the first-order derivative of the i-th component of $\mathbf{G}(\mathbf{W})$ with respect to the j-th component of $\mathbf{W}$. In the following, the constant matrix $d\mathbf{G}(\mathbf{0})/d\mathbf{W}$ is to be represented by $\boldsymbol{\Gamma}^{(1)} \in \mathbb{R}^{N_\mathrm{G} \times N_\mathrm{W}}$ and referred as the *compatibility matrix*. The superscript (1) indicates that $\boldsymbol{\Gamma}^{(1)}$ is the first-order derivative of the compatibility matrix. Since $\mathbf{G}(\mathbf{0}) = \mathbf{0}$, the first-order approximation of Eq. (2.38) for the moderately small $\mathbf{W}$ can be written as follows:

$$\boldsymbol{\Gamma}^{(1)}\mathbf{W} = \mathbf{0} \tag{2.40}$$

If there is $\mathbf{W}$ satisfying Eq. (2.40), the frame model has at least first-order infinitesimal mechanism [40]. The detailed calculation of the components of $\boldsymbol{\Gamma}^{(1)}$ is provided in Appendix D. An arbitrary $\mathbf{W}$ satisfying Eq. (2.40) can be represented by a linear combination of the bases of $\ker(\boldsymbol{\Gamma}^{(1)})$ [63]. The dimension of $\ker(\boldsymbol{\Gamma}^{(1)})$ denoted by N_D is the number of kinematic indeterminacy and computed as:

$$N_\mathrm{D} = N_\mathrm{W} - \mathrm{rank}(\boldsymbol{\Gamma}^{(1)}) \tag{2.41}$$

When the nodal displacements are appropriately constrained so that the only rigid-body motions of the entire model are constrained, the kinematic indeterminacy is equal to the DOF of infinitesimal rigid-folding mechanism. Let $\boldsymbol{\eta}_1, \ldots, \boldsymbol{\eta}_{N_\mathrm{D}} \in \mathbb{R}^{N_\mathrm{W}}$ denote the right singular vectors of $\boldsymbol{\Gamma}^{(1)}$ corresponding to zero singular values, which are normalized as $\|\boldsymbol{\eta}_i\| = 1$ ($i = 1, \ldots, N_\mathrm{D}$). They are the bases of $\ker(\boldsymbol{\Gamma}^{(1)})$ as explained in Appendix E and referred to as the *first-order infinitesimal mechanism modes* [40]. An arbitrary $\mathbf{W}$ satisfying Eq. (2.40) can be expressed as the linear combination of $\boldsymbol{\eta}_i$ and written as follows:

$$\mathbf{W} = a_1\boldsymbol{\eta}_1 + \cdots + a_{N_\mathrm{D}}\boldsymbol{\eta}_{N_\mathrm{D}} = \begin{bmatrix} \boldsymbol{\eta}_1 & \cdots & \boldsymbol{\eta}_{N_\mathrm{D}} \end{bmatrix} \begin{pmatrix} a_1 \\ \vdots \\ a_{N_\mathrm{D}} \end{pmatrix} = \mathbf{H}\mathbf{a} \tag{2.42}$$

$$\mathbf{H} = \begin{bmatrix} \boldsymbol{\eta}_1 & \cdots & \boldsymbol{\eta}_{N_\mathrm{D}} \end{bmatrix} \in \mathbb{R}^{N_\mathrm{W} \times N_\mathrm{D}}$$

where $\mathbf{a} = (a_1, \ldots, a_{N_\mathrm{D}})^\mathsf{T} \in \mathbb{R}^{N_\mathrm{D}}$ is an arbitrary vector. The matrix $\mathbf{H}$ is divided into three matrices as follows:

$$\mathbf{H} = \begin{bmatrix} \mathbf{H}_\mathrm{U} \\ \mathbf{H}_\mathrm{V} \\ \mathbf{H}_\varphi \end{bmatrix} \tag{2.43}$$

$$\mathbf{H}_\mathrm{U} \in \mathbb{R}^{(6N_\mathrm{N}-N_\mathrm{B})\times N_\mathrm{D}}, \quad \mathbf{H}_\mathrm{V} \in \mathbb{R}^{6N_\mathrm{M}\times N_\mathrm{D}}, \quad \mathbf{H}_\varphi \in \mathbb{R}^{N_\mathrm{H}\times N_\mathrm{D}}$$

where $\mathbf{H}_\mathrm{U}$, $\mathbf{H}_\mathrm{V}$, and $\mathbf{H}_\varphi$ correspond to the nodal displacements $\mathbf{U}$, the member displacements $\mathbf{V}$, and the increments of hinge rotation angles $\boldsymbol{\varphi}$, respectively. Then, arbitrary vectors $\mathbf{U}$, $\mathbf{V}$, and $\boldsymbol{\varphi}$ satisfying Eq. (2.40), which represent the first-order infinitesimal mechanism, can be written as follows:

$$\mathbf{U} = \mathbf{H}_\mathrm{U}\mathbf{a} \tag{2.44}$$

$$\mathbf{V} = \mathbf{H}_\mathrm{V}\mathbf{a} \tag{2.45}$$

$$\boldsymbol{\varphi} = \mathbf{H}_\varphi\mathbf{a} \tag{2.46}$$

As described above, the deformation modes of rigid origami represented by the frame model are obtained by using the mechanism analysis method of the partially rigid frames. The displacement modes of the vertices and the folding angle variation modes of rigid origami can be easily and simultaneously obtained from the nodal displacement modes of the frame and the hinge rotation modes, respectively, whereas only one of them can be obtained using the truss model or the rotational hinge model.

2.4 Conclusions

In this chapter, the review of the numerical models representing the shape and the kinematics of a rigid origami are first provided for a rotational hinge model, a truss model, a FE model, and a frame model. The frame model is used in this study for the form generation and the deformation path analysis of the rigid origami. It consists of frame elements and hinges and can represent a rigid origami in a simpler way than the other three models mentioned above.

The equations reflecting the geometric constraints on the nodal coordinates of the frame model are formulated based on the locations of the nodes on the origami surface so that the frame model represents the corresponding rigid origami appropriately. From the formulated constraint equations, the independent nodal coordinates are identified by utilizing the properties of the RREF of a matrix. The equations to obtain the position of the origami vertices from the nodal coordinates of the frame model are also formulated.

In addition, the infinitesimal mechanism of the frame model is investigated by the analysis method for partially rigid frames. The generalized displacement vector is defined as the assemblage of the unconstrained translational and rotational displacements of nodes, the translational and rotational displacements of center points of members, and the increments of the hinge rotation angles. The compatibility equations satisfied by the generalized

displacement are formulated at each member end with respect to the compatibility between the translational and rotational displacement of the member end and the node to which the member end connects. The kinematic indeterminacy and the first-order infinitesimal mechanism modes are derived from the compatibility matrix which is the first-order derivative of the incompatibility vector with respect to the generalized displacement. The geometric properties and the method of the kinematic analysis of the frame model introduced in this chapter is used in the following chapters.

Chapter 3

Form generation of rigid origami for approximating a curved surface

In this chapter, a method is presented for approximating a curved surface by a developable rigid origami with and without cuts along edges. Geometric properties of polyhedral surfaces such as Gaussian curvature are utilized to formulate developability conditions of the origami surface and approximation error functions between the target surface and the origami surface. Variables are selected according to the definition of the approximation error function so that the calculation of the error function is performed efficiently. The independent variables are identified to satisfy the linear constraint equations such as those describing the symmetry of the origami surface. An optimization approach is utilized to minimize the approximation error of the target surface under the developability conditions. Form generation starts from a triangulated surface, and crease lines of the origami surface are sequentially fixed to reduce the degrees of freedom of the rigid-folding mechanism. The crease lines to be fixed are determined by the selection criteria introduced in this study reflecting the infinitesimal mechanism of the rigid origami, which help to prevent the crease lines to be locked during the deployment process. The frame model introduced in Chapter 2 is used for the infinitesimal and finite mechanism analysis of the obtained solutions. Only the form generation method and examples of an origami surface with locked crease lines are shown in this chapter, and case studies of the form generation are presented in Chapter 4.

3.1 Introduction

3.1.1 Background

Origami has the advantage that it can be folded from a flat or folded state to form complex three-dimensional shapes, and various form generation methods have been proposed to obtain a rigid origami which can realize a desired shape. Various approaches have been proposed to generalize well-known crease patterns; e.g., Dudte *et al.* [41] and Song *et al.* [42] used Miura-ori, Tachi [43] used Resch's pattern, Zhao *et al.* [44] used waterbomb tessellation, and Wu [45] used Yoshimura pattern. A rigid origami with non-regular quadrilateral

crease pattern has also been generated by Tachi [23, 46] and He and Guest [47, 48] based on the necessary and sufficient condition for the rigid-foldability of a quadrilateral mesh which is expressed with respect to the folding angles and the sector angles (angles between the adjacent crease lines) and called the *loop condition*. Although a rigid origami that approximates the desired shape can be obtained by the above methods through a trial-and-error or optimization approach, those methods are not suitable for generating rigid origami structures with various non-typical crease patterns and degrees of freedom (DOFs) of rigid-folding mechanism because the topology of the crease lines is limited. On the other hand, the methods which does not rely on the typical crease patterns have also been proposed by utilizing the topology optimization approach [49, 50], and various crease patterns can be obtained by these methods. However, these methods focus on obtaining a crease pattern which achieves the desired actuation and are not suitable for approximating a curved shape. Therefore, a form generation method utilizing non-regular crease patterns for the approximation of a target shape can improve the flexibility of the origami design.

The idea of kirigami [65, 66] and papercraft [67, 68] is also utilized to realize a curved surface from a flat or folded state. Compared to origami without cuts or holes, the introduction of cuts greatly increases the degree of freedom of curved surface shapes that can be generated from a flat surface. However, papercrafts generally consist of multiple parts, and it is difficult to join them in a complex manner for application to architectural-scale structures. In addition, the size of the joints is often neglected in the existing methods of approximating a curved surface using kirigami, and the faces are connected at very narrow widths or even points. There are also many examples of large degrees of freedom of mechanism. From the viewpoint of construction and safety, a structure with large degrees of freedom of mechanism is not suitable for application in the architectural scale such as a roof, and it is desirable to obtain a structure with small degrees of freedom of mechanism.

In this chapter, a method for form generation of a rigid origami approximating an open curved surface is proposed based on Refs. [28–30, 52]. A rigid origami developable to a plane can be obtained by using an optimization method that does not depend on the typical crease patterns. Thus, flat panels are connected at ground level by hinges, and then folded up to obtain a three-dimensional polyhedral shape. The three-dimensional polyhedral shape of a rigid origami approximating the target surface obtained by the proposed method is especially referred to as the *folded shape* although the shape in the process of being developed into a plane is also a folded three-dimensional shape. A rigid origami considered in this chapter may have the cuts along with its edges which may generate holes in the development diagram while there are no holes in the folded shape as explained in Sections 3.1.2 and 3.2.3. To obtain a shape of a developable origami, the *developability conditions* are formulated in Section 3.2 with respect to the geometric properties of a polyhedral surface such as discrete Gaussian curvature defined as the *angle defect* [69]. The developability condition here refers to the condition that the origami faces can be placed on a plane without any deformation while the connectivity of the adjacent faces in the folded shape is maintained except at the specified cuts. The approximation accuracy of the target surface is measured

for several aspect such as the Euclidean distance, the surface area, and the normal vectors as shown in Section 3.3.1. The form generation procedure in Section 3.4 starts from the triangulated surface, and the shape of origami is obtained by solving the optimization problem formulated in Section 3.3.3 to minimize the error of the developability or the approximation of the target surface. However, a rigid origami with only triangular faces has a very large number of DOFs, which leads to the undesirable situation in view of engineering application where the mechanism cannot be stabilized by simply supporting a part of the structure and the rotation of the crease lines should be constrained to maintain the curved polyhedral shape. Therefore, some crease lines are to be sequentially fixed (removed) to reduce the DOFs. The adjacent facets connected to each fixed crease line are integrated into a flat face with more than three edges by adding the squared norm of the cross product of their unit normal vectors to the objective function of the optimization problem. By solving the optimization problem multiple times while increasing the number of fixed crease lines, multiple optimal shapes with the different DOFs can be obtained. The variables in the optimization problem are selected in Section 3.3.2 for the efficient calculations of the errors of the developability and surface approximation. The crease lines to be fixed are selected taking into account the shape and the deformation mechanism of the rigid origami to prevent crease lines to be *locked*; i.e. some crease lines that are not fixed become unable to rotate by fixing an inappropriate crease line. If there is a locked crease line, the faces adjacent to it cannot rotate around it even though they are not coplanar, and consequently, the rigid origami cannot be developed to a plane without deformation of its faces. Therefore, the transition of the deformation mechanism of the rigid origami due to choosing and fixing some crease lines is predicted based on the kinematic analysis of the frame model, and the selection criteria of the crease lines to be fixed reflecting this prediction are proposed in Section 3.5. To evaluate the transition of the deformation mechanism, the stiffness matrix assembled using the rigid-folding modes and the fictitious stiffness of the hinges is introduced. The criterion introduced in this study reduces the number of times to solve the optimization problems and improves the computational efficiency compared to the case where the crease lines to be fixed are selected only by considering the shape of the rigid origami.

3.1.2 Structure of origami surface

As introduced in Chapters 1 and 2, a polyhedral origami surface is regarded as a mesh and consists of *vertices*, *edges*, and *faces* as shown in Fig. 3.1. In the following, unless otherwise noted, an origami surface is considered to be a triangular mesh and all faces are assumed to be triangle; every mention of *faces* is taken to mean triangular faces. An origami surface may contain *cuts* which may generate holes and gaps in the development diagram while there are no holes and gaps in the folded shape as shown in Fig. 3.2. A cut is defined as the sets of edges which are connected each other and referred to as the *cut lines*. In the three dimensional shape, it is assumed that the structure of a graph consists of cut lines of a single cut and relating cut vertices is a tree; i.e., it is connected and does not have any loops. In addition, a cut is assumed not to break the origami surface into multiple parts,

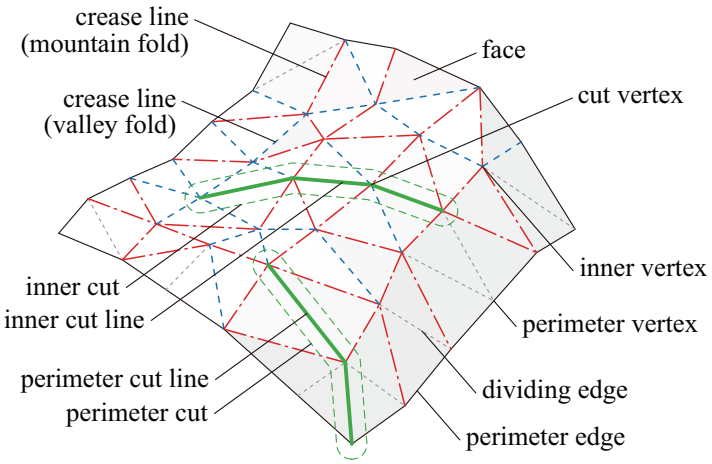

Figure 3.1: Structure of an origami surface.

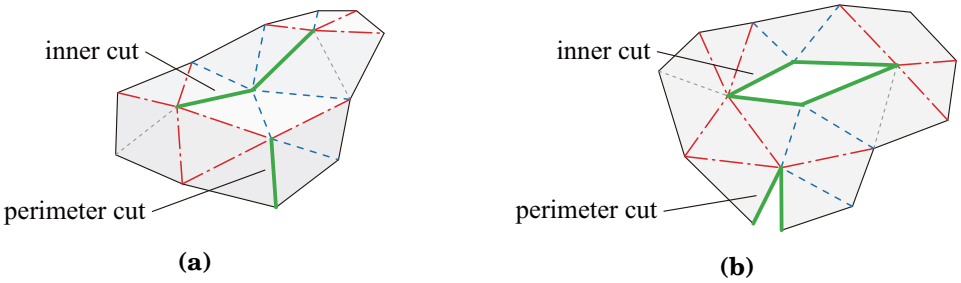

Figure 3.2: Inner cut and perimeter cut; (a) folded shape, (b) development diagram.

and the origami faces are allowed to overlap each other around the cut in the development diagram. Cuts are further classified according to the positions of the endpoints of its cut lines into

- *inner cut* where no endpoints of its cut lines exist on the perimeter of the origami surface, and
- *perimeter cut* where one of the endpoints of its cut lines exists on the perimeter of the origami surface.

Then, the edges of an origami surface are classified into

- *crease line* which is the inner edge around which origami faces rotate,
- *perimeter edge* at the exterior boundary of the origami surface,
- *dividing edge* which divides a face with more than three edges into triangular faces,
- *inner cut line* consisting of an inner cut of the origami surface, and
- *perimeter cut line* consisting of a perimeter cut of the origami surface.

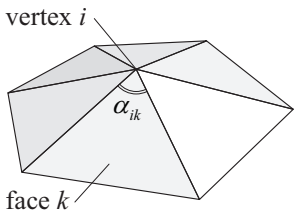

Figure 3.3: Inner angle of triangular face k at inner vertex i.

A single cut line in the folded shape corresponds to two edges in the development diagram, and the number of cut lines in the development diagram is twice as the number of cut lines in the folded shape. In addition, the vertices are classified into

- *cut vertex* which is an endpoint of the inner or perimeter cut lines,
- *perimeter vertex* which is at the perimeter of the origami surface and not a cut vertex, and
- *inner vertex* which is not a perimeter or cut vertex.

3.2 Developability conditions

In this section, the conditions for the developability of an origami surface are formulated considering **1)** developability around each inner vertex, **2)** flatness of the faces with more than three edges, and **3)** developability around each inner cut [28–30, 52]. Note that an overlap of faces in the development diagram and a self-intersection of faces in the development process are allowed and neglected in the formulation of the developability conditions, and thus, an origami surface is always locally developable to a plane around a perimeter cut. The developability conditions are first locally formulated in Sections 3.2.1 – 3.2.3, and they are assembled for an entire origami surface in Section 3.2.4. The optimization problem for generating a development diagram is also proposed in Section 3.2.4.

3.2.1 Developability around an inner vertex

When an origami surface can be developed to a plane around its inner vertices, the Gaussian curvature at each inner vertex must be equal to zero. The Gaussian curvature is defined as the *angle defect* [69], which is equal to the difference between 2π and the sum of the inner angles of the triangular faces around an inner vertex. Let N_{V} and $\mathscr{F}_i^{\mathrm{V}}$ $(i = 1, \ldots, N_{\mathrm{V}})$ denote the number of origami vertices and the set of global indices of the triangular faces adjacent to vertex i, where i is the global vertex index, respectively. In the following, unless otherwise noted, the indices of the components of an origami surface such as vertices, edges, and faces are global indices defined for the entire origami surface. Note that $\mathscr{F}_i^{\mathrm{V}}$ is defined for all the vertices; vertex i is not necessarily an inner vertex and can be a cut vertex or a perimeter vertex. As shown in Fig. 3.3, the inner angle of face $k \in \mathscr{F}_i^{\mathrm{V}}$ at vertex i is denoted

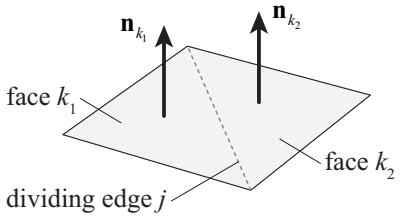

Figure 3.4: Unit normal vectors of faces k_1 and k_2 adjacent to dividing edge j.

by $\alpha_{ik} \in \mathbb{R}$. When vertex i is not a perimeter vertex, the Gaussian curvature κ_i at vertex i is defined as follows:

$$\kappa_i = 2\pi - \sum_{k \in \mathscr{F}_i^{\mathrm{V}}} \alpha_{ik} \tag{3.1}$$

Then, the developability condition at inner vertex $i \in \mathscr{V}_{\mathrm{in}}$ is formulated as

$$\kappa_i = 0 \tag{3.2}$$

where $\mathscr{V}_{\mathrm{in}}$ is the set of indices of inner vertices.

3.2.2 Flatness of a face with more than three edges

In order for the origami surface to be developable to a plane by the rigid-folding deformation, its faces with more than three edges must be flat; i.e., the faces adjacent to each dividing edge must be in the same plane. Let $\mathscr{F}_j^{\mathrm{E}}$ denote the set of indices of faces adjacent to edge j. As shown in Fig. 3.4, the unit normal vector of face k is denoted by $\mathbf{n}_k \in \mathbb{R}^3$. Defining $\mathscr{E}_{\mathrm{div}}$ as the set of global edge indices of the dividing edges, the condition for the flatness of the face at dividing edge $j \in \mathscr{E}_{\mathrm{div}}$ is formulated as

$$\|\mathbf{n}_{k_1} \times \mathbf{n}_{k_2}\| = 0 \quad (k_1, k_2 \in \mathscr{F}_j^{\mathrm{E}}) \tag{3.3}$$

3.2.3 Developability around cuts

The developability around a single inner cut is considered, and the global indices of cuts are omitted for simplicity although it is necessary to identify the cut. The cut is assumed to consist of M_{C} cut lines in the folded shape. As shown in Fig. 3.5, the local indices of cut lines $1, \ldots, 2M_{\mathrm{C}}$ in the development diagram are assigned so that they are in ascending order when the cut lines in the development diagram are traced such that the hole by the cut exists on the left side and the face exists on the right side of each cut line when viewed from the positive side of the z-axis. A pair cut lines in the development diagram correspond to the same cut line in the folded shape; e.g., edge 2 and $j+2$ in Fig. 3.5 are the same cut line in the three-dimensional shape. The length and the direction vector of edge j $(= 1, \ldots, 2M_{\mathrm{C}})$ in the development diagram are denoted by $\bar{l}_j \in \mathbb{R}$ and $\bar{\mathbf{e}}_j \in \mathbb{R}^2$, respectively. $\bar{\mathbf{e}}_j$ is a unit vector and directed from the vertex between edges $j-1$ and j to the vertex between edges j and $j+1$. The local edge indices 0 and $2M_{\mathrm{C}}+1$ are regarded to be $2M_{\mathrm{C}}$ and 1, respectively. The local vertex indices in the development diagram are also defined so that vertex j is located

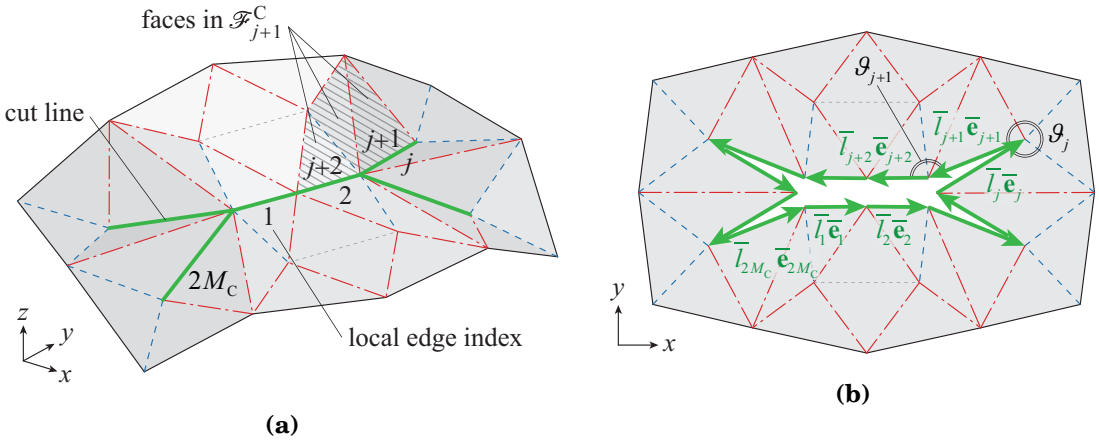

Figure 3.5: Configuration of an inner cut; (a) Local edge indices and angles around cut lines in the three-dimensional shape, (b) Vectors along cut lines and angles around cut lines in the development diagram shape.

between edge j and $j+1$. Let $\mathscr{F}^{\mathrm{C}}_j$ denote the set of global indices of the faces connected to vertex j in the development diagram. Note that $\mathscr{F}^{\mathrm{C}}_j$ is a subset of $\mathscr{F}^{\mathrm{V}}_i$ when i is the global index of vertex j, where j is the local index. As shown in Fig. 3.5, the sum of the inner angles of the triangular faces at the vertex j in the development diagram is denoted by $\vartheta_j \in \mathbb{R}$ and calculated as follows:

$$\vartheta_j = \sum_{k \in \mathscr{F}^{\mathrm{C}}_j} \alpha_{jk} \tag{3.4}$$

where α_{jk} the inner angle of face k at vertex j. Then, the edge direction vector $\bar{\mathbf{e}}_{j+1}$ in the development diagram satisfies the following equation for $j = 1, \ldots, 2M_{\mathrm{C}}$:

$$\begin{aligned} \bar{\mathbf{e}}_{j+1} &= \mathbf{R}(\vartheta_j - \pi)\bar{\mathbf{e}}_j \\ &= \mathbf{R}(\vartheta_j - \pi)\cdots\mathbf{R}(\vartheta_1 - \pi)\bar{\mathbf{e}}_1 \\ &= \mathbf{R}\left(\sum_{m=1}^{j} \vartheta_m - j\pi\right)\bar{\mathbf{e}}_1 \end{aligned} \tag{3.5}$$

where $\mathbf{R}(\theta) \in \mathbb{R}^{2\times 2}$ represents the rotation matrix which rotate a vector counterclockwise on a plane by the angle θ and is defined as

$$\mathbf{R}(\theta) = \begin{bmatrix} \cos\theta & -\sin\theta \\ \sin\theta & \cos\theta \end{bmatrix}$$

$\bar{\mathbf{e}}_{2M_{\mathrm{C}}+1}$ obtained from Eq. (3.5) by assigning $j = 2M_{\mathrm{C}}$ need to be identical to $\bar{\mathbf{e}}_1$, and the following equation holds:

$$\mathbf{R}\left(\sum_{j=1}^{2M_{\mathrm{C}}} \vartheta_j - 2M_{\mathrm{C}}\pi\right)\bar{\mathbf{e}}_1 = \bar{\mathbf{e}}_1 \;\Leftrightarrow\; \left[\mathbf{R}\left(\sum_{j=1}^{2M_{\mathrm{C}}} \vartheta_j - 2M_{\mathrm{C}}\pi\right) - \mathbf{I}_2\right]\bar{\mathbf{e}}_1 = \mathbf{0} \tag{3.6}$$

Since the choice of edge 1 on the cut and the placement of the development diagram on the xy-plane are arbitrary, Eq. (3.6) holds for any $\bar{\mathbf{e}}_1$. Therefore, the following equation is

obtained for an arbitrary integer m:

$$\sum_{j=1}^{2M_\mathrm{C}} \vartheta_j - 2M_\mathrm{C}\pi = 2m\pi \;\Leftrightarrow\; \sum_{j=1}^{2M_\mathrm{C}} \vartheta_j = 2(M_\mathrm{C}+m)\pi \tag{3.7}$$

According to Eq. (3.6), m represents the number of counterclockwise 2π rotations of the direction vector of the edge when the cut is passed around on the development diagram, and is called the *turning number* used in the field such as geometric topology and differential geometry. If the polygon on the development diagram formed by the cut lines does not have any self-intersections and the faces do not overlap each other as shown in Fig. 3.5, the turning number m is equal to 1. Conversely, if the faces are allowed to overlap each other, it is not necessarily equal to 1. However, it is assumed that $m = 1$ holds in this study, and the case where m is more or less than 1 is neglected since the three-dimensional shape is expected to be too complicated for an architectural purposes if m is not 1. On the other hand, since the number of the cut vertices is $M_\mathrm{C}+1$ in the folded shape and there is no loop in the cut in the three-dimensional shape, the sum of the Gaussian curvature of the cut vertices satisfies following equation:

$$\begin{aligned}\sum_{i\in\mathscr{V}_\mathrm{C}} \kappa_i &= \sum_{i\in\mathscr{V}_\mathrm{C}} \left(2\pi - \sum_{k\in\mathscr{F}_i^\mathrm{V}} \alpha_{ik}\right) \\ &= 2(M_\mathrm{C}+1)\pi - \sum_{j=1}^{2M_\mathrm{C}} \sum_{k\in\mathscr{F}_j^\mathrm{C}} \alpha_{jk} \\ &= 2(M_\mathrm{C}+1)\pi - \sum_{j=1}^{2M_\mathrm{C}} \vartheta_j\end{aligned} \tag{3.8}$$

According to Eqs. (3.7) and (3.8) and the assumption of $m = 1$, the following equation needs to be satisfied for the developability around the cut:

$$\sum_{i\in\mathscr{V}_\mathrm{C}} \kappa_i = 2(1-m)\pi = 0 \tag{3.9}$$

Furthermore, in addition to the condition for the direction of the cut lines on the development diagram represented by Eq. (3.9), there must be a condition for the inner cut lines to form a loop on the development diagram, which can be written as follows:

$$\sum_{j=1}^{2M_\mathrm{C}} \bar{l}_j \bar{\mathbf{e}}_j = \mathbf{0} \tag{3.10}$$

Substituting Eq. (3.5) into the left-hand side of Eq. (3.10), the following equation is obtained:

$$\begin{aligned}\sum_{j=1}^{2M_\mathrm{C}} \bar{l}_j \bar{\mathbf{e}}_j &= \bar{l}_1 \bar{\mathbf{e}}_1 + \sum_{j=1}^{2M_\mathrm{C}-1} \bar{l}_{j+1} \bar{\mathbf{e}}_{j+1} \\ &= \bar{l}_1 \bar{\mathbf{e}}_1 + \sum_{j=1}^{2M_\mathrm{C}-1} \bar{l}_{j+1} \left\{\mathbf{R}\left(\sum_{m=1}^{j} \vartheta_m - j\pi\right) \bar{\mathbf{e}}_1\right\} \\ &= \left[\bar{l}_1 \mathbf{I}_2 \sum_{j=1}^{2M_\mathrm{C}-1} (-1)^j \bar{l}_{j+1} \mathbf{R}\left(\sum_{m=1}^{j} \vartheta_m\right)\right] \bar{\mathbf{e}}_1\end{aligned} \tag{3.11}$$

According to Eq. (3.11), the conditions for the existence of $\bar{\mathbf{e}}_1$ satisfying Eq. (3.10) can be written as follows:

$$\begin{aligned} &\det\left[\bar{l}_1\mathbf{I}_2\sum_{j=1}^{2M_\mathrm{C}-1}(-1)^j\bar{l}_{j+1}\mathbf{R}\left(\sum_{m=1}^{j}\vartheta_m\right)\right]=0 \\ \Leftrightarrow&\left\{\bar{l}_1+\sum_{j=1}^{2M_\mathrm{C}-1}(-1)^j\bar{l}_{j+1}\cos\left(\sum_{m=1}^{j}\vartheta_m\right)\right\}^2+\left\{\sum_{j=1}^{2M_\mathrm{C}-1}(-1)^j\bar{l}_{j+1}\sin\left(\sum_{m=1}^{j}\vartheta_m\right)\right\}^2=0 \end{aligned} \tag{3.12}$$

Consequently, $\bar{l}_j$ and ϑ_j ($j=1,\ldots,2M_\mathrm{C}$) need to satisfy the following equations:

$$\bar{l}_1+\sum_{j=1}^{2M_\mathrm{C}-1}(-1)^j\bar{l}_{j+1}\cos\left(\sum_{m=1}^{j}\vartheta_m\right)=0 \tag{3.13}$$

$$\sum_{j=1}^{2M_\mathrm{C}-1}(-1)^j\bar{l}_{j+1}\sin\left(\sum_{m=1}^{j}\vartheta_m\right)=0 \tag{3.14}$$

Conversely, if $\bar{l}_j$ and ϑ_j for $j=1,\ldots,2M_\mathrm{C}$ satisfy Eqs. (3.13) and (3.14), Eq. (3.10) holds for an arbitrary $\bar{\mathbf{e}}_1$. Therefore, the conditions for the cut lines to form a loop on the development diagram are represented by Eqs. (3.13) and (3.14). From the above, the developability conditions around an inner cut are represented by the three equations (3.9), (3.13), and (3.14).

3.2.4 Developability of entire origami surface

The developability conditions formulated in the previous sections are assembled for all the inner vertices, dividing edges, and inner cuts to formulate the developability condition of the entire origami surface. Let N_Vin, N_Ediv, and N_Cin denote the number of inner vertices, dividing edges, and inner cuts, respectively. Then, the total number of the developability conditions is $N_\mathrm{Vin}+N_\mathrm{Ediv}+3N_\mathrm{Cin}$, and the left-hand sides of Eqs. (3.2), (3.3), (3.9), (3.13), and (3.14) are assembled for all the inner vertices, dividing edges, and inner cuts into a vector $\mathbf{D}\in\mathbb{R}^{N_\mathrm{Vin}+N_\mathrm{Ediv}+3N_\mathrm{Cin}}$, which represents the violation of the developability conditions. The values of components of $\mathbf{D}$ can be determined only from the quantities defined in the folded shape, and the development diagram is not necessary to calculate $\mathbf{D}$. Then, the developability condition for the entire origami surface is written in a vector form as follows:

$$\mathbf{D}=\mathbf{0} \tag{3.15}$$

The form generation of the rigid origami is performed so that the developability condition formulated as Eq. (3.15) is satisfied.

Since Eq. (3.15) is only the necessary condition for the developability of an origami surface, the developability of an obtained solution in the form generation procedure should be confirmed by generating a development diagram. The development diagram of an origami surface is generated by minimizing the sum of the squared edge length errors between the development diagram and the folded shape according to the surface flattening method proposed by Wang *et al.* [70]. The development diagram is to be generated on the xy-plane. The

variables for the development diagram generation are selected according to the optimization problem for generating the origami surface described in Section 3.3, which are the x- and y- coordinates of vertices or the independent x- and y- coordinates of nodes of the frame model determined in Chapter 2. In both cases, let $\bar{\mathbf{X}}$ denote the vector of the variables. The length of edge j ($j = 1, \ldots, \bar{N}_{\mathrm{E}}$) in the folded shape and in the development diagram are represented by l_j and $\bar{l}_j \in \mathbb{R}$, respectively, where $\bar{N}_{\mathrm{E}}$ is the number of origami edges in the development diagram. Note that l_j is constant while $\bar{l}_j$ is the function of $\bar{\mathbf{X}}$ which can be written as $\bar{l}_j(\bar{\mathbf{X}})$. $\bar{N}_{\mathrm{E}}$ can be different from the number of edges in the folded shape since each cut line in the folded shape corresponds to two edges in the development diagram as shown in Fig. 3.5. When the number of origami edges in the folded shape is N_{E} and the number of inner and perimeter cut lines is N_{Ecut}, $\bar{N}_{\mathrm{E}}$ is calculated as $\bar{N}_{\mathrm{E}} = N_{\mathrm{E}} + N_{\mathrm{Ecut}}$. Let $\bar{\mathbf{n}}_k(\bar{\mathbf{X}}) \in \mathbb{R}^3$ ($k = 1, \ldots, N_{\mathrm{F}}$) denote the unit normal vector of face k of the development diagram where N_{F} is the number of triangular origami faces. The direction of $\bar{\mathbf{n}}_k(\bar{\mathbf{X}})$ is defined so that the relation $\bar{\mathbf{n}}_k(\bar{\mathbf{X}}) \cdot \mathbf{e}_{\mathrm{z}} \geq 0$ is satisfied where $\mathbf{e}_{\mathrm{z}} = (0, 0, 1)^{\mathsf{T}}$, if all the faces are not flipped. Then, the development diagram is obtained by solving the following optimization problem which minimizes the non-negative function $F_{\mathrm{dev}}(\bar{\mathbf{X}})$:

$$
\begin{cases}
\underset{\bar{\mathbf{X}}}{\min.} & F_{\mathrm{dev}}(\bar{\mathbf{X}}) = \dfrac{\displaystyle\sum_{j=1}^{\bar{N}_{\mathrm{E}}} \left\{\bar{l}_j(\bar{\mathbf{X}}) - l_j\right\}^2}{\displaystyle\sum_{j=1}^{\bar{N}_{\mathrm{E}}} l_j^2} \\
\text{s.t.} & \bar{\mathbf{n}}_k(\bar{\mathbf{X}}) \cdot \mathbf{e}_{\mathrm{z}} \geq 0 \quad (k = 1, \ldots, N_{\mathrm{F}}) \\
& \bar{\mathbf{X}} \in \bar{\chi}
\end{cases}
\tag{3.16}
$$

where $\bar{\chi}$ denotes the range of variables assigned so that the vertex positions of the development diagram are determined uniquely and the optimization problem (3.16) has the good convergence. The initial guess of the problem (3.16) can be arbitrarily set under the condition that it has the consistent connectivity of edges as the folded shape and satisfies the constraints of the optimization problem. In this study, the projected shape of the folded shape onto xy-plane is used as the initial guess.

3.3 Optimization problems for form generation of a developable origami surface

In this section, optimization problems for generating a single origami shape developable to a plane are formulated. The approximation error functions are formulated with respect to the distance between the origami surface and the target surface, the error of the surface area, and the difference between the unit normal vectors of the origami surface and the target surface defined in Section 3.3.1. There are some candidates for the design variables in the optimization problem; e.g., the vertex coordinates of the origami surface, the nodal coordinates of the frame model, and other parameters representing the position of the vertices measured from the points on the target surface. They are selected in view of the efficiency

of the calculation of the approximation error, and the discussion about the selection of the design variables is provided in Sections 3.3.1 and 3.3.2. The optimization problems for the form generation are proposed in several patterns in Section 3.3.3.

3.3.1 Definition of approximation error functions

(1) Target surface

A target surface is defined by the tensor product Bézier surface [51] of order $M_\mathrm{s} \times M_\mathrm{t}$. Let $\tilde{\mathbf{p}}_{ij} = (\tilde{p}^\mathrm{x}_{ij}, \tilde{p}^\mathrm{y}_{ij}, \tilde{p}^\mathrm{z}_{ij})^\mathsf{T} \in \mathbb{R}^3$ $(i = 0, \ldots, M_\mathrm{s};\ j = 0, \ldots, M_\mathrm{t})$ denote the position vector of a control point of the Bézier surface. The surface is parametrized by s and t $(0 \le s, t \le 1)$, and the position vector of the point on the surface corresponding to the parameter (s, t) which is denoted by $\tilde{\mathbf{r}}(s,t) \in \mathbb{R}^3$ is determined as follows:

$$\tilde{\mathbf{r}}(s,t) = \sum_{i=0}^{M_\mathrm{s}} \sum_{j=0}^{M_\mathrm{t}} \tilde{\mathbf{p}}_{ij} B_i^{M_\mathrm{s}}(s) B_j^{M_\mathrm{t}}(t) \tag{3.17}$$

where $B_i^{M_\mathrm{s}}(s)$ and $B_j^{M_\mathrm{t}}(t)$ are the Bernstein basis polynomials defined as follows:

$$B_i^{M_\mathrm{s}}(s) = \left(\begin{array}{c} M_\mathrm{s} \\ i \end{array} \right) s^i (1-s)^{M_\mathrm{s}-i},\ B_j^{M_\mathrm{t}}(t) = \left(\begin{array}{c} M_\mathrm{t} \\ j \end{array} \right) t^j (1-t)^{M_\mathrm{t}-j}$$

In particular, when the control points are uniformly spaced in the x-direction with interval Δp_x and in the y-direction with interval Δp_y as $\tilde{\mathbf{p}}_{ij} = (\tilde{p}^\mathrm{x}_{00} + i\Delta\tilde{p}_\mathrm{x}, \tilde{p}^\mathrm{y}_{00} + j\Delta\tilde{p}_\mathrm{y}, \tilde{p}^\mathrm{z}_{ij})^\mathsf{T}$, the z-coordinate of the Bézier surface can be represented as a function of the (x, y) coordinates as follows:

$$z = \sum_{i=0}^{M_\mathrm{s}} \sum_{j=0}^{M_\mathrm{t}} \tilde{p}^\mathrm{z}_{ij} B_i^{M_\mathrm{s}} \left(\frac{x - \tilde{p}^\mathrm{x}_{00}}{M_\mathrm{s}\Delta\tilde{p}_\mathrm{x}} \right) B_j^{M_\mathrm{t}} \left(\frac{y - \tilde{p}^\mathrm{y}_{00}}{M_\mathrm{t}\Delta\tilde{p}_\mathrm{y}} \right) \tag{3.18}$$

$$\tilde{p}^\mathrm{x}_{00} \le x \le \tilde{p}^\mathrm{x}_{00} + M_\mathrm{s}\Delta\tilde{p}_\mathrm{x}$$
$$\tilde{p}^\mathrm{y}_{00} \le y \le \tilde{p}^\mathrm{y}_{00} + M_\mathrm{t}\Delta\tilde{p}_\mathrm{y}$$

In addition, the unit normal vector of the Bézier surface at the point $\tilde{\mathbf{r}}(s,t)$ which is denoted by $\tilde{\mathbf{n}}(s,t)$ can be calculated as follows [71]:

$$\tilde{\mathbf{n}}(s,t) = \frac{\displaystyle\sum_{i=0}^{2M_\mathrm{s}-1} \sum_{j=0}^{2M_\mathrm{t}-1} \tilde{\mathbf{q}}_{ij} B_i^{2M_\mathrm{s}-1}(s) B_j^{2M_\mathrm{t}-1}(t)}{\left\| \displaystyle\sum_{i=0}^{2M_\mathrm{s}-1} \sum_{j=0}^{2M_\mathrm{t}-1} \tilde{\mathbf{q}}_{ij} B_i^{2M_\mathrm{s}-1}(s) B_j^{2M_\mathrm{t}-1}(t) \right\|} \tag{3.19}$$

$$\tilde{\mathbf{q}}_{ij} = \frac{M_\mathrm{s} M_\mathrm{s}}{\left(\begin{array}{c} 2M_\mathrm{s}-1 \\ i \end{array} \right) \left(\begin{array}{c} 2M_\mathrm{t}-1 \\ j \end{array} \right)} \sum_{\substack{m_1+m_2=i \\ 0 \le m_1 \le M_\mathrm{s}-1 \\ 0 \le m_2 \le M_\mathrm{s}}} \sum_{\substack{n_1+n_2=j \\ 0 \le n_1 \le M_\mathrm{t} \\ 0 \le n_2 \le M_\mathrm{t}-1}}$$
$$\left\{ \left(\begin{array}{c} M_\mathrm{s}-1 \\ m_1 \end{array} \right) \left(\begin{array}{c} M_\mathrm{s} \\ m_2 \end{array} \right) \left(\begin{array}{c} M_\mathrm{t} \\ n_1 \end{array} \right) \left(\begin{array}{c} M_\mathrm{t}-1 \\ n_2 \end{array} \right) \left(\tilde{\mathbf{p}}_{(n_1+1)m_1} - \tilde{\mathbf{p}}_{n_1 m_1} \right) \times \left(\tilde{\mathbf{p}}_{n_2+(m_2+1)} - \tilde{\mathbf{p}}_{n_2 m_2} \right) \right\}$$

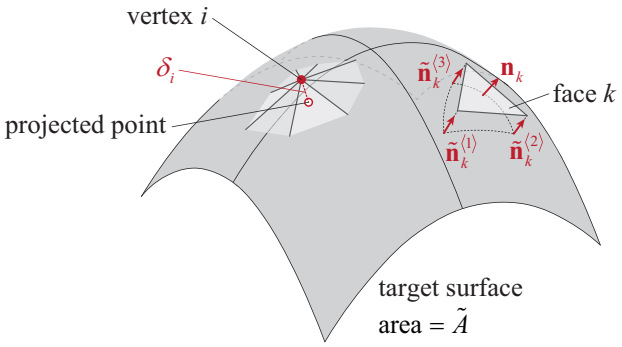

Figure 3.6: Quantities for defining approximation error function.

(2) Approximation error function for Euclidean distance

It is necessary to associate the point on the target surface with an origami vertex to measure the approximation error with respect to the Euclidean distance between the origami surface and the target surface. As shown in Fig. 3.6, the associated point on the target surface with an origami vertex is referred to as the *projected point*, and the distance between vertex i and its projected point is denoted by $\delta_i \in \mathbb{R}$. Note that δ_i is signed according to which side of the target surface vertex i is located. In Ref. [30], a projected point is defined as the point on the target surface which have the same (x, y) coordinates with the associated vertex. In this case, it is assumed that the control points of the target surface are aligned with the constant intervals in the x- and y-directions, and the position of the projected point is determined by the z-coordinates in Eq. (3.18). Therefore, it is straightforward to select the vertex coordinates of the origami surface or the nodal coordinates of the frame model as the variables of the optimization problem for the form generation. When the nodal coordinates are used as the variables, the coordinates of the vertices are obtained by Eqs. (2.19) or (2.21) formulated in Chapter 2.

On the other hand, a projected point is defined as the orthogonal projection of the vertex onto the target surface in Ref. [52]. In this case, the recursive calculation is necessary to determine the position of a projected point from the given vertex position [72], and this is computationally inefficient. Therefore, the opposite approach is adopted in Ref. [52]; i.e., the position of a origami vertex is determined from the given position of the associated projected point as the sum of the position vector of the projected point represented by Eq. (3.17) and the vector representing the amount and the direction of the *offset* from the target surface. For example, if δ_i is measured in the direction of the normal vector of the target surface, the position vector of vertex i denoted by $\boldsymbol{\xi}_i \in \mathbb{R}^3$ on the origami surface is written as follows:

$$\boldsymbol{\xi}_i = \tilde{\mathbf{r}}(s_i, t_i) + \delta_i \tilde{\mathbf{n}}(s_i, t_i) \tag{3.20}$$

where s_i and t_i are the parameters associated with vertex i which determine the position vector of the point on the target Bézier surface. In the following, the amount of offset δ_i is simply referred to as the offset. The parameters s_i and t_i and the offset δ_i for all the vertices are used as the variables in the optimization problem. The direction of the offset is

Table 3.1: Combinations of the suitable variables and the conditions to measure the approximation error with respect to the distance.

	Ref. [30]	Ref. [52]
Variables	Coordinates of vertices or nodes	Parameters of Bézier surface and offset distances
Arrangement of control points	Regularly aligned	Arbitrarily aligned
Direction to measure distance	z-direction	Arbitrary

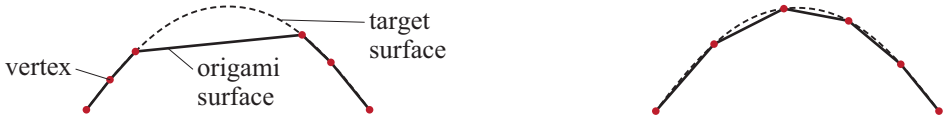

(a) **(b)**

Figure 3.7: Comparison of the appearance of two origami surfaces whose all vertices are on the target surface but which have different surface areas; (a) Large approximation error for surface area, (b) Small approximation error for surface area.

not limited to the normal of the target surface and can be arbitrary; e.g., in the z-direction as in Ref. [30] where $\tilde{\mathbf{n}}(s_i, t_i)$ in Eq. (3.20) is replaced with $\mathbf{e}_z = (0, 0, 1)^\mathsf{T}$. This approach also can be used when the control points of the target Bézier surface are not aligned regularly and the z-coordinate of the point on the Bézier surface cannot be determined from its x- and y-coordinates. Combinations of the selection of variables, the arrangement of control points of the target Bézier surface, and the direction in which the distance between each origami vertex and the target surface are summarized in Table. 3.1. In both cases, the approximation error function F_{dist} for the distance between the origami and the target surface is defined as follows:

$$F_{\text{dist}} = \frac{1}{2} \sum_{i=1}^{N_\text{V}} \delta_i^2 \tag{3.21}$$

(3) Approximation error function for surface area

As shown in Fig. 3.7(a), the *appearance* of the origami surface may not be similar to that of the target surface even when all the origami vertices are on the target surface. Therefore, the approximation accuracy with respect to the surface area is considered to obtain the origami surface like Fig. 3.7(b) which has a similar appearance to the target surface. Let A and $\tilde{A} \in \mathbb{R}$ denote the area of the origami surface and the target surface. The approximation error function F_{area} for the error of the surface area between the origami and the target surface is defined as

$$F_{\text{area}} = |A - \tilde{A}| \tag{3.22}$$

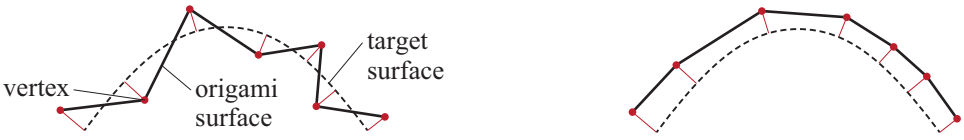

Figure 3.8: Comparison of the appearance of two origami surfaces whose each vertex has equal distance but face normal vectors are in the different directions from the target surface; (a) Large approximation error for face normal vectors, (b) Small approximation error for face normal vectors.

where A is calculated as the sum of the areas of all the triangular faces of the origami surface, and $\tilde{A}$ is approximated by triangulating the target surface into a fine mesh and summing up the area of all the triangular faces.

(4) Approximation error function for face normal vector

Approximation accuracy with respect to the direction of the normal vectors of the origami faces is considered since the angles of the faces are important factors for the appearance of the polyhedral surface as shown in Fig. 3.8. The two origami surfaces in Fig. 3.8 have the same value of F_{dist}; however, the surface in Fig. 3.8(b) has more similar appearance to the target surface than the surface in Fig. 3.8(a) since the directions of the normal vectors of the faces of the former surface approximate those of the target surface while those of the latter surface do not. As shown in Fig. 3.6, let $\tilde{\mathbf{n}}_k^{\langle 1\rangle}$, $\tilde{\mathbf{n}}_k^{\langle 2\rangle}$, and $\tilde{\mathbf{n}}_k^{\langle 3\rangle} \in \mathbb{R}^3$ denote the unit normal vectors of the target surface evaluated at the projected points of the three vertices of face k. Then the unit reference normal vector of face k is defined as follows:

$$\tilde{\mathbf{n}}_k^{\text{ref}} = \frac{\tilde{\mathbf{n}}_k^{\langle 1\rangle} + \tilde{\mathbf{n}}_k^{\langle 2\rangle} + \tilde{\mathbf{n}}_k^{\langle 3\rangle}}{\left\| \tilde{\mathbf{n}}_k^{\langle 1\rangle} + \tilde{\mathbf{n}}_k^{\langle 2\rangle} + \tilde{\mathbf{n}}_k^{\langle 3\rangle} \right\|} \tag{3.23}$$

The approximation error function F_{normal} for the error of the direction of the normal vectors between the origami faces and the reference normal vectors of the target surface is defined as follows:

$$F_{\text{normal}} = \frac{1}{2} \sum_{k=1}^{N_{\text{F}}} \left\| \mathbf{n}_k - \tilde{\mathbf{n}}_k^{\text{ref}} \right\|^2 \tag{3.24}$$

Note that the initial direction of $\mathbf{n}_k$ is defined so that $\mathbf{n}_k \cdot \tilde{\mathbf{n}}_k^{\text{ref}} \geq 0$ holds for $k = 1, \ldots, N_{\text{F}}$ in the initial shape of the form generation.

3.3.2 Independent variables for form generation

As discussed in Section 3.3.1, design variables of the optimization problem for generating a developable origami surface are the coordinates of origami vertices, the nodal coordinates of the frame model, or the pairs of the parameters and the offset which determine the points on the target Bézier surface and the distances from these points to the origami vertices. When

the nodal coordinates of a frame model are used, the independent coordinates are identified from the linear constraints on the nodal coordinates for the consistent representation of the origami surface by the frame model as shown in Chapter 2. The variables are selected according to the computational efficiency of the approximation errors as shown in Table. 3.1. In this section, further reduction of the number of design variables is considered by taking into account the linear constraints on the boundary shape and the symmetry of the origami surface [30].

(1) Linear constraints on coordinates of vertices of origami surface or nodes of frame model

Consider the case where the coordinates of origami vertices or the nodes of frame model are used as the variables. To prevent the perimeter shape of the origami surface from being drastically different from that of the target surface, the *boundary planes* where the perimeter vertices exist are introduced. Here, it is assumed that a perimeter curve of the target Bézier surface is on the boundary plane defined as $\beta_{\mathrm{bnd}}^{(1)}x + \beta_{\mathrm{bnd}}^{(2)}y + \beta_{\mathrm{bnd}}^{(3)}z + 1 = 0$ for the coefficients $\beta_{\mathrm{bnd}}^{(j)} \in \mathbb{R}$ $(j = 1,2,3)$. Note that the Bézier surface has four perimeter curves obtained by setting the parameters as $(s,0), (s,1), (0,t), (1,t)$ $(0 \le s,t \le 1)$ in Eq. (3.17). When the vertex i is on the boundary plane, its position vector $\boldsymbol{\xi}_i$ needs to satisfy the following equation:

$$\begin{bmatrix} \boldsymbol{\beta}_{\mathrm{bnd}}^{\mathsf{T}} & 1 \end{bmatrix} \begin{pmatrix} \boldsymbol{\xi}_i \\ 1 \end{pmatrix} = 0 \tag{3.25}$$

where $\boldsymbol{\beta}_{\mathrm{bnd}} = (\beta_{\mathrm{bnd}}^{(1)}, \beta_{\mathrm{bnd}}^{(2)}, \beta_{\mathrm{bnd}}^{(3)})^{\mathsf{T}} \in \mathbb{R}^3$. Let $\boldsymbol{\Xi} \in \mathbb{R}^{3N_{\mathrm{V}}}$ denote the assemblage of the position vectors of all the vertices. Then, Eq. (3.25) for all the vertices on the boundary planes are combined into the following equation:

$$\mathbf{B}_{\mathrm{bnd}} \begin{pmatrix} \boldsymbol{\Xi} \\ 1 \end{pmatrix} = \mathbf{0} \tag{3.26}$$

where N_{bnd} is the number of constraint equations for the perimeter vertices and $\mathbf{B}_{\mathrm{bnd}} \in \mathbb{R}^{N_{\mathrm{bnd}} \times (3N_{\mathrm{V}}+1)}$ is a constant matrix whose components are 0, 1, or the coefficients of the equations of the boundary planes. In addition, the vertices at the corners of the origami surface are fixed at their original position. When the initial position vector of the vertex i at the corner of the origami surface is $\bar{\boldsymbol{\xi}}_i$, this condition is formulated as

$$\boldsymbol{\xi}_i - \bar{\boldsymbol{\xi}}_i = \begin{bmatrix} \mathbf{I}_3 & -\bar{\boldsymbol{\xi}}_i \end{bmatrix} \begin{pmatrix} \boldsymbol{\xi}_i \\ 1 \end{pmatrix} = \mathbf{0} \tag{3.27}$$

Equation (3.27) for all the corner vertices are combined into the following equation:

$$\mathbf{B}_{\mathrm{cnr}} \begin{pmatrix} \boldsymbol{\Xi} \\ 1 \end{pmatrix} = \mathbf{0} \tag{3.28}$$

where $\mathbf{B}_{\mathrm{cnr}} \in \mathbb{R}^{12 \times (3N_{\mathrm{V}}+1)}$ is a constant matrix whose components are 0, 1, or the initial coordinates of the corner vertices.

If the target surface and the crease pattern of the origami surface have the symmetry property, the form generation is carried out so that the symmetry is preserved. In this study, at most two planes of symmetry are considered, and if two planes of symmetry are considered, they are assumed to be perpendicular to each other. Suppose the vertices i and i' are located symmetrically with respect to a plane of symmetry while they are assumed not to be on the plane. When a plane of symmetry is defined as $\beta_{\mathrm{sym}}^{(1)}x+\beta_{\mathrm{sym}}^{(2)}y+\beta_{\mathrm{sym}}^{(3)}z+1=0$ for the coefficients $\beta_{\mathrm{sym}}^{(j)}\in\mathbb{R}$ $(j=1,2,3)$, the position vectors of vertices i and i' denoted by $\boldsymbol{\xi}_i$ and $\boldsymbol{\xi}_{i'}\in\mathbb{R}^3$, respectively, need to satisfy the following equation throughout the process of the form generation:

$$\begin{aligned}\boldsymbol{\xi}_i-\boldsymbol{\xi}_{i'}&=2\frac{\begin{bmatrix}\beta_{\mathrm{sym}}^{(1)} & \beta_{\mathrm{sym}}^{(2)} & \beta_{\mathrm{sym}}^{(3)} & 1\end{bmatrix}\begin{pmatrix}\boldsymbol{\xi}_i\\1\end{pmatrix}}{\left(\beta_{\mathrm{sym}}^{(1)}\right)^2+\left(\beta_{\mathrm{sym}}^{(2)}\right)^2+\left(\beta_{\mathrm{sym}}^{(3)}\right)^2}\begin{pmatrix}\beta_{\mathrm{sym}}^{(1)}\\\beta_{\mathrm{sym}}^{(2)}\\\beta_{\mathrm{sym}}^{(3)}\end{pmatrix}\\ \Leftrightarrow&\begin{bmatrix}\mathbf{I}_3-\dfrac{2\boldsymbol{\beta}_{\mathrm{sym}}\left(\boldsymbol{\beta}_{\mathrm{sym}}\right)^{\mathsf{T}}}{\left\|\boldsymbol{\beta}_{\mathrm{sym}}\right\|^2} & -\mathbf{I}_3 & -\dfrac{2\boldsymbol{\beta}_{\mathrm{sym}}}{\left\|\boldsymbol{\beta}_{\mathrm{sym}}\right\|^2}\end{bmatrix}\begin{pmatrix}\boldsymbol{\xi}_i\\\boldsymbol{\xi}_{i'}\\1\end{pmatrix}=\mathbf{0}\end{aligned}\tag{3.29}$$

where $\boldsymbol{\beta}_{\mathrm{sym}}=(\beta_{\mathrm{sym}}^{(1)},\beta_{\mathrm{sym}}^{(2)},\beta_{\mathrm{sym}}^{(3)})^{\mathsf{T}}\in\mathbb{R}^3$. When the number of constraint equations for the symmetry in Eq. (3.29) for all the pairs of vertices and for all the planes of symmetry is N_{sym}, all the equations are combined into a vector form using a constant matrix $\mathbf{B}_{\mathrm{sym}}\in\mathbb{R}^{N_{\mathrm{sym}}\times(3N_{\mathrm{V}}+1)}$ as follows:

$$\mathbf{B}_{\mathrm{sym}}\begin{pmatrix}\boldsymbol{\Xi}\\1\end{pmatrix}=\mathbf{0}\tag{3.30}$$

The components of $\mathbf{B}_{\mathrm{sym}}$ are determined by the coefficient matrix of $(\boldsymbol{\xi}_i^{\mathsf{T}},\boldsymbol{\xi}_{i'}^{\mathsf{T}},1)^{\mathsf{T}}$ in the left-hand side of the second equation of Eq. (3.29). If vertex i is on the plane of symmetry represented as $\beta_{\mathrm{sym}}^{(1)}x+\beta_{\mathrm{sym}}^{(2)}y+\beta_{\mathrm{sym}}^{(3)}z+1=0$, vertex i needs to stay on the plane of symmetry and its position vector $\boldsymbol{\xi}_i$ should satisfy the following equation throughout the process of the form generation:

$$\begin{bmatrix}\boldsymbol{\beta}_{\mathrm{sym}}^{\mathsf{T}} & 1\end{bmatrix}\begin{pmatrix}\boldsymbol{\xi}_i\\1\end{pmatrix}=0\tag{3.31}$$

Equation (3.31) for all the vertices on the planes of symmetry and for all the planes of symmetry are combined into the following equation:

$$\mathbf{B}_{\mathrm{on}}\begin{pmatrix}\boldsymbol{\Xi}\\1\end{pmatrix}=\mathbf{0}\tag{3.32}$$

where N_{on} is the number of constraint equations for the vertices on the planes of symmetry and $\mathbf{B}_{\mathrm{on}}\in\mathbb{R}^{N_{\mathrm{on}}\times(3N_{\mathrm{V}}+1)}$ is a constant matrix whose components are 0, 1, or the coefficients of the equations of the planes of symmetry.

When the number of linear constraint equations on the vertex coordinates represented by Eqs. (3.26), (3.28), (3.30), and (3.32) is denoted by $N_{\mathrm{con}}=N_{\mathrm{bnd}}+12+N_{\mathrm{sym}}+N_{\mathrm{on}}$, these

constraint equations are combined into a vector equation as follows:

$$\mathbf{B}_{\mathrm{V}} \begin{pmatrix} \boldsymbol{\Xi} \\ 1 \end{pmatrix} = \mathbf{0} \tag{3.33}$$

$$\mathbf{B}_{\mathrm{V}} = \begin{bmatrix} \mathbf{B}_{\mathrm{bnd}} \\ \mathbf{B}_{\mathrm{cnr}} \\ \mathbf{B}_{\mathrm{sym}} \\ \mathbf{B}_{\mathrm{on}} \end{bmatrix} \in \mathbb{R}^{N_{\mathrm{con}} \times (3N_{\mathrm{V}}+1)}$$

Note that in the case where the symmetry of the origami surface is not considered, $\mathbf{B}_{\mathrm{sym}}$ and $\mathbf{B}_{\mathrm{on}}$ are omitted from $\mathbf{B}_{\mathrm{V}}$, and the number of the constraint equations is reduced to $N_{\mathrm{con}} = N_{\mathrm{bnd}} + 12$.

Next, consider the case where the nodal coordinates of the frame models are used as the design variable. As shown in Chapter 2, the independent coordinates of nodes are identified by utilizing the properties of the RREF of the matrix representing the equations for the consistent representation of the origami surface by the frame model. Let $\mathbf{Z}_{\mathrm{free}} \in \mathbb{R}^{3N_{\mathrm{V}}}$ denote the vector of assemblage of the independent nodal coordinates. Note that the number of components of $\mathbf{Z}_{\mathrm{free}}$ is equal to that of the vertex coordinates $\boldsymbol{\Xi}$ as explained in Chapter 2. According to Eq. (2.21) in Chapter 2, $\boldsymbol{\Xi}$ and $\mathbf{Z}_{\mathrm{free}}$ have the following relation:

$$\boldsymbol{\Xi} = \mathbf{C}_{\mathrm{NV}} \mathbf{Z}_{\mathrm{free}} \tag{3.34}$$

where $\mathbf{C}_{\mathrm{NV}}$ is a $3N_{\mathrm{V}} \times 3N_{\mathrm{V}}$ constant matrix. Substituting Eq. (3.34) into Eq. (3.33), the following equation is obtained:

$$\mathbf{B}_{\mathrm{V}} \begin{pmatrix} \mathbf{C}_{\mathrm{NV}} \mathbf{Z}_{\mathrm{free}} \\ 1 \end{pmatrix} = \mathbf{B}_{\mathrm{V}} \begin{bmatrix} \mathbf{C}_{\mathrm{NV}} & \mathbf{0} \\ \mathbf{0} & 1 \end{bmatrix} \begin{pmatrix} \mathbf{Z}_{\mathrm{free}} \\ 1 \end{pmatrix} = \mathbf{0} \tag{3.35}$$

Here, define a matrix $\mathbf{B}_{\mathrm{N}}$ as follows:

$$\mathbf{B}_{\mathrm{N}} = \mathbf{B}_{\mathrm{NV}} \begin{bmatrix} \mathbf{C}_{\mathrm{V}} & \mathbf{0} \\ \mathbf{0} & 1 \end{bmatrix} \in \mathbb{R}^{N_{\mathrm{con}} \times (3N_{\mathrm{V}}+1)}$$

Then the linear constraint equations which the independent nodal coordinates vector $\mathbf{Z}_{\mathrm{free}}$ needs to satisfy can be written as follows:

$$\mathbf{B}_{\mathrm{N}} \begin{pmatrix} \mathbf{Z}_{\mathrm{free}} \\ 1 \end{pmatrix} = \mathbf{0} \tag{3.36}$$

(2) Linear constraints on the parameters of Bézier surface and the offsets

Consider the case where the design variables of the optimization problem for the form generation are the pairs of (s,t) parameters and the offset which determine the points on the target Bézier surface and the distances from these points to the origami vertices. In this case, the perimeter shape of the origami surface is constrained by simply fixing the values of (s,t) parameters of the of target Bézier surface if their initial values are 0 or 1. Here,

$\boldsymbol{\omega}_i \in \mathbb{R}^3$ is defined as $\boldsymbol{\omega}_i = (s_i, t_i, \delta_i)^\mathsf{T}$ where s_i and t_i are the parameters of the target Bézier surface corresponding to vertex i and δ_i is the offset value of vertex i from the target Bézier surface, respectively. If the initial value of s_i which is denoted by $\bar{s}_i$ is equal to 0 or 1, $\boldsymbol{\omega}_i$ needs to satisfy the following equation:

$$\begin{bmatrix} 1 & 0 & 0 & -\bar{s}_i \end{bmatrix} \begin{pmatrix} \boldsymbol{\omega}_i \\ 1 \end{pmatrix} = 0 \tag{3.37}$$

On the other hand, if the initial value of t_i which is denoted by $\bar{t}_i$ is equal to 0 or 1, $\boldsymbol{\omega}_i$ needs to satisfy the following equation:

$$\begin{bmatrix} 0 & 1 & 0 & -\bar{t}_i \end{bmatrix} \begin{pmatrix} \boldsymbol{\omega}_i \\ 1 \end{pmatrix} = 0 \tag{3.38}$$

Let $\boldsymbol{\Omega} \in \mathbb{R}^{3N_\mathrm{V}}$ denote the assemblage of $\boldsymbol{\omega}_i$ for all the vertices. When the number of constraints represented by Eqs. (3.37) and (3.38) is $\tilde{N}_\mathrm{bnd}$, these constraints for all the perimeter vertices are combined into the following equation:

$$\tilde{\mathbf{B}}_\mathrm{bnd} \begin{pmatrix} \boldsymbol{\Omega} \\ 1 \end{pmatrix} = \mathbf{0} \tag{3.39}$$

where $\tilde{\mathbf{B}}_\mathrm{bnd} \mathbb{R}^{\tilde{N}_\mathrm{bnd} \times (3N_\mathrm{V}+1)}$ is a constant matrix whose components are 0 or 1. Note that the number of constraints N_bnd and $\tilde{N}_\mathrm{bnd}$ may be different. The constraints for the positions of corner vertices are also easily satisfied by fixing their offset values δ_i to 0 for all the corner vertices under the assumption that the constraint equation (3.39) is satisfied. In a similar manner as the derivation of Eq. (3.28), this condition can be written as follows:

$$\tilde{\mathbf{B}}_\mathrm{cnr} \begin{pmatrix} \boldsymbol{\Omega} \\ 1 \end{pmatrix} = \mathbf{0} \tag{3.40}$$

where $\tilde{\mathbf{B}}_\mathrm{cnr} \in \mathbb{R}^{4 \times (3N_\mathrm{V}+1)}$ is a constant matrix which has only one non-zero component in each row that is 1 and corresponds to the offset value of a corner vertex.

If the target surface and the crease pattern of the origami surface have the symmetry property, the constraints for the symmetry is considered in the parameter space (s,t). When a plane of symmetry in the parameter space is defined as $\tilde{\beta}^{(1)}_\mathrm{sym} s + \tilde{\beta}^{(2)}_\mathrm{sym} t + 1 = 0$ for the coefficients $\tilde{\beta}^{(1)}_\mathrm{sym}$ and $\tilde{\beta}^{(2)}_\mathrm{sym} \in \mathbb{R}$, the parameters and the offset values of vertices i and i' which are located symmetrically with respect to the plane need to satisfy the following equation throughout the process of the form generation:

$$\begin{bmatrix} \mathbf{I}_3 - \dfrac{2\tilde{\boldsymbol{\beta}}_\mathrm{sym} \left(\tilde{\boldsymbol{\beta}}_\mathrm{sym}\right)^\mathsf{T}}{\left\|\tilde{\boldsymbol{\beta}}_\mathrm{sym}\right\|^2} & -\mathbf{I}_3 & -\dfrac{2\tilde{\boldsymbol{\beta}}_\mathrm{sym}}{\left\|\tilde{\boldsymbol{\beta}}_\mathrm{sym}\right\|^2} \end{bmatrix} \begin{pmatrix} \boldsymbol{\omega}_i \\ \boldsymbol{\omega}_{i'} \\ 1 \end{pmatrix} = \mathbf{0} \tag{3.41}$$

where $\boldsymbol{\omega}_i = (s_i, t_i, \delta_i)^\mathsf{T} \in \mathbb{R}^3$ and $\tilde{\boldsymbol{\beta}}_\mathrm{sym} = (\tilde{\beta}^{(1)}_\mathrm{sym}, \tilde{\beta}^{(2)}_\mathrm{sym}, 0)^\mathsf{T} \in \mathbb{R}^3$. Let $\boldsymbol{\Omega} \in \mathbb{R}^{3N_\mathrm{V}}$ denote the assemblage of the parameters s_i and t_i, and the offset value δ_i for all the vertices. Then, all the constraint equations for the symmetry are combined into a following equation:

$$\tilde{\mathbf{B}}_\mathrm{sym} \begin{pmatrix} \boldsymbol{\Omega} \\ 1 \end{pmatrix} = \mathbf{0} \tag{3.42}$$

where $\tilde{\mathbf{B}}_{\mathrm{sym}}$ is a $N_{\mathrm{sym}} \times (3N_{\mathrm{V}}+1)$ constant matrix whose components are determined by the coefficient matrix in the left-hand side of Eq. (3.41). If vertex i is on the plane of symmetry represented as $\tilde{\beta}^{(1)}_{\mathrm{sym}} s + \tilde{\beta}^{(2)}_{\mathrm{sym}} t + 1 = 0$, its parameters s_i and t_i need to satisfy the following equation throughout the process of the form generation:

$$\begin{bmatrix} \tilde{\boldsymbol{\beta}}^{\mathsf{T}}_{\mathrm{sym}} & 1 \end{bmatrix} \begin{pmatrix} \boldsymbol{\omega}_i \\ 1 \end{pmatrix} = 0 \tag{3.43}$$

Equation (3.43) for all the vertices on the planes of symmetry and for all the planes of symmetry are combined into the following equation:

$$\tilde{\mathbf{B}}_{\mathrm{on}} \begin{pmatrix} \boldsymbol{\Omega} \\ 1 \end{pmatrix} = \mathbf{0} \tag{3.44}$$

where $\tilde{\mathbf{B}}_{\mathrm{on}} \mathbb{R}^{N_{\mathrm{on}} \times (3N_{\mathrm{V}}+1)}$ is a constant matrix whose components are 0, 1, or the coefficients of the equations of the planes of symmetry. Note that the number of constraints for the vertices located at the symmetric positions and the constraints for the vertices on the planes of symmetry are equal to the above two cases of design variables. When the number of linear constraint equations on the parameters and the offset values represented by Eqs. (3.39), (3.40), (3.42), and (3.44) is denoted by $\tilde{N}_{\mathrm{con}} = \tilde{N}_{\mathrm{bnd}} + 4 + N_{\mathrm{sym}} + N_{\mathrm{on}}$, these constraint equations are combined into a vector equation as follows:

$$\mathbf{B}_{\mathrm{P}} \begin{pmatrix} \boldsymbol{\Omega} \\ 1 \end{pmatrix} = \mathbf{0} \tag{3.45}$$

$$\mathbf{B}_{\mathrm{P}} = \begin{bmatrix} \tilde{\mathbf{B}}_{\mathrm{bnd}} \\ \tilde{\mathbf{B}}_{\mathrm{cnr}} \\ \tilde{\mathbf{B}}_{\mathrm{sym}} \\ \tilde{\mathbf{B}}_{\mathrm{on}} \end{bmatrix} \in \mathbb{R}^{\tilde{N}_{\mathrm{con}} \times (3N_{\mathrm{V}}+1)}$$

Note that in the case where the symmetry of the origami surface is not considered, $\tilde{\mathbf{B}}_{\mathrm{sym}}$ and $\tilde{\mathbf{B}}_{\mathrm{on}}$ are omitted from $\mathbf{B}_{\mathrm{P}}$, and the number of the constraint equations is reduced to $N_{\mathrm{con}} = \tilde{N}_{\mathrm{bnd}} + 4$ as in the previous section.

(3) Variable reduction reflecting the linear constraints

Let a matrix $\bar{\mathbf{B}}$ represent $\mathbf{B}_{\mathrm{V}} \in \mathbb{R}^{N_{\mathrm{con}} \times (3N_{\mathrm{V}}+1)}$ in Eq. (3.33), $\mathbf{B}_{\mathrm{N}} \in \mathbb{R}^{(N_{\mathrm{con}}+3N_{\mathrm{Ein}}+3N_{\mathrm{F}}) \times (3N_{\mathrm{V}}+1)}$ in Eq. (3.36), or $\mathbf{B}_{\mathrm{P}} \in \mathbb{R}^{\tilde{N}_{\mathrm{con}} \times (3N_{\mathrm{V}}+1)}$ in Eq. (3.45). In addition, let a vector $\bar{\mathbf{X}}$ represent $\boldsymbol{\Xi} \in \mathbb{R}^{3N_{\mathrm{V}}}$ in Eq. (3.33), $\mathbf{Z}_{\mathrm{free}} \in \mathbb{R}^{3N_{\mathrm{V}}}$ in Eq. (3.36), or $\boldsymbol{\Omega} \in \mathbb{R}^{3N_{\mathrm{V}}}$ in Eq. (3.45). $\bar{\mathbf{B}}$ and $\bar{\mathbf{X}}$ are determined in accordance with the selection of the design variables. Then, the linear constraint equations (3.33), (3.36), and (3.45) are written in a common form as follows:

$$\bar{\mathbf{B}} \begin{pmatrix} \bar{\mathbf{X}} \\ 1 \end{pmatrix} = \mathbf{0} \tag{3.46}$$

According to the identification method of the independent variables introduced in Appendix A, $\bar{\mathbf{X}}$ satisfying Eq. (3.46) is divided into the vectors of the independent and dependent components $\hat{\mathbf{X}}$ and $\mathbf{X}$, respectively. Defining $\mathbf{B}$ as the matrix which is an assemblage of the

components of the RREF of $\bar{\mathbf{B}}$ in the non-zero rows and the non-pivot columns, Eq. (3.46) is rewritten as the following form:

$$\begin{bmatrix} \mathbf{I}_{\mathrm{rank}(\bar{\mathbf{B}})} & \mathbf{B} \end{bmatrix} \begin{pmatrix} \hat{\mathbf{X}} \\ \mathbf{X} \\ 1 \end{pmatrix} = \hat{\mathbf{X}} + \mathbf{B} \begin{pmatrix} \mathbf{X} \\ 1 \end{pmatrix} = \mathbf{0} \tag{3.47}$$

Therefore, the vector of the dependent components of $\bar{\mathbf{X}}$ satisfying Eq. (3.46) is calculated as

$$\hat{\mathbf{X}} = -\mathbf{B} \begin{pmatrix} \mathbf{X} \\ 1 \end{pmatrix} \tag{3.48}$$

Here, the size of $\mathbf{B}$ and the number of independent variables are $\mathrm{rank}(\bar{\mathbf{B}}) \times (3N_\mathrm{V} - \mathrm{rank}(\bar{\mathbf{B}}) + 1)$ and $3N_\mathrm{V} - \mathrm{rank}(\bar{\mathbf{B}})$, respectively, regardless of the choice of variables. Consequently, $\mathbf{X}$ is used as the independent variables in the optimization problem for the form generation of a developable origami surface.

3.3.3 Formulation of optimization problems

Optimization problems are formulated to obtain an origami surface which can be developed to a plane. The design variables used for optimization are identified as shown in Sections 3.3.1 and 3.3.2. A vector of the design variables is denoted by $\mathbf{X} \in \mathbb{R}^{3N_\mathrm{V} - \mathrm{rank}(\bar{\mathbf{B}})}$ where $\bar{\mathbf{B}}$ is the matrix representing linear constraints reflecting the perimeter shape and the symmetry of the origami surface. Then, the vector representing the errors of the developability conditions in Eq. (3.15) is regarded as a function of $\mathbf{X}$ written as $\mathbf{D}(\mathbf{X}) \in \mathbb{R}^{N_\mathrm{Vin} + N_\mathrm{Ediv} + 3N_\mathrm{Cin}}$. The non-negative approximation error functions defined as Eqs. (3.21), (3.22), and (3.24) are also regarded as functions of $\mathbf{X}$ and written as $F_\mathrm{dist}(\mathbf{X})$, $F_\mathrm{area}(\mathbf{X})$, and $F_\mathrm{normal}(\mathbf{X}) \in \mathbb{R}$, respectively. To generate a developable origami surface which approximates the target surface, the weighted sum of the approximation error functions is defined as

$$F_\mathrm{app}(\mathbf{X}) = F_\mathrm{dist}(\mathbf{X}) + c_\mathrm{area} F_\mathrm{area}(\mathbf{X}) + c_\mathrm{normal} F_\mathrm{normal}(\mathbf{X}) \tag{3.49}$$

The non-negative function $F_\mathrm{app}(\mathbf{X})$ is minimized under the developability conditions $\mathbf{D}(\mathbf{X}) = \mathbf{0}$ where c_area and $c_\mathrm{normal} \in \mathbb{R}$ are the non-negative weight coefficients. To avoid an excessively acute triangular faces, the upper bound α_max and lower bound α_min are assigned for $\alpha_{ik}(\mathbf{X})$, which is the inner angle of face k at vertex i ($i = 1, \ldots, N_\mathrm{V}$; $k = 1, \ldots, N_\mathrm{F}$). In addition, the lower bound l_min is assigned for the length of each edge $l_j(\mathbf{X})$ ($j = 1, \ldots, N_\mathrm{E}$) to prevent the faces from degenerating into lines or points, and the angle between each face normal vector $\mathbf{n}_k(\mathbf{X})$ ($k = 1, \ldots, N_\mathrm{F}$) and its reference unit normal vector $\tilde{\mathbf{n}}_k^\mathrm{ref}(\mathbf{X})$ is restricted to less than or equal to $\pi/2$ to avoid a flipped face. The ranges of the design variables denoted as $\mathbf{X} \in \chi$ are also incorporated so that if the design variables are the parameters of the target Bézeir surface, they are in the range between 0 and 1. The ranges of the offset may also be incorporated to assign the upper bound of the approximation error for the distance between the origami surface and the target surface. If the design variables are the vertex

coordinates or the nodal coordinates, the ranges of the design variables are assigned for improving convergence of the optimization process.

The optimization problem to obtain a developable origami surface approximating the target surface is formulated as follows as a nonlinear programming (NLP) problem [52]:

$$\begin{cases} \min\limits_{\mathbf{X}} & F_{\mathrm{app}}(\mathbf{X}) \\ \text{s.t.} & \mathbf{D}(\mathbf{X}) = \mathbf{0} \\ & \alpha_{\min} \le \alpha_{ik}(\mathbf{X}) \le \alpha_{\max} \quad (i = 1,\ldots,N_{\mathrm{V}};\ k = 1,\ldots,N_{\mathrm{F}}) \\ & l_j(\mathbf{X}) \ge l_{\min} \quad (j = 1,\ldots,N_{\mathrm{E}}) \\ & \mathbf{n}_k(\mathbf{X}) \cdot \tilde{\mathbf{n}}_k^{\mathrm{ref}}(\mathbf{X}) \ge 0 \quad (k = 1,\ldots,N_{\mathrm{F}}) \\ & \mathbf{X} \in \chi \end{cases} \tag{3.50}$$

Since the form generation starts from the triangulated target surface as explained in Section 3.4, the initial shape of the form generation does not satisfy the developability conditions $\mathbf{D}(\mathbf{X}) = \mathbf{0}$. When the target surface has the large Gaussian curvature and the errors of $\mathbf{D}(\mathbf{X}) = \mathbf{0}$ are too large in the initial triangulated shape, a feasible solution of Problem (3.50) with sufficiently small errors of the developability conditions may not be found. Therefore, if an initial solution without fixed crease lines is not found, the following optimization problem is solved to find an initial guess of Problem (3.50) satisfying the developability conditions with small errors [30]:

$$\begin{cases} \min\limits_{\mathbf{X}} & F_{\mathrm{dev}}(\mathbf{X}) = \|\mathbf{D}(\mathbf{X})\|^2 \\ \text{s.t.} & \alpha_{\min} \le \alpha_{ik}(\mathbf{X}) \le \alpha_{\max} \quad (i = 1,\ldots,N_{\mathrm{V}};\ k = 1,\ldots,N_{\mathrm{F}}) \\ & l_j(\mathbf{X}) \ge l_{\min} \quad (j = 1,\ldots,N_{\mathrm{E}}) \\ & \mathbf{n}_k(\mathbf{X}) \cdot \tilde{\mathbf{n}}_k^{\mathrm{ref}}(\mathbf{X}) \ge 0 \quad (k = 1,\ldots,N_{\mathrm{F}}) \\ & \mathbf{X} \in \chi \end{cases} \tag{3.51}$$

Developability and rigid-foldability of the obtained origami surface are also confirmed by generation of the development diagram and large-deformation analysis to simulate the deployment process, respectively.

3.4 Overall procedure of form generation to obtain the multiple solutions

In this section, an overall form generation procedure is explained to obtain several developable and rigid-foldable origami shapes approximating the target surface with different number of fixed crease lines and the DOFs of mechanism. The form generation starts from the triangulated target surface whose edge topology defines the basic crease pattern of the rigid origami to be generated. The optimization problem (3.50) is repeatedly solved to obtain the shape of the developable rigid origami while the crease lines are sequentially fixed and converted to the dividing edges to reduce the DOF of the rigid-folding mechanism. The

variables of the optimization problem are selected from the vertex coordinates, the nodal coordinates, and the pair of (s,t) parameters of the target Bézier surface and the offsets from the target surface in accordance with the arrangement of the control points of the target surface and the direction to measure the distance between the origami vertices and the target surface as described in Section 3.3.1. The number of independent variables is reduced by the method introduced in Section 3.3.2. If a solution process of Problem (3.50) is not converged with sufficiently small errors of the developability conditions when Problem (3.50) is first solved in Step 4 of the form generation procedure, Problem (3.51) is solved to obtain a shape satisfying the developability conditions with small errors. The tolerances of the errors of the developability conditions are set empirically in this study. In the second and subsequent iteration of Step 4, the solution obtained in the last iteration is used for the initial shape of the optimization. This may help to find a feasible solution by directly solving Problem (3.50) from the second optimization process. If some crease lines that are not fixed are locked in the solution of the problem (3.50), alternative crease lines are to be selected. The method for finding the locked crease lines and the criteria for selecting the crease line to be fixed are proposed in Section 3.5. The procedure of form generation of developable rigid origamis that have faces with more than three edges and small DOFs is summarized as follows [28–30]:

Step 1. Define the target surface as the Bézier surface and triangulate it to define the basic crease line topology.

Step 2. Select the design variables used in Step 4 and identify the independent variables by the method shown in Section 3.3.2.

Step 3. Initialize the index set of fixed crease lines and the solution set as $\mathscr{E}_{\mathrm{div}} = \phi$ and $\mathscr{S}_{\mathrm{sol}} = \phi$, respectively.

Step 4. Solve Problem (3.50) to obtain a developable origami shape using the initial triangulated target surface or the solution of the previous step as the initial guess.

Step 5. If the optimization is not converged with sufficiently small errors, go to Step 6; otherwise, go to Step 8.

Step 6. If the last optimization process in Step 4 is the first one, go to Step 7; otherwise, go to Step 10.

Step 7. Solve Problem (3.51), and return to Step 4 if a feasible solution is obtained; otherwise, no developable origami surface is obtained and try a different triangulation pattern.

Step 8. Evaluate the infinitesimal mechanism using the method for partially rigid frames [38–40] summarized in Chapter 2. If DOF ≥ 1 and there is no locked crease line, add the solution to $\mathscr{S}_{\mathrm{sol}}$ and go to Step 9; if DOF ≥ 1 and the locked crease line exists, go to Step 10; otherwise, go to Step 11.

Step 9. Add the specified number of indices of the crease lines to be fixed to $\mathscr{E}_{\mathrm{div}}$ in accordance with the criterion presented in Section 3.5, and return to Step 4.

Step 10. If $\mathscr{E}_{\mathrm{div}} = \phi$, no developable polyhedron is obtained and try a different triangulation pattern; otherwise, replace the indices of the last fixed crease lines in $\mathscr{E}_{\mathrm{div}}$ with indices of the other crease lines.

Step 11. Generate the development diagram of each obtained origami shape in $\mathscr{S}_{\mathrm{sol}}$ by solving the optimization problem (3.16), and evaluate the errors between the lengths of corresponding edges in the folded shape and the development diagram.

Step 12. Carry out large-deformation analysis of each origami shape in $\mathscr{S}_{\mathrm{sol}}$ to simulate the deployment process, and evaluate its finite rigid-foldability.

The optimal shapes obtained in Step 4 satisfy the developability conditions with small errors. However, the conditions introduced in Section 3.2 are only the necessary conditions for developability, and we should confirm in Step 11 that the development diagram of the obtained solutions can be generated with good accuracy instead of simply confirming that the values of components of $\mathbf{D}(\mathbf{X})$ are approximately zero. The global finite rigid-foldability of each solution also need to be confirmed by the large-deformation analysis since the developability conditions only guarantee the local rigid-foldability in the neighborhood of each inner vertex. The case studies of the form generation with various target surfaces are described in Chapter 4.

3.5 Selection criteria of crease lines to be fixed

In this section, the selection criteria of the crease lines to be fixed are proposed reflecting the infinitesimal mechanism of the frame model. The infinitesimal mechanism of the frame model is evaluated by the method for partially rigid frames [38–40]. To predict the existence of locked crease lines and to define the selection criteria, a *pseudo stiffness matrix* of the frame model is introduced using the total potential energy of the frame model defined under the assumption that the members are rigid and the hinges have fictitious rotational stiffness. The selection criteria are defined as the scores of the hinges obtained from eigenvalue analysis of the pseudo stiffness matrix.

3.5.1 Infinitesimal displacement modes of the frame model

The number of nodes, members, and hinges of the frame model are denoted by N_{N}, N_{M}, and N_{H}, respectively. The total number of fixed nodal displacement degrees of freedom including both the translation and rotation is denoted by N_{B}. Let $\mathbf{U} \in \mathbb{R}^{6N_{\mathrm{N}}-N_{\mathrm{B}}}$, $\mathbf{V} \in \mathbb{R}^{6N_{\mathrm{M}}}$, and $\boldsymbol{\varphi} \in \mathbb{R}^{N_{\mathrm{H}}}$ denote vectors of the assemblages of the free nodal displacements, the displacements of center points of members, and the increments of hinge rotation angles from the initial state to the deformed state, respectively. Note that the nodal displacements and the member displacements consist of translations and rotations of the nodes and the center points of

members. A generalized displacement vector is defined as $\mathbf{W} = (\mathbf{U}^\mathsf{T}, \mathbf{V}^\mathsf{T}, \boldsymbol{\varphi}^\mathsf{T})^\mathsf{T} \in \mathbb{R}^{N_\mathrm{W}}$ where the number of components of $\mathbf{W}$ is calculated as $N_\mathrm{W} = 6N_\mathrm{N} - N_\mathrm{B} + 6N_\mathrm{M} + N_\mathrm{H}$. Then, the incompatibility vector $\mathbf{G}(\mathbf{W}) \in \mathbb{R}^{N_\mathrm{G}}$ is defined as the function of $\mathbf{W}$ so that its components represents the errors of the relative displacements between the nodes and the member ends of the frame model as shown in in Chapter 2. The number of components of $\mathbf{G}(\mathbf{W})$ is $N_\mathrm{G} = 12N_\mathrm{M}$, and the gradient of $\mathbf{G}(\mathbf{W})$ with respect to $\mathbf{W}$ evaluated at $\mathbf{W} = \mathbf{0}$ is denoted in a matrix form by the compatibility matrix $\boldsymbol{\Gamma}^{(1)} \in \mathbb{R}^{N_\mathrm{G} \times N_\mathrm{W}}$. As shown in Chapter 2, a generalized displacement vector $\mathbf{W}$ satisfying the following equation is a *first-order infinitesimal mechanism*:

$$\boldsymbol{\Gamma}^{(1)}\mathbf{W} = \mathbf{0} \tag{3.52}$$

Assuming that the nodal displacements are constrained so that the only rigid-body motions of the entire model are constrained, the DOF of an infinitesimal rigid-folding mechanism is calculated as follows:

$$N_\mathrm{D} = N_\mathrm{W} - \mathrm{rank}(\boldsymbol{\Gamma}^{(1)}) \tag{3.53}$$

An arbitrary first-order infinitesimal mechanism $\mathbf{W}$, which satisfies Eq. (3.52), can be expressed as a linear combination of the *first-order infinitesimal mechanism modes* which are the bases of $\ker(\boldsymbol{\Gamma}^{(1)})$ [40]. Defining $\mathbf{H} \in \mathbb{R}^{N_\mathrm{W} \times N_\mathrm{D}}$ as a matrix whose columns are the first-order infinitesimal mechanism modes, a vector $\mathbf{W}$ satisfying Eq. (3.52) can be written for a coefficient vector $\mathbf{a} \in \mathbb{R}^{N_\mathrm{D}}$ as follows:

$$\mathbf{W} = \mathbf{H}\mathbf{a} \tag{3.54}$$

The first-order infinitesimal mechanism modes are assumed to be orthonormal bases of an N_W-dimensional vector space; i.e., $\mathbf{H}$ satisfies the following equation:

$$\mathbf{H}^\mathsf{T}\mathbf{H} = \mathbf{I}_{\mathrm{N_D}} \tag{3.55}$$

Vectors $\mathbf{U}$, $\mathbf{V}$, and $\boldsymbol{\varphi}$ satisfying Eq. (3.52), which represent the first-order infinitesimal mechanism, can be written as follows:

$$\mathbf{U} = \mathbf{H}_\mathrm{U}\mathbf{a} \tag{3.56}$$

$$\mathbf{V} = \mathbf{H}_\mathrm{V}\mathbf{a} \tag{3.57}$$

$$\boldsymbol{\varphi} = \mathbf{H}_\varphi\mathbf{a} \tag{3.58}$$

where $\mathbf{H}_\mathrm{U} \in \mathbb{R}^{(6N_\mathrm{N} - N_\mathrm{B}) \times N_\mathrm{D}}$, $\mathbf{H}_\mathrm{V} \in \mathbb{R}^{6N_\mathrm{M} \times N_\mathrm{D}}$, and $\mathbf{H}_\varphi \in \mathbb{R}^{N_\mathrm{H} \times N_\mathrm{D}}$ are the submatrices of $\mathbf{H}$. In the following, $\mathbf{U}$, $\mathbf{V}$, and $\boldsymbol{\varphi}$ represented as Eqs. (3.56), (3.57), and (3.58), respectively, are also referred to as first-order infinitesimal mechanisms or simply infinitesimal mechanisms. The details of the derivation of the infinitesimal mechanism are presented in Chapter 2.

When the displacement is restricted to the infinitesimal mechanism, an equilibrium equation of the frame model is derived by assigning fictitious rotational stiffness K_h (≥ 0) at hinge h ($= 1, \ldots, N_\mathrm{H}$). An external load $\mathbf{P} \in \mathbb{R}^{6N_\mathrm{N} - N_\mathrm{B}}$ is applied to the unconstrained degrees of freedom of nodal displacement. A total potential energy Π of the frame model is

formulated for a diagonal matrix of hinge stiffness $\mathbf{K}_\mathrm{H} = \mathrm{diag}(K_h) \in \mathbb{R}^{N_\mathrm{H} \times N_\mathrm{H}}$ as follows:

$$\begin{aligned} \Pi &= \frac{1}{2}\boldsymbol{\varphi}^\top \mathbf{K}_\mathrm{H} \boldsymbol{\varphi} - \mathbf{P}^\top \mathbf{U} \\ &= \frac{1}{2}\mathbf{a}^\top \left(\mathbf{H}_\varphi^\top \mathbf{K}_\mathrm{H} \mathbf{H}_\varphi \right) \mathbf{a} - (\mathbf{H}_\mathrm{U}\mathbf{P})^\top \mathbf{a} \end{aligned} \tag{3.59}$$

Here, the *pseudo stiffness matrix* $\tilde{\mathbf{K}} \in \mathbb{R}^{N_\mathrm{D} \times N_\mathrm{D}}$ and the *pseudo external load* $\tilde{\mathbf{P}} \in \mathbb{R}^{N_\mathrm{D}}$ are defined as follows [30]:

$$\tilde{\mathbf{K}} = \mathbf{H}_\varphi^\top \mathbf{K}_\mathrm{H} \mathbf{H}_\varphi \tag{3.60}$$

$$\tilde{\mathbf{P}} = \mathbf{H}_\mathrm{U} \mathbf{P} \tag{3.61}$$

The *pseudo displacement* is also defined as a vector $\mathbf{a} \in \mathbb{R}^{N_\mathrm{D}}$ in Eq. (3.59). Substituting Eqs. (3.60) and (3.61) into Eq. (3.59), the total potential energy is rewritten as follows:

$$\Pi = \frac{1}{2}\mathbf{a}^\top \tilde{\mathbf{K}} \mathbf{a} - \tilde{\mathbf{P}}^\top \mathbf{a} \tag{3.62}$$

According to the stationary condition of the total potential energy Π with respect to $\mathbf{a}$, the equilibrium equation is derived as

$$\tilde{\mathbf{P}} = \tilde{\mathbf{K}} \mathbf{a} \tag{3.63}$$

The i-th eigenvalue $\lambda_i \in \mathbb{R}$ and the corresponding eigenvector $\boldsymbol{\alpha}_i \in \mathbb{R}^{N_\mathrm{D}}$ $(i = 1, \ldots, N_\mathrm{D})$ of $\tilde{\mathbf{K}}$ satisfy the following equation:

$$\tilde{\mathbf{K}} \boldsymbol{\alpha}_i = \lambda_i \boldsymbol{\alpha}_i \tag{3.64}$$

Because the eigenvectors form the orthonormal bases of a N_D-dimensional vector space, they are normalized as $\|\boldsymbol{\alpha}_i\| = 1$ for $i = 1, \ldots, N_\mathrm{D}$ and are orthogonal to each other. Since $\boldsymbol{\alpha}_i$ satisfies $\boldsymbol{\Gamma}^{(1)} \mathbf{H} \boldsymbol{\alpha}_i = \mathbf{0}$ for each $i = 1, \ldots, N_\mathrm{D}$, $\mathbf{H}\boldsymbol{\alpha}_i$ can also be used as an infinitesimal mechanism mode of the frame model. According to Eq. (3.64), λ_i can be regarded as the stiffness of the frame model in the direction of $\mathbf{H}\boldsymbol{\alpha}_i$. The eigenvector $\boldsymbol{\alpha}_i$ is combined into a matrix $\mathbf{A} \in \mathbb{R}^{N_\mathrm{D} \times N_\mathrm{D}}$ which is a matrix whose i-th column is $\boldsymbol{\alpha}_i$ $(i = 1, \ldots, N_\mathrm{D})$, and according to Eq. (3.55), the following equation holds:

$$(\mathbf{HA})^\top (\mathbf{HA}) = \mathbf{A}^\top \mathbf{H}^\top \mathbf{HA} = \mathbf{I}_{N_\mathrm{D}} \tag{3.65}$$

Therefore, $\mathbf{H}\boldsymbol{\alpha}_i$, which is the i-th column of $\mathbf{HA}$, is orthogonal to each other. As in Eq. (3.58), a vector $\boldsymbol{\varphi}$ representing the infinitesimal mechanism for the hinge rotation angles can be expressed as a linear combination of $\boldsymbol{\phi}_i = \mathbf{H}_\varphi \boldsymbol{\alpha}_i$ for $i = 1, \ldots, N_\mathrm{D}$. On the other hand, $\boldsymbol{\alpha}_i$ satisfies the following relationship derived from Eq. (3.64):

$$\boldsymbol{\alpha}_j^\top \tilde{\mathbf{K}} \boldsymbol{\alpha}_i = \lambda_i \boldsymbol{\alpha}_j^\top \boldsymbol{\alpha}_i = \begin{cases} 0 & (i \neq j) \\ \lambda_i & (i = j) \end{cases} \tag{3.66}$$

Substituting $\tilde{\mathbf{K}} = \mathbf{H}_\varphi^\top \mathbf{K}_\mathrm{H} \mathbf{H}_\varphi$ and $\boldsymbol{\phi}_i = \mathbf{H}_\varphi \boldsymbol{\alpha}_i$ into Eq. (3.66), the following equation is obtained:

$$\boldsymbol{\phi}_j^\top \mathbf{K}_\mathrm{H} \boldsymbol{\phi}_i = \begin{cases} 0 & (i \neq j) \\ \lambda_i & (i = j) \end{cases} \tag{3.67}$$

3.5.2 Prediction of the existence of locked crease lines

In this section, transition of the deformation mechanism by fixing the crease lines is predicted based on the result of the analysis of infinitesimal mechanism presented in Section 3.5.1 and Ref. [30]. The infinitesimal mechanism modes before fixing the crease lines are used for estimation of an infinitesimal mechanism after fixing the crease lines. To ensure validity of the estimation of the transition of an infinitesimal mechanism, it should be assumed that the difference is small between the shapes of the origami surface before and after fixing the crease lines. The process of fixing a crease line and reducing the DOF of the mechanism is modeled as a process of reducing the size of the pseudo stiffness matrix; however, this is also approximately simulated as a process of increasing one eigenvalue of the pseudo stiffness matrix to infinity as the stiffness of a hinge is increased to infinity. Suppose the rotational stiffness of hinge h $(= 1, \ldots, N_{\mathrm{H}})$ of the frame model is increased to a moderately large value by ΔK_h $(\gg 0)$ to simulate the process of fixing the corresponding crease line. It is assumed that there is no locked hinge (crease line) before fixing hinge h. Let $\Delta \mathbf{K}_h \in \mathbb{R}^{\mathrm{N_H} \times \mathrm{N_H}}$ denote a matrix whose (h,h) element is ΔK_h and the other elements are 0. Then, the diagonal matrix of the hinge rotational stiffness after increasing the stiffness of hinge h is represented as $\mathbf{K}'_{\mathrm{H}} = \mathbf{K}_{\mathrm{H}} + \Delta \mathbf{K}_h \in \mathbb{R}^{\mathrm{N_H} \times \mathrm{N_H}}$. Assuming that the infinitesimal mechanism modes for the hinge rotation angles are invariant under the process of fixing hinge h, the pseudo stiffness matrix after increasing the stiffness of hinge h is calculated as $\tilde{\mathbf{K}}' = \mathbf{H}_\varphi^{\mathsf{T}} \mathbf{K}'_{\mathrm{H}} \mathbf{H}_\varphi = \mathbf{H}_\varphi^{\mathsf{T}} (\mathbf{K}_{\mathrm{H}} + \Delta \mathbf{K}_h) \mathbf{H}_\varphi$ where $\mathbf{H}_\varphi$ is invariant. The i-th eigenvalue and the corresponding eigenvector of the pseudo stiffness matrix $\tilde{\mathbf{K}}'$ are denoted by $\lambda'_i \in \mathbb{R}$ and $\boldsymbol{\alpha}'_i \in \mathbb{R}^{N_{\mathrm{D}}}$ $(i = 1, \ldots, N_{\mathrm{D}})$, respectively. In addition, the infinitesimal mechanism mode $\boldsymbol{\phi}'_i \in \mathbb{R}^{N_{\mathrm{H}}}$ for the hinge rotation angles is defined as $\boldsymbol{\phi}'_i = \mathbf{H}_\varphi \boldsymbol{\alpha}'_i$, and its j-th component is denoted by ϕ'_{ij}. When ΔK_h is sufficiently large, the following approximation holds:

$$
\begin{aligned}
\frac{1}{\Delta K_h} \boldsymbol{\alpha}_j'^{\mathsf{T}} \tilde{\mathbf{K}}' \boldsymbol{\alpha}'_i &= \frac{1}{\Delta K_h} \boldsymbol{\phi}_j'^{\mathsf{T}} (\mathbf{K}_{\mathrm{H}} + \Delta \mathbf{K}_h) \boldsymbol{\phi}'_i \\
&= \frac{1}{\Delta K_h} \left(\sum_{k=1}^{N_{\mathrm{H}}} K_k \phi'_{ik} \phi'_{jk} + \Delta K_h \phi'_{ih} \phi'_{jh} \right) \\
&\simeq \phi'_{ih} \phi'_{jh}
\end{aligned}
\tag{3.68}
$$

According to Eq. (3.66), the following approximations are obtained:

$$
\begin{cases}
\phi'_{ih} \phi'_{jh} \simeq 0 & (i \neq j) \\
\phi'^2_{ih} \simeq \dfrac{\lambda'_i}{\Delta K_h} & (i = j)
\end{cases}
\tag{3.69}
$$

The first approximation in Eq. (3.69) implies that at least one of ϕ'_{ih} and ϕ'_{jh} $(i \neq j)$ which are in the different infinitesimal mechanism modes is approximately zero after increasing the rotational stiffness of hinge h. On the other hand, the second approximation in Eq. (3.69) implies that if $\phi'_{ih} \simeq 0$, λ'_i has a finite value; and if ϕ'_{ih} is not close to zero, an absolute value of λ'_i is extremely large. When the rotational stiffness of hinge h is increased,

the case where $\phi'_{ih} \simeq 0$ holds for all $i = 1,\ldots,N_{\mathrm{D}}$ does not likely occur since λ'_i has a finite value for all $i = 1,\ldots,N_{\mathrm{D}}$ in this case and the DOF of the mechanism is not reduced unless ϕ'_{ik} is approximately zero for all $k = 1,\ldots,N_{\mathrm{H}}$. Therefore, the number of ϕ'_{ih} which is not close to zero can be assumed to be one, and hinge h can rotate only in this infinitesimal mechanism mode. Consequently, the following property holds:

Property 3.1. The increment of the rotation angle of hinge h in the infinitesimal mechanism mode i ($i = 1,\ldots,N_{\mathrm{D}}$) after increasing the rotational stiffness of hinge h, which is denoted by ϕ'_{ih}, is approximately equal to zero except for one mode, say mode i'. The eigenvalue $\lambda'_{i'}$ of the pseudo stiffness matrix corresponding to mode i' has a extremely large value, and this lead to a extremely high stiffness of the frame in the direction corresponding to the infinitesimal mechanism mode i'. Therefore, hinge h becomes fixed as its rotational stiffness is increased to a moderately large value.

The transition of eigenvalues and eigenvectors of the pseudo stiffness matrix $\tilde{\mathbf{K}}$ under the process of increasing the rotational stiffness of a hinge can be estimated by the derivatives of eigenvalues and eigenvectors of $\tilde{\mathbf{K}}$ for the rotational stiffness. In this study, the distinct eigenvalues λ_i ($i = 1,\ldots,N_{\mathrm{D}}$) of $\tilde{\mathbf{K}}$ are assumed. Differentiating Eq. (3.64) with respect to K_h ($h = 1,\ldots,N_{\mathrm{H}}$) and rearranging its terms, the following equation is obtained [73]:

$$\left(\tilde{\mathbf{K}} - \lambda_i \mathbf{I}_{N_{\mathrm{D}}}\right) \frac{\partial \boldsymbol{\alpha}_i}{\partial K_h} = -\left(\frac{\partial \tilde{\mathbf{K}}}{\partial K_h} - \frac{\partial \lambda_i}{\partial K_h}\mathbf{I}_{N_{\mathrm{D}}}\right)\boldsymbol{\alpha}_i \quad (i = 1,\ldots,N_{\mathrm{D}}) \tag{3.70}$$

According to Eq. (3.64) and $\tilde{\mathbf{K}}^{\mathsf{T}} = \tilde{\mathbf{K}}$, the left-hand side of Eq. (3.70) is to be equal to zero by pre-multiplying $\boldsymbol{\alpha}_i^{\mathsf{T}}$. Therefore, the following equation is obtained by pre-multiplying $\boldsymbol{\alpha}_i^{\mathsf{T}}$ to the both sides of Eq. (3.70):

$$\boldsymbol{\alpha}_i^{\mathsf{T}}\left(\frac{\partial \tilde{\mathbf{K}}}{\partial K_h} - \frac{\partial \lambda_i}{\partial K_h}\mathbf{I}_{N_{\mathrm{D}}}\right)\boldsymbol{\alpha}_i = \boldsymbol{\alpha}_i^{\mathsf{T}}\frac{\partial \tilde{\mathbf{K}}}{\partial K_h}\boldsymbol{\alpha}_i - \frac{\partial \lambda_i}{\partial K_h} = 0 \quad (i = 1,\ldots,N_{\mathrm{D}}) \tag{3.71}$$

Hence, the derivative of eigenvalue λ_i with respect to K_h can be derived as follows:

$$\begin{aligned}\frac{\partial \lambda_i}{\partial K_h} &= \boldsymbol{\alpha}_i^{\mathsf{T}}\frac{\partial \tilde{\mathbf{K}}}{\partial K_h}\boldsymbol{\alpha}_i = \boldsymbol{\alpha}_i^{\mathsf{T}}\mathbf{H}_{\varphi}^{\mathsf{T}}\frac{\partial \mathbf{K}_{\mathrm{H}}}{\partial K_h}\mathbf{H}_{\varphi}\boldsymbol{\alpha}_i \\ &= \boldsymbol{\phi}_i^{\mathsf{T}}\frac{\partial \mathbf{K}_{\mathrm{H}}}{\partial K_h}\boldsymbol{\phi}_i = \phi_{ih}^2\end{aligned} \tag{3.72}$$

where ϕ_{ih} is the h-th element of $\boldsymbol{\phi}_i$.

Remark 3.2. Since the rotational stiffness at each hinge is fictitious and can be assigned arbitrarily, assumption of distinct eigenvalues is generally satisfied by appropriately assign the stiffness of hinges to avoid repeated eigenvalues. If there are repeated eigenvalues due to symmetry properties of the origami surface, small random variations may be given for the hinge stiffnesses without any effect on the criteria introduced below.

Since an eigenvalue of the pseudo stiffness matrix represents the stiffness of the frame and the increase of the stiffness to a moderately large value leads to a fixed crease line, it is natural to select the hinge with the maximum sensitivity coefficient of eigenvalue $\partial\lambda_i/\partial K_h$

to efficiently reduce the DOF of the mechanism. However, for more detailed investigation and the prediction of the existence of locked crease lines, we need to consider the variation of eigenvectors.

The derivative of the i-th eigenvector $\boldsymbol{\alpha}_i$ with respect to K_h corresponding to the distinct eigenvalue is determined by Eq. (3.70). Since the rank of $\left(\tilde{\mathbf{K}} - \lambda_i \mathbf{I}_{N_\mathrm{D}}\right)$ in the left-hand-side of Eq. (3.70) is less than $N_\mathrm{D} - 1$, $\partial \boldsymbol{\alpha}_i / \partial K_h$ cannot be determined uniquely from Eq. (3.70). However, using a coefficient vector $\mathbf{b} = (b_1, \ldots, b_{N_\mathrm{D}})^\mathsf{T} \in \mathbb{R}^{N_\mathrm{D}}$, it can be expressed as a linear combination of N_D orthonormal eigenvectors $\boldsymbol{\alpha}_i$ $(i = 1, \ldots, N_\mathrm{D})$ as follows [73]:

$$\frac{\partial \boldsymbol{\alpha}_i}{\partial K_h} = b_1 \boldsymbol{\alpha}_1 + \cdots + b_{N_\mathrm{D}} \boldsymbol{\alpha}_{N_\mathrm{D}} = \begin{bmatrix} \boldsymbol{\alpha}_1 & \cdots & \boldsymbol{\alpha}_{N_\mathrm{D}} \end{bmatrix} \begin{pmatrix} b_1 \\ \vdots \\ b_{N_\mathrm{D}} \end{pmatrix} = \mathbf{A}\mathbf{b} \tag{3.73}$$

Substituting Eq. (3.73) into Eq. (3.70) and pre-multiplying $\mathbf{A}^\mathsf{T}$ to both sides of the equation, the following equation is obtained:

$$\mathbf{A}^\mathsf{T} \left(\tilde{\mathbf{K}} - \lambda_i \mathbf{I}_{N_\mathrm{D}}\right) \mathbf{A}\mathbf{b} = (\mathbf{A}^\mathsf{T} \tilde{\mathbf{K}} \mathbf{A} - \lambda_i \mathbf{I}_{N_\mathrm{D}}) \mathbf{b} = -\mathbf{A}^\mathsf{T} \left(\frac{\partial \tilde{\mathbf{K}}}{\partial K_h} - \frac{\partial \lambda_i}{\partial K_h} \mathbf{I}_{N_\mathrm{D}} \right) \boldsymbol{\alpha}_i \tag{3.74}$$

Here, according to Eq. (3.66), $\mathbf{A}^\mathsf{T} \tilde{\mathbf{K}} \mathbf{A}$ can be calculated as follows:

$$\mathbf{A}^\mathsf{T} \tilde{\mathbf{K}} \mathbf{A} = \begin{bmatrix} \boldsymbol{\alpha}_1^\mathsf{T} \tilde{\mathbf{K}} \boldsymbol{\alpha}_1 & \cdots & \boldsymbol{\alpha}_1^\mathsf{T} \tilde{\mathbf{K}} \boldsymbol{\alpha}_{N_\mathrm{D}} \\ \vdots & \ddots & \vdots \\ \boldsymbol{\alpha}_{N_\mathrm{D}}^\mathsf{T} \tilde{\mathbf{K}} \boldsymbol{\alpha}_1 & \cdots & \boldsymbol{\alpha}_{N_\mathrm{D}}^\mathsf{T} \tilde{\mathbf{K}} \boldsymbol{\alpha}_{N_\mathrm{D}} \end{bmatrix} = \begin{bmatrix} \lambda_i & & 0 \\ & \ddots & \\ 0 & & \lambda_{N_\mathrm{D}} \end{bmatrix} \tag{3.75}$$

Defining $\boldsymbol{\Lambda} = \mathrm{diag}(\lambda_1, \ldots, \lambda_{N_\mathrm{D}}) \in \mathbb{R}^{N_\mathrm{D} \times N_\mathrm{D}}$, Eq. (3.74) can be rewritten as follows:

$$(\boldsymbol{\Lambda} - \lambda_i \mathbf{I}_{N_\mathrm{D}}) \mathbf{b} = -\mathbf{A}^\mathsf{T} \left(\frac{\partial \tilde{\mathbf{K}}}{\partial K_h} - \frac{\partial \lambda_i}{\partial K_h} \mathbf{I}_{N_\mathrm{D}} \right) \boldsymbol{\alpha}_i \tag{3.76}$$

Since $\partial \tilde{\mathbf{K}} / \partial K_h = \mathbf{H}_\varphi^\mathsf{T} (\partial \mathbf{K}_\mathrm{H} / \partial K_h) \mathbf{H}_\varphi$, the j-th component of the right-hand side of Eq. (3.76) $(j = 1, \ldots, N_\mathrm{D})$ can be calculated as follows:

$$-\boldsymbol{\alpha}_j^\mathsf{T} \left(\frac{\partial \tilde{\mathbf{K}}}{\partial K_h} - \frac{\partial \lambda_i}{\partial K_h} \mathbf{I}_{N_\mathrm{D}} \right) \boldsymbol{\alpha}_i = -\boldsymbol{\phi}_j^\mathsf{T} \frac{\partial \mathbf{K}_\mathrm{H}}{\partial K_h} \boldsymbol{\phi}_i + \frac{\partial \lambda_i}{\partial K_h} \boldsymbol{\phi}_j^\mathsf{T} \boldsymbol{\phi}_i = \begin{cases} 0 & (i = j) \\ -\phi_{ih} \phi_{jh} & (i \neq j) \end{cases} \tag{3.77}$$

Therefore, assuming $\lambda_j \neq \lambda_i$ for $j \neq i$, b_j can be determined from Eq. (3.76) for $j = 1, \ldots, N_\mathrm{D}$ $(j \neq i)$ as follows:

$$b_j = -\frac{1}{\lambda_j - \lambda_i} \phi_{ih} \phi_{jh} \tag{3.78}$$

In addition, b_i can be determined by differentiating $\boldsymbol{\alpha}_i^\mathsf{T} \boldsymbol{\alpha}_i = 1$ with respect to K_h and dividing it by 2 as follows:

$$\frac{1}{2} \left\{ \left(\frac{\partial \boldsymbol{\alpha}_i}{\partial K_h} \right)^\mathsf{T} + \boldsymbol{\alpha}_i^\mathsf{T} \frac{\partial \boldsymbol{\alpha}_i}{\partial K_h} \right\} = \boldsymbol{\alpha}_i^\mathsf{T} \mathbf{A}\mathbf{b} = b_i = 0 \tag{3.79}$$

Consequently, $\partial \boldsymbol{\alpha}_i / \partial K_h$ can be expressed as follows:

$$\frac{\partial \boldsymbol{\alpha}_i}{\partial K_h} = -\sum_{\substack{j=1 \\ j \neq i}}^{N_\mathrm{D}} \frac{1}{\lambda_j - \lambda_i} \phi_{jh} \phi_{ih} \boldsymbol{\alpha}_j \tag{3.80}$$

Using the relation $\boldsymbol{\phi}_i = \mathbf{H}_\varphi \boldsymbol{\alpha}_i$, the first-order derivative of $\boldsymbol{\phi}_i$ with respect to K_h can be written as follows:

$$\frac{\partial \boldsymbol{\phi}_i}{\partial K_h} = \mathbf{H}_\varphi \frac{\partial \boldsymbol{\alpha}_i}{\partial K_h} = -\sum_{\substack{j=1 \\ j\neq i}}^{N_\mathrm{D}} \frac{1}{\lambda_j - \lambda_i} \phi_{ih} \phi_{jh} \boldsymbol{\phi}_j \tag{3.81}$$

Let $\boldsymbol{\psi}_j = (\psi_{j1}, \ldots, \psi_{jN_\mathrm{D}})^\mathsf{T}$ represent a normalized vector whose i-th element ψ_{ji} is defined as follows:

$$\psi_{ji} = \frac{\phi_{ij}}{\sqrt{\sum_{i=1}^{N_\mathrm{D}} \phi_{ij}^2}} \tag{3.82}$$

Suppose that there are hinge h and h' ($h' \neq h$) approximately satisfying $\boldsymbol{\psi}_h \cdot \boldsymbol{\psi}_{h'} = \pm 1$. In other words, $\phi_{ih'} \simeq \gamma \phi_{ih}$ is satisfied for all modes $i = 1, \ldots, N_\mathrm{D}$ with a constant $\gamma \in \mathbb{R}$. Then, according to Eq. (3.81), $\partial \phi_{ih} / \partial K_h \simeq \gamma \partial \phi_{ih'} / \partial K_h$ is satisfied. This implies that $\boldsymbol{\psi}_h \cdot \boldsymbol{\psi}_{h'} \simeq 1$ or $\phi_{ih'} \simeq \gamma \phi_{ih}$ is always satisfied, and according to Property 3.1, both ϕ_{ih} and $\phi_{ih'}$ ($h \neq h'$) converge to 0 as K_j is increased to a moderately large value except for mode i' corresponding to a large increment of the eigenvalue. Therefore, the following property holds:

Property 3.3. If hinge h is fixed and there exists hinge h' ($h' \neq h$) approximately satisfying $\boldsymbol{\psi}_h \cdot \boldsymbol{\psi}_{h'} = \pm 1$ or $\phi_{ih} = \gamma \phi_{ih'}$ for all $i = 1, \ldots, N_\mathrm{D}$, then hinge h' is likely to be locked.

Furthermore, substituting $\phi_{ih} = \mathrm{sgn}(\phi_{ih}) \sqrt{\partial \lambda_i / \partial K_h}$ obtained from Eq. (3.72) into Eq. (3.81) where $\mathrm{sgn}(x)$ is a sign function whose value is 1 if $x \geq 0$ and -1 if $x < 0$, the derivatives of the distinct eigenvalue and the corresponding eigenvector satisfy the following equation:

$$\frac{\partial \boldsymbol{\phi}_i}{\partial K_h} = -\sum_{\substack{j=1 \\ j\neq i}}^{N_\mathrm{D}} \frac{\mathrm{sgn}(\phi_{ih}) \mathrm{sgn}(\phi_{jh})}{\lambda_j - \lambda_i} \sqrt{\frac{\partial \lambda_i}{\partial K_h} \frac{\partial \lambda_j}{\partial K_h}} \boldsymbol{\phi}_j \tag{3.83}$$

According to Eqs. (3.72) and (3.83), if $\partial \lambda_i / \partial K_h$ has a large value compared to the other hinges, the absolute value of $\partial \phi_{ih} / \partial K_h$ for each $i = 1, \ldots, N_\mathrm{D}$ is also large, and the value of ϕ_{ih} for each $i = 1, \ldots, N_\mathrm{D}$ rapidly converges to 0 except mode i' as K_h is increased to fix hinge h while the values of $\phi_{ih'}$ ($h' \neq h$) corresponding to the other hinges are not drastically changed as demonstrated in the numerical examples in Section 3.5.4. Therefore, in this case, hinge h can be fixed independently without locking other hinges. Consequently, the following properties hold:

Property 3.4. When hinge h with large eigenvalue derivatives is fixed, it is unlikely that there exists a locked hinge among the unfixed hinges when the rotation of hinge h in the infinitesimal mechanism is modified to 0 to reduce the DOF of the mechanism.

In particular, since the largest eigenvalue derivative has the most influence on the value of $\partial \phi_{ih} / \partial K_h$, the largest eigenvalue is focused on in this study to define the selection criteria of the crease lines to be fixed.

3.5.3 Selection criteria of a crease line to be fixed

In this section, selection criteria of the crease lines be fixed is presented. The definitions of the crease line scores are in accordance with Ref. [30]. It is important to fix an appropriate crease line so that the objective function of the optimization problem (3.50) easily converges to zero and unfixed crease lines are not locked after fixing the crease line. Therefore, it is necessary to determine the crease lines to be fixed in consideration of both the shape of the polyhedron approximating the target surface and the possibility of existence of a locked crease line as discussed in Section 3.5.2.

The absolute value of folding angle $\rho_h \geq 0$ of hinge h $(= 1, \ldots, N_{\mathrm{H}})$ is defined as follows:

$$\rho_h = \arccos\left\{\mathbf{n}_{k_1} \cdot \mathbf{n}_{k_2}\right\} \quad (k_1, k_2 \in \mathscr{F}_h^{\mathrm{H}}) \tag{3.84}$$

where $\mathscr{F}_h^{\mathrm{H}}$ is a set of indices of the origami faces adjacent to the crease line corresponding to hinge h and $\mathbf{n}_{k_1}$ and $\mathbf{n}_{k_2} \in \mathbb{R}^3$ are the unit normal vectors of faces k_1 and k_2. Then, the score of hinge h in terms of the shape of the origami surface is denoted by σ_h^{S} and is defined as follows:

$$\sigma_h^{\mathrm{S}} = \frac{\rho_h}{\sum_{j=1}^{N_{\mathrm{H}}} \rho_j} \tag{3.85}$$

A small value of σ_h^{S} implies that the faces adjacent to the crease line corresponding to hinge h are nearly parallel, and consequently, the shape change of the origami surface after fixing the crease line corresponding to hinge h is expected to be small. Thus, the developability conditions for the flatness of the faces with more than three edges considered in Problem (3.50) are likely to be satisfied with small errors when the crease line corresponding to the smallest score σ_h^{S} is fixed.

On the other hand, the score σ_h^{F} of hinge h which reflects the prediction of the existence of locked crease lines is defined by the eigenvalue derivatives of the pseudo stiffness matrix $\tilde{\mathbf{K}}$ with respect to the rotational stiffness K_h of hinge h as follows:

$$\sigma_h^{\mathrm{F}} = \frac{\max_i \left(\dfrac{\partial \lambda_i}{\partial K_h}\right)}{\sum_{j=1}^{N_{\mathrm{H}}} \max_i \left(\dfrac{\partial \lambda_i}{\partial K_j}\right)} \tag{3.86}$$

According to the properties of the eigenmodes of the pseudo stiffness matrix described in Section 3.5.2, a larger value of σ_h^{F} leads to a smaller possibility of locking a crease line that is not fixed. Furthermore, if all the eigenvalues of $\tilde{\mathbf{K}}$ are distinct, σ_h^{F} can be expressed by substituting Eq. (3.72) into Eq. (3.86) as

$$\sigma_h^{\mathrm{F}} = \frac{\max_i \left(\phi_{ih}^2\right)}{\sum_{j=1}^{N_{\mathrm{H}}} \max_i \left(\phi_{ij}^2\right)} \tag{3.87}$$

The numerator of σ_h^{F} indicates how dominant the rotation of hinge h is among the rotations in all the deformation modes. Because ϕ_{ih} is the h-th component of $\boldsymbol{\phi}_i$, a large value of σ_h^{F}

suggests that hinge h can rotate independently, and there is a small possibility of locking an unfixed crease line. Therefore, σ_h^{F} can be used to define the score of hinge h in terms of the deformation mechanism. However, since the vector $\boldsymbol{\phi}_i$ is not normalized for each $i = 1,\ldots,N_{\mathrm{D}}$, simply comparing the values of ϕ_{ih}^2 may be insufficient to determine the crease line to be fixed. Here, assuming that $\lambda_i > 0$ ($i = 1,\ldots,N_{\mathrm{D}}$), a vector $\hat{\boldsymbol{\phi}}_i \in \mathbb{R}^{N_{\mathrm{H}}}$ is defined so that its j-th component $\hat{\phi}_{ij}$ ($j = 1,\ldots,N_{\mathrm{H}}$) is $\hat{\phi}_{ij} = \sqrt{K_j/\lambda_i}\phi_{ij}$. Then, according to Eq. (3.67), $\hat{\boldsymbol{\phi}}_i$ satisfies the following equation:

$$\begin{aligned}
\hat{\boldsymbol{\phi}}_i^{\mathsf{T}}\hat{\boldsymbol{\phi}}_i &= \sum_{j=1}^{N_{\mathrm{H}}} \hat{\phi}_{ij}^2 \\
&= \frac{1}{\lambda_i}\sum_{j=1}^{N_{\mathrm{H}}} K_j\phi_{ij}^2 \\
&= \frac{1}{\lambda_i}\boldsymbol{\phi}_i^{\mathsf{T}}\mathbf{K}_{\mathrm{H}}\boldsymbol{\phi}_i \\
&= 1
\end{aligned} \tag{3.88}$$

Furthermore, when $i' \neq i$, the following equation holds:

$$\begin{aligned}
\hat{\boldsymbol{\phi}}_i^{\mathsf{T}}\hat{\boldsymbol{\phi}}_{i'} &= \sum_{j=1}^{N_{\mathrm{H}}} \hat{\phi}_{ij}\hat{\phi}_{i'j} \\
&= \frac{1}{\sqrt{\lambda_i\lambda_{i'}}}\sum_{j=1}^{N_{\mathrm{H}}} K_j\phi_{ij}\phi_{i'j} \\
&= \frac{1}{\sqrt{\lambda_i\lambda_{i'}}}\boldsymbol{\phi}_i^{\mathsf{T}}\mathbf{K}_{\mathrm{H}}\boldsymbol{\phi}_{i'} \\
&= 0
\end{aligned} \tag{3.89}$$

Consequently, $\hat{\boldsymbol{\phi}}_i$ can be used as the normalized infinitesimal displacement mode for the hinge rotation angle. Instead of σ_h^{F} in Eq. (3.86), another score $\hat{\sigma}_h^{\mathrm{F}}$ of hinge h can be defined by the j-th element $\hat{\phi}_{ij}$ of $\hat{\boldsymbol{\phi}}_i$ as follows:

$$\hat{\sigma}_h^{\mathrm{F}} = \frac{\max\limits_i\left(\hat{\phi}_{ih}^2\right)}{\sum\limits_{j=1}^{N_{\mathrm{H}}}\max\limits_i\left(\hat{\phi}_{ij}^2\right)} \tag{3.90}$$

To incorporate both of the change of the shape and the change of the deformation mechanism of the origami surface after fixing a crease line, the following two different scores σ_h and $\hat{\sigma}_h$ of hinge h ($= 1,\ldots,N_{\mathrm{H}}$) are used as the criteria to determine the crease line to be fixed in the process of form generation described in Section 3.4:

$$\sigma_h = \frac{\sigma_h^{\mathrm{S}}}{\sigma_h^{\mathrm{F}}} \tag{3.91}$$

$$\hat{\sigma}_h = \frac{\sigma_h^{\mathrm{S}}}{\hat{\sigma}_h^{\mathrm{F}}} \tag{3.92}$$

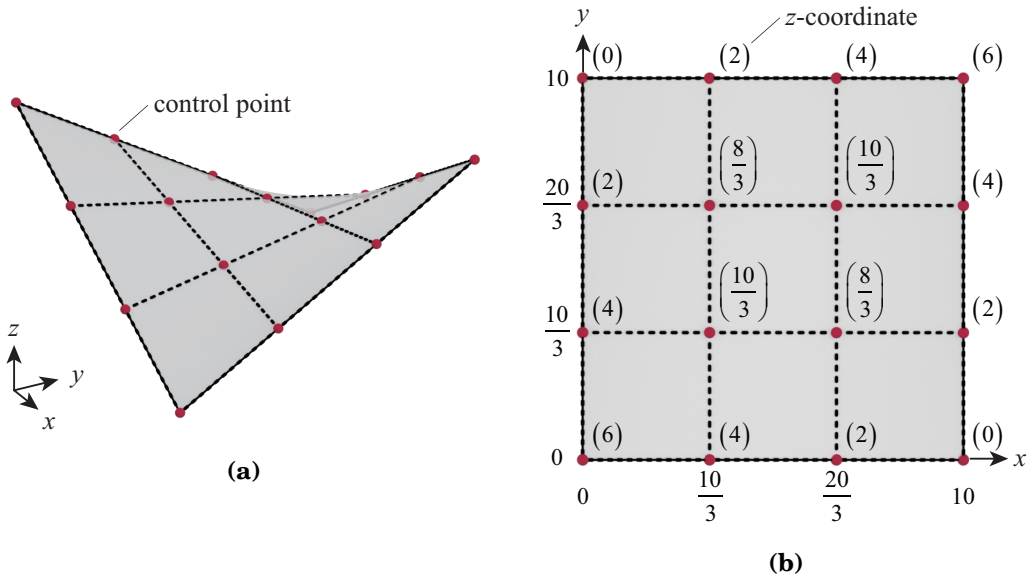

Figure 3.9: Target surface and its control points; (a) Isometric view, (b) Plan view and coordinates of control points (numbers in the parentheses are the z-coordinates of control points).

The crease line corresponding to the hinge that has the lowest score is fixed sequentially. Multiple crease lines can also be fixed simultaneously if the origami surface has a symmetry property. The normalized score $\hat{\sigma}_h$ should basically be used for the form generation, however, the results of the form generation using σ_h and $\hat{\sigma}_h$ are compared in Chapter 4.

3.5.4 Example including locked crease lines

An example of optimization process is shown where some crease lines that are not fixed will be locked after fixing another crease line. In this section, only the results of the form generation and the infinitesimal mechanism analysis are shown while the development diagrams and the results of large deformation analysis are not shown. Each analysis is carried out by using a Python 3.9 program. The optimization problems (3.50) and (3.51) are solved using sequential quadratic programming library SNOPT Ver. 7 [74] with the Python interface of pyOpt [75, 76]. First-order infinitesimal modes are obtained by the method explained in Appendix E, and the singular value decomposition of the compatibility matrix is carried out by the function linalg.svd [77] in Python library Numpy.

The target surface of the form generation is an HP surface shown in Fig 3.9 and it is triangulated as shown in Fig. 3.10. The initial triangulated surface has 25 vertices and 40 crease lines. The conditions of the form generation are assigned as follows:

- The design variables in the optimization are the independent nodal coordinates of the frame model.
- Offset distances between origami vertices and the target surface are measured in z-

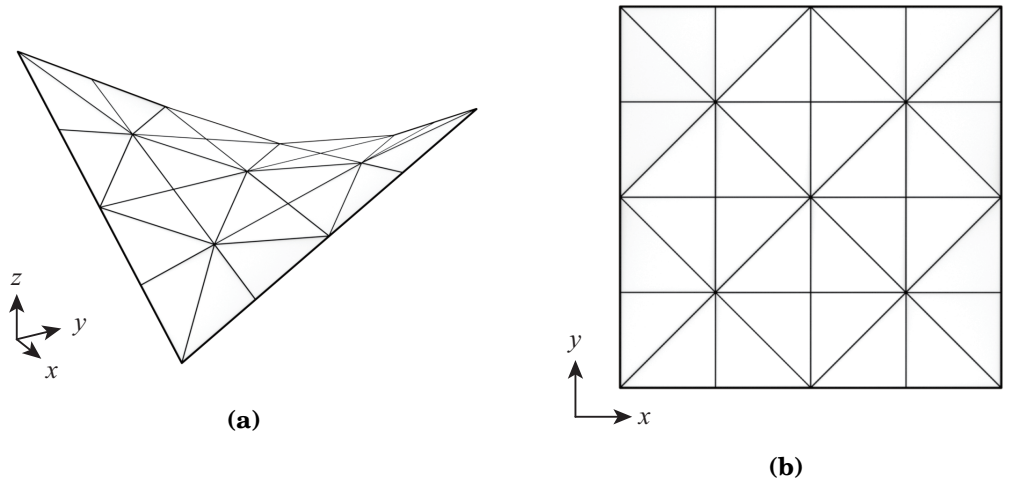

Figure 3.10: Initial triangulation pattern with 25 vertices and 40 crease lines; (a) Isometric view, (b) Plan view.

direction.

- A cut is not included.
- Symmetry of an origami surface is not considered, and the crease lines are fixed one by one.
- Boundary planes of the surface are perpendicular to the xy-plane.
- Weight coefficients in the approximation error function $F_{\text{app}}(\mathbf{X})$ are set to $c_{\text{area}} = 0.3$ and $c_{\text{normal}} = 0.6$.
- Upper and lower bounds of the inner angles of faces in Problems (3.50) and (3.51) are assigned as $\alpha_{\min} = \pi/6$ and $\alpha_{\max} = 5\pi/6$.
- Lower bound of the edge lengths in Problems (3.50) and (3.51) is assigned as $l_{\min} = 1$.
- The x- and y-coordinates of the nodes are constrained to be in the range 0 to 10 and the z-coordinate in the range -3 to 9.
- Crease lines are randomly fixed instead of using the scores defined in Section 3.5.3 to obtain the origami surface with locked crease lines.

The 2 DOF optimal shape with eleven fixed crease lines and without locked crease lines is obtained as shown in Fig. 3.11. If crease line 6 in Fig. 3.11 is fixed in the following iteration of the form generation, the 1 DOF origami surface with twenty-four locked crease lines is obtained as shown in Fig. 3.12. Only crease lines 20, 32, 33, 34 can rotate in the origami surface in Fig. 3.12. On the other hand, if crease line 32 is fixed for the solution in Fig. 3.11, the 1 DOF origami surface without locked crease lines is obtained as shown in Fig. 3.13. The values of σ_h^{S}, $1/\sigma_h^{\text{F}}$, and, $1/\hat{\sigma}_h^{\text{F}}$ are shown in Table 3.2 for the crease lines

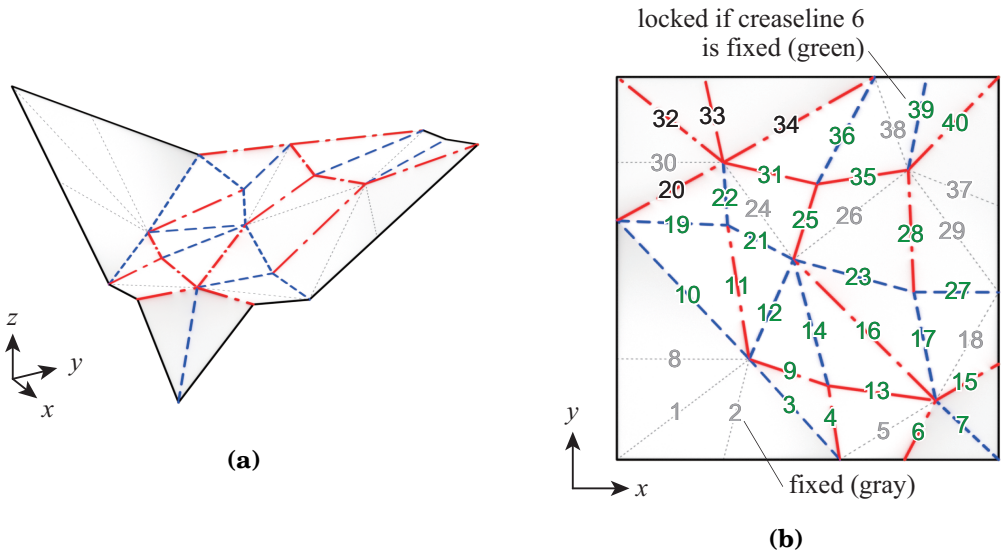

Figure 3.11: 2 DOF optimal shape with eleven fixed crease lines and no locked crease lines; (a) Isometric view, (b) Plan view and edge indices of crease lines (gray: fixed; green: to be locked if crease line 6 is fixed).

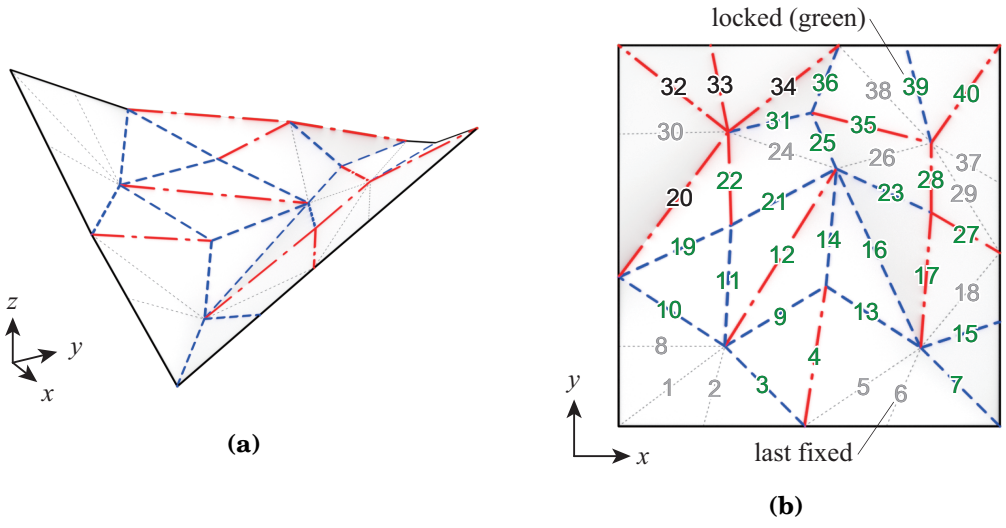

Figure 3.12: 1 DOF optimal shape with twelve fixed crease lines and twenty-four locked crease lines; (a) Isometric view, (b) Plan view and edge indices of crease lines (gray: fixed; green: locked).

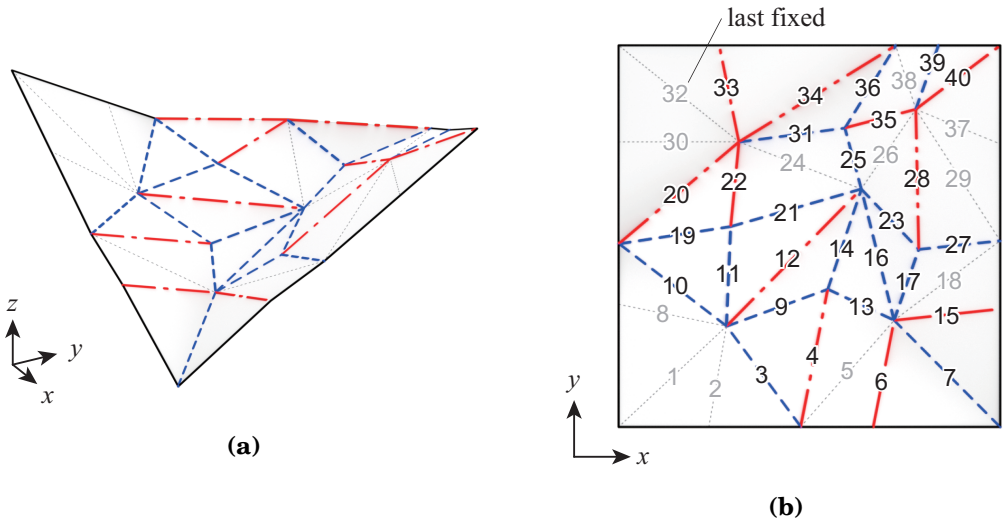

Figure 3.13: 1 DOF optimal shape with twelve fixed crease lines and no locked crease lines; (a) Isometric view, (b) Plan view and edge indices of crease lines (gray: fixed).

which are the candidates for the crease lines to be fixed in the origami surface in Fig. 3.11. As shown in Table 3.2, crease lines 3–16 have the large values of $1/\sigma_h^{\mathrm{F}}$, and, $1/\hat{\sigma}_h^{\mathrm{F}}$, and this indicates that the crease lines are likely to be locked if one of crease lines 3–16 is fixed.

Next, the transition of the deformation mechanism is investigated for the origami surface in Fig. 3.11 by increasing the rotational stiffness of the hinges of the frame model corresponding to the crease lines. The size of the pseudo stiffness matrix is 2×2 since the DOF is 2, and two eigenvalues of the pseudo stiffness matrix are $\lambda_1 = 7.24 \times 10^{-3}$ and $\lambda_2 = 1.86 \times 10^{-1}$ when the rotational stiffness of all the hinges are 1. Table 3.3 shows the values of the components of the hinge rotation angle modes $\boldsymbol{\phi}_1$ in the second column, the components of $\boldsymbol{\phi}_2$ in the third column, the inner products $\boldsymbol{\psi}_h \cdot \boldsymbol{\psi}_{h'}$ of the vectors corresponding to crease line 6 and the other crease lines in the forth column, and the inner products of the vectors corresponding to crease line 32 and the other crease lines in the fifth column. According to Property 3.3 and Table 3.3, it can be predicted that crease lines 3–16 are likely to be locked if crease line 6 is fixed. Conversely, it is unlikely that they are not locked if crease line 32 is fixed. Then, the rotational stiffness of the hinges corresponding to crease lines 6 and 32 are increased by 10^{20} and 10^{14} times, respectively, so that the crease lines 6 and 32 are fixed. The values of the components of $\boldsymbol{\phi}_1$ abd $\boldsymbol{\phi}_2$ after the rotational stiffness of the hinges corresponding to crease lines 6 and 32 are increased are shown in Tables 3.4 and 3.5. When the rotational stiffness corresponding to crease lines 6 is increased, the eigenvalues of the pseudo stiffness matrix becomes $\lambda_1 = 1.00$ and $\lambda_2 = 6.92 \times 10^{15}$. Therefore, the second mode can be regarded to be fixed by increasing the rotational stiffness the to moderately large value. As shown in Table 3.4, the components of $\boldsymbol{\phi}_1$ corresponding to crease lines 3–16 are approximately zero, and thus, crease lines 3–16 are locked if crease lines 6 is fixed. On the other hand, when the rotational stiffness corresponding to crease lines 32

Table 3.2: Values of scores of the crease lines of the origami surface in Fig. 3.11.

Edge index	σ_h^{S}	$1/\sigma_h^{\mathrm{F}}$	$1/\hat{\sigma}_h^{\mathrm{F}}$
3	8.78×10^{-2}	1.46×10^{3}	1.10×10^{2}
6	8.30×10^{-2}	2.71×10^{3}	2.03×10^{2}
7	2.53×10^{-2}	2.17×10^{4}	1.61×10^{3}
10	7.70×10^{-2}	1.83×10^{3}	1.37×10^{2}
12	1.82×10^{-2}	3.73×10^{4}	2.77×10^{3}
15	9.57×10^{-2}	1.89×10^{3}	1.41×10^{2}
16	2.27×10^{-2}	2.34×10^{4}	1.75×10^{3}
20	1.07×10^{-1}	50.4	4.29
32	9.11×10^{-5}	1.90	3.65
33	5.50×10^{-5}	2.50	4.78
34	8.94×10^{-2}	20.2	4.28

Table 3.3: Components of the hinge rotation angle modes $\boldsymbol{\phi}_i$ and the values of inner products $\boldsymbol{\psi}_h \cdot \boldsymbol{\psi}_{h'}$ of crease line 6 and the other crease lines and of crease line 32 and the other crease lines.

Edge Index	Components of $\boldsymbol{\phi}_1$ ($\lambda_1 = 7.24\times10^{-3}$)	Components of $\boldsymbol{\phi}_2$ ($\lambda_2 = 1.86\times10^{-1}$)	Values of $\boldsymbol{\psi}_6 \cdot \boldsymbol{\psi}_h$	Values of $\boldsymbol{\psi}_{32} \cdot \boldsymbol{\psi}_h$
3	-1.13×10^{-2}	7.56×10^{-4}	-1.00	5.27×10^{-2}
6	8.30×10^{-3}	-5.56×10^{-4}	1.00	-5.27×10^{-2}
7	-2.93×10^{-3}	1.96×10^{-4}	-1.00	5.27×10^{-2}
10	-1.01×10^{-2}	6.77×10^{-4}	-1.00	5.27×10^{-2}
12	-2.24×10^{-3}	1.50×10^{-4}	-1.00	5.27×10^{-2}
15	-9.95×10^{-3}	6.66×10^{-4}	-1.00	5.27×10^{-2}
16	2.82×10^{-3}	-1.89×10^{-4}	1.00	-5.27×10^{-2}
20	-5.70×10^{-2}	-6.08×10^{-2}	-6.33×10^{-1}	-7.39×10^{-1}
32	4.43×10^{-3}	3.13×10^{-1}	-5.27×10^{-2}	1.00
33	-2.50×10^{-3}	-2.73×10^{-1}	5.77×10^{-2}	-1.00
34	-5.72×10^{-2}	9.61×10^{-2}	-5.68×10^{-1}	8.52×10^{-1}

is increased, the eigenvalues of the pseudo stiffness matrix becomes $\lambda_1 = 7.28\times10^{-3}$ and $\lambda_2 = 9.83\times10^{12}$. According to Table 3.5, it can be concluded that crease line 32 is fixed while the other crease lines can rotate. From the above, Properties 3.1, 3.3, and 3.4 have been illustrated for the origami surface shown in Fig. 3.11.

3.6 Conclusions

This chapter has presented a form generation method of a developable rigid origami structure based on the mechanical property of partially rigid frames. A generated polyhedral sur-

Table 3.4: Components of the hinge rotation angle modes $\boldsymbol{\phi}_1$ and $\boldsymbol{\phi}_2$ after the rotational stiffness of the hinge corresponding to crease line 6 is increased by 10^{20} times.

Edge Index	Components of $\boldsymbol{\phi}_1$ ($\lambda_1 = 1.00$)	Components of $\boldsymbol{\phi}_2$ ($\lambda_2 = 6.92 \times 10^{15}$)	State of crease line
3	-1.35×10^{-14}	1.13×10^{-2}	locked
6	-4.34×10^{-19}	-8.32×10^{-3}	fixed
7	8.45×10^{-16}	2.94×10^{-3}	locked
10	-1.58×10^{-14}	1.01×10^{-2}	locked
12	-2.66×10^{-15}	2.24×10^{-3}	locked
15	-1.07×10^{-15}	9.97×10^{-3}	locked
16	2.81×10^{-15}	-2.83×10^{-3}	locked
20	6.45×10^{-2}	5.28×10^{-2}	
32	-3.13×10^{-1}	1.65×10^{-2}	
33	2.73×10^{-1}	-1.58×10^{-2}	
34	-9.20×10^{-2}	6.35×10^{-2}	

Table 3.5: Components of the hinge rotation angle modes $\boldsymbol{\phi}_1$ and $\boldsymbol{\phi}_2$ after the rotational stiffness of the hinge corresponding to crease line 32 is increased by 10^{14} times.

Edge Index	Components of $\boldsymbol{\phi}_1$ ($\lambda_1 = 7.28 \times 10^{-3}$)	Components of $\boldsymbol{\phi}_2$ ($\lambda_2 = 9.83 \times 10^{12}$)	State of crease line
3	-1.13×10^{-2}	5.96×10^{-3}	
6	8.31×10^{-3}	-4.38×10^{-3}	
7	-2.94×10^{-3}	1.55×10^{-3}	
10	-1.01×10^{-2}	5.34×10^{-3}	
12	-2.24×10^{-3}	1.18×10^{-3}	
15	-9.95×10^{-3}	5.25×10^{-3}	
16	2.83×10^{-3}	-1.49×10^{-3}	
20	-5.61×10^{-2}	-6.16×10^{-2}	
32	9.71×10^{-17}	3.14×10^{-1}	fixed
33	1.36×10^{-3}	-2.73×10^{-1}	
34	-5.85×10^{-2}	9.53×10^{-2}	

face approximates a target curved surface based on Refs. [28–30]. Form generation starts from a triangulated target surface and its crease lines are sequentially fixed to reduce the DOF of the deformation mechanism. The transition of the deformation mechanism due to fixing the crease lines is predicted, and selection criteria of the crease lines to be fixed are proposed to prevent the unfixed crease lines from being locked. The deformation mechanism of rigid origami is investigated by using the frame model, and the deformation modes are derived by the method for stability and mechanism analysis of a partially rigid frame with arbitrary inclined hinges.

An optimization problem for generating a developable origami surface has been formulated to minimize an approximation error function under developability conditions. Developability conditions are considered around each inner vertex, dividing edge, and inner cuts, and they are formulated with respect to the geometric properties of the origami surface such as the discrete Gaussian curvatures, normal vectors of the faces, and the sets of the inner angles of the faces and the length of edges constituting a cut. The approximation error function is defined as the weighted sum of the three functions reflecting the distance between the origami vertices and the target surface, the difference of the surface area, and the difference of the face normal vectors, respectively. The design variables of the optimization are selected from vertex coordinates of the origami surface, nodal coordinates of the frame model, or the pairs of the parameters to determine the points on the target Bézier surface and the offsets from the target surface. When the vertex coordinates or the nodal coordinates are used, the shape of the origami surface can be restricted directly by assigning the constraints on the range of the design variable while the arrangement of the control points of the target surface is limited. Om the other hand, when the pairs of the parameters of the target Bézier surface and the offsets from the target surface are the design variables, an arbitrary arrangement of the control points can be used while the positions of the origami vertices are represented by non-linear functions. The number of design variables are reduced by taking into account the linear constraints on the boundary shape and the symmetry of the origami surface.

A method has also been proposed for predicting the existence of a locked crease line in the optimal shape after fixing a crease line based on the eigenvalue and eigenvector derivatives of the pseudo stiffness matrix of the frame model. The fictious rotational stiffness of the hinges of the frame model is assumed, and the pseudo stiffness matrix is defined by the first-order infinitesimal mechanism of the frame and the rotational stiffness of the hinges. The relationship between the first-order derivatives of the distinct eigenvalues and eigenvectors of the pseudo stiffness matrix has been derived in to show that a locked crease line likely exists if a crease line with the relatively small maximum eigenvalue derivative is fixed. The properties related to the prediction method are illustrated for the origami surface approximating an HP surface.

Based on the shape of the origami surface and the prediction of the existence of a locked crease line, selection criteria of the crease line to be fixed have been defined to efficiently carry out the form generation. The folding angle of each crease line is utilized to define a score of a crease line with respect to the shape of the origami surface, and a crease line or more crease lines are fixed so that the shape change of the origami surface before and after fixing a crease line (crease lines) is reasonably small. Scores with respect to the infinitesimal mechanism are defined by using the maximum eigenvalue derivatives or the maximum squared elements of the orthonormalized rotation modes of the crease lines to prevent the crease lines from being locked. Although two scores before and after normalized are proposed, the normalized score is expected to have the better performance and should be used basically for the form generation as demonstrated in Chapter 4.

In Chapter 4, the performances of the introduced criteria will be confirmed in numerical examples. In addition, to establish a guideline for setting the values of weight coefficients, the effect of the weight coefficients on the shape generation results will be examined. The selection of the design variables, the initial triangulation patterns, and the arrangement of the cuts will be also investigated.

Chapter 4

Case studies of form generation of rigid origami

In this chapter, case studies of the form generation method proposed in Chapter 3 are presented. Randomly generated surfaces, HP surfaces with two different heights, and dome surfaces with two different heights are approximated. Form generation with the randomly generated surfaces is carried out to confirm effectiveness of the selection criteria of the crease lines to be fixed introduced in Chapter 3. The investigation on the weight coefficients in the approximation error function and the arrangements of cuts are made for the examples of HP and dome surfaces.

4.1 General settings for form generation

As stated in Section 3.5.4 of Chapter 3, each analysis is carried out by using a Python 3.9 program. The optimization problems (3.16), (3.50), and (3.51) are solved using sequential quadratic programming library SNOPT Ver. 7 [74] with the Python interface of pyOpt [75,

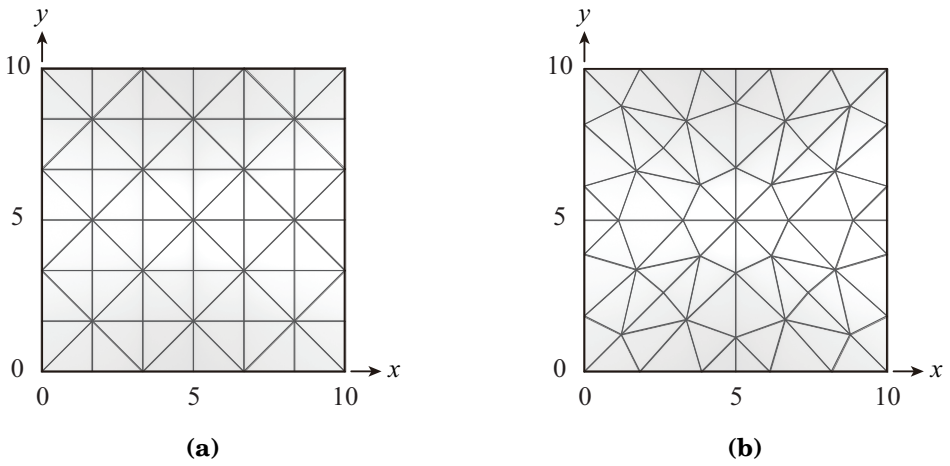

Figure 4.1: Initial triangulation patterns of a target surface; (a) Pattern G, (b) Pattern R.

Table 4.1: Cases of form generation; combinations of the initial triangulation patterns of the target surface, design variables in the optimization, and the directions in which the offsets are measured.

Case index	Triangulation	Design variables	Offset direction
Case G1	Pattern G	Nodal coordinates	Global z-direction
Case G2	Pattern G	Parameters of the Bézier surface and the offsets	Global z-direction
Case G3	Pattern G	Parameters of the Bézier surface and the offsets	Normal direction of the target surface
Case R1	Pattern R	Nodal coordinates	Global z-direction
Case R2	Pattern R	Parameters of the Bézier surface and the offsets	Global z-direction
Case R3	Pattern R	Parameters of the Bézier surface and the offsets	Normal direction of the target surface

76]. The singular value decomposition of the compatibility matrix is carried out by the function linalg.svd [77] in Python library Numpy. As shown in Fig. 4.1, two patterns of initial triangulation referred to as Patterns G and R are used in this study. Pattern G has 49 vertices and 96 inner edges, and Pattern R has 53 vertices and 108 inner edges. The projected shape of a target surface onto the xy-plane is a 10×10 m square in all the examples. Since the unit of length does not affect the result of form generation, it is omitted hereafter unless necessary. Note that the unit of angle is radian while it is omitted. Two types of design variables of the optimization problems (3.50) and (3.51) are considered in this chapter; the nodal coordinates of the frame model and the pairs of the (s,t) parameters of the target Bézier surface and the offsets. The direction in which the offset is measured is considered along the z-direction or the normal direction of the target surface. Consequently, three combinations of the design variables and the direction of the offset are considered for each initial triangulation pattern as summarized in Table 4.1, and the six combinations are referred to as Cases G1–G3 and R1–R3. The weight coefficients c_{area} and c_{normal} in the approximation error function $F_{\text{app}}(\mathbf{X})$ are assigned in each examples. The following conditions of the optimization problems (3.50) and (3.51) for form generation are commonly used in this chapter:

- Boundary planes of the surface are perpendicular to the xy-plane when the design variables are the nodal coordinates.
- Upper and lower bounds of the inner angles of faces in Problems (3.50) and (3.51) are assigned as $\alpha_{\min} = \pi/6$ and $\alpha_{\max} = 5\pi/6$.
- Lower bound of the edge lengths in Problems (3.50) and (3.51) is assigned as $l_{\min} = 1$.

- The x- and y-coordinates of the nodes are constrained to be in the range 0 to 10 and the z-coordinate in the range -3 to 9 when the design variables are the nodal coordinates.
- The upper and lower bounds of the offsets are assigned to ± 3 when the design variables are the parameters of the target Bézier surface and the offsets.
- The tolerance of the violation of the developability condition (upper bound of the absolute value of each component of $\mathbf{D}(\mathbf{X})$ in Problem (3.50) is 10^{-4}.
- A crease line is regarded to be locked if the increments of its rotation angle in all the first-order infinitesimal mechanism modes are less than 10^{-9}. However, if the folding angles of all the locked crease lines are less than 10^{-6}, the existence of the locked crease lines are neglected because an origami surface is developable to a plane even when there are locked crease lines if all the locked crease lines are unfolded.
- The rotation stiffness of the hinges to compute the pseudo stiffness matrix are randomly set in the range between 0.995 and 1.005 (Nm) to avoid the existence of repeated eigenvalues.

The large deformation analysis is carried out using Abaqus 2020 [78] to confirm the rigid foldability of each solution. To simulate the deployment process, the forced displacements along the z-direction to the xy-plane are applied to the nodes of the frame model which are on the faces of an origami surface. The frame model is constructed with three-dimensional beam elements which have cylindrical cross sections of 20 mm diameter and 1 mm wall thickness. Their Young's modulus and Poisson's ratio are 200 GPa and 0.3, respectively. Hinge connectors representing the revolute joints are used for modeling the crease lines. Although the rotation stiffness of the hinge connector is not necessary to the large-deformation analysis, the small rotation stiffness 1.0×10^{-3} (Nm) is introduced to each hinge connector to stabilize the analysis. The elongation of edges and the error of the dihedral angles between the pairs of faces connected to fixed crease lines are calculated from the coordinates of origami vertices which are obtained by solving Eq. (2.20) using the nodal displacements of the frame model in the analysis. If these edge length error and face flatness error are sufficiently small, the obtained surface is regarded to be rigid-foldable. Note that these parameters of the large deformation analysis have little impact on the evaluation of the rigid-foldability of the solutions obtained by solving the optimization problem.

4.2 Randomly generated surface

In this section, 100 randomly generated Bézier surfaces are used as the target surfaces to confirm the effectiveness of the selection criteria of the crease lines to be fixed introduced in Chapter 3. The example of an target surface is shown in Fig. 4.2. The (x, y) coordinates of the 5×5 control points are uniformly arranged as shown in Fig. 4.2(b), and the z-coordinates of the control points are randomly distributed in the range from -4 to 4. Form generation is carried out for Cases G1, G2, R1, and R2 in Table 4.1. The weight coefficients in $F_{\text{app}}(\mathbf{X})$ are

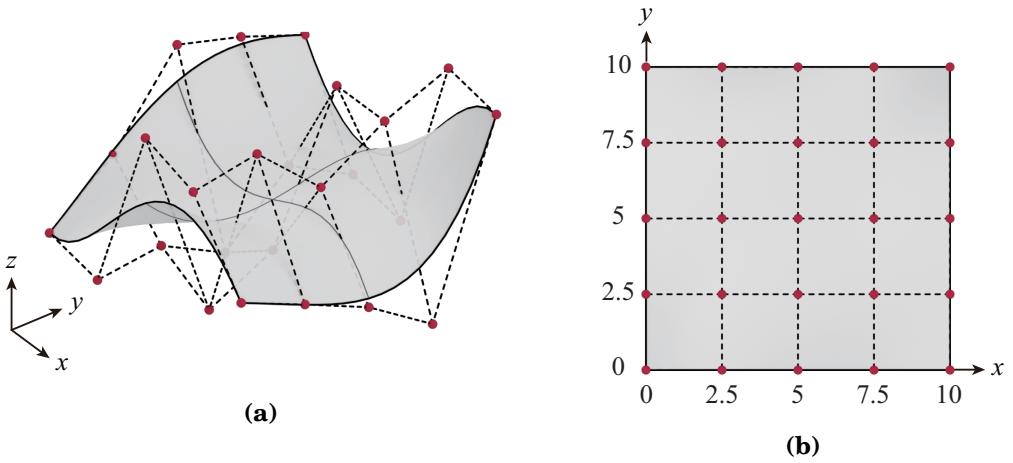

Figure 4.2: Randomly generated target surface; (a) Isometric view, (b) Plan view and arrangement of control points.

assigned as $(c_{\text{area}}, c_{\text{normal}}) = (0.3, 0.6)$ to approximately unify the order of $F_{\text{dist}}(\mathbf{X})$, $F_{\text{area}}(\mathbf{X})$, and $F_{\text{normal}}(\mathbf{X})$.

Five selection criteria of crease lines to be fixed are used in the form generation; the crease line with smallest value of σ_h, $\hat{\sigma}_h$, σ_h^{S}, $1/\sigma_h^{\text{F}}$, or $1/\hat{\sigma}_h^{\text{F}}$ is fixed in each iteration of the form generation process. In addition, the case where crease lines are randomly fixed is also considered. Therefore, form generation is carried out six times for each target surface with the different selection criterion of crease lines to be fixed, and 600 trials of form generation are made in total in Case G1, G2, R1, and R2. The number of times when the optimization problem (3.50) is successfully converged without locked crease lines (No. of solutions), when the problem (3.50) is not converged in good accuracy (No. of failures), and when the optimization problem (3.50) is converged with locked crease lines (No. of locking) are counted and compared to evaluate the performance of each selection criterion.

The results of form generation in Case G1, G2, R1, and R2 are summarized in Tables 4.2–4.5. The maximum, minimum, and average values among the 100 trials for each item in the first columns of Tables 4.2–4.5 are shown. As shown in Tables 4.2–4.5, the overall trend is that the number of locking is reduced when the criteria σ_h or $\hat{\sigma}_h$ is used, which reflects the shape and the deformation mechanism of an origami surface. The number of solutions and failures tends to be larger and smaller, respectively, than when σ_h^{S} is used, while this tendency is opposite when $1/\sigma_h^{\text{F}}$ or $1/\hat{\sigma}_h^{\text{F}}$ is used or the crease lines are randomly fixed. In addition, when σ_h or $\hat{\sigma}_h$ is used, the values of approximation error function $F_{\text{app}}(\mathbf{X})$ of the solutions tend to be smaller than especially when $1/\sigma_h^{\text{F}}$ or $1/\hat{\sigma}_h^{\text{F}}$ is used or the crease lines are randomly fixed. Therefore, considering the overall trend, σ_h and $\hat{\sigma}_h$ can improve the performance of form generation by reducing the times to solve the optimization problem and improving the approximation accuracy compared to the other criteria. Especially when $\hat{\sigma}_h$ is used, the values of approximation error function $F_{\text{app}}(\mathbf{X})$ of the solutions can be effectively reduced. Note that the minimum values of $F_{\text{app}}(\mathbf{X})$ are the same for all the selection

criteria since these values are the solutions without fixed crease lines; i.e., the solutions are the same for all the selection criteria.

The 1 DOF optimal shapes obtained in Cases G1 and R1 by using $\hat{\sigma}_h$ are shown in Figs. 4.3 and 4.4 which approximate the target surface shown in Fig. 4.2(a). The length errors of edges are both less than 10^{-5} % in the development diagrams of the 1 DOF solutions, and it has been confirmed that the solutions can be developed to a plane with good accuracy. In the large deformation analysis, the solution in Fig. 4.3 has been developed to a plane with the edge length error of up to 0.60 % and the angular error between the pairs of faces adjacent to the dividing edges of up to 5.5×10^{-3} radians, which are calculated from the nodal displacement of the frame model. The average values of the edge length error and the angular error are much smaller than the maximum values, and they are about 0.031 % and 6.5×10^{-4} radians, respectively. Therefore, the solution in Fig. 4.3 can be regarded as rigid-foldable. On the other hand, the edge length error and the angular error of the solution in Fig. 4.4 in the large deformation analysis are larger than those of the solution in Fig. 4.3, and the maximum and average values of them are about 29 %, 1.0 %, 1.0 radians, and 0.096 radians, respectively. Even if the error in the development diagram is small, the error in the large deformation analysis may be large. This is considered to be due to the fact that the solution has the crease lines with the large folding angles near the center. From the above, a rigid-folding development path to the xy-plane was not obtained for the solution shown in Fig. 4.4 at least for the forced displacement setting considered in this section.

When the results are compared with respect to the choice of the design variables, it can be seen from Tables 4.2–4.5 that the form generation process has better performance for the convergence of the optimization and for the approximation accuracy when the nodal coordinates are used in Cases G1 and R1. When the design variables are nodal coordinates, the number of solutions tends to be larger, and the values of the approximation error function tends to be smaller. Since the offset directions are the same among Cases G1, G2, R1, and R2, this tendency is attributed to the nonlinear representations of the coordinates of vertices in Cases G2 and R2, which may affect the performance of the optimization. The topology of the initial triangulation is also affect the performance of form generation. Although the difference of the values of $F_{\mathrm{app}}(\mathbf{X})$ is small, the number of failures is much larger in Cases R1 and R2.

Table 4.2: Results among 100 trials of form generation in Case G1 with five selection criteria of the crease lines to be fixed.

Selection criterion		σ_h	$\hat{\sigma}_h$	σ_h^{S}	$1/\sigma_h^{\mathrm{F}}$	$1/\hat{\sigma}_h^{\mathrm{F}}$	Random
No. of solutions	max.	25	22	27	24	21	29
	min.	1	1	1	1	1	1
	avg.	4.42	4.34	4.08	4.12	4.65	5.40
No. of failures	max.	196	148	255	126	118	178
	min.	23	22	41	47	46	31
	avg.	65.04	63.35	71.29	59.07	57.47	64.12
No. of locking	max.	8	3	19	8	0	13
	min.	0	0	0	0	0	0
	avg.	0.18	0.03	1.15	0.22	0.00	0.66
Min. DOF	max.	21	21	21	21	21	21
	min.	1	1	1	1	1	1
	avg.	17.67	17.68	18.27	17.98	17.35	16.86
Avg. $F_{\mathrm{app}}(\mathbf{X})$	max.	23.99	13.33	11.26	24.16	44.73	17.43
	min.	0.58	0.58	0.58	0.58	0.58	0.58
	avg.	2.81	2.61	2.42	2.79	3.93	3.29

Table 4.3: Results among 100 trials of form generation in Case G2 with five selection criteria of the crease lines to be fixed.

Selection criterion		σ_h	$\hat{\sigma}_h$	σ_h^{S}	$1/\sigma_h^{\mathrm{F}}$	$1/\hat{\sigma}_h^{\mathrm{F}}$	Random
No. of solutions	max.	22	21	28	21	21	21
	min.	1	1	1	1	1	1
	avg.	2.84	2.66	2.60	2.51	2.47	2.52
No. of failures	max.	229	217	358	194	152	199
	min.	13	47	47	46	30	47
	avg.	64.53	61.38	67.99	62.00	54.31	56.12
No. of locking	max.	2	0	16	1	0	9
	min.	0	0	0	0	0	0
	avg.	0.03	0.00	0.46	0.01	0.00	0.11
Min. DOF	max.	21	21	21	21	21	21
	min.	1	1	1	1	1	1
	avg.	19.17	19.34	19.52	19.49	19.53	19.49
Avg. $F_{\mathrm{app}}(\mathbf{X})$	max.	34.48	26.72	27.68	35.44	43.95	39.22
	min.	0.46	0.46	0.46	0.46	0.46	0.46
	avg.	4.25	3.77	3.89	4.18	4.51	4.42

Table 4.4: Results among 100 trials of form generation in Case R1 with five selection criteria of the crease lines to be fixed.

Selection criterion		σ_h	$\hat{\sigma}_h$	σ_h^{S}	$1/\sigma_h^{\mathrm{F}}$	$1/\hat{\sigma}_h^{\mathrm{F}}$	Random
No. of solutions	max.	21	21	26	22	22	28
	min.	0	0	0	0	0	0
	avg.	4.68	4.51	4.87	5.50	5.69	5.07
No. of failures	max.	442	360	650	295	222	391
	min.	2	2	2	2	2	2
	avg.	109.78	113.81	131.86	98.92	93.27	105.37
No. of locking	max.	0	0	30	6	1	14
	min.	0	0	0	0	0	0
	avg.	0.00	0.00	1.03	0.13	0.02	0.57
Min. DOF	max.	21	21	21	21	21	21
	min.	1	1	1	1	1	1
	avg.	17.27	17.44	17.31	16.47	16.28	17.12
Avg. $F_{\mathrm{app}}(\mathbf{X})$	max.	9.77	12.16	22.35	17.71	34.06	29.73
	min.	0.55	0.55	0.55	0.55	0.55	0.55
	avg.	2.61	2.51	2.72	3.45	4.24	3.19

Table 4.5: Results among 100 trials of form generation in Case R2 with five selection criteria of the crease lines to be fixed.

Selection criterion		σ_h	$\hat{\sigma}_h$	σ_h^{S}	$1/\sigma_h^{\mathrm{F}}$	$1/\hat{\sigma}_h^{\mathrm{F}}$	Random
No. of solutions	max.	21	21	32	23	21	29
	min.	1	1	1	1	1	1
	avg.	4.23	4.20	4.56	4.44	4.42	4.78
No. of failures	max.	504	486	694	359	218	331
	min.	91	40	91	92	39	41
	avg.	155.37	147.28	181.45	126.76	106.78	126.66
No. of locking	max.	0	0	59	1	0	11
	min.	0	0	0	0	0	0
	avg.	0.00	0.00	1.09	0.01	0.00	0.29
Min. DOF	max.	21	21	21	21	21	21
	min.	1	1	1	1	1	1
	avg.	17.77	17.8	17.75	17.59	17.58	17.45
Avg. $F_{\mathrm{app}}(\mathbf{X})$	max.	41.78	74.01	58.56	45.12	40.19	50.84
	min.	0.54	0.54	0.54	0.54	0.54	0.54
	avg.	5.93	5.96	7.04	6.33	6.52	6.87

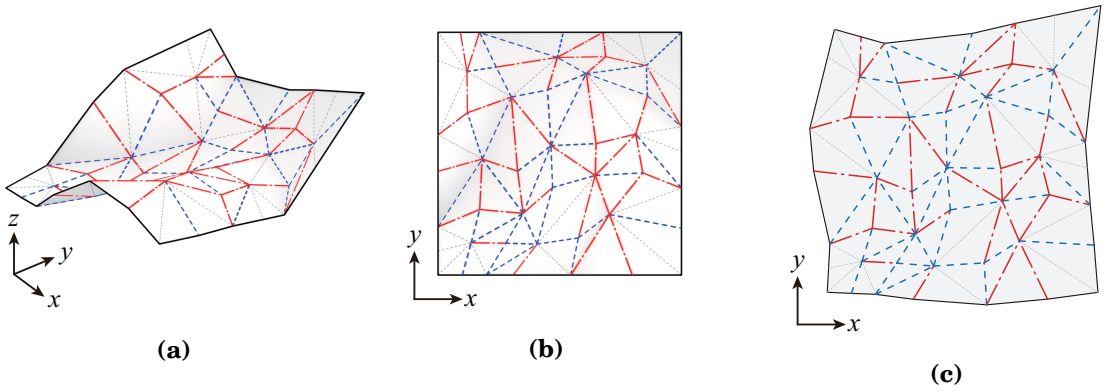

Figure 4.3: 1 DOF origami surface in Case G1 approximating the target surface in Fig. 4.2(a) generated by using the score $\hat{\sigma}_h$; (a) Isometric view, (b) Plan view, (c) Development diagram.

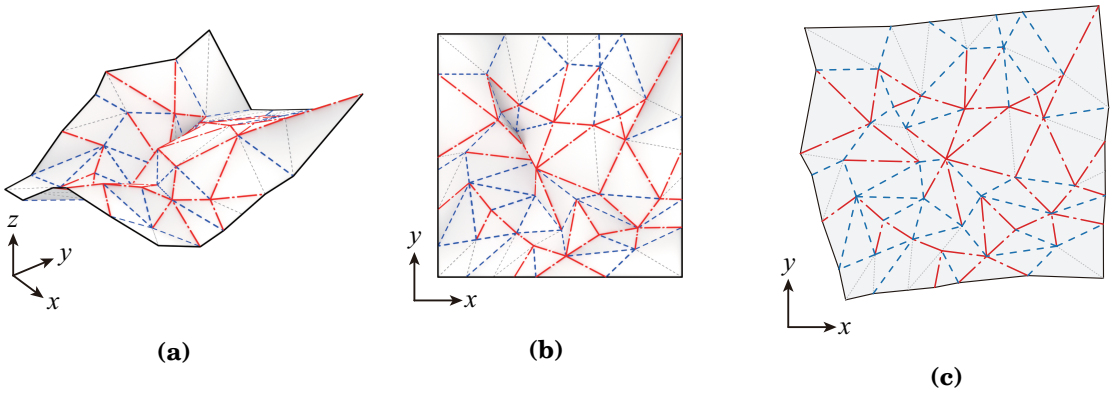

Figure 4.4: 1 DOF origami surface in Case R1 approximating the target surface in Fig. 4.2(a) generated by using the score $\hat{\sigma}_h$; (a) Isometric view, (b) Plan view, (c) Development diagram.

4.3 Regular surfaces

In this section, an HP surface in Fig. 4.5 and a dome surface in Fig. 4.6 are used as the target surfaces to demonstrate applicability of the proposed method to the curved surface with negative and positive Gaussian curvatures, respectively. The coordinates of the control points are shown in Figs. 4.5(b) and 4.6(b). The initial shapes and the planes of symmetry are shown in Figs. 4.5 and 4.6. As in Section 4.2, two patterns of initial triangulation of the target surfaces are considered, which are shown in Fig. 4.1 and referred to as Patterns G and R. Three cut patterns referred to as Cut patterns C, E, and X are introduced in this study for each initial triangulation pattern as shown in Fig. 4.7. Form generation is performed in Cases G1–R3 in Table 4.1. Crease lines to be fixed are selected by using $\hat{\sigma}_h$, and the crease lines in the symmetric positions are simultaneously fixed. Since the origami surface is symmetrical, the scores are also expected to be approximately symmet-

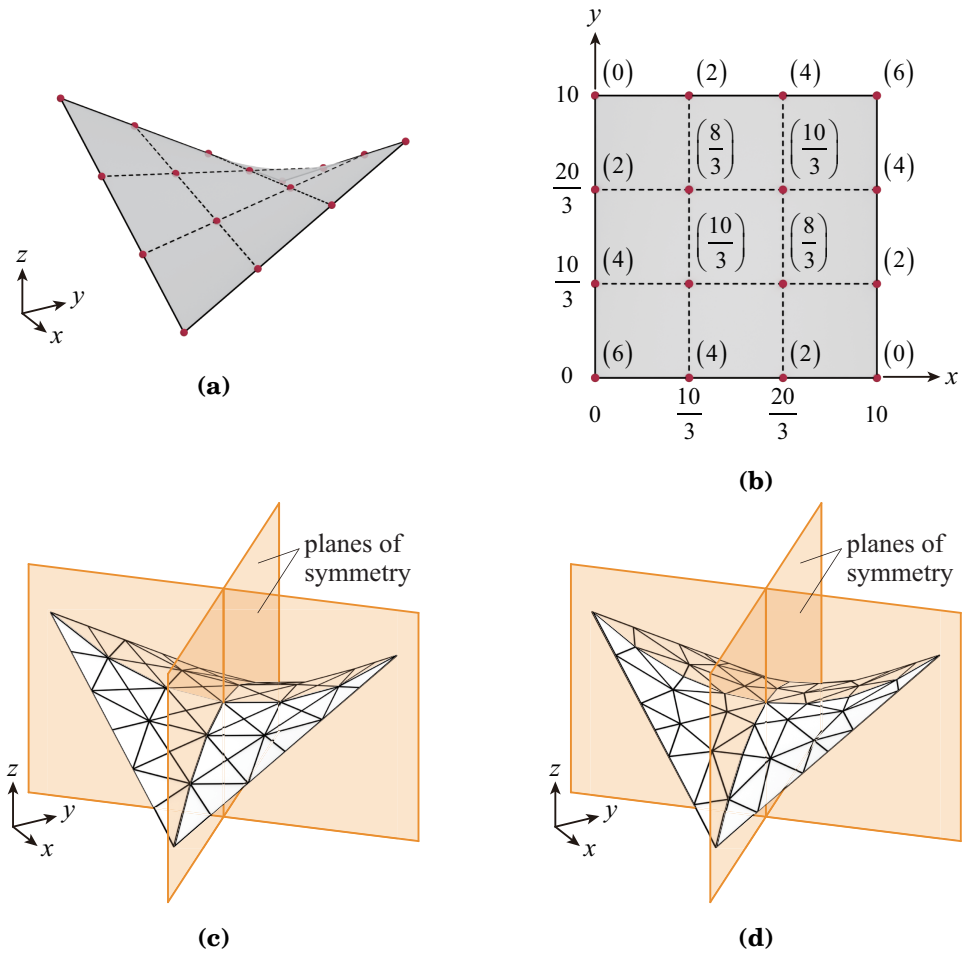

Figure 4.5: HP surface; (a) Isometrix view of the target HP surface, (b) Plan view and the coordinates of the control points, (c) Isometric view of Pattern G, (d) Isometric view of Pattern R.

rically distributed. Therefore, the crease line with the smallest score is selected, and one or three other crease lines symmetrically located with that crease line are also selected at the same time. The weight coefficients in $F_{\text{app}}(\mathbf{X})$ are set to $(c_{\text{area}}, c_{\text{normal}}) = (0, 0)$, $(0.2, 0.5)$, $(0.2, 1.0)$, $(0.4, 0.5)$, or $(0.4, 1.0)$, and the results of form generation with each pair of weight coefficients are compared to each other in Section 4.3.1 to investigate how c_{area} and c_{normal} influence the values of $F_{\text{dist}}(\mathbf{X})$, $F_{\text{area}}(\mathbf{X})$, and $F_{\text{normal}}(\mathbf{X})$. The results are also compared between Case G1–R3 without cuts and with $(c_{\text{area}}, c_{\text{normal}}) = (0.2, 1.0)$ in Section 4.3.2. Then, the optimal shapes are shown in Sections 4.3.3 and 4.3.4, and the effects of cut patterns on the approximation accuracy are examined.

4.3.1 Comparison between values of weight coefficients

The influence of c_{area} and c_{normal} on the values of $F_{\text{dist}}(\mathbf{X})$, $F_{\text{area}}(\mathbf{X})$, and $F_{\text{normal}}(\mathbf{X})$ is investigated for Case G1 without cuts, where the nodal coordinates are used as the design

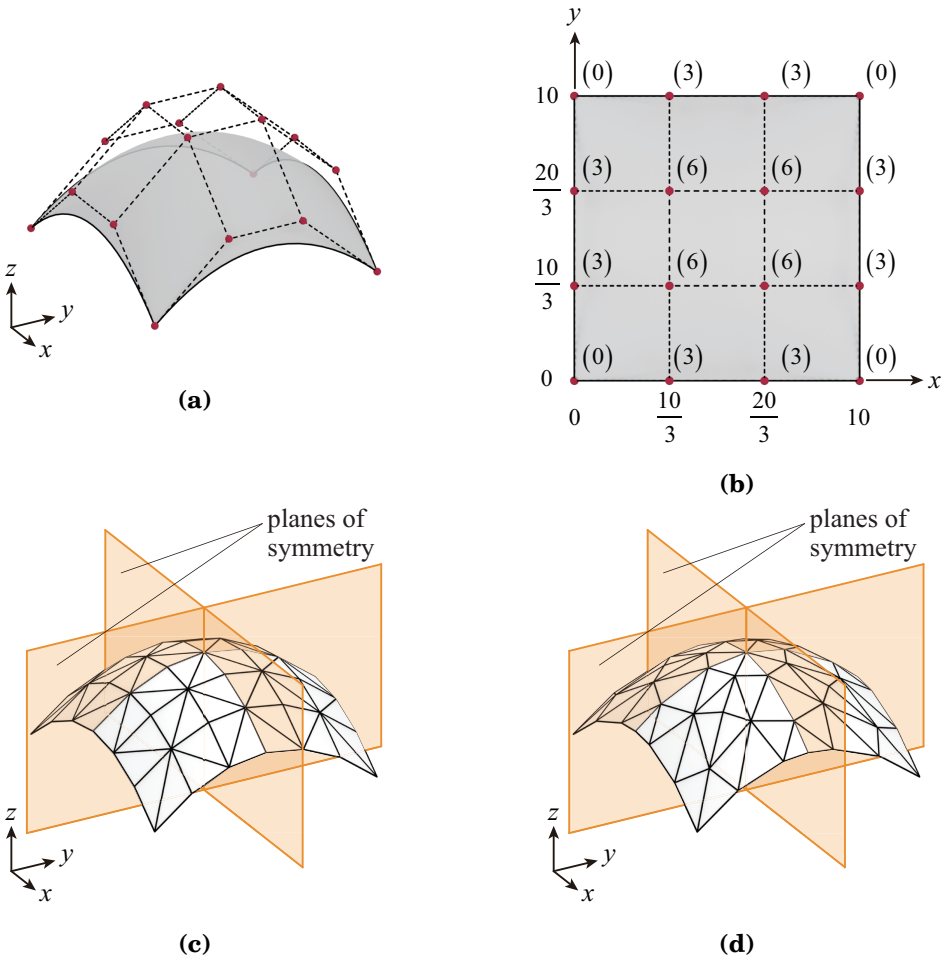

Figure 4.6: Dome surface; (a) Isometrix view of the target dome surface, (b) Plan view and the coordinates of the control points, (c) Isometric view of Pattern G, (d) Isometric view of Pattern R.

variables and the offsets are measured along the z-direction. The maximum, minimum, and average values of $F_{\text{dist}}(\mathbf{X})$, $F_{\text{area}}(\mathbf{X})$, and $F_{\text{normal}}(\mathbf{X})$ among the solutions obtained in each form generation process are shown in Table 4.6. The number of solutions without locked crease lines and the minimum DOF among the solutions are also shown in the table. The DOFs and the values of $F_{\text{dist}}(\mathbf{X})$, $F_{\text{area}}(\mathbf{X})$, and $F_{\text{normal}}(\mathbf{X})$ of each solutions are plotted in Fig. 4.8. The results for the approximation of the HP and dome surfaces are shown in Figs. 4.8(a)–4.8(d) and 4.8(e)–4.8(h), respectively. The results in the other cases are summarized in Appendix F. Appendix F also shows graphs of the values of the approximation error functions versus the number of fixed crease lines for each cases.

It is confirmed from Table 4.6 and Fig. 4.8 that the values of $F_{\text{area}}(\mathbf{X})$ and $F_{\text{normal}}(\mathbf{X})$ tend to be reduced by assigning values greater than 0 to c_{area} and c_{normal}. It is reasonable to observe that as the value of the weight coefficient increases, the value of the corresponding approximation error function decreases, as seen in the table and graphs. However, the

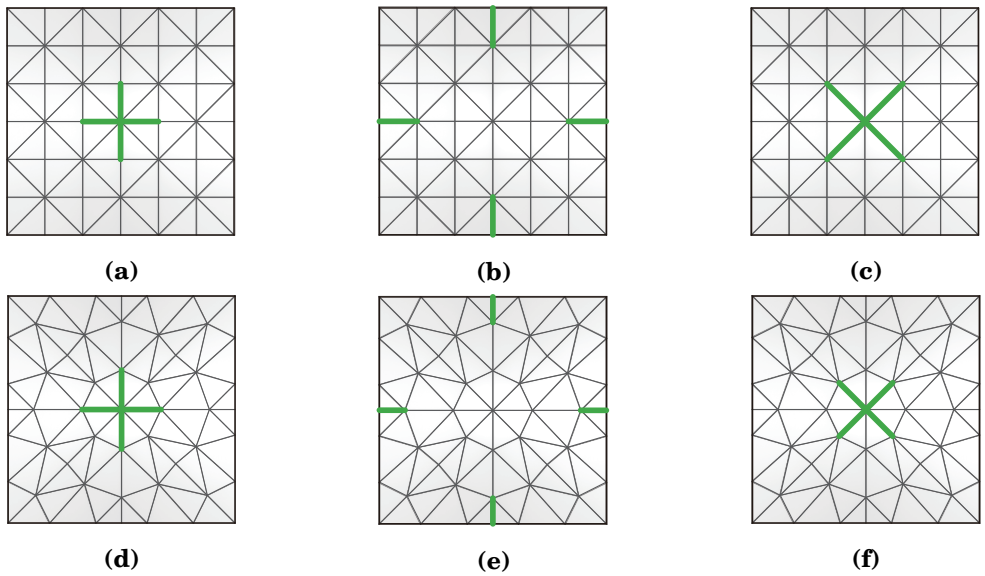

Figure 4.7: Cut patterns for initial triangulation patterns G and R; (a) and (d) Cut pattern C, (b) and (e) Cut pattern E, (c) and (f) Cut pattern X.

value of $F_{\text{dist}}(\mathbf{X})$ does not necessarily increase when c_{area} and c_{normal} are greater than 0, and there is no clear trade-off relationship between the values of $F_{\text{dist}}(\mathbf{X})$, $F_{\text{area}}(\mathbf{X})$, and $F_{\text{normal}}(\mathbf{X})$. This trend can also be seen in the other cases as shown in Appendix F. Therefore, it is appropriate to use the weight coefficients c_{area} and c_{normal} to balance the order of magnitude of each approximation error function, and the detailed adjustment of the values of c_{area} and c_{normal} should be done by referring to the results of the form generation to

Table 4.6: Form generation results without cuts in Case G1.

		HP surface					dome surface				
c_{area}		0.0	0.2	0.2	0.4	0.4	0.0	0.2	0.2	0.4	0.4
c_{normal}		0.0	0.5	1.0	0.5	1.0	0.0	0.5	1.0	0.5	1.0
No. solutions		7	7	6	7	8	7	7	7	7	1
Min. DOF		3	1	5	1	1	3	1	1	3	21
$F_{\text{dist}}(\mathbf{X})$	max.	4.95	3.80	1.90	2.23	4.64	2.50	33.22	5.93	18.33	2.32
	min.	1.79	1.51	1.82	1.87	1.98	2.06	2.24	2.61	2.18	2.32
	avg.	2.33	2.44	1.87	2.03	2.49	2.30	11.40	4.17	9.82	2.32
$F_{\text{area}}(\mathbf{X})$	max.	6.73	9.20	3.43	3.65	3.45	1.25	8.82	3.35	4.31	0.00
	min.	5.17	2.94	2.93	2.37	2.31	0.00	0.00	0.00	0.00	0.00
	avg.	6.41	4.72	3.15	2.96	2.76	0.56	2.25	0.56	0.62	0.00
$F_{\text{normal}}(\mathbf{X})$	max.	4.38	4.01	2.28	2.69	3.95	4.43	15.83	8.11	13.44	2.31
	min.	3.75	2.19	2.06	2.11	2.02	4.12	3.21	2.70	3.35	2.31
	avg.	4.22	2.88	2.16	2.38	2.39	4.21	8.43	4.14	8.58	2.31

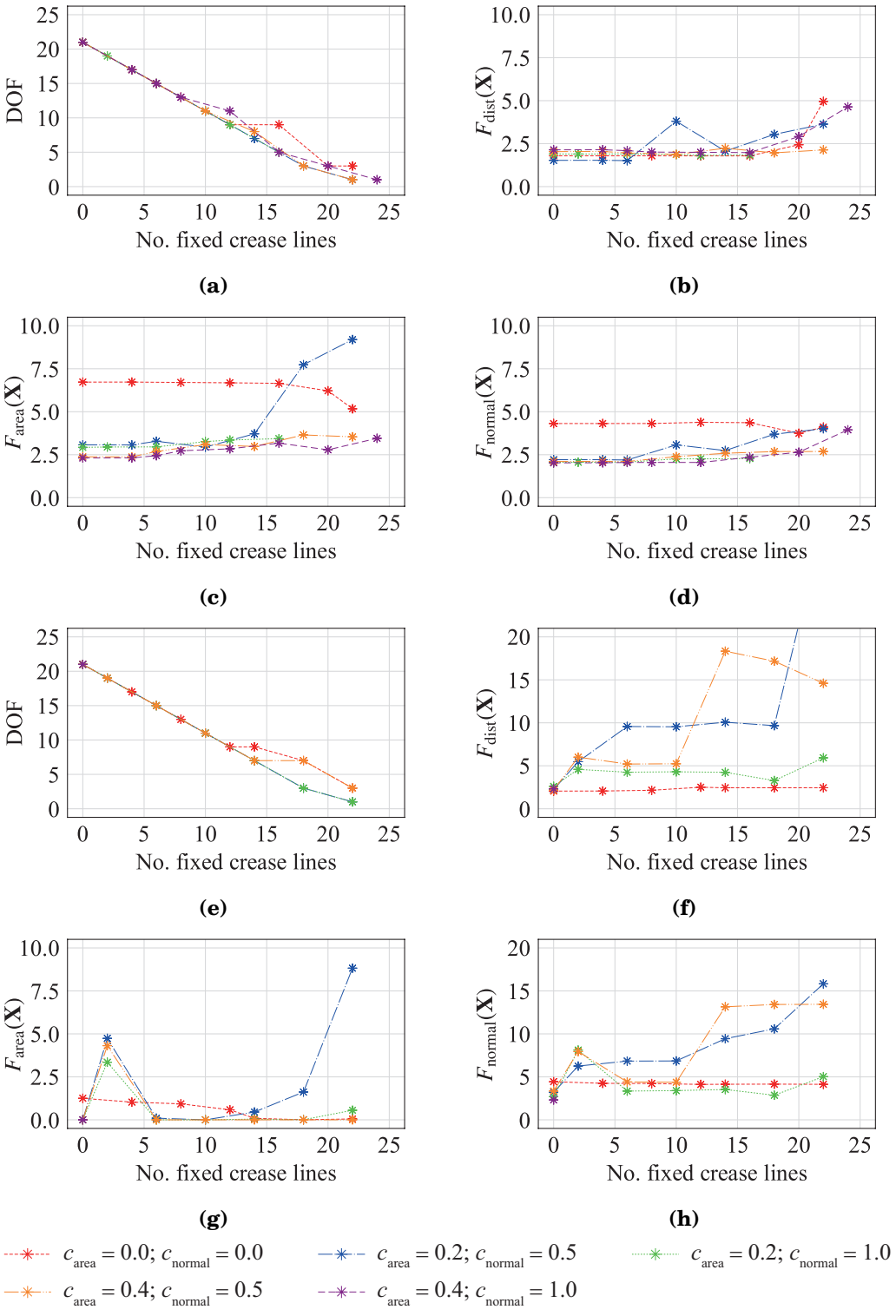

Figure 4.8: DOFs and the values of $F_{\mathrm{dist}}(\mathbf{X})$, $F_{\mathrm{area}}(\mathbf{X})$, and $F_{\mathrm{normal}}(\mathbf{X})$ of the solutions with different combinations of the weight coefficients c_{area} and c_{normal} and without cuts in Case G1; (a)–(d) Results for the HP surface, (e)–(h) Results for the dome surface.

Table 4.7: Results for the approximation of the HP surface without cuts and with $(c_{\text{area}}, c_{\text{normal}}) = (0.2, 0.5)$.

Cases		G1	G2	G3	R1	R2	R3
No. solutions		7	1	10	6	1	9
Min. DOF		1	21	3	1	21	1
$F_{\text{dist}}(\mathbf{X})$	max.	3.80	5.80	46.56	2.00	8.71	21.65
	min.	1.51	5.80	3.53	1.62	8.71	17.85
	avg.	2.44	5.80	22.46	1.71	8.71	20.05
$F_{\text{area}}(\mathbf{X})$	max.	9.20	0.00	9.93	5.11	0.00	4.70
	min.	2.94	0.00	2.83	4.01	0.00	2.61
	avg.	4.72	0.00	4.76	4.36	0.00	2.86
$F_{\text{normal}}(\mathbf{X})$	max.	4.01	2.31	7.41	3.83	2.34	5.23
	min.	2.19	2.31	2.03	3.37	2.34	1.96
	avg.	2.88	2.31	3.52	3.45	2.34	2.34

Table 4.8: Results for the approximation of the dome surface without cuts and with $(c_{\text{area}}, c_{\text{normal}}) = (0.2, 0.5)$.

Cases		G1	G2	G3	R1	R2	R3
No. solutions		7	5	9	2	1	1
Min. DOF		1	5	1	19	21	21
$F_{\text{dist}}(\mathbf{X})$	max.	33.22	23.34	17.28	2.95	3.36	4.66
	min.	2.24	8.56	6.12	2.25	3.36	4.66
	avg.	11.40	16.52	9.53	2.60	3.36	4.66
$F_{\text{area}}(\mathbf{X})$	max.	8.82	0.00	0.03	0.00	0.00	0.00
	min.	0.00	0.00	0.00	0.00	0.00	0.00
	avg.	2.25	0.00	0.01	0.00	0.00	0.00
$F_{\text{normal}}(\mathbf{X})$	max.	15.83	3.60	11.10	4.49	2.85	2.89
	min.	3.21	2.61	4.16	2.75	2.85	2.89
	avg.	8.43	3.14	5.88	3.62	2.85	2.89

improve the appearances of the obtained shapes. As a method for the initial setting of the weight coefficients, the values of c_{area} and c_{normal} can be determined approximately from the values of $F_{\text{dist}}(\mathbf{X})/F_{\text{area}}(\mathbf{X})$ and $F_{\text{dist}}(\mathbf{X})/F_{\text{normal}}(\mathbf{X})$ after the order of the approximation error functions is checked by applying imperfections to the initial triangulated shape.

4.3.2 Comparison between choices of design variables and initial triangulation patterns

The results in Case G1–R3 are compared to each other for the HP surface and the dome surface. In this section, cuts are not considered and the weight coefficients in the approxi-

mation error function are set to $(c_{\text{area}}, c_{\text{normal}}) = (0.2, 0.5)$. For the results in the other conditions, see Appendix F. The maximum, minimum, and average values of $F_{\text{dist}}(\mathbf{X})$, $F_{\text{area}}(\mathbf{X})$, and $F_{\text{normal}}(\mathbf{X})$ among the solutions obtained in each condition are shown in Tables 4.7 and 4.8. The number of solutions without locked crease lines and the minimum DOF among the solutions are also shown in those tables.

As shown in Tables 4.7 and 4.8, few solutions are obtained especially in Cases G2 and R2. This trend is common to the results for the examples with the random target surfaces. As mentioned in Section 4.2, this may attributed to the nonlinear representations of the coordinates of vertices in Cases G2 and R2. On the other hand, more solutions are obtained in Cases G3 and R3, which are not considered in Section 4.2, while the values of the approximation error functions are larger than those in Cases G1 and R1. This is because the boundary planes are not considered in Cases G3 and R3, and the vertices can be located more widely than in Cases G1 and R1. This reason also can explain why the values of the approximation error functions are larger in Cases G2 and R2 especially for $F_{\text{dist}}(\mathbf{X})$.

When the dome surface is approximated, the values of the approximation error functions tend to be larger than those of the HP surface except for $F_{\text{area}}(\mathbf{X})$ although the height of the target dome surface is lower than the HP surface. The results obtained by assigning the other conditions shown in Appendix F have the approximately same trend. In addition, the number of the solutions drastically changes according to the conditions of form generation as shown in Table 4.8 and Appendix F when the proposed method is applied to the dome surface. This implies that the approximation of the dome surface is more *difficult* than the approximation of the HP surface.

4.3.3 Approximation of HP surface in Case G3

In this section, the effects of cut patterns on the approximation accuracy are examined in Case G3 for the HP surface in Fig. 4.5. The weight coefficients in the approximation error function are set to $(c_{\text{area}}, c_{\text{normal}}) = (0.2, 1.0)$. The DOFs and the values of the approximation error functions $F_{\text{dist}}(\mathbf{X})$, $F_{\text{area}}(\mathbf{X})$, and $F_{\text{normal}}(\mathbf{X})$ at each number of fixed crease lines are plotted in Fig. 4.9.

As shown in Fig. 4.9, the values of the approximation error functions are reduced by introducing the cut of pattern E. However, they are not improved when the cuts of patterns C and X are introduced. A possible reason for this is that the inner cuts only change the distribution of the Gaussian curvature at the interior vertices without changing the sum, whereas the exterior cuts can directly relax the conditions of the Gaussian curvature. Therefore, an inner cut is expected to have an effect on improving the approximation accuracy when it is placed across parts of the surface with different signs of Gaussian curvature.

The maximum DOFs among the solutions without cuts and with Cut pattern C, E, and X are 21, 26, 26, and 29, respectively, and the minimum DOFs are 1, 6, 1, and 2, respectively. Comparing solutions with the same number of fixed crease lines, the approximation error tends to be smaller when a cut is introduced than when no cut is introduced, whereas the DOF tend to be larger. On the other hand, when compared for solutions with the same

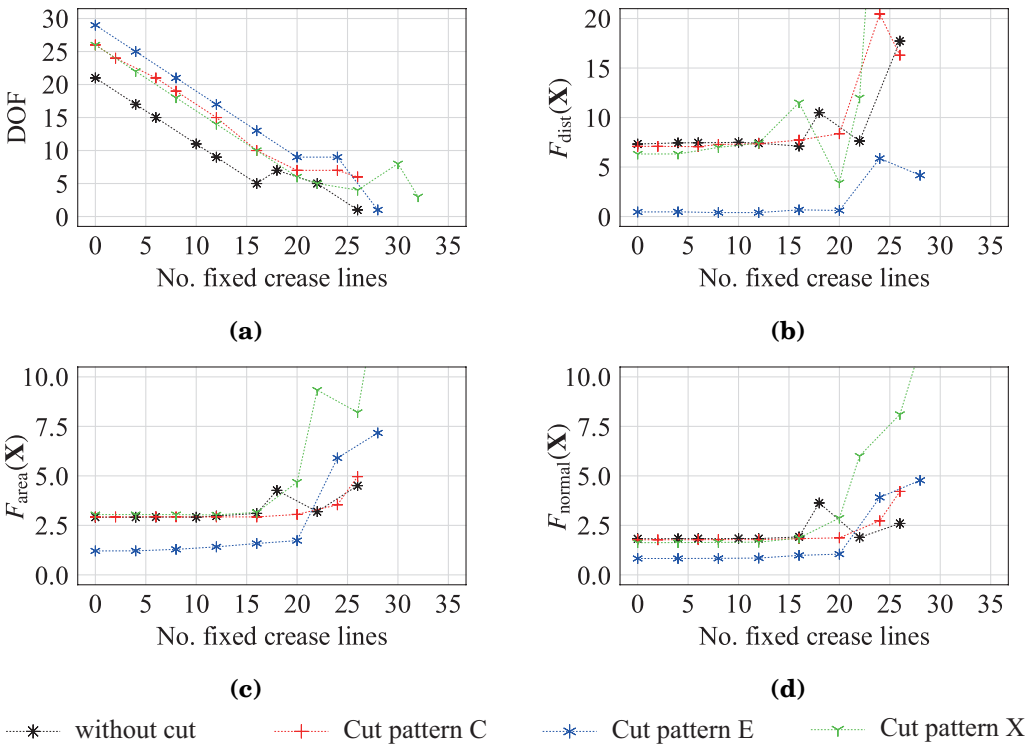

Figure 4.9: DOFs and the values of $F_{\mathrm{dist}}(\mathbf{X})$, $F_{\mathrm{area}}(\mathbf{X})$, and $F_{\mathrm{normal}}(\mathbf{X})$ of the solutions for the HP surface in Case G3.

DOF, the approximation accuracy may be worse when a cut is introduced than when no cut is introduced because the number of fixed crease lines becomes larger. Although the DOF of the mechanism is preferred to be small in view of the stability of the deployment motion of the origami surface, the above results show an approximate trade-off relationship between approximation accuracy and deformation degree of freedom.

Here, the optimal solutions with the similar number of fixed crease lines are shown

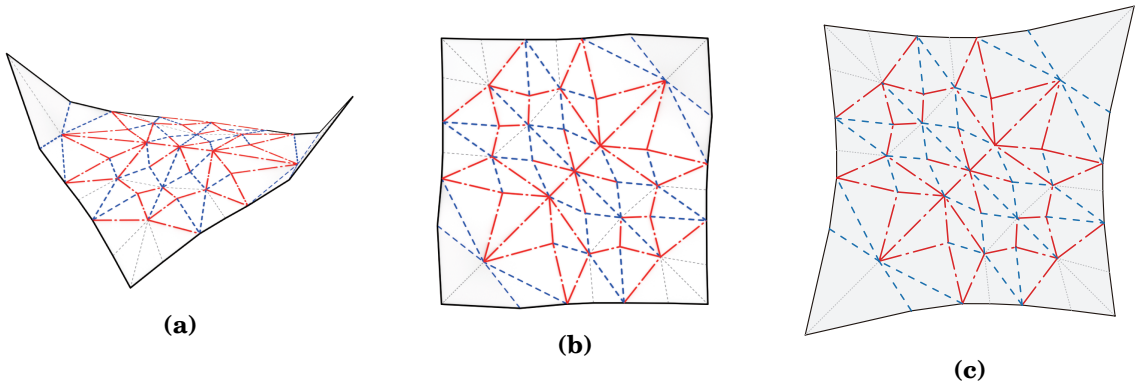

Figure 4.10: Optimal shape approximating the HP surface without cuts in Case G3; (a) Isometric view, (b) Plan view, (c) Development diagram.

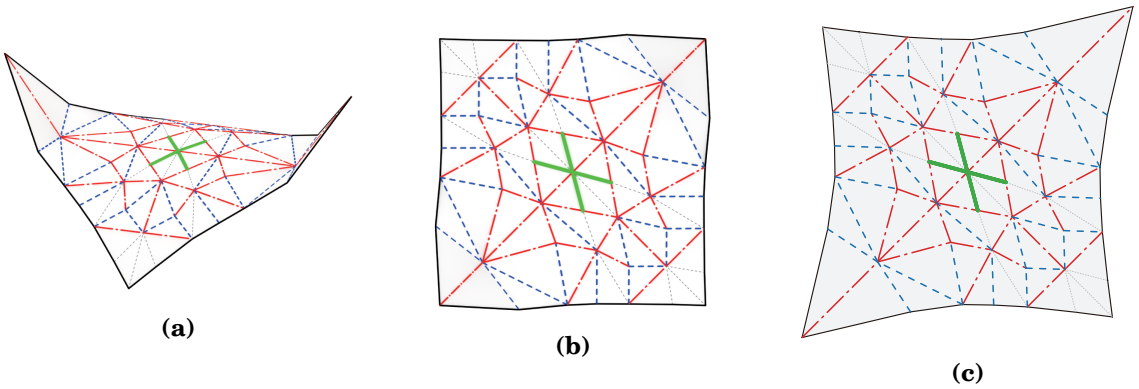

Figure 4.11: Optimal shape approximating the HP surface with Cut pattern C in Case G3; (a) Isometric view, (b) Plan view, (c) Development diagram.

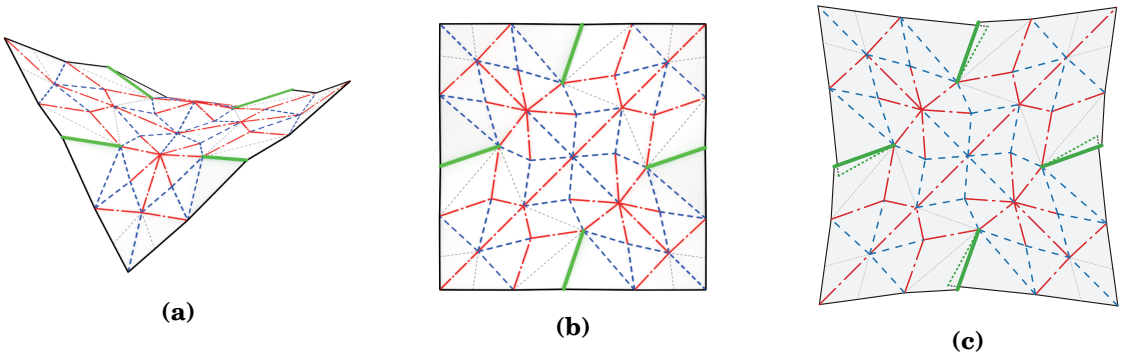

Figure 4.12: Optimal shape approximating the HP surface with Cut pattern E in Case G3; (a) Isometric view, (b) Plan view, (c) Development diagram.

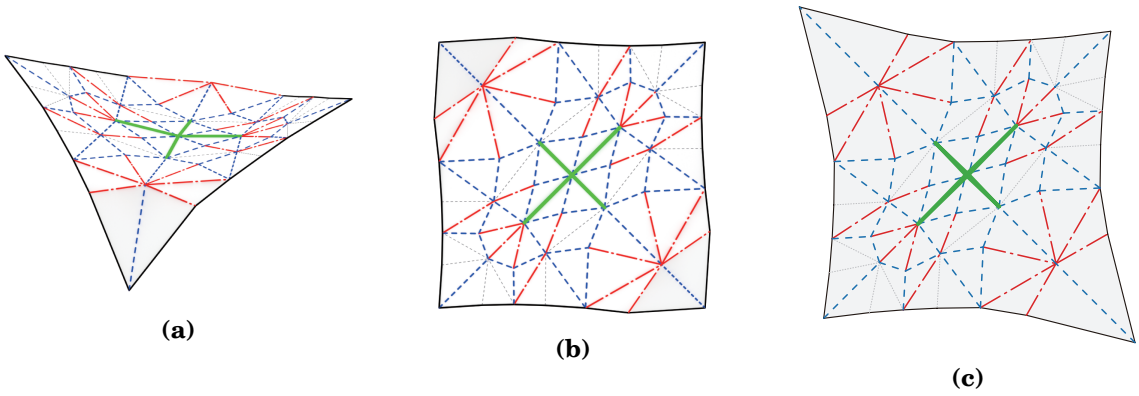

Figure 4.13: Optimal shape approximating the HP surface with Cut pattern C in Case G3; (a) Isometric view, (b) Plan view, (c) Development diagram.

Table 4.9: Values of the optimal shapes in Figs. 4.10–4.13 approximating the HP surface with $(c_{\text{area}}, c_{\text{normal}}) = (0.2, 1.0)$ in Case G3.

	without cuts	Cut pattern C	Cut pattern E	Cut pattern X
No. of fixed crease lines	16	16	16	16
DOFs of mechanism	5	10	13	10
$F_{\text{dist}}(\mathbf{X})$	7.11	7.72	0.67	11.50
$F_{\text{area}}(\mathbf{X})$	3.10	2.93	1.59	3.16
$F_{\text{normal}}(\mathbf{X})$	1.92	1.83	0.98	1.86
Avg. $\left\|dl_j^{\text{dev}}\right\|$ [m]	1.31×10^{-6}	1.49×10^{-6}	2.81×10^{-6}	1.52×10^{-6}
Max. $\left\|dl_j^{\text{dev}}\right\|$ [m]	8.47×10^{-6}	7.94×10^{-6}	8.31×10^{-6}	8.89×10^{-6}
Avg. $\left\|dl_j^{\text{dev}}/l_j\right\|$ [%]	6.34×10^{-7}	7.17×10^{-7}	1.30×10^{-6}	7.27×10^{-7}
Max. $\left\|dl_j^{\text{dev}}/l_j\right\|$ [%]	2.74×10^{-6}	3.51×10^{-6}	3.68×10^{-6}	2.77×10^{-6}
Avg. $\left\|dl_j^{\text{lda}}\right\|$ [m]	1.89×10^{-4}	1.12×10^{-4}	2.65×10^{-5}	8.79×10^{-5}
Max. $\left\|dl_j^{\text{lda}}\right\|$ [m]	2.38×10^{-3}	1.63×10^{-3}	2.98×10^{-4}	8.30×10^{-4}
Avg. $\left\|dl_j^{\text{lda}}/l_j\right\|$ [%]	7.86×10^{-3}	4.64×10^{-3}	1.29×10^{-3}	3.80×10^{-3}
Max. $\left\|dl_j^{\text{lda}}/l_j\right\|$ [%]	1.01×10^{-1}	5.58×10^{-2}	1.36×10^{-2}	3.69×10^{-2}
Avg. $d\rho_j^{\text{lda}}$ [rad]	2.31×10^{-4}	8.45×10^{-5}	4.14×10^{-6}	2.84×10^{-5}
Max. $d\rho_j^{\text{lda}}$ [rad]	2.90×10^{-3}	3.60×10^{-4}	1.85×10^{-5}	1.41×10^{-4}

in Figs. 4.10–4.13. Table 4.9 summarizes the number of fixed crease lines, the number of DOFs, the values of the approximation error functions, and the shape errors in the development diagrams and the large deformation analyses of the solutions in Figs. 4.10–4.13. In Table 4.9, l_j represents the length of edge j, and dl_j^{dev} and dl_j^{lda} are the elongation of edge j in the development diagram and the large deformation analysis. $d\rho_j^{\text{lda}}$ is the error of the dihedral angle between the faces connected to dividing edge j from π; i.e., the error of the flatness of a face with more than three edges. The maximum value of $\left|dl_j^{\text{lda}}/l_j\right|$, which represents the absolute strain of an edge in the process of deployment, is about 10 times larger than the average, and the local deformation may occur. However, the average error of the edge length is less than 1 mm, and the maximum value is also small compared to the span of the surface. In addition, the errors of face flatness is quite small. Therefore, the solutions in Figs. 4.10–4.13 can be regarded to be approximately rigid-foldable.

As shown Figs. 4.10–4.13, when a cut is not introduced or the inner cuts are introduced, the solutions are almost flat near the center and the corners are intensively folded. On the other hand, this tendency is alleviated in the solution with Cut pattern E shown in Fig. 4.12, which looks more similar to the target surface. In the solutions for Cut patterns C and X shown in Figs. 4.11 and 4.13, the cuts are hardly open in the development diagrams, and this also indicates that the effect on improving the approximation accuracy is small for

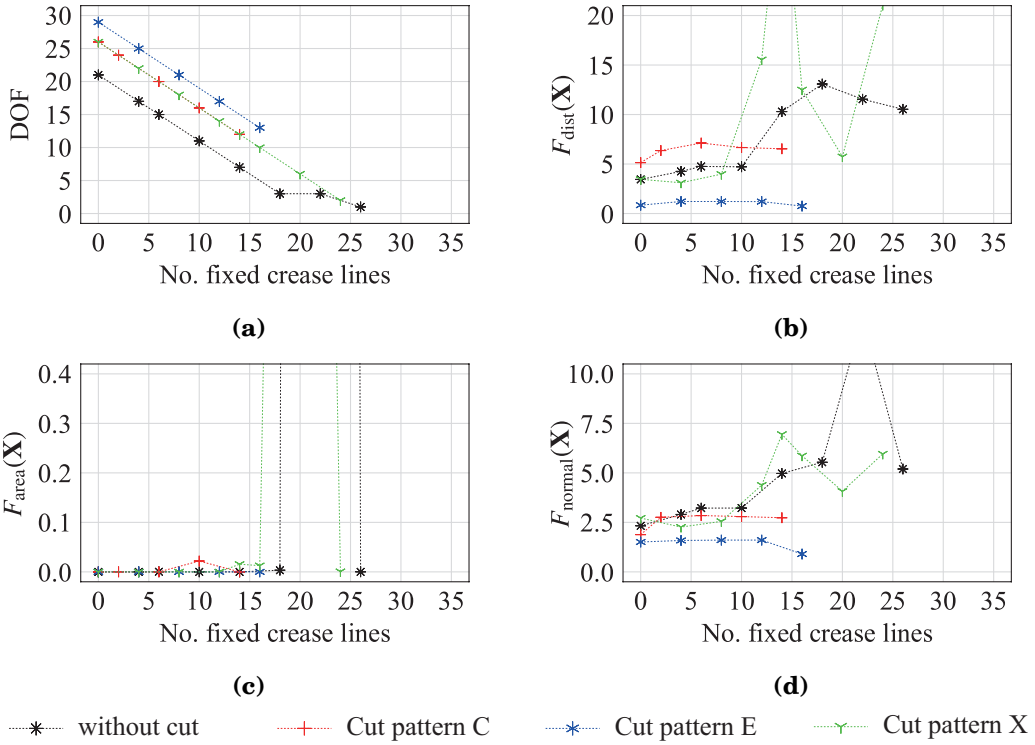

Figure 4.14: DOFs and the values of $F_{\mathrm{dist}}(\mathbf{X})$, $F_{\mathrm{area}}(\mathbf{X})$, and $F_{\mathrm{normal}}(\mathbf{X})$ of the solutions for the dome surface in Case G3.

the inner cuts. Note that when the Cut pattern E is introduced, faces are overlapped each other at the cuts in the development diagram as shown in Fig. 4.12(c).

4.3.4 Approximation of dome surface

In this section, the effects of cut patterns on the approximation accuracy are examined in Case G3 with $(c_{\mathrm{area}}, c_{\mathrm{normal}}) = (0.2, 1.0)$ for the dome surface in Fig. 4.6. The DOFs and

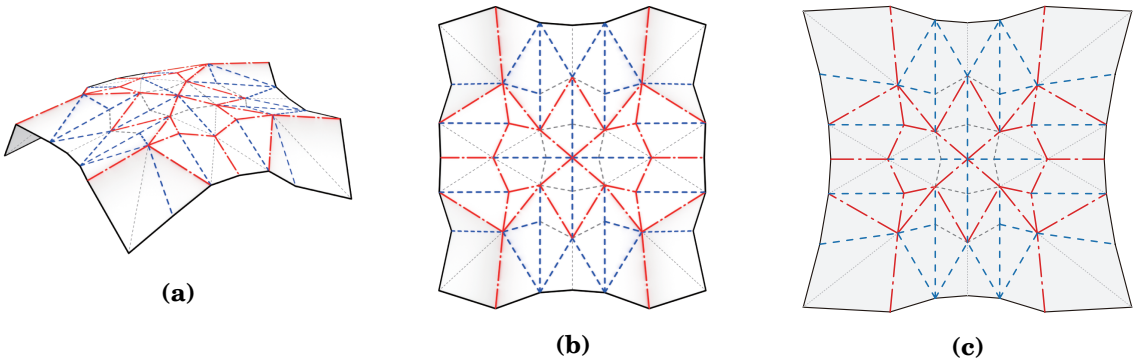

Figure 4.15: Optimal shape approximating the dome surface without cuts in Case G3; (a) Isometric view, (b) Plan view, (c) Development diagram.

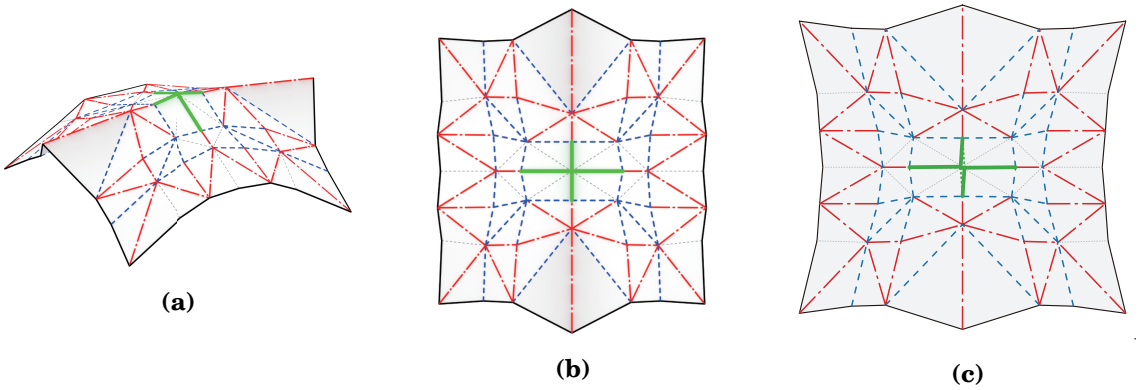

Figure 4.16: Optimal shape approximating the dome surface with Cut pattern C in Case G3; (a) Isometric view, (b) Plan view, (c) Development diagram.

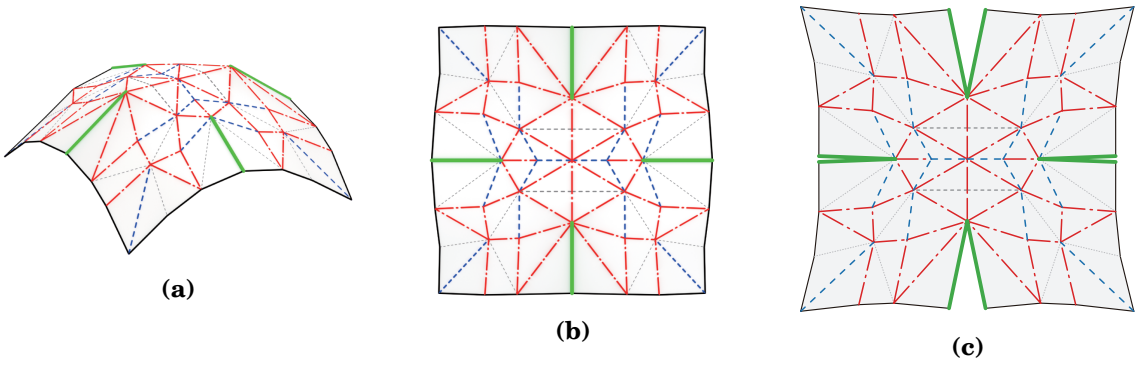

Figure 4.17: Optimal shape approximating the dome surface with Cut pattern E in Case G3; (a) Isometric view, (b) Plan view, (c) Development diagram.

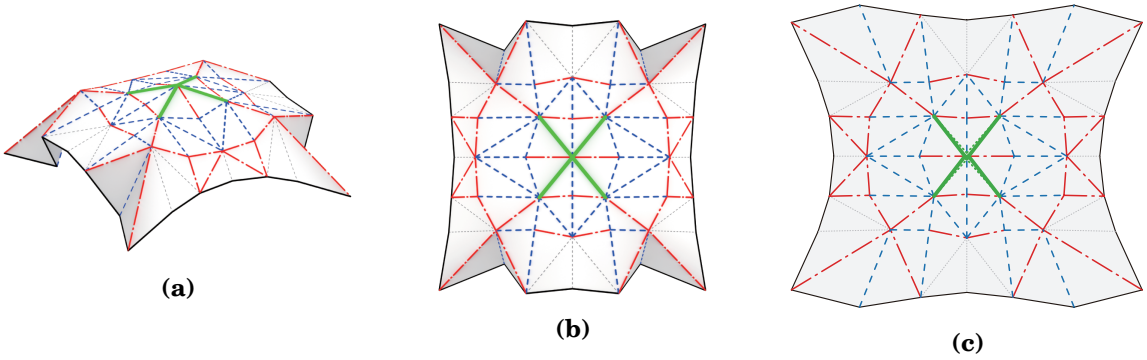

Figure 4.18: Optimal shape approximating the dome surface with Cut pattern C in Case G3; (a) Isometric view, (b) Plan view, (c) Development diagram.

Table 4.10: Values of the optimal shapes in Figs. 4.15–4.18 approximating the dome surface with $(c_{\text{area}}, c_{\text{normal}}) = (0.2, 1.0)$ in Case G3.

	without cuts	Cut pattern C	Cut pattern E	Cut pattern X
No. of fixed crease lines	14	14	16	16
DOFs of mechanism	7	12	13	10
$F_{\text{dist}}(\mathbf{X})$	10.30	6.54	0.75	12.50
$F_{\text{area}}(\mathbf{X})$	1.32×10^{-6}	1.54×10^{-7}	2.08×10^{-7}	1.26×10^{-2}
$F_{\text{normal}}(\mathbf{X})$	4.97	2.73	0.90	5.86
Avg. $\left\lvert dl_j^{\text{dev}}\right\rvert$ [m]	1.24×10^{-6}	1.23×10^{-6}	3.47×10^{-6}	2.11×10^{-6}
Max. $\left\lvert dl_j^{\text{dev}}\right\rvert$ [m]	5.80×10^{-6}	6.40×10^{-6}	2.11×10^{-5}	1.46×10^{-5}
Avg. $\left\lvert dl_j^{\text{dev}}/l_j\right\rvert$ [%]	5.28×10^{-7}	5.53×10^{-7}	1.53×10^{-6}	8.92×10^{-7}
Max. $\left\lvert dl_j^{\text{dev}}/l_j\right\rvert$ [%]	1.72×10^{-6}	1.66×10^{-6}	6.03×10^{-6}	3.34×10^{-6}
Avg. $\left\lvert dl_j^{\text{lda}}\right\rvert$ [m]	1.29×10^{-3}	3.71×10^{-4}	2.58×10^{-5}	5.61×10^{-3}
Max. $\left\lvert dl_j^{\text{lda}}\right\rvert$ [m]	1.17×10^{-2}	5.65×10^{-3}	1.69×10^{-4}	6.61×10^{-2}
Avg. $\left\lvert dl_j^{\text{lda}}/l_j\right\rvert$ [%]	6.59×10^{-2}	1.84×10^{-2}	1.39×10^{-3}	2.71×10^{-1}
Max. $\left\lvert dl_j^{\text{lda}}/l_j\right\rvert$ [%]	6.59×10^{-1}	2.16×10^{-1}	1.27×10^{-2}	3.33
Avg. $d\rho_j^{\text{lda}}$ [rad]	2.64×10^{-4}	9.31×10^{-5}	2.51×10^{-5}	1.25×10^{-2}
Max. $d\rho_j^{\text{lda}}$ [rad]	1.49×10^{-3}	4.81×10^{-4}	1.94×10^{-4}	7.53×10^{-2}

the values of the approximation error functions $F_{\text{dist}}(\mathbf{X})$, $F_{\text{area}}(\mathbf{X})$, and $F_{\text{normal}}(\mathbf{X})$ at each number of fixed crease lines are plotted in Fig. 4.14.

As shown in Fig. 4.14, the values of the approximation error functions $F_{\text{dist}}(\mathbf{X})$ and $F_{\text{normal}}(\mathbf{X})$ are reduced by introducing the cut of pattern E, while $F_{\text{area}}(\mathbf{X})$ is approximately equal to zero in almost solutions. The maximum DOFs among the solutions without cuts and with Cut pattern C, E, and X are 21, 26, 26, and 29, respectively, and the minimum DOFs are 1, 12, 13, and 2, respectively. The trend of the values of the approximation error functions are similar to that of the HP surface.

The optimal solutions with 14 or 16 fixed crease lines are shown in Figs. 4.15–4.18. The number of fixed crease lines, the number of DOFs, the values of the approximation error functions, and the shape errors in the development diagrams and the large deformation analyses are summarized in Table 4.10. Although the values of $\left\lvert dl_j^{\text{dev}}\right\rvert$ and $d\rho_j^{\text{lda}}$ are sufficiently small, the values of $\left\lvert dl_j^{\text{lda}}\right\rvert$ are about 10 times larger than those of the HP surface. However, they are still small compared to the span of the surface. Therefore, the solutions in Figs. 4.15–4.18 can be regarded to be approximately rigid-foldable.

As shown Figs. 4.15–4.18, the approximation error tends to concentrate at the boundary edges of the surface when the dome surface is approximated. For the examples in Figs. 4.15, 4.16, and 4.18, the entire surfaces appears to approach cylindrical shapes which have curva-

ture in only one direction rather than dome shapes which have curvature in two directions. Then, the approximation accuracy is significantly improved when the exterior cuts are introduced. In the development diagrams in Figs. 4.16(c) and 4.18(c), the faces are locally overlapped each other around the cuts. However, the cuts are mostly closed, and it can be inferred that the effects of the cuts are minor.

4.4 Conclusions

Case studies of the approximation of curved surfaces by the method proposed in Chapter 3 have been provided. As demonstrated in this chapter, curved surfaces with positive and negative Gaussian curvature have been approximated by a developable rigid origami structure. First, the form generation procedure has been carried out for 100 randomly generated target surfaces with two types of crease patterns and two combinations of design variables and direction of offsets. It is confirmed from the 400 trials of form generation that the two selection criteria of crease lines to be fixed which reflect the shape and the deformation mechanism of an origami surface can improve the efficiency of form generation by preventing the crease lines from being locked and reducing the times of solving the optimization problems compared to the other selection criteria which only reflect the shape or the mechanism. Furthermore, comparing the two proposed criteria, the performance of the criterion defined by the orthonormalized hinge rotation modes is better than the other criterion defined by the eigenvalue derivatives of the pseudo stiffness matrix of the frame model. The approximation accuracy is also better when these two criteria are used. Therefore, the normalized score should basically be used for the form generation.

Form generation has also been carried out for an HP and a dome surfaces to demonstrate the impacts of the weight coefficients in the approximation error function, the choice of the design variables, and the introduction of cuts. In these examples, five combinations of the weight coefficients and three combinations of the design variables and the direction of offsets are considered. Although the values of the approximation error functions are reduced by increasing the corresponding weight coefficients, there is no clear trade-off relation between the three approximation error functions, and the weight coefficients should basically be used to balance the order of magnitude of each approximation error function. For further improvement of the surface appearance, the values of the weight coefficients are adjusted manually by referring to the results of the form generation. On the other hand, the choice of the design variables may affect the stability of the process of form generation. When the design variables are the pairs of parameters of the Bézier surface and offsets, and the directions of the offsets are the z-direction, the number of solutions without locked crease lines tend to be smaller because of the nonlinear representations of the coordinates of vertices. However, when the directions of the offsets are the normal directions of the target surface, more solutions are obtained since the boundary planes of the origami surface is not considered while the approximation error becomes larger. Therefore, it is preferable to use the coordinates of the origami vertices or the nodal coordinates of the frame model as

variables when the arrangement of the control points of the target Bézier surface is uniform in x- and y-coordinates.

The form generation for the HP and the dome surfaces is performed with two types of inner cuts and one type of exterior cut. As shown in the examples, exterior cuts can significantly improve the approximation accuracy while the inner cuts does not. This is because the inner cuts only change the distribution of the Gaussian curvature at the interior vertices without changing the sum of it, whereas the exterior cuts can directly relax the conditions of the Gaussian curvature.

This study only considered a limited number of types of crease and cut patterns, and the optimization of these patterns are not studied. Therefore, design of origami surfaces using the proposed method may require trial and error with respect to the crease and cut patterns, and it is not always possible to select the best crease and cut patterns for surface approximation. In future research, it is important to investigate methods for finding good crease and cut patterns.

Chapter 5

Equilibrium path analysis

In this chapter, methods of equilibrium path analysis and stability analysis of an equilibrium state are proposed for a rigid origami represented by the frame model. The equilibrium state of a frame model with the external loads applied to the nodes is investigated. It is uniquely determined by assuming a small rotational stiffness proportional to the length of a crease line and by minimizing the total potential energy under the compatibility conditions so that the displacements of the nodes and the members are compatible. The augmented Lagrangian method is utilized to solve the minimization problem, and the stability of the equilibrium state is evaluated with respect to the positive definiteness of the Hessian of the augmented Lagrangian. When an eigenvalue of the Hessian of the augmented Lagrangian is equal to zero, the equilibrium state is unstable, and a critical eigenmode corresponding to the zero eigenvalue is numerically compared to the infinitesimal mechanism of a frame model to investigate the relationship between them. An equilibrium path is traced by the incremental loading analysis, and bifurcation of the equilibrium path is investigated in the numerical examples.

5.1 Introduction

It is important to understand the properties of rigid-folding motions for engineering applications utilizing the kinematics of rigid origami that can be efficiently and safely deployed. However, the folding/unfolding process of rigid origami is quite complicated and nonlinear, and generally exhibits a multi-degree-of-freedom mechanism except for some special crease patterns such as Miura-ori [79]. Therefore, it is difficult to obtain an analytical solution of the deformation path (folding path) of a rigid origami, and a numerical solution such as Newton's method is generally used to iteratively obtain the folding states of rigid origami to trace the path. In general, a numerical path tracing can be regarded as the process of iteratively finding a solution to the nonlinear equations $\mathbf{f}(\mathbf{x}) = \mathbf{0}$ representing the compatibility equations and the equilibrium equations [80]. Here, $\mathbf{x}$ is the vector of variables such as folding angles and nodal displacements (possibly including a load factor and Lagrange multipliers), and $\mathbf{f}(\mathbf{x})$ is a vector-valued function. The process of path tracing often starts

from a known solution of $\mathbf{f}(\mathbf{x}) = \mathbf{0}$, and this equation is iteratively solved while $\mathbf{x}$ is updated as $\mathbf{x} \leftarrow \mathbf{x} + \Delta\mathbf{x}$. The increment $\Delta\mathbf{x}$ along the path is determined as a vector satisfying the following equation:

$$\frac{d\mathbf{f}(\mathbf{x})}{d\mathbf{x}}\Delta\mathbf{x} + \mathbf{e} = \mathbf{0}$$

where $df(\mathbf{x})/d\mathbf{x}$ is a matrix form of the gradient of $\mathbf{f}$(x) and $\mathbf{e}$ is a residual vector.

The existing path tracing methods that follow the above directions can mainly be categorized into two types. One is the pure mechanism analysis that considers only geometric constraints based on the assumption that faces are completely rigid, and $\mathbf{f}(\mathbf{x}) = \mathbf{0}$ represents the compatibility equations. A rotational hinge model introduced in Chapter 2 is often used for this pure mechanism analysis; e.g. Refs. [24, 32]. The other is the structural analysis to trace an *equilibrium path*; a sequence of equilibrium states under external loads or forced displacements assuming rotational stiffness of crease lines and/or elastic deformation of the faces of a rigid origami, and $\mathbf{f}(\mathbf{x}) = \mathbf{0}$ represents the equilibrium equations. A truss model introduced in Chapter 2 is often used for this equilibrium path analysis by allowing the deformation of bars; e.g. Refs. [34, 53, 54]. In both analysis types, there may exist a singular point where the rank of $df(\mathbf{x})/d\mathbf{x}$ changes in the process of tracing the deformation path, and the increment $\Delta\mathbf{x}$ cannot be determined uniquely. Since the singular point can be a *bifurcation point* where one or more branching paths exist or a *limit point* where a snap-through behavior can be observed, special consideration should be given to path tracing analysis including singularity. In the analysis of pure mechanisms, it has been shown that it is necessary to consider the second-order or higher-order derivative of $\mathbf{f}(\mathbf{x})$ with respect to $\mathbf{x}$ at the singular point for tracing the path satisfying the nonlinear compatibility conditions [81–83]. Besides, in the analysis of equilibrium path, the bifurcation or the snap-through may occur at the singular point, and various studies exist based on the general theory of elastic stability [84]. For rigid origami, Gillman *et al.* [85] proposed a method for the analysis of equilibrium paths including bifurcation and limit points.

Many studies have been done for the pure mechanism analysis and the equilibrium path analysis including singular points as mentioned above, however, there are few studies on the method for investigating the equilibrium path of a rigid origami with strictly rigid faces; i.e. the hybrid analysis of the pure mechanism and the structural analysis. This type of analysis is also important to understand the foldability [55] of a crease pattern and for the prototyping of the deployable structure using a rigid-fold mechanism. The study on the equilibrium of a rotational hinge model is provided by He and Guest [33]. However, the physical interpretation of the loads and the internal forces considered in their study is difficult to grasp intuitively since they are torques applied at crease lines. On the other hand, an exact rigid-folding path reflecting the equilibrium obtained by using the truss model has been studied by Li [86], although the equilibrium condition is not strictly satisfied.

In this chapter, the frame model described in Chapter 2 and shown in Fig. 5.1 is utilized to perform an equilibrium path analysis and a stability analysis of an equilibrium state of a rigid origami. An equilibrium state is considered between a nodal load and moments of springs introduced at the hinges of a frame model as in most equilibrium path analyses

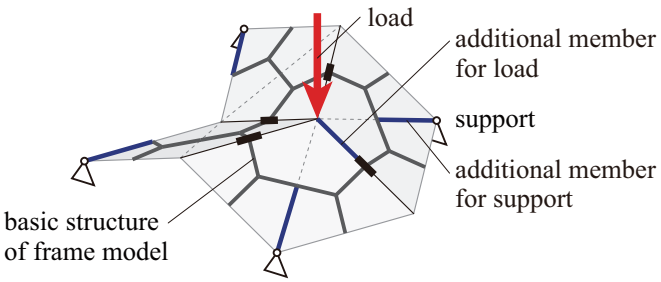

Figure 5.1: Configuration of a frame model for the equilibrium path analysis.

using truss models. To incorporate a nodal load and a support constraining the displacement of a rigid origami, the members indicated by blue bold lines in Fig. 5.1 are added to the basic structure of the frame model whose members are indicated by gray bold lines in Fig. 5.1. One end of each additional member is rigidly connected to the basic structure, while the other end is loaded or supported. In this study, an energy minimization approach is adopted to the equilibrium analysis, and the total potential energy minimization problem is solved under the compatibility conditions of the displacement to obtain an equilibrium path with the exact rigid-folding motion. The proposed method in this chapter has the following features [31].

- The springs are introduced at the hinges of a frame model to stabilize the equilibrium and to determine the deformation path uniquely except for the possible existence of singular points. This enables us to avoid the difficulty of determining the direction of the path exploration in tracing a deformation path caused by the possible existence of many multiple bifurcation points [87, 88] on the deformation path which may exist if the rotation stiffnesses of the hinges are not incorporated.

- The process of directly solving the equilibrium equations with the compatibility equations often fails to converge due to its nonlinearity. Therefore, the equilibrium state is obtained by minimizing the total potential energy to use the stability theories based on the energy principle and to obtain the equilibrium state by utilizing sophisticated optimization techniques.

- The total potential energy minimization problem under the compatibility conditions of the displacement is solved by the augmented Lagrangian method [89, 90], which often has better convergence than the conventional Lagrangian and penalty methods.

- Positive definiteness of the Hessian matrix of the augmented Lagrangian is evaluated to determine the stability of the equilibrium state of a rigid origami.

- The eigenvector of the Hessian matrix of the augmented Lagrangian corresponding to a zero eigenvalue can be regarded as the unstable displacement mode, and it is numerically compared to the infinitesimal mechanism of a frame model to investigate the relationship between the eigenvector and the first-order and second-order infinitesimal mechanism.

The structure of this chapter is as follows. A brief review is provided in Section 5.2 about the formulations of the compatibility equations of a frame model presented in Chapter 2. Section 5.3 presents the definition of the total potential energy to be minimized and the method of equilibrium path analysis of a rigid origami using the frame model. The compatibility equations formulated in Chapter 2, which guarantees the rigid-folding motion, are used as equality constraints for the minimization problem of the total potential energy. An equilibrium path analysis is carried out by the incremental loading analysis where a load factor increases from zero to a finite value. In Section 5.4, a method is presented for investigating the stability of an equilibrium state by using the Hessian matrix of the augmented Lagrangian. Section 5.5 provides a method for numerically investigating the relationship between the first-order and second-order infinitesimal mechanism and the eigenvector of the Hessian matrix of the augmented Lagrangian corresponding to a zero eigenvalue which can be regarded as the unstable displacement mode. Examples of equilibrium path and stability analyses using the proposed method are shown in Section 5.6. It is confirmed that the proposed method can accurately detect the singularity phenomenon by the analysis of a two-dimensional two-member model which can analytically determine the singularity on the equilibrium path. The analysis of a rigid origami is performed for a unit cell of waterbomb tessellation which has a single inner vertex and multiple degrees of freedom of rigid-folding mechanism. A unit cell of waterbomb tessellation is referred to as the *waterbomb cell*, and there are some examples of the deformation path analyses including a bifurcation and a limit point; e.g., Gillman *et al.* [85]. A fully developed flat state that is a singular point on the deformation path of a rigid origami as pointed out in Ref. [91] is especially investigated, and it is shown that the degrees of freedom of the mechanism decreases when the out-of-plane deformation occurs. Although a waterbomb cell has often been studied, the stability of a flat state and a bifurcation path from the flat state have not been investigated well. In this study, the stabilities and the equilibrium paths of the flat states with two types of boundary and load conditions are investigated. Note again that the springs at the hinges of a frame model enable us to uniquely determine the equilibrium path although the waterbomb cell has the multiple degrees of freedom mechanism. By assigning the initial imperfection in addition to the rotational springs, the multiple bifurcation at the flat state, which is investigated in Ref. [92], can be avoided. In Section 5.7, the conclusions of this chapter are given. Methods and examples to be described in this chapter is based on Ref. [31].

5.2 Preliminaries on compatibility equations of frame model

In this section, a brief review of the formulations of the compatibility equations of a frame model presented in Chapter 2 is provided. Let N_{N}, N_{M}, and N_{H} denote the number of nodes, members, and hinges, respectively. The vectors $\mathbf{U}_k$, $\boldsymbol{\Theta}_k$, $\mathbf{V}_i$, and $\boldsymbol{\Psi}_i \in \mathbb{R}^3$ are defined as the translation and rotation vectors of node k $(= 1,\ldots,N_{\mathrm{N}})$ and member i $(= 1,\ldots,N_{\mathrm{M}})$, respectively. The increment of the rotation angle of hinge h $(= 1,\ldots,N_{\mathrm{H}})$ from the unde-

formed state to the deformed state is denoted by $\varphi_h \in \mathbb{R}$. According to Eqs. (2.28) and (2.36) in Chapter 2, when the j-th end ($j = 1, 2$) of member i is connected to node k, the compatibility equation for the translational displacement at the j-th end of member i is written as follows:

$$\Delta\mathbf{U}_{ij} = \mathbf{U}_k - \mathbf{V}_i - \{\mathbf{R}(\mathbf{\Psi}_i) - \mathbf{I}_3\}\mathbf{d}_{ij} = \mathbf{0} \tag{5.1}$$

where $\mathbf{R}(\mathbf{\Psi}_i) \in \mathbb{R}^{3\times3}$ and $\mathbf{d}_{ij} \in \mathbb{R}^3$ are the Rodrigues' rotation matrix with respect to $\mathbf{\Psi}_i$ [64] and the vector directing from the center point of member i to the j-th end of member i at the undeformed state, respectively. $\Delta\mathbf{U}_{ij} \in \mathbb{R}^3$ is the translational incompatibility vector at the j-th end of member i. According to Eqs. (2.29) and (2.37) in Chapter 2, the compatibility equation for the rotational displacement at the j-th end of member i is written as the following equation when the j-th end of member i is rigidly connected to node k:

$$\Delta\mathbf{\Theta}_{ij} = \mathbf{\Theta}_k - \mathbf{\Psi}_i = \mathbf{0} \tag{5.2}$$

where $\Delta\mathbf{\Theta}_{ij} \in \mathbb{R}^3$ is the rotational incompatibility vector at the j-th end of member i. On the other hand, when the j-th end of member i is connected to node k via hinge h, the compatibility equation for the rotational displacement at the j-th end of member i is written as

$$\Delta\mathbf{\Theta}_{ij} = \mathbf{\Phi}_{ij}(\mathbf{\Psi}_i, \mathbf{\Theta}_k, \varphi_h) = \mathbf{0} \tag{5.3}$$

where $\mathbf{\Phi}_{ij}(\mathbf{\Psi}_i, \mathbf{\Theta}_k, \varphi_h) \in \mathbb{R}^3$ is defined by Eqs. (2.34) and (2.35) in Chapter 2 as follows:

$$\begin{aligned}
\mathbf{\Phi}_{ij}(\mathbf{\Psi}_i, \mathbf{\Theta}_k, \varphi_h) &= \begin{pmatrix} \Phi_{ij}^{(1)}(\mathbf{\Psi}_i, \mathbf{\Theta}_k, \varphi_h) \\ \Phi_{ij}^{(2)}(\mathbf{\Psi}_i, \mathbf{\Theta}_k, \varphi_h) \\ \Phi_{ij}^{(3)}(\mathbf{\Psi}_i, \mathbf{\Theta}_k, \varphi_h) \end{pmatrix} \\
\Phi_{ij}^{(1)}(\mathbf{\Psi}_i, \mathbf{\Theta}_k, \varphi_h) &= \left(\mathbf{R}(\mathbf{\Psi}_i)\boldsymbol{\tau}_h^{\langle1\rangle}\right) \cdot \left(\mathbf{R}(\mathbf{\Theta}_k)\boldsymbol{\tau}_h^{\langle2\rangle}\right) \\
\Phi_{ij}^{(2)}(\mathbf{\Psi}_i, \mathbf{\Theta}_k, \varphi_h) &= \left(\mathbf{R}(\mathbf{\Psi}_i)\boldsymbol{\tau}_h^{\langle1\rangle}\right) \cdot \left(\mathbf{R}(\mathbf{\Theta}_k)\boldsymbol{\tau}_h^{\langle3\rangle}\right) \\
\Phi_{ij}^{(3)}(\mathbf{\Psi}_i, \mathbf{\Theta}_k, \varphi_h) &= \left(\mathbf{R}(\mathbf{\Psi}_i)\boldsymbol{\tau}_h^{\langle2\rangle}\right) \cdot \left\{\sin\varphi_h \left(\mathbf{R}(\mathbf{\Theta}_k)\boldsymbol{\tau}_h^{\langle2\rangle}\right) + \cos\varphi_h \left(\mathbf{R}(\mathbf{\Theta}_k)\boldsymbol{\tau}_h^{\langle3\rangle}\right)\right\}
\end{aligned} \tag{5.4}$$

Here, $\boldsymbol{\tau}_h^{\langle l\rangle} \in \mathbb{R}^3$ ($l = 1,2,3$) are the unit vectors representing a reference frame of hinge h ($= 1,\ldots,N_\mathrm{H}$) in the initial state.

The unconstrained components of $\mathbf{U}_k$ and $\mathbf{\Theta}_k$ for all nodes, the components of $\mathbf{V}_i$ and $\mathbf{\Psi}_i$ for all members, and φ_h for all hinges are assembled into vectors $\mathbf{U} \in \mathbb{R}^{6N_\mathrm{N}-N_\mathrm{B}}$, $\mathbf{V} \in \mathbb{R}^{6N_\mathrm{M}}$, and $\boldsymbol{\varphi} \in \mathbb{R}^{N_\mathrm{H}}$, respectively. These vectors are combined into a generalized displacement vector $\mathbf{W} \in \mathbb{R}^{N_\mathrm{W}}$ defined as $\mathbf{W} = (\mathbf{U}^\mathsf{T}, \mathbf{V}^\mathsf{T}, \boldsymbol{\varphi}^\mathsf{T})^\mathsf{T}$ whose number of components is calculated as $N_\mathrm{W} = 6N_\mathrm{N} - N_\mathrm{B} + 6N_\mathrm{M} + N_\mathrm{H}$. The translational and rotational incompatibility vectors $\Delta\mathbf{U}_{ij}$ and $\Delta\mathbf{\Theta}_{ij}$ in Eqs. (5.1), (5.2), and (5.3) for all the member ends are combined into an incompatibility vector $\mathbf{G}(\mathbf{W}) \in \mathbb{R}^{N_\mathrm{G}}$ which is regarded as the nonlinear function of $\mathbf{W}$ and whose number of components is $N_\mathrm{G} = 12N_\mathrm{M}$. Then the compatibility equations are represented in a vector form as follows:

$$\mathbf{G}(\mathbf{W}) = \mathbf{0} \tag{5.5}$$

Note that Eq. (5.5) is the same as Eq. (2.38) in Chapter 2.

5.3 Energy minimization for equilibrium path analysis

This section presents an energy minimization problem and a method to solve it for the analysis of the equilibrium path and stability of the equilibrium state. The analysis is carried out in the case where nodal loads are applied to a frame model with rotational springs introduced at the hinges. The members of a frame model are assumed to be rigid, and the total potential energy of a frame model is considered with respect to the strain energy of the springs and the work by the nodal loads. The variables of the energy minimization problem are the generalized displacements defined in Chapter 2 and Section 5.2. A load factor is denoted by Λ, and the pair $(\mathbf{W}, \Lambda)$ is referred to as the *equilibrium point* when the generalized displacement vector $\mathbf{W}$ minimizes the total potential energy. An *equilibrium path* is defined as a curve in the space of the load factor and the generalized displacements which is the trajectory drawn by the equilibrium points. In the following, the total potential energy is regarded to be zero at $\mathbf{W} = \mathbf{0}$ while the initial displacement for the equilibrium analysis is assigned as $\mathbf{W} = \mathbf{W}_0 = (\mathbf{U}_0^\mathsf{T}, \mathbf{V}_0^\mathsf{T}, \boldsymbol{\varphi}_0^\mathsf{T})^\mathsf{T}$; i.e., the initial displacement vector for the analysis is not necessarily equal to zero. This initial displacement is intended to assign the initial imperfection to avoid the multiple bifurcation at the flat state.

5.3.1 Formulation of energy minimization problem

Let $\Lambda\mathbf{P}_\mathrm{U} \in \mathbb{R}^{6N_\mathrm{N}-N_\mathrm{B}}$ denote the nodal load vector applied to the unconstrained degrees of freedom of the nodal displacement where $\mathbf{P}_\mathrm{U} \in \mathbb{R}^{6N_\mathrm{N}-N_\mathrm{B}}$ is a constant vector. In this study, the increments of the rotation angles of the hinges, which are assembled into $\boldsymbol{\varphi}$, may be different from the rotation angles of the springs, and the assemblage of the residual rotation angles of the springs at the initial state $\mathbf{W} = \mathbf{W}_0$ is represented by $\tilde{\boldsymbol{\varphi}} \in \mathbb{R}^{N_\mathrm{H}}$. Therefore, the rotation angles of the springs at $\mathbf{W}$ can be denoted by $\boldsymbol{\varphi} - \tilde{\boldsymbol{\varphi}}$. If they are set to zero at the initial state $\mathbf{W} = \mathbf{W}_0$, $\tilde{\boldsymbol{\varphi}}$ is assigned as $\tilde{\boldsymbol{\varphi}} = \boldsymbol{\varphi}_0$. Here, $\mathbf{K}_\mathrm{H} \in \mathbb{R}^{N_\mathrm{H}\times N_\mathrm{H}}$ is defined as the diagonal matrix whose (h,h) component is the rotational stiffness K_h of the spring at hinge h $(= 1,\ldots,N_\mathrm{H})$. In a similar manner as Eq. (3.59) in Chapter 3, the total potential energy with the constant load factor Λ is defined as $\Pi_\Lambda^\varphi(\boldsymbol{\varphi}, \mathbf{U})$ which is the function of $\boldsymbol{\varphi}$ and $\mathbf{U}$ as follows:

$$\Pi_\Lambda^\varphi(\boldsymbol{\varphi}, \mathbf{U}) = \frac{1}{2}(\boldsymbol{\varphi} - \tilde{\boldsymbol{\varphi}})^\mathsf{T}\mathbf{K}_\mathrm{H}(\boldsymbol{\varphi} - \tilde{\boldsymbol{\varphi}}) - \mathbf{U}^\mathsf{T}(\Lambda\mathbf{P}_\mathrm{U}) \tag{5.6}$$

To write the total potential energy as the function of a generalized displacement vector $\mathbf{W}$, the following constant vectors and matrix are defined:

$$\tilde{\mathbf{W}} = \begin{pmatrix} \mathbf{0}_{N_\mathrm{D}-N_\mathrm{H}} \\ \tilde{\boldsymbol{\varphi}} \end{pmatrix} \in \mathbb{R}^{N_\mathrm{W}}$$

$$\mathbf{P} = \begin{pmatrix} \mathbf{P}_\mathrm{U} \\ \mathbf{0}_{6N_\mathrm{M}+N_\mathrm{H}} \end{pmatrix} \in \mathbb{R}^{N_\mathrm{W}}$$

$$\mathbf{K} = \begin{bmatrix} \mathbf{O}_{(N_\mathrm{W}-N_\mathrm{H})\times(N_\mathrm{W}-N_\mathrm{H})} & \mathbf{O}_{(N_\mathrm{W}-N_\mathrm{H})\times N_\mathrm{H}} \\ \mathbf{O}_{N_\mathrm{H}\times(N_\mathrm{W}-N_\mathrm{H})} & \mathbf{K}_\mathrm{H} \end{bmatrix} \in \mathbb{R}^{N_\mathrm{W}\times N_\mathrm{W}}$$

Then, incorporating $\mathbf{W} = (\mathbf{U}^\mathsf{T}, \mathbf{V}^\mathsf{T}, \boldsymbol{\varphi}^\mathsf{T})^\mathsf{T}$, the total potential energy can be reformulated as the function of the generalized displacement vector $\mathbf{W}$ as follows:

$$\Pi_\Lambda(\mathbf{W}) = \frac{1}{2}\left(\mathbf{W} - \tilde{\mathbf{W}}\right)^\mathsf{T} \mathbf{K}\left(\mathbf{W} - \tilde{\mathbf{W}}\right) - \mathbf{W}^\mathsf{T}(\Lambda \mathbf{P}) \tag{5.7}$$

When the load factor Λ is constant, the equilibrium point is determined as the stationary point of the total potential energy $\Pi_\Lambda(\mathbf{W})$ with respect to the generalized displacement $\mathbf{W}$. Therefore, the equilibrium state which obeys the exact rigid-folding motion under the constant nodal load $\Lambda \mathbf{P}_\mathrm{U}$ is obtained as the solution (stationary point) of the following optimization problem whose variables are the components of $\mathbf{W}$:

$$\begin{cases} \min\limits_{\mathbf{W}} & \Pi_\Lambda(\mathbf{W}) \\ \text{s.t.} & \mathbf{G}(\mathbf{W}) = \mathbf{0} \end{cases} \tag{5.8}$$

In this study, general contact between nodes and members is neglected, however, it is confirmed that no contact occurs along the equilibrium path of the examples shown in Section 5.6.

5.3.2 Augmented Lagrangian method

First, the stationary conditions of Problem (5.8) are formulated with respect to the conventional Lagrangian. The (conventional) Lagrangian of Problem (5.8) is defined with the Lagrange multiplier $\boldsymbol{\lambda} \in \mathbb{R}^{N_\mathrm{G}}$ as

$$L(\mathbf{W}, \boldsymbol{\lambda}) = \Pi_\Lambda(\mathbf{W}) + \mathbf{G}(\mathbf{W})^\mathsf{T} \boldsymbol{\lambda} \tag{5.9}$$

As in the similar manner to Chapter 2, the compatibility matrix is defined as the function of $\mathbf{W}$ and denoted by $\boldsymbol{\Gamma}^{(1)}(\mathbf{W}) \in \mathbb{R}^{N_\mathrm{G} \times N_\mathrm{W}}$ whose (i,j) component is $\partial G_i(\mathbf{W})/\partial W_j$ where $G_i(\mathbf{W})$ and W_j are the i-th component of $\mathbf{G}(\mathbf{W})$ and the j-th component of $\mathbf{W}$, respectively. Then, the gradient of the Lagrangian $L(\mathbf{W}, \boldsymbol{\lambda})$ with respect to $\mathbf{W}$ is written as follows:

$$\begin{aligned} \frac{\partial L(\mathbf{W}, \boldsymbol{\lambda})}{\partial \mathbf{W}} &= \frac{d\Pi_\Lambda(\mathbf{W})}{d\mathbf{W}} + \boldsymbol{\Gamma}^{(1)}(\mathbf{W})^\mathsf{T} \boldsymbol{\lambda} \\ &= \mathbf{K}\left(\mathbf{W} - \tilde{\mathbf{W}}\right) - \Lambda \mathbf{P} + \boldsymbol{\Gamma}^{(1)}(\mathbf{W})^\mathsf{T} \boldsymbol{\lambda} \end{aligned} \tag{5.10}$$

The detailed calculation of $\boldsymbol{\Gamma}^{(1)}(\mathbf{W})$ is shown in Appendix D. When $\mathbf{W}^*$ and $\boldsymbol{\lambda}^*$ are the solution and the corresponding Lagrange multiplier of Problem (5.8), respectively, they satisfy the following stationary conditions:

$$\frac{\partial L(\mathbf{W}^*, \boldsymbol{\lambda}^*)}{\partial \mathbf{W}} = \mathbf{K}\left(\mathbf{W}^* - \tilde{\mathbf{W}}\right) - \Lambda \mathbf{P} + \boldsymbol{\Gamma}^{(1)}(\mathbf{W}^*)^\mathsf{T} \boldsymbol{\lambda}^* = \mathbf{0} \tag{5.11}$$

$$\frac{\partial L(\mathbf{W}^*, \boldsymbol{\lambda}^*)}{\partial \boldsymbol{\lambda}} = \mathbf{G}(\mathbf{W}^*) = \mathbf{0} \tag{5.12}$$

Next, the process of solving the optimization problem (5.8) by the augmented Lagrangian method (ALM) [89, 90] is presented. Let $c_\mathrm{p} \in \mathbb{R}$ denote the positive penalty parameter, and the augmented Lagrangian $L_c(\mathbf{W})$ is defined as follows:

$$\begin{aligned} L_c(\mathbf{W}) &= \Pi_\Lambda(\mathbf{W}) + \mathbf{G}(\mathbf{W})^\mathsf{T} \boldsymbol{\lambda} + \frac{c_\mathrm{p}}{2} \mathbf{G}(\mathbf{W})^\mathsf{T} \mathbf{G}(\mathbf{W}) \\ &= \frac{1}{2}\left(\mathbf{W} - \tilde{\mathbf{W}}\right)^\mathsf{T} \mathbf{K}\left(\mathbf{W} - \tilde{\mathbf{W}}\right) - \mathbf{W}^\mathsf{T}(\Lambda \mathbf{P}) + \mathbf{G}(\mathbf{W})^\mathsf{T}\left(\boldsymbol{\lambda} + \frac{c_\mathrm{p}}{2} \mathbf{G}(\mathbf{W})\right) \end{aligned} \tag{5.13}$$

In the ALM, the Lagrange multiplier $\boldsymbol{\lambda}$ is regarded to be constant, and the augmented Lagrangian $L_c(\mathbf{W})$ is the function of only $\mathbf{W}$. The augmented Lagrangian $L_c(\mathbf{W})$ has an additional penalty term $(c_\mathrm{p}/2)\mathbf{G}(\mathbf{W})^\mathsf{T}\mathbf{G}(\mathbf{W})$ compared to the conventional Lagrangian $L(\mathbf{W},\boldsymbol{\lambda})$ defined as Eq. (5.9). This penalty term contributes to the convergence of the method. According to Eq. (5.13), the gradient of $L_c(\mathbf{W})$ with respect to $\mathbf{W}$ can be calculated as follows:

$$\frac{dL_c(\mathbf{W})}{d\mathbf{W}} = \mathbf{K}\left(\mathbf{W}-\tilde{\mathbf{W}}\right) - \Lambda\mathbf{P} + \boldsymbol{\Gamma}^{(1)}(\mathbf{W})^\mathsf{T}\left(\boldsymbol{\lambda} + c_\mathrm{p}\mathbf{G}(\mathbf{W})\right) \tag{5.14}$$

Therefore, $\mathbf{W}^*$ and $\boldsymbol{\lambda}^*$ satisfying Eqs. (5.11) and (5.12), which are the solution and the corresponding Lagrange multiplier of Problem (5.8), respectively, satisfy the following equation:

$$\frac{dL_c(\mathbf{W}^*)}{d\mathbf{W}} = \mathbf{K}\left(\mathbf{W}^*-\tilde{\mathbf{W}}\right) - \Lambda\mathbf{P} + \boldsymbol{\Gamma}^{(1)}(\mathbf{W}^*)^\mathsf{T}\left(\boldsymbol{\lambda}^* + c_\mathrm{p}\mathbf{G}(\mathbf{W}^*)\right) = \mathbf{0} \tag{5.15}$$

Hence, $\mathbf{W}^*$ is the solution to the following optimization problem with the Lagrange multiplier $\boldsymbol{\lambda}^*$ which corresponds to a solution of Problem (5.8):

$$\min_{\mathbf{W}} \quad L_c(\mathbf{W}) \tag{5.16}$$

Conversely, if $\bar{\mathbf{W}}$ is the solution of Problem (5.16) and satisfies the compatibility equation (5.5), it satisfies both the stationary condition of Problem (5.16) represented by Eq. (5.15) and the stationary conditions of Problem (5.8) represented by Eqs. (5.11) and (5.12) where $\boldsymbol{\lambda}^*$ is the Lagrange multiplier corresponding to a solution of Problem (5.8). Therefore, $\bar{\mathbf{W}}$ is also the solution of Problem (5.8), and the equilibrium point can be obtained by solving the optimization problem (5.16) and checking that the solution satisfies the compatibility equations instead of solving the optimization problem (5.8) directly. Note that the load factor Λ is given and constant in the process of obtaining an equilibrium point by the ALM.

Although the appropriate Lagrange multiplier $\boldsymbol{\lambda}^*$ corresponding to the solution to Problem (5.8) is unknown, it can be estimated by solving problem (5.16) successively while updating $\boldsymbol{\lambda}$ as follows [89, 90]:

$$\boldsymbol{\lambda} \leftarrow \boldsymbol{\lambda} + c_\mathrm{p}\mathbf{G}(\bar{\mathbf{W}})$$

The magnitude of the penalty parameter c_p affects the convergence of the above update process, and it is preferable to be adjusted automatically in the process of the ALM. In this study, c_p is updated by the following method proposed by Birgin and Martínez [90]. In the k-th iteration of the process of the augmented Lagrangian method, the values of the generalized displacement $\mathbf{W}$, the Lagrange multiplier $\boldsymbol{\lambda}$, and the penalty parameter c_p are denoted by $\mathbf{W}^{(k)}$, $\boldsymbol{\lambda}^{(k)}$, and $c_\mathrm{p}^{(k)}$, respectively. The function $C(\mathbf{W}^{(k)})$ is defined as

$$C(\mathbf{W}^{(k)}) = \frac{1}{2}\mathbf{G}(\mathbf{W}^{(k)})^\mathsf{T}\mathbf{G}(\mathbf{W}^{(k)})$$

In addition, the binary function $O(\mathbf{W}^{(k)},\boldsymbol{\lambda}^{(k)})$ that indicates convergence of the optimization problem (5.16) with sufficient small error in Eq. (5.15) is defined as

$$O(\mathbf{W}^{(k)},\boldsymbol{\lambda}^{(k)}) = \begin{cases} 1 & \text{(Optimization process is converged)} \\ 0 & \text{(Otherwise)} \end{cases}$$

Algorithm 5.1 Augmented Lagrangian method

Input: $\mathbf{W}^{(0)}, \boldsymbol{\lambda}^{(1)}, \epsilon_{\text{tol}} > 0, \bar{c}_{\text{p}} > 0, 0 < c_{\min} < c_{\max}, \gamma > 1, 0 \le \alpha \le 1$

Output: $\mathbf{W}^* = \mathbf{W}^{(k)}$, $\boldsymbol{\lambda}^* = \boldsymbol{\lambda}^{(k)}$

$k \leftarrow 1$, $\beta_k \leftarrow 0$,
$c_{\text{p}}^{(k)} \leftarrow \min\left\{\max\left\{c_{\min}, \bar{c}_{\text{p}} \frac{\max\{1, \Pi(\mathbf{W}^{(0)})\}}{\max\{1, C(\mathbf{W}^{(0)})\}}\right\}, c_{\max}\right\}$
while $O(\mathbf{W}^{(k)}, \boldsymbol{\lambda}^{(k)}) = 0$ and $\max_i |G_i(\mathbf{W}^{(k)})| > \epsilon_{\text{tol}}$ **do**
  Solve Problem(5.16) with $\boldsymbol{\lambda} = \boldsymbol{\lambda}^{(k)}$, and let the solution be $\mathbf{W}^{(k)}$.
  $\boldsymbol{\lambda}^{(k+1)} \leftarrow \boldsymbol{\lambda}^{(k)} + c_{\text{p}}^{(k)} \mathbf{G}(\mathbf{W}^{(k)})$
  if $k = 1$ **then**
    $\beta_{k+1} \leftarrow \beta_k$,
    $c_{\text{p}}(k+1) \leftarrow \min\left\{\max\left\{c_{\min}, \bar{c}_{\text{p}} \frac{\max\{1, \Pi(\mathbf{W}^{(k)})\}}{\max\{1, C(\mathbf{W}^{(k)})\}}\right\}, c_{\max}\right\}$
  else if $\max_i |G_i(\mathbf{W}^{(k)})| \le \epsilon_{\text{tol}}$ **then**
    if $k \ge 3$ and $\max_i |G_i(\mathbf{W}^{(k)})| \le \epsilon_{\text{tol}}$ and $O(\mathbf{W}^{(k-1)}, \boldsymbol{\lambda}^{(k-1)}) = O(\mathbf{W}^{(k)}, \boldsymbol{\lambda}^{(k)}) = 0$ **then**
      $\beta_{k+1} \leftarrow \beta_k + 1$,
      $c_a \leftarrow \min\{\gamma^{\beta_k} c_{\min}, 1\}$, $c_b \leftarrow \max\{\gamma^{-\beta_k} c_{\max}, 1\}$,
      $c_{\text{p}}^{(k+1)} \leftarrow \min\left\{\max\left\{c_a, \bar{c}_{\text{p}} \frac{\max\{1, \Pi(\mathbf{W}^{(k)})\}}{\max\{1, C(\mathbf{W}^{(k)})\}}\right\}, c_b, c_{\text{p}}^{(k)}\right\}$
    else
      $\beta_{k+1} \leftarrow \beta_k$, $c_{\text{p}}^{(k+1)} \leftarrow c_{\text{p}}^{(k)}$
    end if
  else
    $\beta_{k+1} \leftarrow \beta_k$
    if $\|\mathbf{G}(\mathbf{W}^{(k)})\| \le \alpha \|\mathbf{G}(\mathbf{W}^{(k-1)})\|$ **then**
      $c_{\text{p}}^{(k+1)} \leftarrow c_{\text{p}}^{(k)}$
    else
      $c_{\text{p}}^{(k+1)} = \max\{\gamma c_{\text{p}}^{(k)}, \gamma^{\beta_k} c_{\min}\}$
    end if
  end if
  $k \leftarrow k + 1$
end while

The update process of the Lagrange multiplier $\boldsymbol{\lambda}$ and the penalty parameter c_{p} is repeated until the maximum absolute value among the components of the incompatibility vector $\mathbf{G}(\mathbf{W})$ is less than or equal to the tolerance $\epsilon_{\text{tol}} > 0$. The process of obtaining the solution $\mathbf{W}^*$ and the corresponding Lagrange multiplier $\boldsymbol{\lambda}^*$ of Problem (5.8) using the ALM is presented in Algorithm 5.1. As stated in Ref. [93], there is some flexibility in the choice of the initial value of $\boldsymbol{\lambda}$ since the ALM has good global convergence property and robustness under the degenerate constraints.

5.3.3 Equilibrium path tracing by the incremental loading analysis

The equilibrium path is traced by iteratively obtaining the equilibrium points by solving Problem (5.8) while updating the load factor as $\Lambda \leftarrow \Lambda + d\Lambda$ ($d\Lambda > 0$), i.e., the equilibrium path is traced by the incremental loading analysis. The initial value of the load factor increment is denoted by $d\Lambda_0$, and if the ALM does not terminate with the sufficient accuracy, $d\Lambda$ decreases to find an equilibrium point. Defining a and b ($0 < a < 1, b > 1$) as the user-specified update ratios of the load factor increment, $d\Lambda$ is updated as $d\Lambda \leftarrow \max\{b(d\Lambda), d\Lambda_0\}$, if the ALM terminates successfully; otherwise, $d\Lambda$ is reduced as $d\Lambda \leftarrow a(d\Lambda)$. The equilibrium path analysis starts from $\Lambda = 0$ and continues until one of the following termination conditions is satisfied:

- The specified component W_i of $\mathbf{W}$ reaches the target value $W_i^{\max}$ or $W_i^{\min}$ ($W_i^{\min} < W_i^{\max}$).
- The load factor Λ is greater than the specified maximum value $\Lambda_{\max} > 0$.
- The load factor increment $d\Lambda$ is less than the specified minimum value $d\Lambda_{\min} > 0$.

The first two conditions indicate that the equilibrium path analysis has progressed to the user-specified degree. On the other hand, third condition implies that the equilibrium point cannot be found with a load factor greater than that of the last step. In this study, the constraints for avoiding general contact between nodes and members are not incorporated in Problem (5.8), and therefore, the presence of contact is checked manually after the process presented above is terminated.

5.4 Stability of equilibrium state

In this section, the stability of an equilibrium point is investigated. According to the stability theories based on the energy principle [94], the equilibrium point at a given load factor Λ is stable if the solution to the energy minimization problem (5.8) is an isolated local minimum. Assume that $\bar{\mathbf{W}}$ and $\boldsymbol{\lambda}$ are the local minimum solution of Problem (5.16) and the corresponding Lagrange multiplier, respectively, with a given load factor Λ, and $\mathbf{G}(\bar{\mathbf{W}}) = \mathbf{0}$ is satisfied with the specified tolerance ϵ_{tol}. When a neighborhood of $\bar{\mathbf{W}}$ is represented by $\bar{\mathbf{W}} + \delta\bar{\mathbf{W}}$ ($\delta\bar{\mathbf{W}} \in \mathbb{R}^{N_{\text{W}}}$), the inequality $L_c(\bar{\mathbf{W}}) < L_c(\bar{\mathbf{W}} + \delta\bar{\mathbf{W}})$ holds for any $\delta\bar{\mathbf{W}}$. Furthermore, if a neighborhood is restricted to the range satisfying $\mathbf{G}(\bar{\mathbf{W}} + \delta\bar{\mathbf{W}}) = \mathbf{0}$, the equation $\Pi_\Lambda(\bar{\mathbf{W}} + \delta\bar{\mathbf{W}}) = L_c(\bar{\mathbf{W}} + \delta\bar{\mathbf{W}})$ holds for any $\delta\bar{\mathbf{W}}$ from Eq. (5.13). Accordingly, $\Pi_\Lambda(\bar{\mathbf{W}}) < \Pi_\Lambda(\bar{\mathbf{W}} + \delta\bar{\mathbf{W}})$ always holds, and the isolated local minimum solution of Problem (5.16) satisfying the compatibility equation (5.5) is also the isolated local minimum solution of Problem (5.8) [89]; i.e., $(\bar{\mathbf{W}}, \Lambda)$ is a stable equilibrium point. When $\bar{\mathbf{W}}$ satisfies $\mathbf{G}(\bar{\mathbf{W}}) = \mathbf{0}$, it is an isolated local minimum solution of Problem (5.16), if and only if the stationary condition $dL_c(\bar{\mathbf{W}})/d\mathbf{W} = \mathbf{0}$ is satisfied and the Hessian matrix of the augmented Lagrangian $d^2L_c(\bar{\mathbf{W}})/d\mathbf{W}^2 \in \mathbb{R}^{N_{\text{W}} \times N_{\text{W}}}$ is positive definite [95]. The Hessian matrix of $L_c(\mathbf{W})$ is a matrix whose (j,k) component is

$\partial^2 L_c(\mathbf{W})/\partial W_j \partial W_k$ and can be written as follows if $\mathbf{G}(\mathbf{W}) = \mathbf{0}$ is satisfied:

$$\frac{d^2 L_c(\mathbf{W})}{d\mathbf{W}^2} = \mathbf{K} + \boldsymbol{\lambda}^\top \boldsymbol{\Gamma}^{(2)}(\mathbf{W}) + c_\mathrm{p} \boldsymbol{\Gamma}^{(1)}(\mathbf{W})^\top \boldsymbol{\Gamma}^{(1)}(\mathbf{W}) \tag{5.17}$$

Here, $\boldsymbol{\Gamma}^{(2)}(\mathbf{W})$ is the order-three tensor of size $N_\mathrm{G} \times N_\mathrm{W} \times N_\mathrm{W}$ whose (i,j,k) component is $\partial^2 G_i(\mathbf{W})/\partial W_j \partial W_k$, and the second term in the right-hand side of Eq. (5.17) is calculated as

$$\boldsymbol{\lambda}^\top \boldsymbol{\Gamma}^{(2)}(\mathbf{W}) = \sum_{i=1}^{N_\mathrm{G}} \lambda_i \frac{d^2 G_i(\mathbf{W})}{d\mathbf{W}^2} = \sum_{i=1}^{N_\mathrm{G}} \lambda_i \begin{bmatrix} \dfrac{\partial^2 G_i(\mathbf{W})}{\partial W_1 \partial W_1} & \cdots & \dfrac{\partial^2 G_i(\mathbf{W})}{\partial W_1 \partial W_{N_\mathrm{W}}} \\ \vdots & \ddots & \vdots \\ \dfrac{\partial^2 G_i(\mathbf{W})}{\partial W_{N_\mathrm{W}} \partial W_1} & \cdots & \dfrac{\partial^2 G_i(\mathbf{W})}{\partial W_{N_\mathrm{W}} \partial W_{N_\mathrm{W}}} \end{bmatrix} \tag{5.18}$$

From the above, relationship between the stability of an equilibrium point and the augmented Lagrangian can be summarized as follows:

Property 5.1. The equilibrium point $(\bar{\mathbf{W}}, \Lambda)$ is stable for a given load factor Λ, if the solution $\bar{\mathbf{W}}$ of Problem (5.16) satisfies the compatibility equation (5.5) and the Hessian matrix $d^2 L_c(\bar{\mathbf{W}})/d\mathbf{W}^2$ is positive definite, where $\boldsymbol{\lambda}$ is the Lagrange multiplier obtained by the ALM. Conversely, if $d^2 L_c(\bar{\mathbf{W}})/d\mathbf{W}^2$ is not positive definite, $(\bar{\mathbf{W}}, \Lambda)$ is an unstable equilibrium point. In particular, if one or more eigenvalues of $d^2 L_c(\bar{\mathbf{W}})/d\mathbf{W}^2$ are equal to zero, the corresponding load factor and the equilibrium point are referred to as the *critical* load factor and the *critical point*, respectively. In addition, the eigenvector corresponding to a zero eigenvalue of $d^2 L_c(\bar{\mathbf{W}})/d\mathbf{W}^2$ is called the *critical eigenmode*. A critical point is a candidate for a bifurcation or limit point.

5.5 Critical eigenmode and infinitesimal mechanism

The relationship between a critical eigenmode and the infinitesimal mechanism of a frame model is investigated. Since it is not straightforward to discover the relationship analytically, it is investigated numerically in this study. Consider a critical point $(\bar{\mathbf{W}}, \Lambda_\mathrm{cr})$ where Λ_cr is a critical load factor. The critical eigenmode corresponding to the critical load factor Λ_cr is denoted by $\mathbf{w}_\mathrm{cr} \in \mathbb{R}^{N_\mathrm{W}}$, which satisfies $\left(d^2 L_c(\bar{\mathbf{W}})/d\mathbf{W}^2\right)\mathbf{w}_\mathrm{cr} = \mathbf{0}$. On the other hand, a first-order infinitesimal mechanism $\mathbf{W}' \in \mathbb{R}^{N_\mathrm{W}}$ and a second-order infinitesimal mechanism $\mathbf{W}'' \in \mathbb{R}^{N_\mathrm{W}}$ at an equilibrium point $(\bar{\mathbf{W}}, \Lambda_\mathrm{cr})$ satisfy following equations [33, 40]:

$$\boldsymbol{\Gamma}^{(1)}(\bar{\mathbf{W}})\mathbf{W}' = \mathbf{0} \tag{5.19}$$

$$\boldsymbol{\Gamma}^{(1)}(\bar{\mathbf{W}})\mathbf{W}'' + \left[\boldsymbol{\Gamma}^{(2)}(\bar{\mathbf{W}})\mathbf{W}'\right]\mathbf{W}' = \mathbf{0} \tag{5.20}$$

In the following, $\boldsymbol{\Gamma}^{(1)}(\bar{\mathbf{W}})$ and $\boldsymbol{\Gamma}^{(2)}(\bar{\mathbf{W}})$ are always evaluated at $\bar{\mathbf{W}}$, and the argument $(\bar{\mathbf{W}})$ is omitted for a simple expression. Here, $\left[\boldsymbol{\Gamma}^{(2)}(\bar{\mathbf{W}})\mathbf{W}'\right]\mathbf{W}'$ is the N_G-dimensional vector whose i-th component is $\mathbf{W}'^\mathsf{T}\left(d^2 G_i/d\mathbf{W}^2\right)\mathbf{W}'$. The degrees of kinematic indeterminacy N_D

and statical indeterminacy N_{S} are equal to $N_{\mathrm{W}} - \mathrm{rank}\left(\mathbf{\Gamma}^{(1)}\right)$ and $N_{\mathrm{G}} - \mathrm{rank}\left(\mathbf{\Gamma}^{(1)}\right)$, respectively [40]. The left and right singular vectors corresponding to the zero singular values of the compatibility matrix $\mathbf{\Gamma}^{(1)}$ are denoted by $\boldsymbol{\upsilon}_1, \ldots, \boldsymbol{\upsilon}_{N_{\mathrm{S}}} \in \mathbb{R}^{N_{\mathrm{G}}}$ and $\boldsymbol{\eta}_1, \ldots, \boldsymbol{\eta}_{N_{\mathrm{D}}} \in \mathbb{R}^{N_{\mathrm{W}}}$, respectively. Note that $\boldsymbol{\upsilon}_1, \ldots, \boldsymbol{\upsilon}_{N_{\mathrm{S}}}$ and $\boldsymbol{\eta}_1, \ldots, \boldsymbol{\eta}_{N_{\mathrm{D}}}$ are referred to as the first-order self-equilibrium modes and the first-order infinitesimal mechanism modes, respectively [33, 40]. In addition, the remaining left and right singular vectors are denoted by $\boldsymbol{\upsilon}_{N_{\mathrm{S}}+1}, \ldots, \boldsymbol{\upsilon}_{N_{\mathrm{G}}} \in \mathbb{R}^{N_{\mathrm{G}}}$ and $\boldsymbol{\eta}_{N_{\mathrm{D}}+1}, \ldots, \boldsymbol{\eta}_{N_{\mathrm{W}}} \in \mathbb{R}^{N_{\mathrm{W}}}$, respectively, which correspond to the positive singular values. Note that $\boldsymbol{\upsilon}_1, \ldots, \boldsymbol{\upsilon}_{N_{\mathrm{G}}}$ and $\boldsymbol{\eta}_1, \ldots, \boldsymbol{\eta}_{N_{\mathrm{W}}}$ are the orthonormal bases of the N_{G}-dimensional vector space and the N_{W}-dimensional vector space, respectively. Then, $\mathbf{w}_{\mathrm{cr}}$ can be represented as the linear combination of $\boldsymbol{\eta}_1, \ldots, \boldsymbol{\eta}_{N_{\mathrm{W}}}$ with the coefficients $\alpha_1^{\mathrm{cr}}, \ldots, \alpha_{N_{\mathrm{W}}}^{\mathrm{cr}} \in \mathbb{R}$ as follows:

$$\mathbf{w}_{\mathrm{cr}} = \alpha_1^{\mathrm{cr}} \boldsymbol{\eta}_1 + \cdots + \alpha_{N_{\mathrm{W}}}^{\mathrm{cr}} \boldsymbol{\eta}_{N_{\mathrm{W}}} \tag{5.21}$$

When $\mathbf{w}_{\mathrm{cr}}$ and $\boldsymbol{\eta}_1, \ldots, \boldsymbol{\eta}_{N_{\mathrm{W}}}$ are given, the coefficients α_i^{cr} $(i = 1, \ldots, N_{\mathrm{W}})$ are determined as

$$\alpha_i^{\mathrm{cr}} = \mathbf{w}_{\mathrm{cr}}^{\mathsf{T}} \boldsymbol{\eta}_i \tag{5.22}$$

According to Eqs. (5.19) and (5.21), $\mathbf{w}_{\mathrm{cr}}$ is the first-order infinitesimal mechanism, if and only if α_i^{cr} is equal to zero for any $i = N_{\mathrm{D}} + 1, \ldots, N_{\mathrm{W}}$; i.e., $\mathbf{w}_{\mathrm{cr}}$ is represented as $\mathbf{w}_{\mathrm{cr}} = \alpha_1^{\mathrm{cr}} \boldsymbol{\eta}_1 + \cdots + \alpha_{N_{\mathrm{D}}}^{\mathrm{cr}} \boldsymbol{\eta}_{N_{\mathrm{D}}}$. Therefore, the value of α_i^{cr} is evaluated in the examples shown in Section 5.6. Considering the numerical error, $\mathbf{w}_{\mathrm{cr}}$ is determined to be the first-order infinitesimal mechanism if the values of $|\alpha_i^{\mathrm{cr}}|$ for $i = N_{\mathrm{D}} + 1, \ldots, N_{\mathrm{W}}$ are sufficiently smaller than those of $|\alpha_i^{\mathrm{cr}}|$ for $i = 1, \ldots, N_{\mathrm{D}}$. As shown in Section 5.6, it can be confirmed that the critical eigenmodes are the first-order infinitesimal mechanism. Furthermore, if $\mathbf{w}_{\mathrm{cr}}$ is the first-order mechanism, the necessary and sufficient condition for existence of the second-order infinitesimal mechanism $\mathbf{W}''$ which satisfies $\mathbf{\Gamma}^{(1)}\mathbf{W}'' + \left[\mathbf{\Gamma}^{(2)}(\bar{\mathbf{W}})\mathbf{W}'\right]\mathbf{W}' = \mathbf{0}$ is that the following equation holds for any $i = 1, \ldots, N_{\mathrm{S}}$ [33, 40]:

$$\boldsymbol{\upsilon}_i^{\mathsf{T}} \left[\mathbf{\Gamma}^{(2)}(\bar{\mathbf{W}})\mathbf{W}'\right]\mathbf{W}' = \mathbf{W}'^{\mathsf{T}} \left[\boldsymbol{\upsilon}_i^{\mathsf{T}} \mathbf{\Gamma}^{(2)}\right]\mathbf{w}_{\mathrm{cr}} = 0 \tag{5.23}$$

Appendix E provides the detailed explanation of this condition. Therefore, the value of $\beta_i^{\mathrm{cr}} \in \mathbb{R}$ which is defined as follows is evaluated for $i = 1, \ldots, N_{\mathrm{S}}$:

$$\beta_i^{\mathrm{cr}} = \boldsymbol{\upsilon}_i^{\mathsf{T}} \left[\mathbf{\Gamma}^{(2)}(\bar{\mathbf{W}})\mathbf{W}'\right]\mathbf{W}' = \mathbf{w}_{\mathrm{cr}}^{\mathsf{T}} \left[\boldsymbol{\upsilon}_i^{\mathsf{T}} \mathbf{\Gamma}^{(2)}\right]\mathbf{w}_{\mathrm{cr}} \tag{5.24}$$

If β_i^{cr} is equal to zero for any $i = 1, \ldots, N_{\mathrm{S}}$, the first-order infinitesimal mechanism $\mathbf{w}_{\mathrm{cr}}$ can be extended to the second-order infinitesimal mechanism. In the similar manner as the evaluation of α_i^{cr}, β_i^{cr} is regarded to be zero if the values of $|\beta_i^{\mathrm{cr}}|$ for $i = 1, \ldots, N_{\mathrm{S}}$ are sufficiently smaller than those of $|\beta_i^{\mathrm{cr}}|$ for $i = N_{\mathrm{S}} + 1, \ldots, N_{\mathrm{G}}$.

5.6 Examples

First, an example of a three-node two-member planar frame, for which an analytical solution can be easily obtained, is presented in Section 5.6.1. Validity of the proposed method is

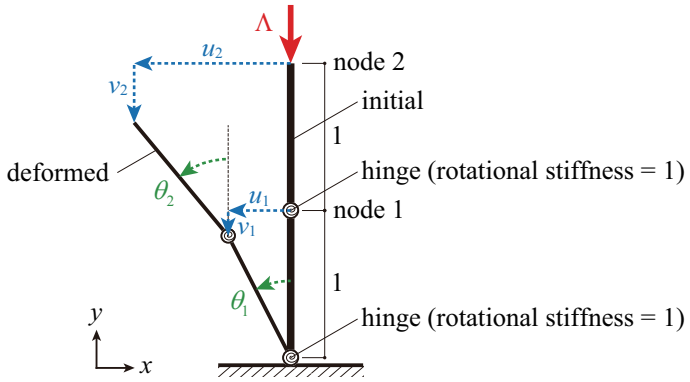

Figure 5.2: Configuration and variables of the planer two bar frame.

verified by comparing the results obtained by the proposed method with the analytical solution. In Sections 5.6.2 and 5.6.3, examples are shown for the analysis of a waterbomb cell, which is a unit of the waterbomb tessellation and has a rigid-foldable crease pattern. Each analysis is carried out by using a Python 3.9 program. The optimization problem (5.16) is solved using an NLP software library L-BFGS-B [96] available in Python library SciPy. The units of length and force are omitted because they do not have an effect on the result. The parameters and the termination conditions of the equilibrium path analysis are specified for each section. Note that the examples described in this chapter are the same as those in Ref. [31].

5.6.1 Planer two bars model

(1) Analytical solution

As shown in Fig. 5.2, consider a three-node two-member planar frame whose length of each member is 1 and each hinge is parallel to the z-axis, i.e., perpendicular to the paper. The rotational stiffness of each spring installed into the hinge is 1. The frame is straight along with y-axis at the initial state, and the translational displacements of node k $(=1,2)$ in x- and y-directions are denoted by u_k and v_k, respectively. Let θ_i denotes the rotation angle of member i $(=1,2)$ which is positive when the member rotates counterclockwise as shown in Fig. 5.2. The load factor is denoted by Λ, and a load of magnitude Λ is applied to node 2 in the negative direction of the y-axis. In this section, only translations of nodes and rotations of members are used to express the compatibility equations for the simple calculation, and the generalized forms of displacement vector and the compatibility equations defined in Section 5.2 are not used for obtaining the analytical solution. Accordingly, the compatibility equations which are to be satisfied by the nodal displacements and the member rotation angles are formulated as follows:

$$u_1 = -\sin\theta_1$$
$$v_1 = \cos\theta_1 - 1$$
$$u_2 = -\sin\theta_1 - \sin\theta_2$$

$$v_2 = \cos\theta_1 + \cos\theta_2 - 2$$

Since the total potential energy of the frame can be written in a polynomial form when θ_1 and θ_2 are treated as the independent variables, the total potential energy $\Pi_\Lambda(\theta_1,\theta_2)$ is formulated as the function of θ_1 and θ_2 as follows:

$$\begin{aligned}\Pi_\Lambda(\theta_1,\theta_2) &= \frac{1}{2}\theta_1^2 + \frac{1}{2}(\theta_2-\theta_1)^2 + \Lambda v_2 \\ &= \frac{1}{2}(2\theta_1^2 + \theta_2^2 - 2\theta_1\theta_2) + \Lambda(\cos\theta_1 + \cos\theta_2 - 2)\end{aligned}$$

The Hessian matrix of $\Pi_\Lambda(\theta_1,\theta_2)$ with respect to θ_1 and θ_2 can be calculated as follows:

$$\begin{bmatrix} \dfrac{\partial^2\Pi_\Lambda}{\partial\theta_1^2} & \dfrac{\partial^2\Pi_\Lambda}{\partial\theta_1\partial\theta_2} \\ \dfrac{\partial^2\Pi_\Lambda}{\partial\theta_1\partial\theta_2} & \dfrac{\partial^2\Pi_\Lambda}{\partial\theta_2^2} \end{bmatrix} = \begin{bmatrix} 2-\Lambda\cos\theta_1 & -1 \\ -1 & 1-\Lambda\cos\theta_2 \end{bmatrix}$$

When $\theta_1 = \theta_2 = 0$, the determinant of the Hessian matrix of $\Pi_\Lambda(\theta_1,\theta_2)$ is calculated as follows:

$$\det\begin{bmatrix} \dfrac{\partial^2\Pi_\Lambda}{\partial\theta_1^2} & \dfrac{\partial^2\Pi_\Lambda}{\partial\theta_1\partial\theta_2} \\ \dfrac{\partial^2\Pi_\Lambda}{\partial\theta_1\partial\theta_2} & \dfrac{\partial^2\Pi_\Lambda}{\partial\theta_2^2} \end{bmatrix} = \Lambda^2 - 3\Lambda + 1 = \left(\Lambda - \frac{3-\sqrt{5}}{2}\right)\left(\Lambda - \frac{3+\sqrt{5}}{2}\right)$$

Since the determinant of the Hessian matrix of $\Pi_\Lambda(\theta_1,\theta_2)$ is zero if an equilibrium point is a critical point, two critical load factors Λ_{cr1} and Λ_{cr2} can be derived as follows at $\theta_1 = \theta_2 = 0$:

$$\begin{aligned}\Lambda_{cr1} &= \frac{3-\sqrt{5}}{2} \simeq 0.382 \\ \Lambda_{cr2} &= \frac{3+\sqrt{5}}{2} \simeq 2.618\end{aligned} \tag{5.25}$$

Note that the equilibrium can be achieved for any Λ at $\theta_1 = \theta_2 = 0$. The eigenvectors $\mathbf{x}_{cr1}$ and $\mathbf{x}_{cr2}$ of the Hessian matrix of $\Pi_\Lambda(\theta_1,\theta_2)$ corresponding to zero eigenvalues at $\Lambda = \Lambda_{cr1}, \Lambda_{cr2}$ are calculated as follows:

$$\begin{aligned}\mathbf{x}_{cr1} &= \frac{1}{\sqrt{10-2\sqrt{5}}}\begin{pmatrix} -1+\sqrt{5} \\ 2 \end{pmatrix} \simeq \begin{pmatrix} 0.526 \\ 0.851 \end{pmatrix} \\ \mathbf{x}_{cr2} &= \frac{1}{\sqrt{10+2\sqrt{5}}}\begin{pmatrix} -1-\sqrt{5} \\ 2 \end{pmatrix} \simeq \begin{pmatrix} -0.851 \\ 0.526 \end{pmatrix}\end{aligned} \tag{5.26}$$

(2) Stability of two bars model at undeformed state

Here, the Hessian matrix of the augmented Lagrangian formulated in Section 5.3 is evaluated for the stability analysis of the planer two bars model, and the validity of the proposed method is confirmed. The generalized displacement vector $\mathbf{W}$ consisting of the displacements of nodes and members and the rotation angle increments of hinges is used in this section. It is set to zero at the initial shape $\theta_1 = \theta_2 = 0$ of the frame shown in Fig. 5.2,

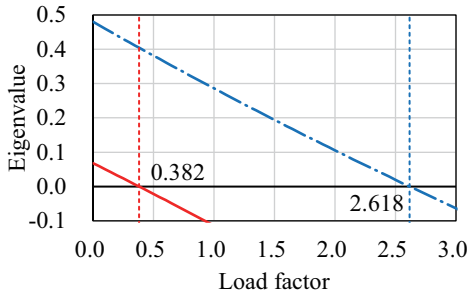

Figure 5.3: Smallest and second smallest eigenvalues of the Hessian matrix of the augmented Lagrangian of the two bar model.

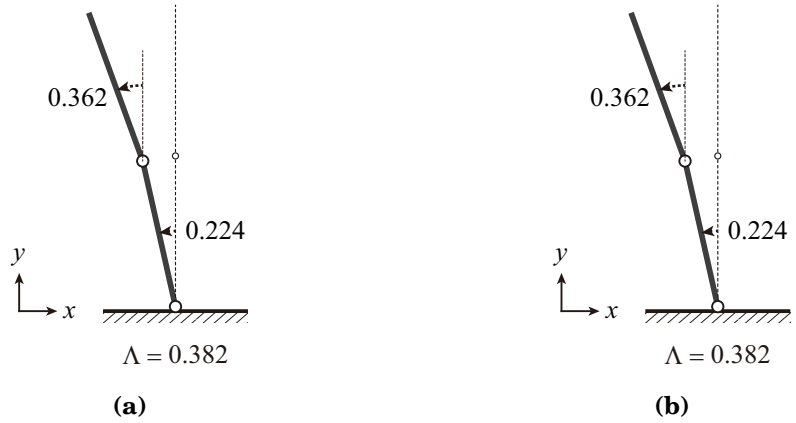

Figure 5.4: Critical eigenmodes of the two bar model at $\mathbf{W} = \mathbf{0}$; (a) First critical eigenmode at $\Lambda = 0.382$, (b) Second critical eigenmode at $\Lambda = 2.618$.

and the stability of the frame is evaluated at $\mathbf{W} = \mathbf{0}$. The Lagrange multiplier $\boldsymbol{\lambda}$ in the augmented Lagrangian $L_c(\mathbf{0})$ is calculated from $dL_c(\mathbf{0})/d\mathbf{W} = \mathbf{0}$ as follows:

$$\bar{\boldsymbol{\lambda}} = -\Lambda \left(\boldsymbol{\Gamma}(\mathbf{0})^{+}\right)^{\mathsf{T}} \mathbf{P} \tag{5.27}$$

where the superscript + denotes the Moore-Penrose inverse [63]. Note that the frame is in the equilibrium state for any Λ at $\mathbf{W} = \mathbf{0}$ if $\boldsymbol{\lambda}$ is determined from Eq. (5.27). Therefore, the critical load factors are investigated at $\mathbf{W} = \mathbf{0}$ by successively increasing the load factor Λ and evaluating the eigenvalues of the Hessian matrix of the augmented Lagrangian. Since the penalty parameter c_{p} in the augmented Lagrangian can be any value at the equilibrium point, it is fixed to $c = 1 \times 10^6$ in this section for simplicity.

Figure 5.3 shows the smallest and second smallest eigenvalues of the Hessian matrix of $L_c(\mathbf{0})$ when the load factor Λ is sequentially increased from 0 to 3. As shown in the figure, an eigenvalue of the Hessian matrix of $L_c(\mathbf{0})$ becomes zero when $\Lambda \simeq \Lambda_{\mathrm{cr1}}, \Lambda_{\mathrm{cr2}}$ where Λ_{cr1} and Λ_{cr2} calculated as Eq. (5.25, and the critical load factors obtained by the proposed method coincide with the analytical solution. In addition, the critical eigenmodes corresponding the critical load factors and the values of θ_1 and θ_2 calculated from the eigenmodes are shown in Fig. 5.4. It can easily be confirmed that the eigenmodes $(0.224, 0.362)^{\mathsf{T}}$ and $(0.348, -0.215)^{\mathsf{T}}$

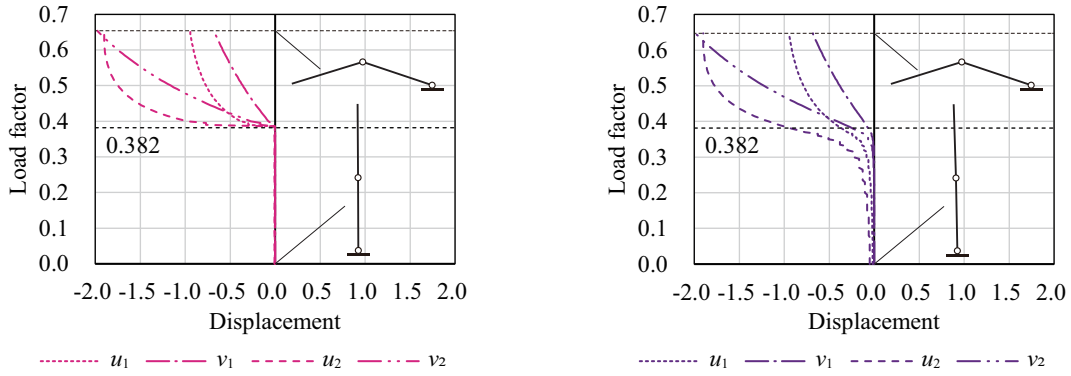

Figure 5.5: Nodal displacements with the initial imperfection corresponding to the first critical eigenmode; (a) $w_{\text{ini}} = 0.01$, (b) $w_{\text{ini}} = 0.05$.

obtained from the Hessian matrix of $L_c(\mathbf{0})$ are identical (proportional) to $\mathbf{x}_{\text{cr1}}$ and $\mathbf{x}_{\text{cr2}}$ in Eq. (5.26), respectively, which are obtained analytically. From above results, it is expected that the stability of the equilibrium state can be determined from the eigenvalue analysis of the Hessian matrix of the augmented Lagrangian.

(3) Equilibrium path analysis of two bars model with initial imperfection

The equilibrium path analysis is performed by increasing the magnitude of load shown in Fig. 5.2. The initial displacement $\mathbf{W}_0$ of the analysis is determined by adding an initial imperfection in proportion to the eigenmodes shown in Fig. 5.4 to the straight state $\mathbf{W} = \mathbf{0}$, and the analysis starts from $\mathbf{W} = \mathbf{W}_0$. The two scales of imperfection are considered so that the maximum nodal translational displacement w_{ini} is $w_{\text{ini}} = 0.01$ and 0.05 for each mode. The rotation angles of the springs introduced in the hinges are set to zero at $\mathbf{W} = \mathbf{W}_0$; i.e., $\tilde{\boldsymbol{\varphi}}$ is set to $\boldsymbol{\varphi}_0$ so that the strain energy of the springs in Eq. (5.7) is equal to zero at $\mathbf{W} = \mathbf{W}_0$. The initial value of Lagrange multiplier vector and the tolerance of the absolute value of an error in incompatibility vector $\mathbf{G}(\mathbf{W})$ are assigned as $\boldsymbol{\lambda}_0 = \mathbf{0}$ and $\epsilon_{\text{tol}} = 1 \times 10^{-8}$, respectively. The load factor is sequentially increased from $\Lambda = 0$ by $d\Lambda_0 = 5.0 \times 10^{-3}$, and the equilibrium path analysis terminates just before v_2 shown in Fig. 5.2 reaches -2. For detailed investigation, the increment of the load factor is reduced from 5.0×10^{-3} when v_2 approaches -2. Since the process of the ALM is stable and shows good convergence, the penalty parameter is fixed at $c_{\text{p}} = 1 \times 10^6$ for simplicity. It is confirmed that the eigenvalues of the Hessian matrix of the augmented Lagrangian change slightly if the updating algorithm of the penalty parameter in Algorithm 5.1 is used.

Figures 5.5 and 5.6 show the nodal displacements obtained from the initial imperfections based on the first and second critical eigenmodes shown in Fig. 5.4, respectively. When the initial imperfection corresponding to the second eigenmode is given with $w_{\text{ini}} = 0.01$, v_2 suddenly exceeds -2 from the initial value as shown in Fig. 5.6(a). Hence, the termination

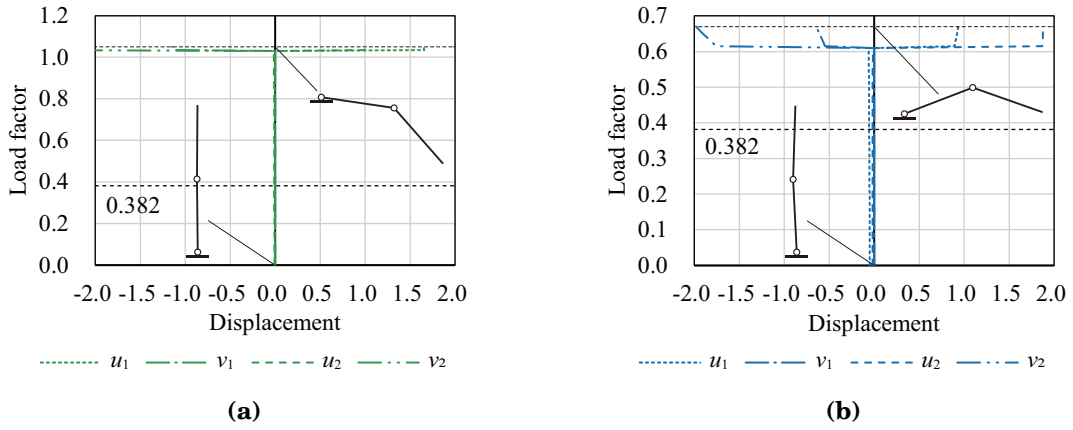

Figure 5.6: Nodal displacements with the initial imperfection corresponding to the second critical eigenmode; (a) $w_{\text{ini}} = 0.01$, (b) $w_{\text{ini}} = 0.05$.

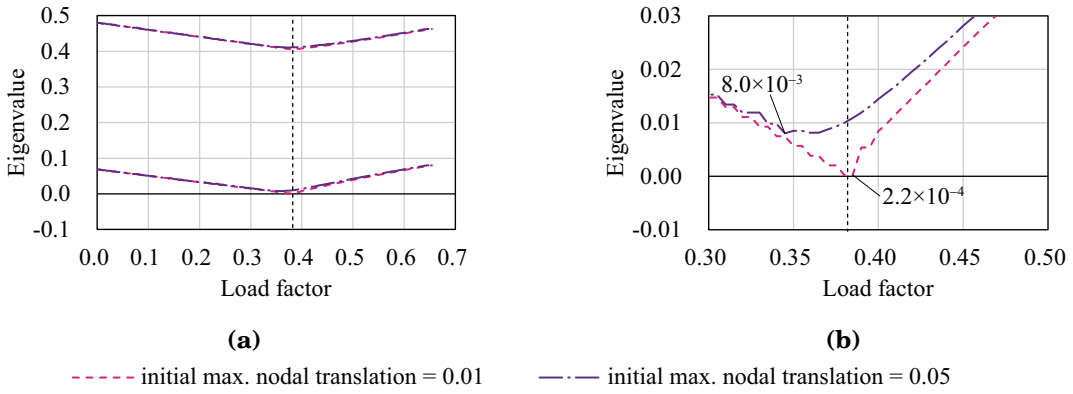

Figure 5.7: Smallest eigenvalues of the Hessian matrix of the augmented Lagrangian with the initial imperfection corresponding to the first critical eigenmode; (a) Overall view, (b) Enlarged view near the critical load factor.

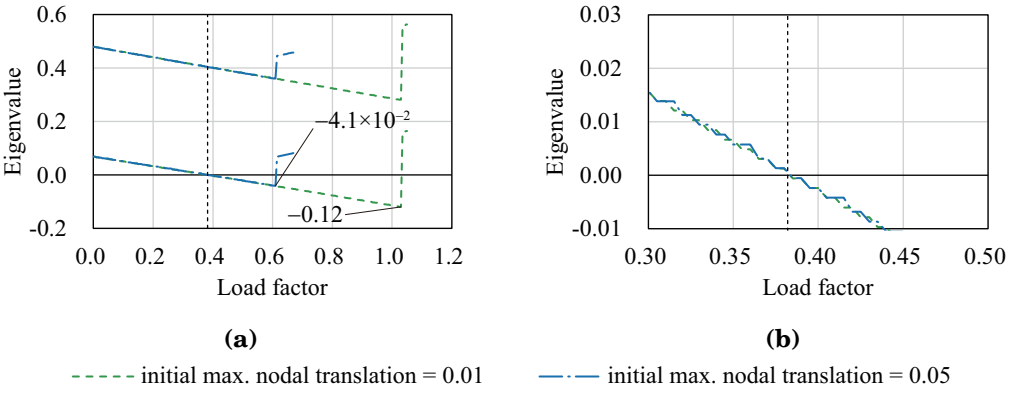

Figure 5.8: Smallest eigenvalues of the Hessian matrix of the augmented Lagrangian with the initial imperfection corresponding to the second critical eigenmode; (a) Overall view, (b) Enlarged view near the critical load factor.

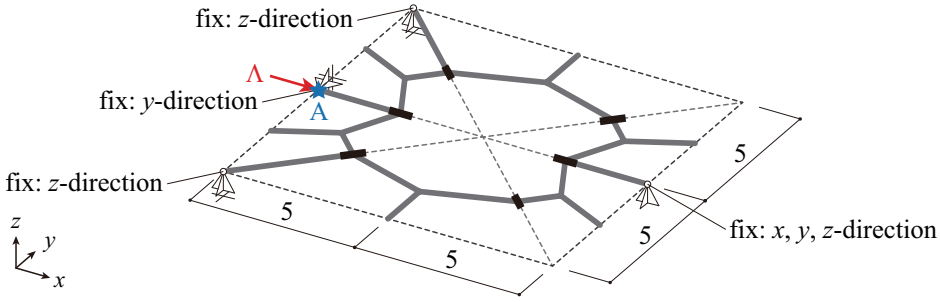

Figure 5.9: Configuration of the analysis model, load, and boundary conditions; The frame model is represented by bold lines, and the edges of waterbomb cell are represented by dotted lines.

condition with respect to v_2 is ignored in this example, and the equilibrium path analysis proceeds until the displacement becomes visible. As shown in Fig. 5.5, when the initial imperfection is based on the first critical eigenmode, the displacements drastically increase around $\Lambda_{\mathrm{cr1}} \simeq 0.382$, and the equilibrium path shows a feature like the Euler buckling of a cantilever column. The values of the eigenvalues of the Hessian matrix of the augmented Lagrangian are shown in Figs. 5.7 and 5.8. It is observed from Fig. 5.7 that the smallest eigenvalue of the Hessian matrix on the equilibrium path takes its minimum value near Λ_{cr1} and approaches zero. In the other region, the smallest eigenvalue is positive, which confirms that the equilibrium path is stable. On the other hand, when the initial imperfection is based on the second eigenmode, almost no displacement occurs around $\Lambda = \Lambda_{\mathrm{cr1}}$, and the displacement progresses rapidly at a point where the load factor exceeds Λ_{cr1} by a certain amount as shown in Fig. 5.6. Figure 5.8 shows that the smallest eigenvalue of the Hessian matrix on the equilibrium path becomes zero at $\Lambda \simeq \Lambda_{\mathrm{cr1}}$ and takes negative value until the displacement occurs. Therefore, the equilibrium state is unstable in the range of $\Lambda > \Lambda_{\mathrm{cr1}}$.

5.6.2 Waterbomb cell (1)

(1) Stability of waterbomb cell (1) at fully developed state

Equilibrium path of the waterbomb cell shown in Fig. 5.9 is investigated. The frame model's number of nodes, members, and hinges are $N_{\mathrm{N}} = 22$, $N_{\mathrm{M}} = 22$, and $N_{\mathrm{H}} = 6$, respectively. Therefore, the number of components of the generalized displacement vector and the incompatibility vector are calculated as $N_{\mathrm{W}} = 264$ and $N_{\mathrm{G}} = 264$, respectively. As shown in Fig. 5.9, the nodal load is applied to node A indicated by blue star in the positive x-direction. The translational displacements of nodes are constrained so that the rigid-body motion of the entire model is restricted. The rotational stiffness of each spring installed in the hinge is assigned to be proportional to the length of the corresponding crease line; 1 for a crease line of length 5 and $\sqrt{2}$ for a crease line of length $5\sqrt{2}$. The generalized displacement vector $\mathbf{W}$ is set to zero at the perfectly flat and developed state where all the nodes are on the xy-plane. At the flat state $\mathbf{W} = \mathbf{0}$, the degrees of kinematic and static indeterminacy calculated

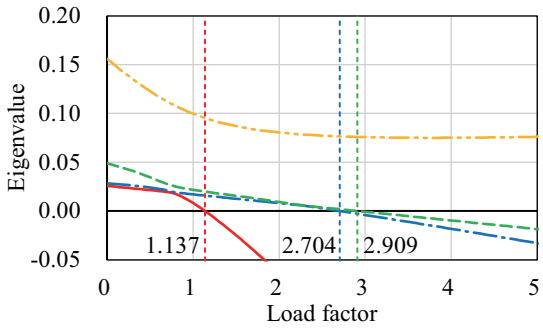

Figure 5.10: Smallest to the fourth smallest eigenvalues of the Hessian matrix of the augmented Lagrangian at $\mathbf{W} = \mathbf{0}$.

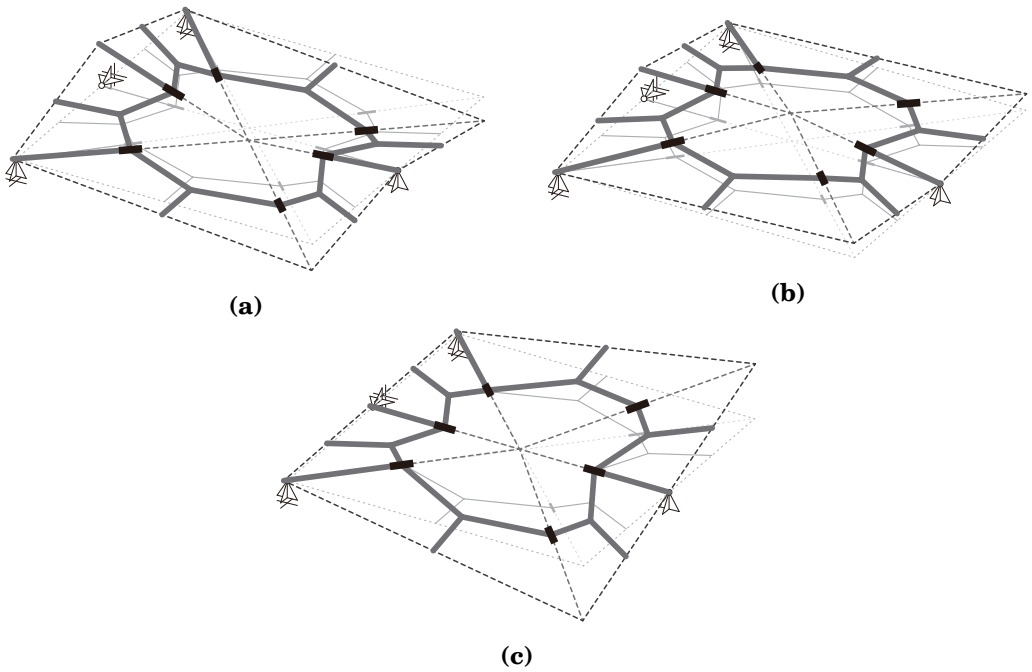

Figure 5.11: Critical eigenmodes at $\mathbf{W} = \mathbf{0}$; (a) First critical eigenmode at $\Lambda \simeq 1.137$, (b) Second critical eigenmode at $\Lambda \simeq 2.704$, (c) Third critical eigenmode at $\Lambda \simeq 2.909$.

from the rank of the compatibility matrix are both 4. Since the equilibrium state can be realized for any Λ at $\mathbf{W} = \mathbf{0}$, the critical load factor is investigated at $\mathbf{W} = \mathbf{0}$ by increasing the load factor and evaluating the eigenvalues of the Hessian matrix of the augmented Lagrangian $L_c(\mathbf{0})$. As in Section 5.6.1, the Lagrange multiplier for each load factor is obtained from Eq. (5.27), and the penalty parameter is fixed at $c_\mathrm{p} = 1 \times 10^6$.

Figure 5.10 shows the four smallest eigenvalues of the Hessian matrix of the augmented Lagrangian $L_c(\mathbf{0})$ when the load factor Λ is increased from 0 to 5. The fifth smallest eigenvalue is about 10000 times larger than the fourth smallest one. Three critical load factors are obtained as $\Lambda_{\mathrm{cr}1} \simeq 1.137$, $\Lambda_{\mathrm{cr}2} \simeq 2.704$, and $\Lambda_{\mathrm{cr}3} \simeq 2.909$, respectively. The critical eigen-

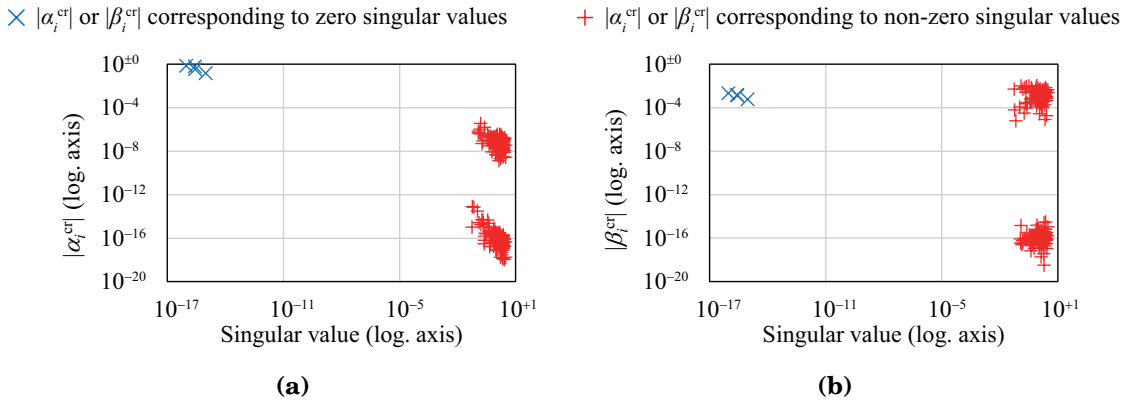

Figure 5.12: Values of $|\alpha_i^{cr}|$ defined in Eq. (5.22) and $|\beta_i^{cr}|$ defined in Eq. (5.24) for the first critical eigenmode; (a) Values of $|\alpha_i^{cr}|$, (b) Values of $|\beta_i^{cr}|$.

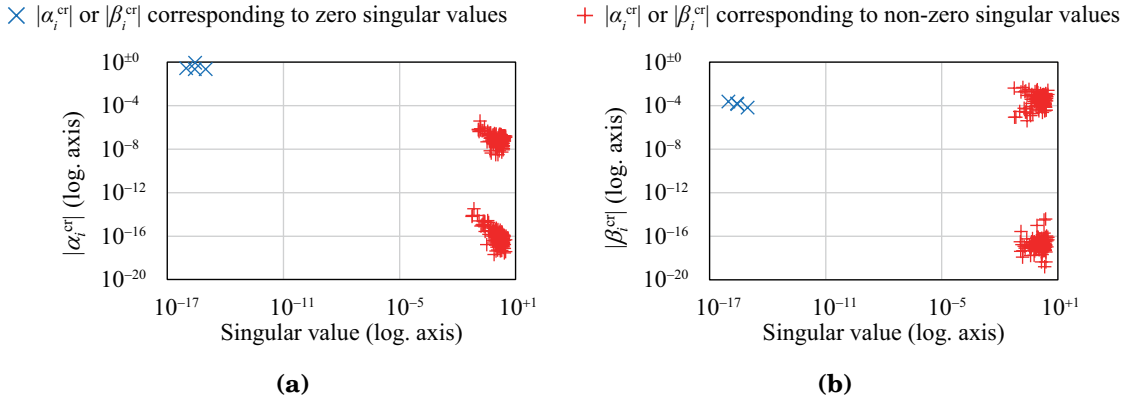

Figure 5.13: Values of $|\alpha_i^{cr}|$ and $|\beta_i^{cr}|$ for the second critical eigenmode; (a) Values of $|\alpha_i^{cr}|$, (b) Values of $|\beta_i^{cr}|$.

modes at $\Lambda = \Lambda_{cr1}, \Lambda_{cr2}, \Lambda_{cr3}$ are shown in Fig. 5.11. Note that the number of critical load factors is equal to the degrees of kinematic indeterminacy at the folded state to be investigated in the next subsection. The obtained critical points are the symmetric bifurcation points; i.e., a critical eigenmode $\mathbf{w}_{cr}$ satisfies $L_c(\mathbf{w}_{cr}) = L_c(-\mathbf{w}_{cr})$.

Next, the values of $|\alpha_i^{cr}|$ defined in Eq. (5.22) and the values of $|\beta_i^{cr}|$ defined in Eq. (5.24) are calculated for each critical eigenmode to investigate the relationship between the critical eigenmodes and the first-order infinitesimal mechanism. The values calculated for all the singular vectors of the compatibility matrix at $\mathbf{W} = \mathbf{0}$ are shown in Figs. 5.12–5.14. Note again that a critical eigenmode is the first-order infinitesimal mechanism if the values of $|\alpha_i^{cr}|$ corresponding to the non-zero singular values, which are indicated by red + in Figs. 5.12(a)–5.14(a), are sufficiently smaller than that corresponding to the zero singular values, which are indicated by blue × in Figs. 5.12(a)–5.14(a). In addition, a critical eigenmode can be extended to the second-order infinitesimal mechanism if the values of $|\beta_i^{cr}|$ corresponding to the zero singular values, which are indicated by blue × in Figs. 5.12(b)–

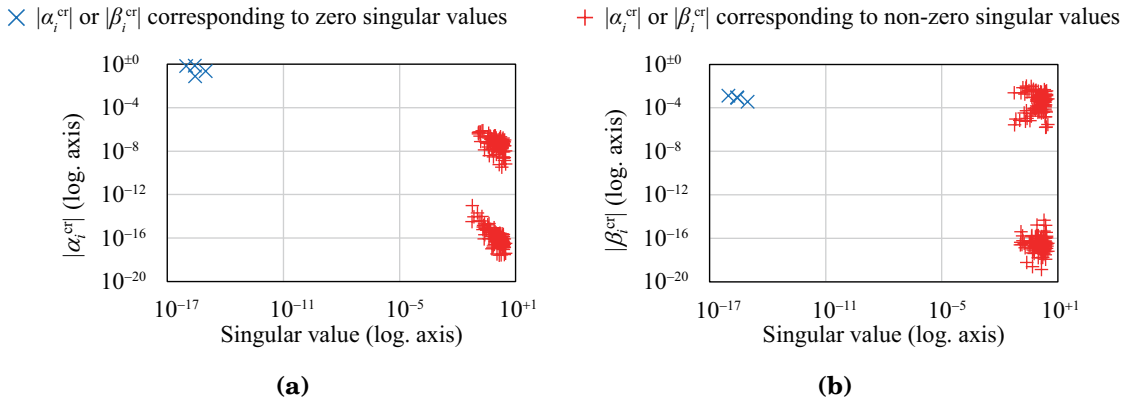

Figure 5.14: Values of $|\alpha_i^{cr}|$ and $|\beta_i^{cr}|$ for the third critical eigenmode; (a) Values of $|\alpha_i^{cr}|$, (b) Values of $|\beta_i^{cr}|$.

5.14(b), are sufficiently smaller than that corresponding to the non-zero singular values, which are indicated by red + in Figs. 5.12(b)–5.14(b). As shown in Figs. 5.12(a)–5.14(a), the values of $|\alpha_i^{cr}|$ corresponding to all the non-zero singular values are less than $1/10^4$ of those corresponding to zero singular values and approximately equal to zero. Therefore, each critical eigenmode can be regarded as the first-order infinitesimal mechanism. On the other hand, the values of $|\beta_i^{cr}|$ corresponding to the zero singular values are not equal to zero as shown in Figs. 5.12(b)–5.14(b), and the critical modes cannot be extended to the second-order mechanism.

(2) Equilibrium path analysis of waterbomb cell (1) with initial imperfection

The equilibrium path analysis is carried out for the waterbomb cell shown in Fig. 5.9. The initial imperfection is assigned by scaling each eigenmode shown in Fig. 5.11, and the three scales of imperfection modes are adopted so that the maximum nodal translation is $w_{\text{ini}} = 0.05, 0.1, 0.5$, respectively. The initial displacement after assigning the imperfection is represented by $\mathbf{W}_0$, and each analysis starts from $\mathbf{W} = \mathbf{W}_0$. The maximum absolute value among the components of the incompatibility vector $\mathbf{G}(\mathbf{W}_0)$ is about 1.07×10^{-2} which corresponds to the translational displacement and is about 1/1000 of the span of the model. As in the case of the two bar model, the rotation angles of the hinges at $\mathbf{W}_0$ are assigned to $\tilde{\boldsymbol{\varphi}}$ to regard the rotation angles of the springs at $\mathbf{W} = \mathbf{W}_0$ as the undeformed state $\boldsymbol{\varphi} - \tilde{\boldsymbol{\varphi}} = \mathbf{0}$. The initial value of $\boldsymbol{\lambda}$ is given as $\boldsymbol{\lambda} = \mathbf{0}$ since it approximately satisfy the stationary conditions of Problem (5.16) and can be a good estimation of the multiplier corresponding to the stationary point of problem (5.8) at $\mathbf{W} = \mathbf{W}_0$ and $\Lambda = 0$. The tolerance of the maximum error of $\mathbf{G}(\mathbf{W})$ is set as $\epsilon_{\text{tol}} = 1 \times 10^{-7}$, and the penalty parameter c_{p} is updated automatically in accordance with Algorithm 5.1 for the stability of the equilibrium path analysis. The initial increment of the load factor is $d\Lambda_0 = 5.0 \times 10^{-3}$, and the update ratios of $d\Lambda$ are $a = 0.125$ and $b = 2.0$. $\Lambda_{\text{max}} = 10.0$ and $d\Lambda_{\text{min}} = 1 \times 10^{-10}$ are assigned as the maximum value of the load factor and the minimum value of the load factor increment, respectively. The trans-

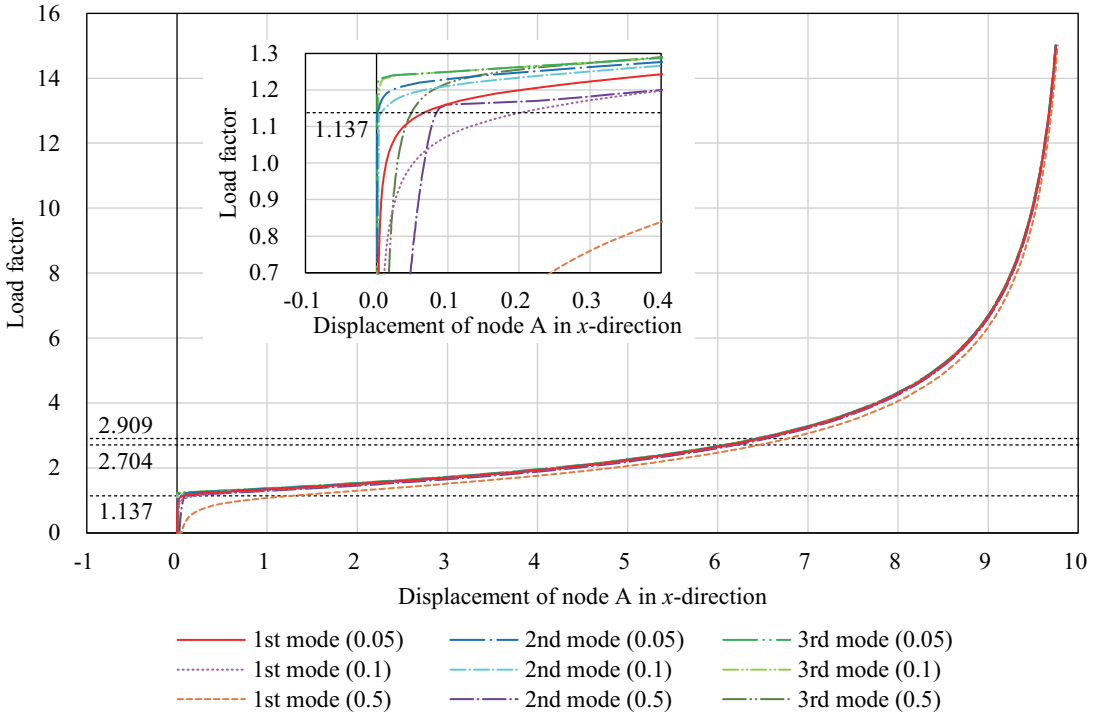

Figure 5.15: Displacement of node A in the x-direction with three different initial imperfection modes with three different magnitudes, respectively.

lational displacement in the x-direction of node A indicated by the blue star in Fig. 5.9 is referred for the termination condition of the equilibrium path analysis with $W_i^{\max} = 10$ and $W_i^{\min} = -1$.

The translational displacement of node A in the x-direction is shown in Fig. 5.15 for the analyses with nine different initial imperfections. Figure. 5.16 shows the transition of the shape of the waterbomb cell on each equilibrium path with $w_{\text{ini}} = 0.05$. The deformed shapes at the end of the analysis are similar for all examples except for the symmetry about the xy-plane. The largest absolute value among the components of the compatibility vector $\mathbf{G}(\mathbf{W})$ is less than 1×10^{-7} throughout each path analysis as shown in Fig. 5.17, and the obtained equilibrium paths can be regarded as the rigid-folding deformation paths.

In each case, the displacement of node A significantly progresses around the first critical load factor $\Lambda_{\text{cr1}} \simeq 1.137$. As shown in Fig.5.15, the displacement progresses gradually before the load factor reaches the first critical load factor when the initial imperfection based on the first eigenmode is applied. On the other hand, the displacement scarcely progresses until the load factor exceeds the first critical load factor when the initial imperfection based on the second or third eigenmode is applied. The deformed shapes at the end of the analysis are similar for all cases except for the symmetry about the xy-plane. This similarity of the final shapes is attributed to the isolated second and third critical load factors which are significantly larger than the first critical load factor; i.e., the deformation occurs before the load factor reaches the second and third critical load factors and the load factor is less than the second and third critical load factors even at the end of the equilibrium path

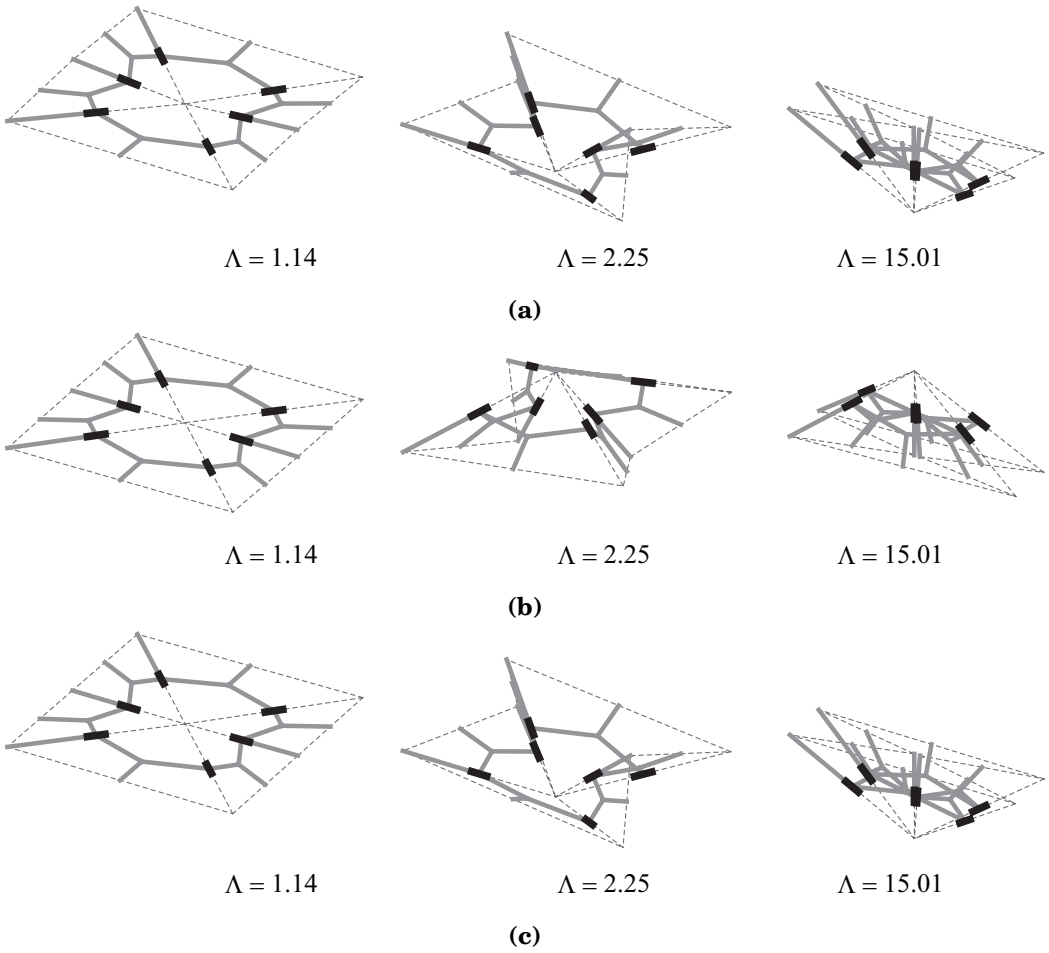

Figure 5.16: Deformation process with $w_{\mathrm{ini}} = 0.05$ in the equilibrium with the rigid-folding motion; (a) Imperfection corresponding to the first critical eigenmode, (b) Imperfection corresponding to the second critical eigenmode, (c) Imperfection corresponding to the third critical eigenmode.

analysis. Consequently, the equilibrium paths approximately converge to the bifurcation path corresponding to the first critical point.

Figures 5.18 and 5.19 show the value of the penalty parameter and the smallest eigenvalue of the Hessian matrix of the augmented Lagrangian on each equilibrium path, respectively. The minimum value of the eigenvalue on each equilibrium path is also plotted in Fig. 5.19 by × mark. The penalty parameters tend to drastically change in the range where the load factor is less than the first critical load factor, and the smallest eigenvalues change as the penalty parameters change. When the penalty parameter is large, it indicates that the maximum error of the compatibility equations is slow to reach the acceptable value. On the other hand, when the penalty parameter is small, the augmented Lagrangian method converges quickly or the minimization of the augmented Lagrangian may fail to converge. Therefore, the drastic change of the penalty parameter in the range $\Lambda < \Lambda_{\mathrm{cr1}}$ indicates the instability of finding the equilibrium point. Although the smallest

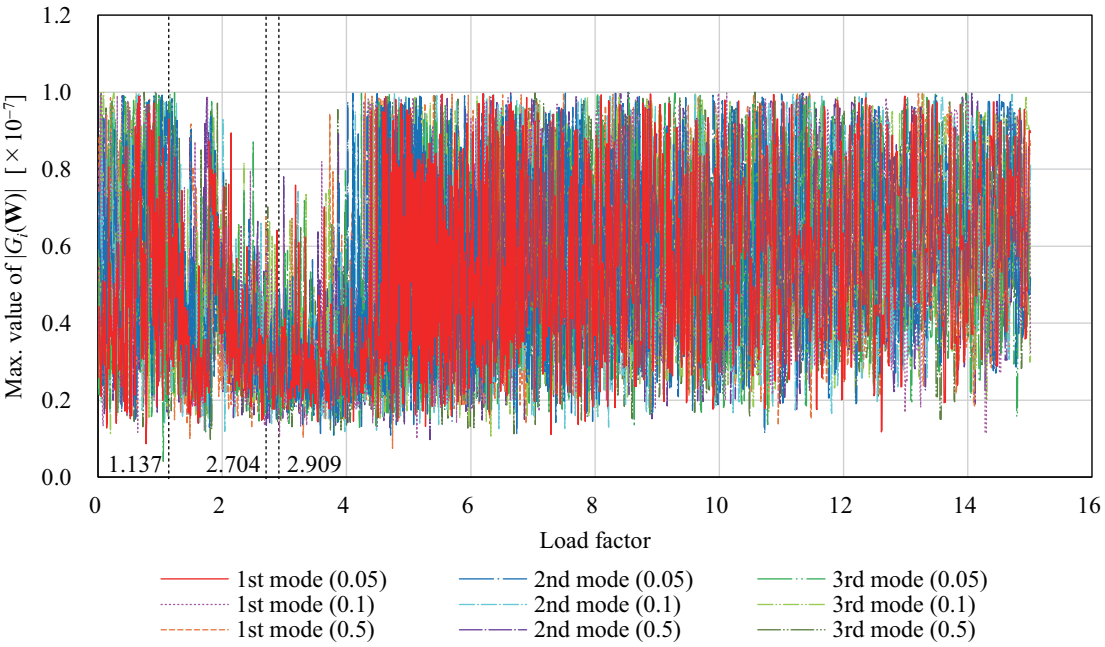

Figure 5.17: Transition of the largest absolute value among the components of the compatibility vector for each initial imperfection mode.

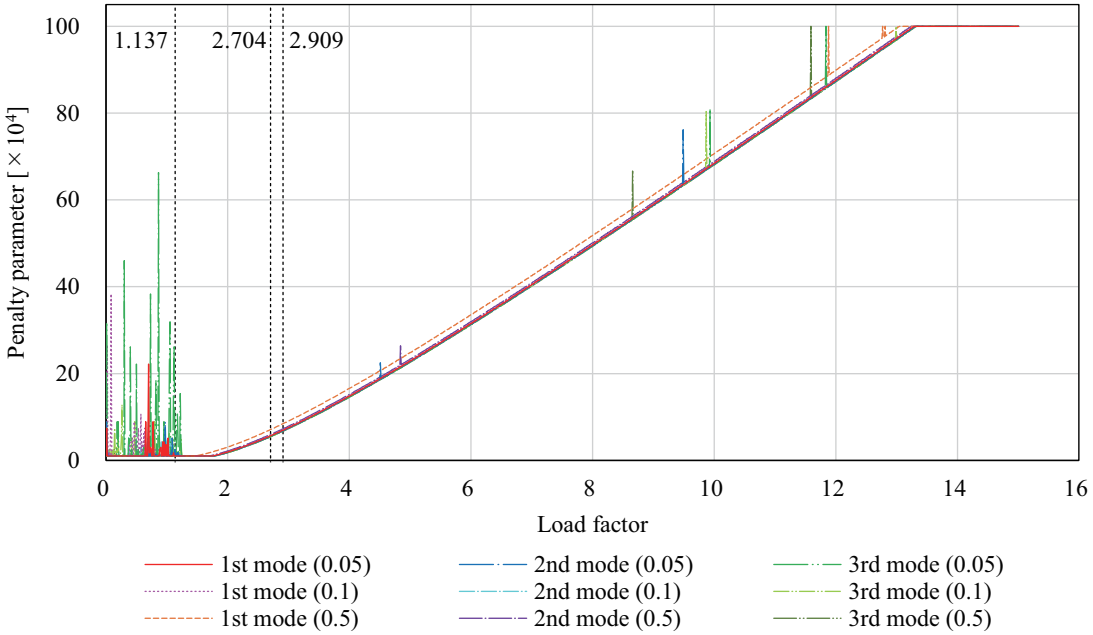

Figure 5.18: Transition of the penalty parameter for each initial imperfection mode.

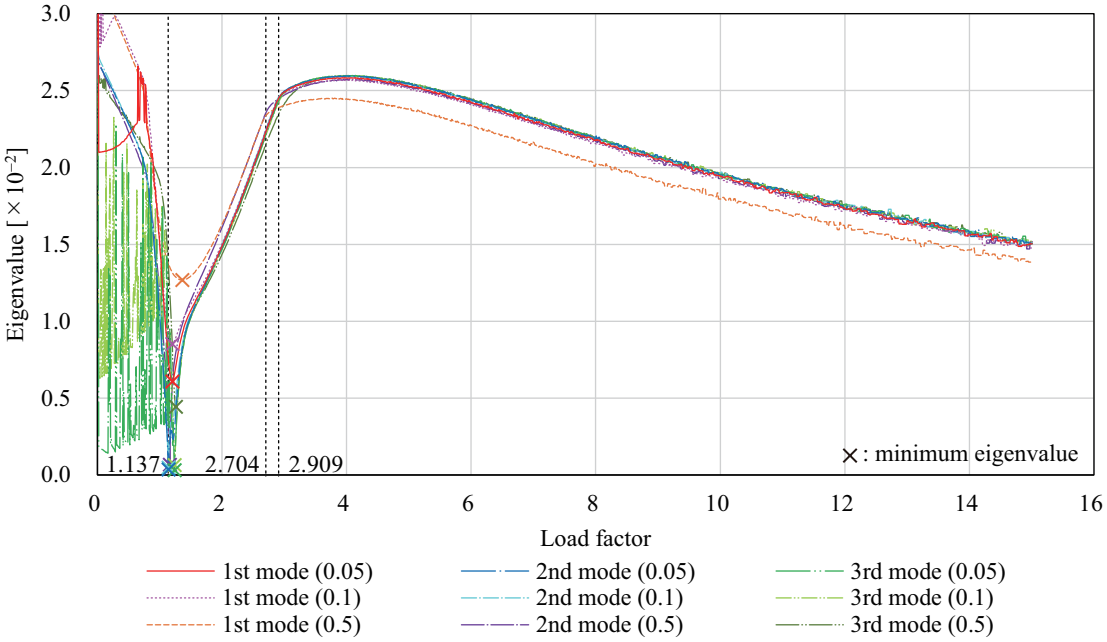

Figure 5.19: Transition of the smallest eigenvalue for each initial imperfection mode.

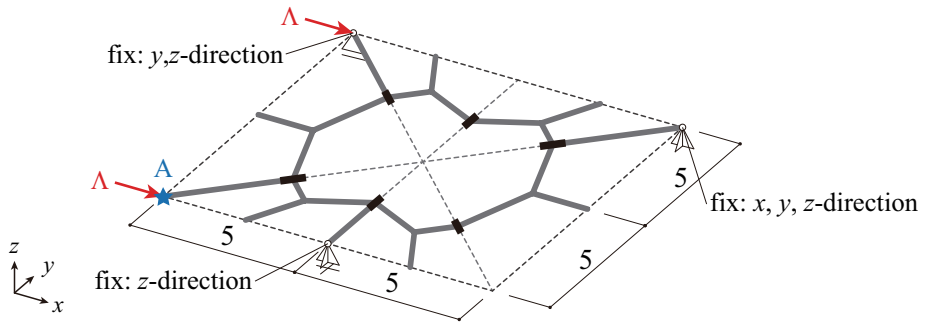

Figure 5.20: Configuration of the analysis model, load, and boundary conditions.

eigenvalues oscillate in the range $\Lambda < \Lambda_{cr1}$, the overall trend is that the eigenvalues have minima near the first critical load factor. It is reasonable that the equilibrium point with a small imperfection in the shape of the second or third eigenmode is difficult to find.

5.6.3 Waterbomb cell (2)

(1) Stability of waterbomb cell (2) at fully developed state

Equilibrium path of the waterbomb cell shown in Fig. 5.20 is investigated. The crease pattern and the rotation stiffness of the springs are the same as those of the previous example, respectively, while the loading and boundary conditions are different. This contributes to obtaining various deformation patterns of the waterbomb cell. The number of nodes, members, and hinges of the frame model are $N_N = 22$, $N_M = 22$, and $N_H = 6$, respectively. Hence, the generailized dispalcement vector and the incompatibility vector have $N_D = 264$ components and $N_G = 264$, respectively. The degrees of kinematic and static indeterminacy are

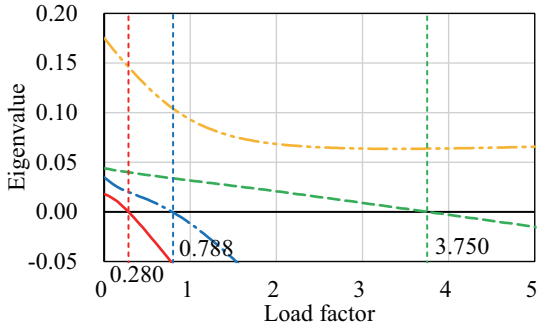

Figure 5.21: Smallest to the fourth smallest eigenvalues of the Hessian matrix of the augmented Lagrangian at $\mathbf{W} = \mathbf{0}$.

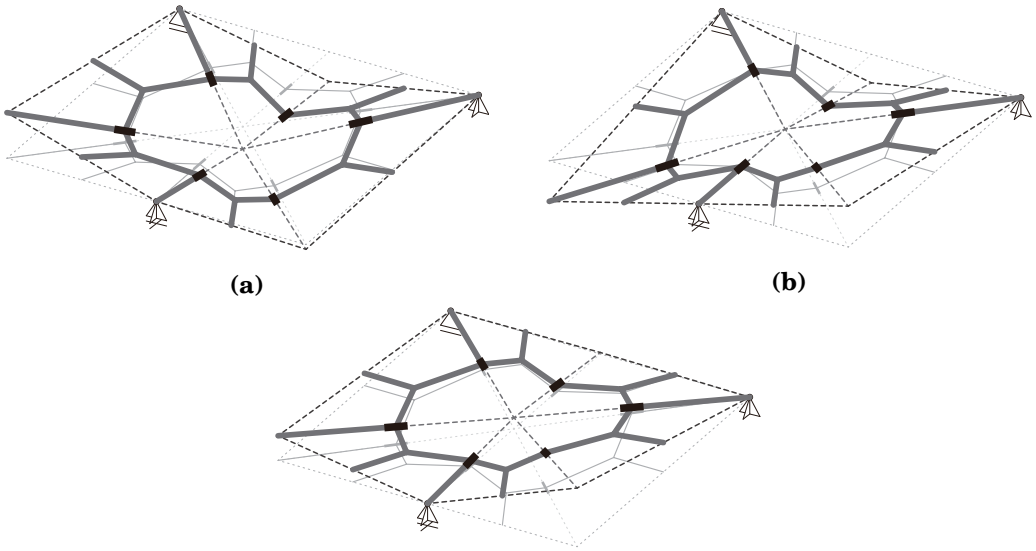

Figure 5.22: Critical eigenmodes at $\mathbf{W} = \mathbf{0}$; (a) First critical eigenmode at $\Lambda \simeq 0.280$, (b) Second critical eigenmode at $\Lambda \simeq 0.788$, (c) Third critical eigenmode at $\Lambda \simeq 3.750$.

both 4 at $\mathbf{W} = \mathbf{0}$. As in the previous subsection, the eigenvalues of the Hessian matrix of the augmented Lagrangian is evaluated to identify the critical load factors at the flat fully developed state $\mathbf{W} = \mathbf{0}$ by successively increasing the load factor from zero. The penalty parameter is fixed at $c_\mathrm{p} = 1 \times 10^6$.

The change of the smallest to the forth smallest eigenvalues of the Hessian matrix of the augmented Lagrangian $L_c(\mathbf{0})$ are shown in Fig. 5.21 when the load factor Λ is increased from 0 to 5. The fifth smallest eigenvalue is more than 10000 times larger than the fourth smallest one. The load factor is critical when it is $\Lambda = \Lambda_{\mathrm{cr}1} \simeq 0.280$, $\Lambda = \Lambda_{\mathrm{cr}2} \simeq 0.788$, and $\Lambda = \Lambda_{\mathrm{cr}3} \simeq 3.750$. Three critical eigenmodes are shown in Fig. 5.22. It is confirmed that $L_c(\mathbf{w}_\mathrm{cr}) = L_c(-\mathbf{w}_\mathrm{cr})$ holds and the obtained critical points are the symmetric bifurcation points.

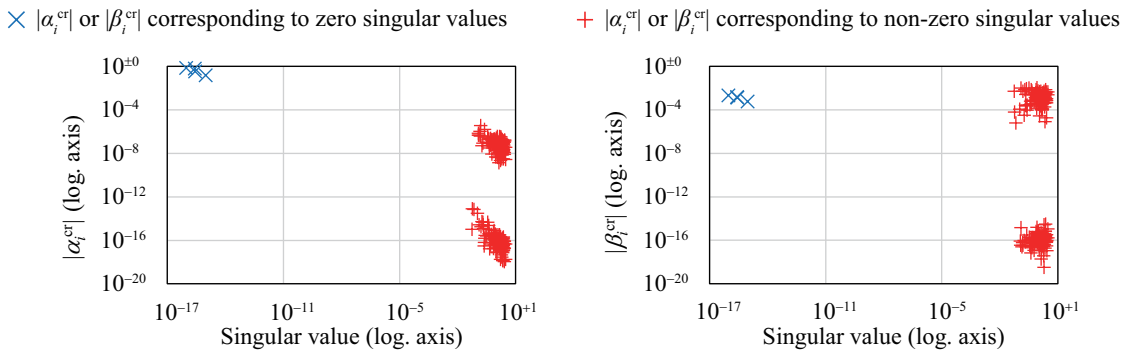

Figure 5.23: Values of $|\alpha_i^{cr}|$ and $|\beta_i^{cr}|$ for the first critical eigenmode; (a) Values of $|\alpha_i^{cr}|$, (b) Values of $|\beta_i^{cr}|$.

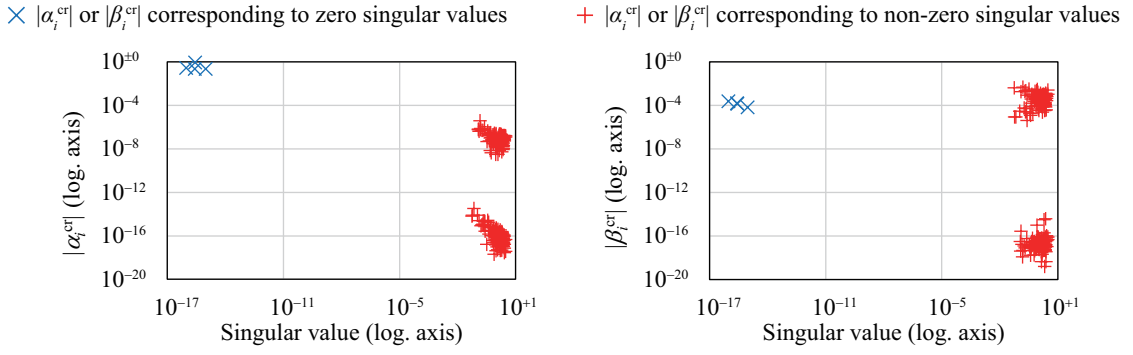

Figure 5.24: Values of $|\alpha_i^{cr}|$ and $|\beta_i^{cr}|$ for the second critical eigenmode; (a) Values of $|\alpha_i^{cr}|$, (b) Values of $|\beta_i^{cr}|$.

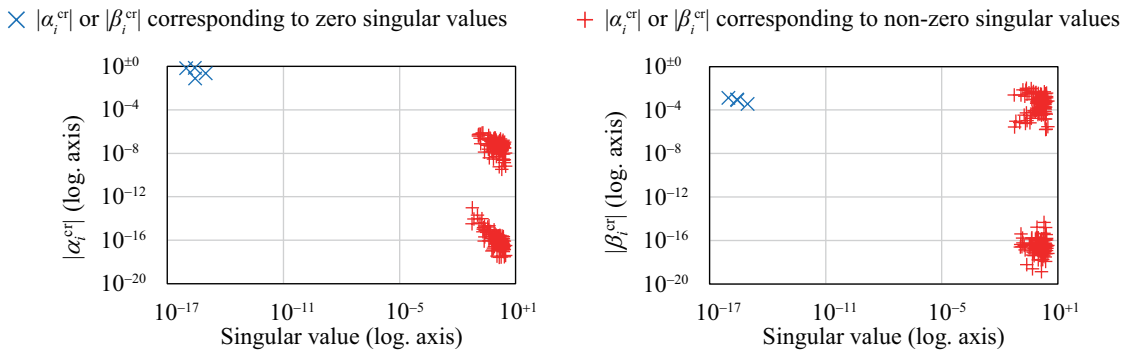

Figure 5.25: Values of $|\alpha_i^{cr}|$ and $|\beta_i^{cr}|$ for the third critical eigenmode; (a) Values of $|\alpha_i^{cr}|$, (b) Values of $|\beta_i^{cr}|$.

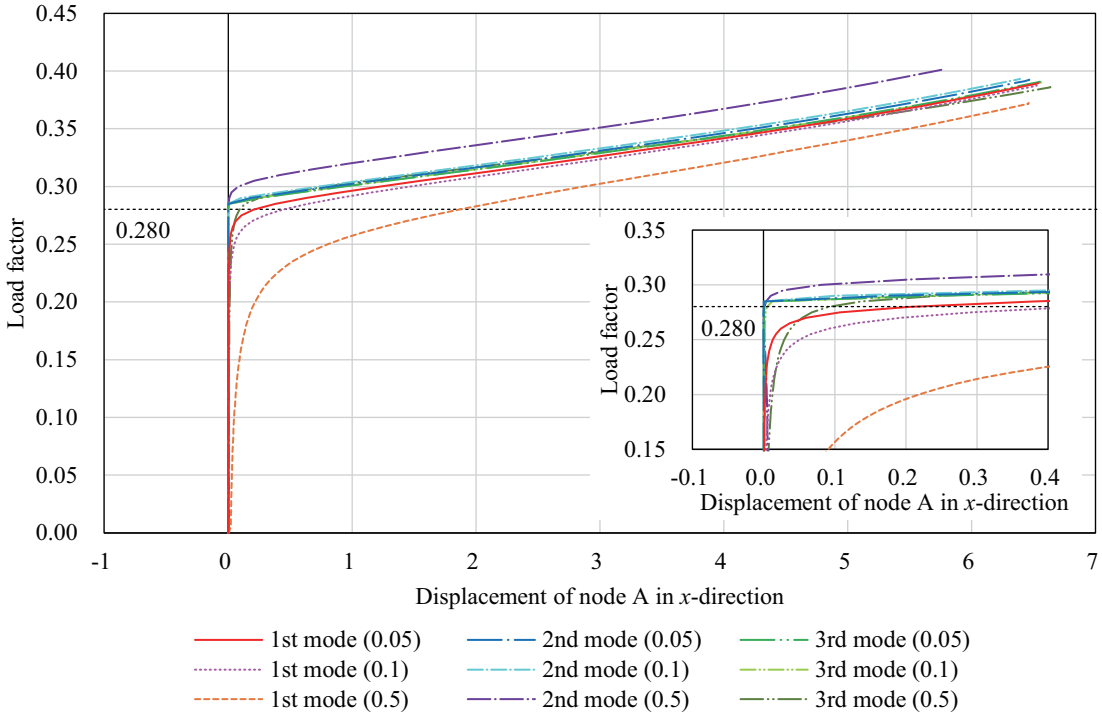

Figure 5.26: Displacement of node A in the x-direction with three different initial imperfection modes with three different magnitudes, respectively.

The values of $|\alpha_i^{\mathrm{cr}}|$ and $|\beta_i^{\mathrm{cr}}|$ are calculated for all the singular vectors of the compatibility matrix at $\mathbf{W} = \mathbf{0}$ and shown in Figs. 5.23–5.25. As shown in Figs. 5.23(a)–5.25(a), the values of $|\alpha_i^{\mathrm{cr}}|$ corresponding to all the non-zero singular values are less than $1/10^4$ of those corresponding to zero singular values and approximately equal to zero. Therefore, each critical eigenmode can be regarded as the first-order infinitesimal mechanism. On the other hand, the critical modes cannot be extended to the second-order mechanism since the values of $|\beta_i^{\mathrm{cr}}|$ corresponding to the zero singular values are not equal to zero as shown in Figs. 5.23(b)–5.25(b).

(2) Equilibrium path analysis of waterbomb cell (2) with initial imperfection

The equlibrium path of the waterbomb cell shown in Fig. 5.20 is traced. The initial imperfections are assigned based on the critical eigenmodes shown in Fig. 5.22. The same conditions as those used in the previus subsection of the analysis of another waterbomb cell are used except for $d\Lambda_0$ and $\Lambda_{\max}$, which are set as $d\Lambda_0 = 0.01$ and $\Lambda_{\max} = 15.0$, respectively. The initial maximum absolute value among the components of $\mathbf{G}(\mathbf{W}_0)$ after assigning the imperfection is about 1.66×10^{-2} which corresponds to the component of the translational incompatibility vector and is about 1/600 of the span of the model. The displacement in the x-direction of node A indicated by blue star in Fig. 5.20 is used as the reference displacement.

Figure 5.26 shows the relationship between the displacement at node A in the x-direction

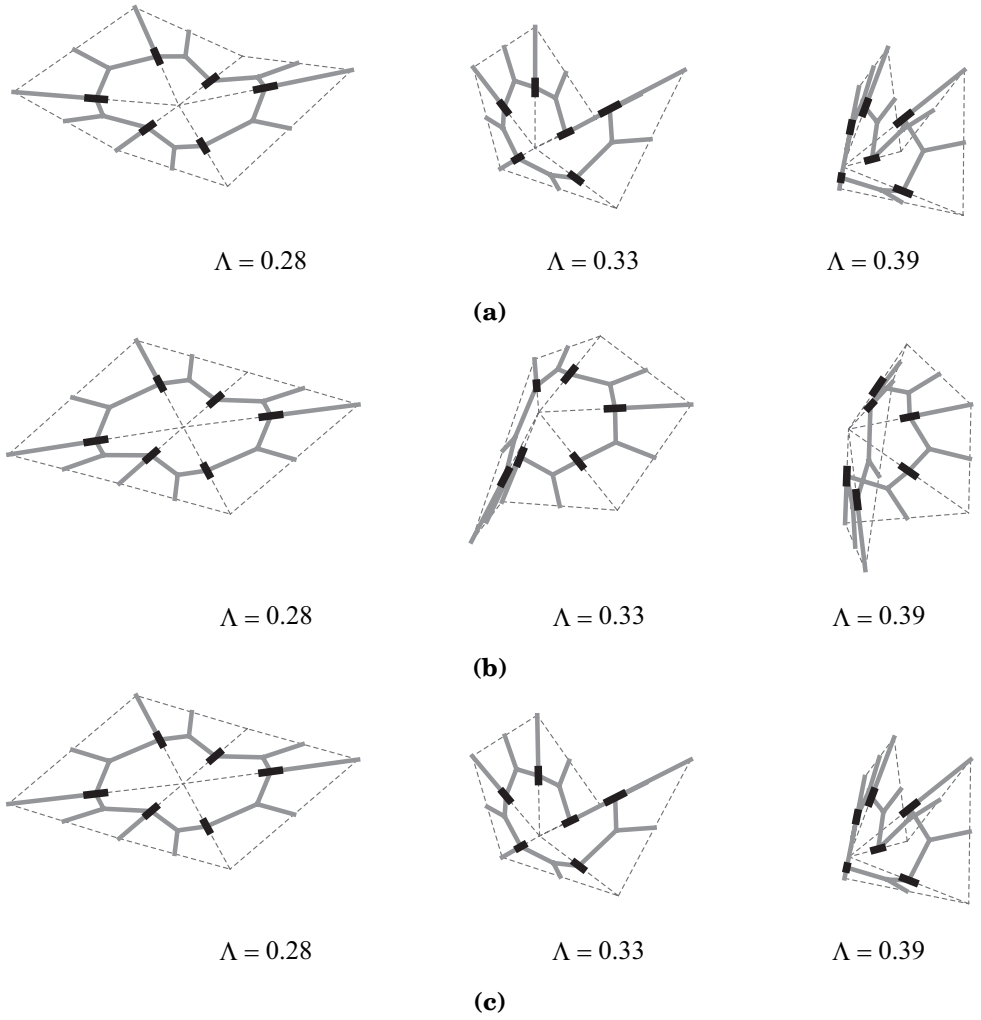

Figure 5.27: Deformation process with $w_{\text{ini}} = 0.05$ in the equilibrium with the rigid-folding motion; (a) Imperfection corresponding to the first critical eigenmode, (b) Imperfection corresponding to the second critical eigenmode, (c) Imperfection corresponding to the third critical eigenmode.

and the value of the load factor. The transition of the shape on each equilibrium path with $w_{\text{ini}} = 0.05$ is shown in Fig. 5.27. As in the previous examples of the waterbomb cell, the final shapes of the analysis are almost identical except for the symmetry about the xy-plane since the critical load factors are isolated. The degrees of kinematic and static indeterminacy are both 3 after the out-of-plane deformation occurs. The obtained equilibrium paths can be regarded as the rigid-folding deformation paths since the largest absolute value among the components of the compatibility vector $\mathbf{G}(\mathbf{W})$ is less than 1×10^{-7} throughout each path analysis as shown in Fig. 5.28.

The overall trends of the analysis results are similar to those of the previous examples. In all the nine cases of initial imperfection, the displacement progresses significantly around the first critical load factor $\Lambda_{\text{cr1}} \simeq 0.280$. A $\times$ mark in Fig. 5.30 represents the

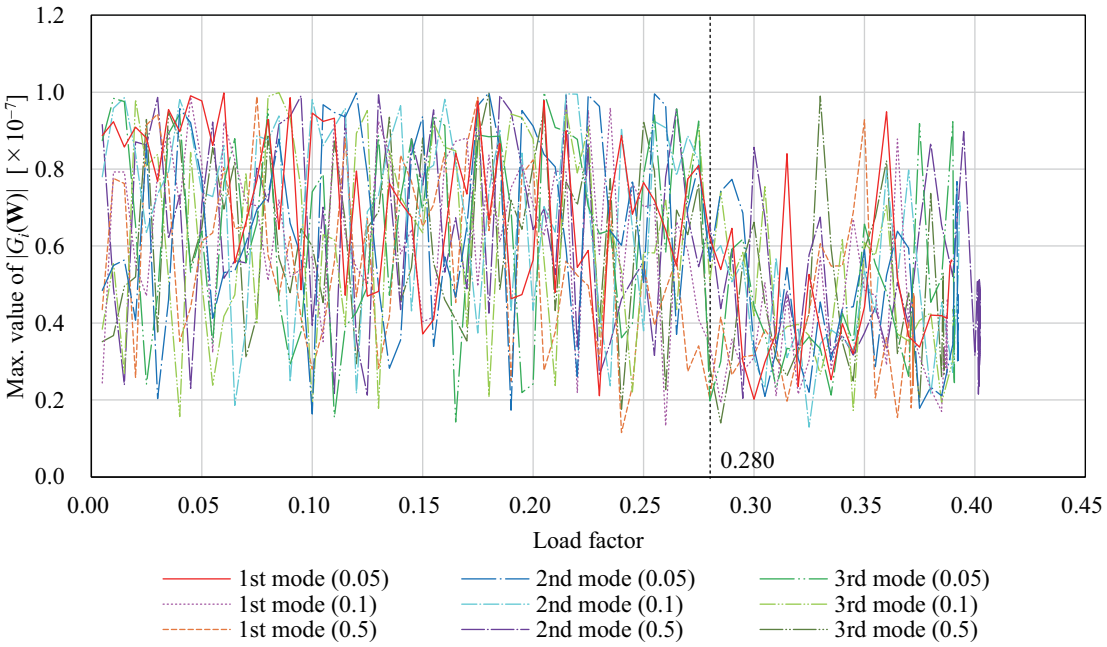

Figure 5.28: Transition of the largest absolute value among the components of the compatibility vector for each initial imperfection mode.

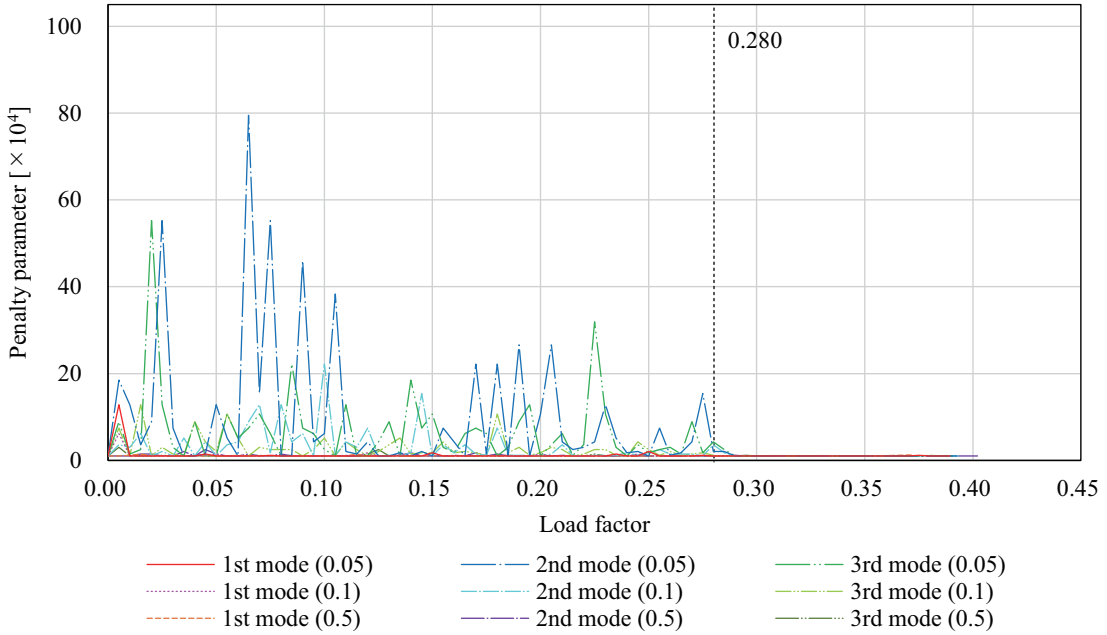

Figure 5.29: Transition of the penalty parameter for each initial imperfection mode.

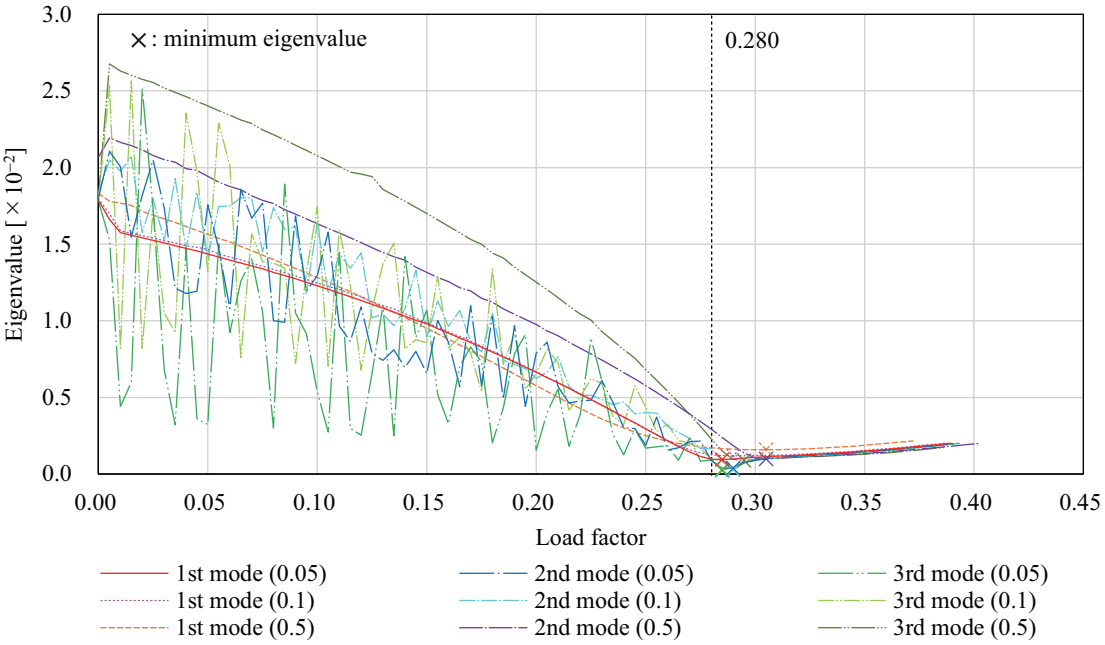

Figure 5.30: Transition of the smallest eigenvalue for each initial imperfection mode.

minimum value of the eigenvalue of the Hessian matrix of the augmented Lagrangian on each equilibrium paths, and all the eigenvalues have minima near the first critical load factor. In contrast to the previous examples of the waterbomb cell, the load factor exceeds the second and third critical load factors at the final stage of analysis. However, when Λ exceeds Λ_{cr1}, a finite deformation occurs and all eigenvalues are positive for each equilibrium path as shown in Fig. 5.30. Therefore, the equilibrium state is always stable after the load factor exceeds the first critical load factor. Since the penalty parameters tend to drastically change, the smallest eigenvalues also oscillate in the range $\Lambda \leq \Lambda_{\mathrm{cr1}}$. Therefore, the equilibrium state before Λ reaches Λ_{cr1} may be unstable.

5.7 Conclusions

A method of equilibrium path and stability analysis of a rigid origami represented by a frame model has been proposed in this chapter. An equilibrium state between the nodal loads and the moments of the springs introduced into the hinges are achieved with the exact rigid-folding motion. The equilibrium path can be uniquely determined locally except at the critical points by introducing the rotation springs. An equilibrium point is found by solving the energy minimization problem under the compatibility equations of a frame model, and an equilibrium path is traced by the incremental loading analysis. The augmented Lagrangian method is adopted to solve the optimization problem since it has good convergence even if the constraints degenerates. The eigenvalues of the Hessian matrix of the augmented Lagrangian are investigated at each equilibrium point to evaluate the stability of the equilibrium state and to find the critical load factor. If the Hessian matrix

is positive definite at an equilibrium point, the total potential energy is local minimum and the equilibrium state is stable. Conversely, if the Hessian matrix has a zero eigenvalue, the equilibrium point is a candidate for a bifurcation or a limit point. The relationship between the first-order infinitesimal mechanism modes and the critical eigenmodes, which are the eigenvectors corresponding to the zero eigenvalues of the Hessian matrix is also numerically investigated for the waterbomb cell examples.

The proposed method was first applied to a planar frame consisting of two members whose analytical solution can be easily obtained. The critical load factors and the critical eigenmodes obtained analytically and from the proposed method agree with good accuracy, and it has been confirmed that the critical load factors that may cause instability in the equilibrium can be determined by the proposed method. After verifying the validity of the proposed method, the method was applied to fully developed flat waterbomb cells with two different loads and boundary conditions. In both cases, three critical load factors are found, and the number of them is equal to the degrees of kinematic indeterminacy at the folded state, not at the flat state. All the critical eigenmodes have been numerically confirmed to be the first-order infinitesimal mechanism while they cannot be extended to the second-order infinitesimal mechanism. In the equilibrium path analysis, the initial imperfection is assigned to avoid the multiple bifurcation at the flat state. The three critical eigenmodes at the flat state are used for each waterbomb cell example to determine the direction of the initial imperfection, and the three different scales of imperfection are assigned to investigate the impact of the initial imperfection on the equilibrium path. The out-of-plane deformation drastically progresses after the load factor exceeds the first critical load factor for each initial imperfection. Since the critical points are isolated, similar final shapes are obtained and the equilibrium paths converge to the bifurcation path of the first critical point. From these results, it can be concluded that the waterbomb cell admits the several deformation paths for different boundary conditions and realizes the stable equilibrium path regardless of the initial imperfection except for around the first equilibrium point.

The proposed method only supports the incremental loading analysis at present, and the equilibrium path may not be fully traced if it contains the limit point where a snap-thorough behavior is observed. To trace this kind of equilibrium path, it is expected in future work that the proposed method is extended to include the incremental displacement method and the arc length method. In addition, the computational cost can be a major issue in the analysis of a large-scale origami which has many faces and crease lines since the augmented Lagrangian is minimized using BFGS in this study and the computational cost of the optimization is proportional to the square of the number of variables which is approximately determined by the number of faces. Therefore, to reduce the cost, the number of variables should be reduced by simplifying the structure of the frame model and by eliminating the dependent variables for the analysis of large-scale origami.

Chapter 6

Conclusions

The methods of form generation and equilibrium path analysis of a rigid origami are proposed in this thesis. The proposed methods are constructed based on the geometric and kinematics of the frame model which can represent a rigid origami in a simpler way than the other models. A form generation method is proposed for surface approximation with non-regular crease patterns, and it may contribute to enhance the flexibility of the design of the roofs and facades utilizing a rigid origami. A method of equilibrium path analysis is proposed to trace the equilibrium path in the exact rigid-folding motion. This hybrid analysis of the pure mechanism and the equilibrium is rarely performed while it is important to understand the deformation properties of a rigid origami with the multi-degrees of freedom mechanism. In the following, the results obtained in Chapters 2–5 are summarized.

In Chapter 2, the review of the numerical models of a rigid origami are provided, and the frame model used in this study is described. A frame model consists of rigid frame elements connected by hinges representing the crease lines of an origami. The equations of the geometric constraints on the nodal coordinates of the frame model are formulated so that the frame model represents the corresponding rigid origami appropriately, and the independent nodal coordinates are identified from these equations. The infinitesimal mechanism of the frame model is investigated by the methods for partially rigid frames. The compatibility equations are formulated by using nonlinear functions of the generalized displacement vector defined as the assemblage of the unconstrained translational and rotational displacements of nodes, the translational and rotational displacements of center points of members, and the increments of the hinge rotation angles. The kinematic indeterminacy and the first-order infinitesimal mechanism modes are derived from the compatibility matrix which is the first-order derivative of the incompatibility vector with respect to the generalized displacement. The geometric properties and the method of the kinematic analysis of the frame model introduced in this chapter is used in the following chapters.

Chapter 3 has presented a form generation method of a developable rigid origami structure approximating a Bézier surface. An optimization problem for generating a developable origami surface has been formulated to minimize an approximation error function under developability conditions. Developability conditions are considered around each inner ver-

tex, dividing edge, and inner cuts, and they are formulated with respect to the geometric properties of the origami surface such as the discrete Gaussian curvatures, normal vectors of the faces, and the sets of the inner angles of the faces and the length of edges constituting a cut. Three approximation error functions are defined reflecting the distance between the origami vertices and the target surface, the difference of the surface area, and the difference of the face normal vectors, respectively. The weighted sum of the three functions are minimized in the optimization problem. Form generation starts from a triangulated target surface and its crease lines are sequentially fixed to reduce the DOF of the deformation mechanism. The transition of the deformation mechanism due to fixing the crease lines is predicted by utilizing the kinematic properties of the frame model. The pseudo stiffness matrix of the frame model is defined by assuming the fictious rotational stiffness of the hinges, and its eigenvalue and eigenvector derivatives are used for the prediction. Selection criteria of the crease lines to be fixed are proposed to prevent the unfixed crease lines from being locked. They are defined based on the shape of an origami surface and the prediction of the transition of the deformation mechanism. The properties related to the prediction method are illustrated for the origami surface approximating an HP surface.

The case studies of form generation are shown in Chapter 4. The form generation procedure has been carried out for 100 randomly generated target surfaces and for an HP and a face surfaces. From the results of the approximation of the randomly generated surface, the proposed selection criteria of crease lines, which reflect both the shape and the deformation mechanism of an origami surface, are confirmed to be able to improve the efficiency of form generation by preventing the crease lines from being locked and reducing the times of solving the optimization problems. Furthermore, the approximation accuracy is also better when the proposed criteria are used. On the other hand, the impacts of the weight coefficients in the approximation error function, the choice of the design variables, and the introduction of cuts on the results of form generation are demonstrated for an HP and a dome surfaces. It can be seen from the results that there is no clear trade-off relation between the three approximation error functions and the values of the weight coefficients do not have large impact on the results while the choice of the design variables may affect the stability of the process of form generation. It is preferable to use the coordinates of the origami vertices or the nodal coordinates of the frame model as variables when the arrangement of the control points of the target Bézier surface is uniform in x- and y-coordinates. Effectiveness of cuts is evaluated for an HP and a dome surface. As shown in the results, exterior cuts can significantly improve the approximation accuracy while the inner cuts does not. Since a limited number of types of crease and cut patterns are considered in this study, it is important to investigate methods for finding good crease and cut patterns in future research.

In Chapter 5, a method of equilibrium path and stability analysis of a rigid origami represented by a frame model has been proposed. An equilibrium state between the nodal loads and the moments of the springs introduced into the hinges are achieved with the exact rigid-folding motion. An equilibrium point is found by solving the energy minimization

problem under the compatibility equations of a frame model, and an equilibrium path is traced by the incremental loading analysis. The augmented Lagrangian method is adopted to solve the optimization problem, and the eigenvalues of the Hessian matrix of the augmented Lagrangian are evaluated to investigate the stability of the equilibrium state and to find the critical load factor. If the Hessian matrix has a zero eigenvalue, the equilibrium point is a candidate for a bifurcation or a limit point. The proposed method was first applied to a planar frame consisting of two members whose analytical solution can be easily obtained, and it has been confirmed that the critical load factors that may cause instability in the equilibrium can be determined by the proposed method. Then, the method was applied to fully developed flat waterbomb cells with two different loads and boundary conditions. Three critical eigenmodes have been found for each example, and it has been numerically confirmed that these eigenmodes are the first-order infinitesimal mechanism while they cannot be extended to the second-order infinitesimal mechanism. The equilibrium path analysis was performed from the flat state with the initial imperfection based on the obtained critical eigenmodes. The out-of-plane deformation drastically progresses after the load factor exceeds the first critical load factor for each initial imperfection. Since the critical points are isolated, similar final shapes are obtained and the equilibrium paths converge to the bifurcation path of the first critical point. It is expected in future work that the proposed method is extended to include the incremental displacement method and the arc length method to fully trace the path which contains the limit point where a snap-thorough behavior is observed. In addition, to reduce the cost, the number of variables should be reduced by simplifying the structure of the frame model and by eliminating the dependent variables for the analysis of large-scale origami.

Appendix A

Identification of independent variables by the reduced row-echelon form of a matrix

Consider the following linear equation for $\mathbf{A} \in \mathbb{R}^{m \times n}$, $\mathbf{b} \in \mathbb{R}^m$, and $\mathbf{x} \in \mathbb{R}^n$:

$$\mathbf{A}\mathbf{x} = \mathbf{b} \tag{A.1}$$

Here, $\mathbf{A}$ and $\mathbf{b}$ are constant and given, and the existence of $\mathbf{x}$ satisfying Eq. (A.1) is assumed. If $\mathrm{rank}(\mathbf{A}) < n$, there are $n - \mathrm{rank}(\mathbf{A})$ components of $\mathbf{x}$ which can be arbitrarily determined, and $\mathrm{rank}(\mathbf{A}) < n$ is assumed in the following. The independent components of $\mathbf{x}$ satisfying Eq. (A.1) can be identified by the method utilizing the reduced row-echelon form (RREF) of a matrix [52, 97, 98]. The RREF of a matrix can be obtained from a finite sequence of linear elementary row operation and has the following three properties [62]:

1. The first nonzero component in any nonzero row is one. This non-zero component is referred to as the *pivot*, and the column including the pivot is referred to as the *pivot column*.

2. All the components other than the pivot are equal to zero in any pivot column, and the pivot columns are linearly independent with each other.

3. The column containing the pivot of a row is to the right of the column containing the pivot above that row.

4. The number of pivots is equal to the rank of the matrix whose RREF is computed.

For the procedure of deriving the RREF of a matrix, see Ref. [62]. If $\mathbf{b} \neq \mathbf{0}$ holds, Eq. (A.1) is rewritten as follows:

$$\begin{bmatrix} \mathbf{A} & -\mathbf{b} \end{bmatrix} \begin{pmatrix} \mathbf{x} \\ 1 \end{pmatrix} = \bar{\mathbf{A}}\bar{\mathbf{x}} = \mathbf{0} \tag{A.2}$$

where $\bar{n} = n + 1$, $\bar{\mathbf{A}} \in \mathbb{R}^{m \times \bar{n}}$, and $\bar{\mathbf{x}} \in \mathbb{R}^{\bar{n}}$. On the other hand, if $\mathbf{b} = \mathbf{0}$ holds, $\bar{n}$, $\bar{\mathbf{A}}$, and $\bar{\mathbf{x}}$ are defined as $\bar{n} = n$, $\bar{\mathbf{A}} = \mathbf{A}$, and $\bar{\mathbf{x}} = \mathbf{x}$, respectively, and the linear equation to be considered

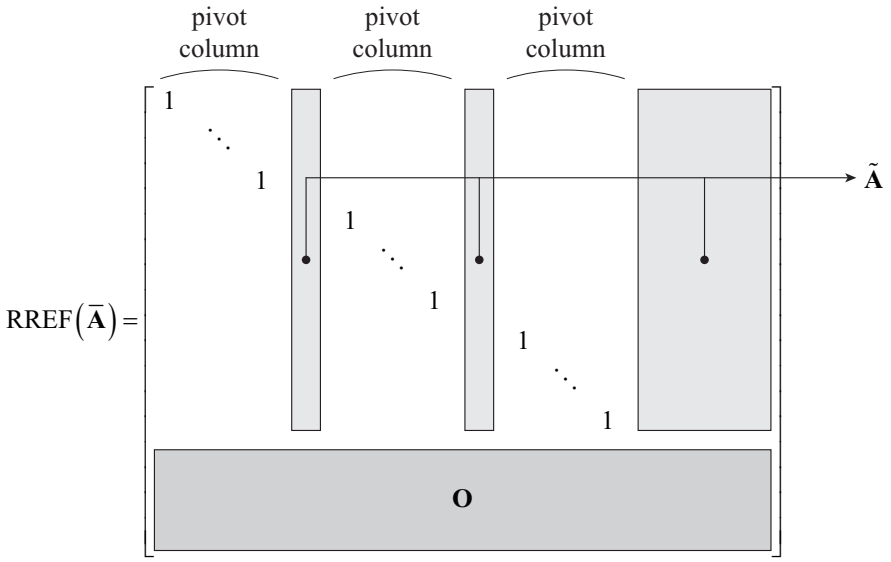

Figure A.1: Reduced row-echelon form of matrix $\bar{\mathbf{A}}$; the leading 1 of each row is pivot, and the gray shaded columns are not the pivot columns.

is written in the same form as Eq. (A.2). Since the existence of $\mathbf{x}$ satisfying Eq. (A.1) is assumed, the rank of $\mathbf{A}$ and $\bar{\mathbf{A}}$ is the same and denoted as $r = \mathrm{rank}(\bar{\mathbf{A}}) = \mathrm{rank}(\mathbf{A})$.

Let $\mathrm{RREF}(\bar{\mathbf{A}}) \in \mathbb{R}^{n \times \bar{n}}$ denote the RREF of $\bar{\mathbf{A}}$. It can be written as in Fig. A.1, and all the components in the last $m - r$ rows are equal to zero. $\mathscr{C}_{\mathrm{pivot}}$ and $\mathscr{C}_{\mathrm{other}}$ are defined as the sets of indices of pivot columns and the other columns of $\mathrm{RREF}(\bar{\mathbf{A}})$, respectively. The number of elements of $\mathscr{C}_{\mathrm{pivot}}$ and $\mathscr{C}_{\mathrm{other}}$ are r and $\bar{n} - r \geq 1$, respectively. As shown in Fig. A.1, $\tilde{\mathbf{A}} \in \mathbb{R}^{r \times (\bar{n} - r)}$ is constructed by assembling the first r components of each column of $\mathrm{RREF}(\bar{\mathbf{A}})$ corresponding to $\mathscr{C}_{\mathrm{other}}$. The columns of $\tilde{\mathbf{A}}$ is arranged in ascending order of the column indices of $\mathrm{RREF}(\bar{\mathbf{A}})$. Here, the vectors $\bar{\mathbf{x}}_{\mathrm{pivot}} \in \mathbb{R}^r$ and $\bar{\mathbf{x}}_{\mathrm{free}} \in \mathbb{R}^{\bar{n} - r}$ are defined as the vectors whose components are the components of $\bar{\mathbf{x}}$ corresponding to the indices in $\mathscr{C}_{\mathrm{pivot}}$ and $\mathscr{C}_{\mathrm{other}}$, respectively, arranged in ascending order of the component indices. Since $\mathrm{RREF}(\bar{\mathbf{A}})$ is obtained from a finite sequence of linear elementary row operation on $\bar{\mathbf{A}}$, Eq. (A.2) is equivalent to the following equation:

$$\begin{bmatrix} \mathbf{I}_r & \tilde{\mathbf{A}} \end{bmatrix} \begin{pmatrix} \bar{\mathbf{x}}_{\mathrm{pivot}} \\ \bar{\mathbf{x}}_{\mathrm{free}} \end{pmatrix} = \bar{\mathbf{x}}_{\mathrm{pivot}} + \tilde{\mathbf{A}} \bar{\mathbf{x}}_{\mathrm{free}} = \mathbf{0} \tag{A.3}$$

Therefore, the independent components and the dependent components of $\bar{\mathbf{x}}$ satisfying Eq. (A.2) are identified as $\bar{\mathbf{x}}_{\mathrm{free}}$ and $\bar{\mathbf{x}}_{\mathrm{pivot}}$, respectively, and $\bar{\mathbf{x}}_{\mathrm{pivot}}$ can be calculated from $\bar{\mathbf{x}}_{\mathrm{free}}$ as follows:

$$\bar{\mathbf{x}}_{\mathrm{pivot}} = -\tilde{\mathbf{A}} \bar{\mathbf{x}}_{\mathrm{free}} \tag{A.4}$$

Note that when $\mathbf{b} \neq \mathbf{0}$; i.e., $\bar{n} = n + 1$, the last 1 in $\bar{\mathbf{x}}$, which is a constant component, is always the last component of $\bar{\mathbf{x}}_{\mathrm{free}}$. In conclusion, the independent components of $\mathbf{x}$ satisfying Eq. (A.1) can be identified as the components corresponding to the first $n - r$ components of $\bar{\mathbf{x}}_{\mathrm{free}}$.

Appendix B

Example of independent nodal coordinates identification

In this appendix, the process of identifying the independent nodal coordinates introduced in Chapter 2 is presented for the single vertex model shown in Fig. B.1. The matrix $\mathbf{C}_{\mathrm{V}}$ for calculating the vertex coordinates from all the nodal coordinates and the matrix $\mathbf{C}_{\mathrm{N}}$ for calculating all the nodal coordinates from the independent nodal coordinates are also shown. When the global indices of vertices and nodes are arranged as shown in Fig. B.1, the edge consistency matrix $\mathbf{C}_{\mathrm{E}} \in \mathbb{R}^{12\times 36}$ is constructed according to Eqs. (2.2) and (2.7) in Chapter 2 as

$$\mathbf{C}_{\mathrm{E}} = \begin{bmatrix} 1 & -1 & 0 & 1 & -1 & 0 & 0 & 0 & 0 & 0 & 0 & 0 \\ 0 & 0 & 1 & -1 & 0 & 1 & -1 & 0 & 0 & 0 & 0 & 0 \\ -1 & 0 & 0 & 0 & 1 & -1 & 0 & 1 & 0 & 0 & 0 & 0 \\ 0 & 1 & -1 & 0 & 0 & 0 & 1 & -1 & 0 & 0 & 0 & 0 \end{bmatrix} \otimes \mathbf{I}_3 \tag{B.1}$$

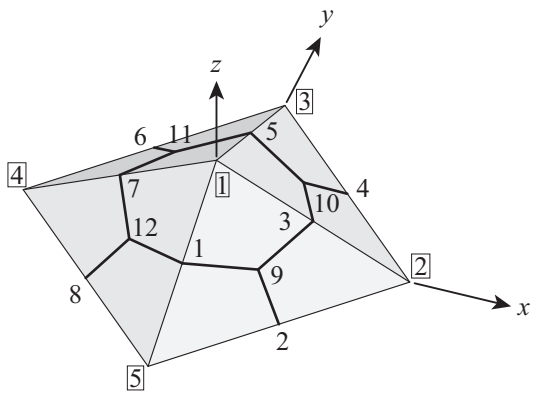

Figure B.1: Vertex and node indices of single vertex model (Each vertex index is surrounded by a rectangle).

where $\mathbf{A} \otimes \mathbf{B} \in \mathbb{R}^{mp \times nq}$ represents the Kronecker product of matrices $\mathbf{A} = [a_{ij}] \in \mathbb{R}^{m \times n}$ and $\mathbf{B} \in \mathbb{R}^{p \times q}$ defined as follows:

$$\mathbf{A} \otimes \mathbf{B} = \begin{bmatrix} a_{11}\mathbf{B} & \dots & a_{1n}\mathbf{B} \\ \vdots & \ddots & \vdots \\ a_{m1}\mathbf{B} & \dots & a_{mn}\mathbf{B} \end{bmatrix}$$

The face consistency matrix $\mathbf{C}_\mathrm{F} \in \mathbb{R}^{12 \times 36}$ is constructed according to Eqs. (2.5), (2.6), and (2.8) as

$$\mathbf{C}_\mathrm{F} = \frac{1}{3} \begin{bmatrix} 1 & 1 & 1 & 0 & 0 & 0 & 0 & 0 & -3 & 0 & 0 & 0 \\ 0 & 0 & 1 & 1 & 1 & 0 & 0 & 0 & 0 & -3 & 0 & 0 \\ 0 & 0 & 0 & 0 & 1 & 1 & 1 & 0 & 0 & 0 & -3 & 0 \\ 1 & 0 & 0 & 0 & 0 & 0 & 1 & 1 & 0 & 0 & 0 & -3 \end{bmatrix} \otimes \mathbf{I}_3 \tag{B.2}$$

The RREF of the node consistency matrix $\mathbf{C}_\mathrm{N} = \left[\mathbf{C}_\mathrm{E}^\mathsf{T}\ \mathbf{C}_\mathrm{F}^\mathsf{T}\right]^\mathsf{T} \in \mathbb{R}^{24 \times 36}$ is calculated as follows [62]:

$$\mathrm{RREF}(\mathbf{C}_\mathrm{N}) = \frac{1}{2} \begin{bmatrix} 2 & 0 & 0 & 0 & 0 & 0 & 2 & 2 & 0 & 0 & 0 & -6 \\ 0 & 2 & 0 & 0 & 0 & 0 & 0 & -2 & 0 & -3 & 3 & 0 \\ 0 & 0 & 2 & 0 & 0 & 0 & -2 & 0 & 0 & -3 & 3 & 0 \\ 0 & 0 & 0 & 2 & 0 & 0 & 0 & -2 & 0 & -3 & 0 & 3 \\ 0 & 0 & 0 & 0 & 2 & 0 & 2 & 2 & 0 & 0 & -3 & -3 \\ 0 & 0 & 0 & 0 & 0 & 2 & 0 & -2 & 0 & 0 & -3 & 3 \\ 0 & 0 & 0 & 0 & 0 & 0 & 0 & 0 & 2 & -2 & 2 & -2 \\ 0 & 0 & 0 & 0 & 0 & 0 & 0 & 0 & 0 & 0 & 0 & 0 \end{bmatrix} \otimes \mathbf{I}_3 \tag{B.3}$$

Therefore, the coordinates of nodes 1–6 and 9 correspond to the pivots of $\mathrm{RREF}(\mathbf{C}_\mathrm{N})$, and the independent coordinates are determined as those of nodes 7, 8 and 10–12. The position vectors of nodes 1–6 and 9 denoted by $\boldsymbol{\zeta}_1, \dots, \boldsymbol{\zeta}_6$, and $\boldsymbol{\zeta}_9 \in \mathbb{R}^3$ are determined by those of nodes 7, 8, and 10–12 denoted by $\boldsymbol{\zeta}_7$, $\boldsymbol{\zeta}_8$, $\boldsymbol{\zeta}_{10}$, $\boldsymbol{\zeta}_{11}$, and $\boldsymbol{\zeta}_{12} \in \mathbb{R}^3$ as follows:

$$\begin{pmatrix} \boldsymbol{\zeta}_1 \\ \boldsymbol{\zeta}_2 \\ \boldsymbol{\zeta}_3 \\ \boldsymbol{\zeta}_4 \\ \boldsymbol{\zeta}_5 \\ \boldsymbol{\zeta}_6 \\ \boldsymbol{\zeta}_9 \end{pmatrix} = -\frac{1}{2} \begin{bmatrix} 2 & 2 & 0 & 0 & -6 \\ 0 & -2 & -3 & 3 & 0 \\ -2 & 0 & -3 & 3 & 0 \\ 0 & -2 & -3 & 0 & 3 \\ 2 & 2 & 0 & -3 & -3 \\ 0 & -2 & 0 & -3 & 3 \\ 0 & 0 & -2 & 2 & -2 \end{bmatrix} \otimes \mathbf{I}_3 \begin{pmatrix} \boldsymbol{\zeta}_7 \\ \boldsymbol{\zeta}_8 \\ \boldsymbol{\zeta}_{10} \\ \boldsymbol{\zeta}_{11} \\ \boldsymbol{\zeta}_{12} \end{pmatrix} \tag{B.4}$$

Consequently, the matrix $\mathbf{C}_{\mathrm{A}} \in \mathbb{R}^{36\times 15}$ for calculating all the nodal coordinates from the independent nodal coordinates is written as

$$\mathbf{C}_{\mathrm{A}} = -\frac{1}{2}\begin{bmatrix} 2 & 2 & 0 & 0 & -6 \\ 0 & -2 & -3 & 3 & 0 \\ -2 & 0 & -3 & 3 & 0 \\ 0 & -2 & -3 & 0 & 3 \\ 2 & 2 & 0 & -3 & -3 \\ 0 & -2 & 0 & -3 & 3 \\ 2 & 0 & 0 & 0 & 0 \\ 0 & 2 & 0 & 0 & 0 \\ 0 & 0 & -2 & 2 & -2 \\ 0 & 0 & 2 & 0 & 0 \\ 0 & 0 & 0 & 2 & 0 \\ 0 & 0 & 0 & 0 & 2 \end{bmatrix} \otimes \mathbf{I}_3 \tag{B.5}$$

On the other hand, according to Eqs. (2.17) and (2.18) in Chapter 2, the matrix $\mathbf{C}_{\mathrm{V}} \in \mathbb{R}^{15\times 36}$ for calculating the vertex coordinates from all the nodal coordinates is constructed as follows:

$$\mathbf{C}_{\mathrm{V}} = \frac{1}{4}\begin{bmatrix} 2 & -1 & 2 & -1 & 2 & -1 & 2 & -1 & 0 & 0 & 0 & 0 \\ -2 & 2 & 4 & 2 & -2 & 0 & 0 & 0 & 0 & 0 & 0 & 0 \\ 0 & 0 & -2 & 2 & 4 & 2 & -2 & 0 & 0 & 0 & 0 & 0 \\ -2 & 0 & 0 & 0 & -2 & 2 & 4 & 2 & 0 & 0 & 0 & 0 \\ 4 & 2 & -2 & 0 & 0 & 0 & -2 & 2 & 0 & 0 & 0 & 0 \end{bmatrix} \otimes \mathbf{I}_3 \tag{B.6}$$

Therefore, the position vectors of vertices 1–5 denoted by $\boldsymbol{\xi}_1, \ldots, \boldsymbol{\xi}_5 \in \mathbb{R}^3$ are determined by the independent noral coordinates as follows:

$$\begin{pmatrix} \boldsymbol{\xi}_1 \\ \boldsymbol{\xi}_2 \\ \boldsymbol{\xi}_3 \\ \boldsymbol{\xi}_4 \\ \boldsymbol{\xi}_5 \end{pmatrix} = -\frac{1}{2}\begin{bmatrix} 2 & 3 & 0 & 0 & -6 \\ -4 & -4 & -6 & 6 & 6 \\ 2 & 0 & 0 & -6 & 0 \\ 0 & -2 & 0 & 0 & 6 \\ 2 & 2 & 0 & 0 & -6 \end{bmatrix} \otimes \mathbf{I}_3 \begin{pmatrix} \boldsymbol{\zeta}_7 \\ \boldsymbol{\zeta}_8 \\ \boldsymbol{\zeta}_{10} \\ \boldsymbol{\zeta}_{11} \\ \boldsymbol{\zeta}_{12} \end{pmatrix} \tag{B.7}$$

Appendix C

Rotation matrix and its derivatives

The Rodrigues' rotation matrix $\mathbf{R}(\boldsymbol{\theta}) \in \mathbb{R}^{3\times 3}$ with respect to a rotation vector $\boldsymbol{\theta} = \theta\mathbf{n}$ that rotates an arbitrary vector in three-dimensional space by an angle θ ($\theta \geq 0$) around the rotation axis $\mathbf{n} = (n_1, n_2, n_3)^\mathsf{T} \in \mathbb{R}^3$ ($\|\mathbf{n}\| = 1$) is written as follows [64]:

$$\begin{aligned}\mathbf{R}(\boldsymbol{\theta}) &= \cos\theta\mathbf{I}_3 + (1-\cos\theta)\mathbf{n}\mathbf{n}^\mathsf{T} + \sin\theta[\mathbf{n}]_\times \\ &= \begin{bmatrix} n_1^2(1-\cos\theta)+\cos\theta & n_1n_2(1-\cos\theta)-n_3\sin\theta & n_3n_1(1-\cos\theta)+n_2\sin\theta \\ n_1n_2(1-\cos\theta)+n_3\sin\theta & n_2^2(1-\cos\theta)+\cos\theta & n_2n_3(1-\cos\theta)-n_1\sin\theta \\ n_3n_1(1-\cos\theta)-n_2\sin\theta & n_2n_3(1-\cos\theta)+n_1\sin\theta & n_3^2(1-\cos\theta)+\cos\theta \end{bmatrix}\end{aligned} \tag{C.1}$$

If θ and $\mathbf{n}$ are considered as functions of the vector $\boldsymbol{\theta} = (\theta_1, \theta_2, \theta_3)^\mathsf{T}$, the following equations hold:

$$\begin{aligned}\theta &= \|\boldsymbol{\theta}\| = \sqrt{\theta_1^2+\theta_2^2+\theta_3^2} \\ \mathbf{n} &= \frac{\boldsymbol{\theta}}{\theta} = \frac{\boldsymbol{\theta}}{\sqrt{\theta_1^2+\theta_2^2+\theta_3^2}}\end{aligned}$$

Accordingly, the first-order derivatives of θ and $\mathbf{n}$ with respect to θ_l ($l = 1,2,3$) are calculated for positive θ as

$$\frac{\partial\theta}{\partial\theta_l} = \frac{\theta_l}{\sqrt{\theta_1^2+\theta_2^2+\theta_3^2}} = n_l \tag{C.2}$$

$$\frac{\partial\mathbf{n}}{\partial\theta_l} = \frac{1}{\theta^2}\left(\theta\frac{\partial\boldsymbol{\theta}}{\partial\theta_l} - \boldsymbol{\theta}\frac{\partial\theta}{\partial\theta_l}\right) = \frac{1}{\theta}(\mathbf{e}_l - n_l\mathbf{n}) \tag{C.3}$$

where $\mathbf{e}_1 = (1,0,0)^\mathsf{T}$, $\mathbf{e}_2 = (0,1,0)^\mathsf{T}$, and $\mathbf{e}_3 = (0,0,1)^\mathsf{T}$. In addition, the derivatives of n_k ($k = 1,2,3$) with respect to θ_l ($l = 1,2,3$) are calculated as

$$\frac{\partial n_k}{\partial\theta_l} = \frac{1}{\theta}(\delta_{kl} - n_k n_l) \tag{C.4}$$

where δ_{kl} is the Kronecker delta. According to Eqs. (C.2) and (C.3), the following equations hold for $l = 1,2,3$:

$$\frac{\partial}{\partial\theta_l}\left(\mathbf{n}\mathbf{n}^\mathsf{T}\right) = \frac{1}{\theta}\left(\mathbf{e}_l\mathbf{n}^\mathsf{T} + \mathbf{n}\mathbf{e}_l^\mathsf{T} - 2n_l\mathbf{n}\mathbf{n}^\mathsf{T}\right) \tag{C.5}$$

$$\frac{\partial}{\partial\theta_l}[\mathbf{n}]_\times = \frac{1}{\theta}([\mathbf{e}_l]_\times - n_l[\mathbf{n}]_\times) \tag{C.6}$$

$$\frac{\partial\cos\theta}{\partial\theta_l} = -n_l\sin\theta \tag{C.7}$$

$$\frac{\partial\sin\theta}{\partial\theta_l} = n_l\cos\theta \tag{C.8}$$

Therefore, the first- and second-order derivatives of $\mathbf{R}(\boldsymbol{\theta})$ are calculated as follows:

$$\begin{aligned}\frac{\partial\mathbf{R}(\boldsymbol{\theta})}{\partial\theta_l} =& -n_l\sin\theta\mathbf{I}_3 + n_l\left(\sin\theta - 2\frac{1-\cos\theta}{\theta}\right)\mathbf{n}\mathbf{n}^\mathsf{T} \\ &+ n_l\left(\cos\theta - \frac{\sin\theta}{\theta}\right)[\mathbf{n}]_\times + \frac{1-\cos\theta}{\theta}\left(\mathbf{e}_l\mathbf{n}^\mathsf{T} + \mathbf{n}\mathbf{e}_l^\mathsf{T}\right) + \frac{\sin\theta}{\theta}[\mathbf{e}_l]_\times\end{aligned} \tag{C.9}$$

$$\begin{aligned}\frac{\partial^2\mathbf{R}(\boldsymbol{\theta})}{\partial\theta_k\partial\theta_l} =& -\left\{n_kn_l\cos\theta + (\delta_{kl} - n_kn_l)\frac{\sin\theta}{\theta}\right\}\mathbf{I}_3 \\ &+ \left\{n_kn_l\cos\theta + (\delta_{kl} - 5n_kn_l)\frac{\sin\theta}{\theta} - 2(\delta_{kl} - 4n_kn_l)\frac{1-\cos\theta}{\theta^2}\right\}\mathbf{n}\mathbf{n}^\mathsf{T} \\ &+ \left\{-n_kn_l\sin\theta + (\delta_{kl} - 3n_kn_l)\left(\frac{\cos\theta}{\theta} - \frac{\sin\theta}{\theta^2}\right)\right\}[\mathbf{n}]_\times \\ &+ \left(\frac{\sin\theta}{\theta} - 2\frac{1-\cos\theta}{\theta^2}\right)\left\{(n_k\mathbf{e}_l + n_l\mathbf{e}_k)\mathbf{n}^\mathsf{T} + \mathbf{n}(n_k\mathbf{e}_l + n_l\mathbf{e}_k)^\mathsf{T}\right\} \\ &+ \frac{1-\cos\theta}{\theta^2}\left(\mathbf{e}_k\mathbf{e}_l^\mathsf{T} + \mathbf{e}_l\mathbf{e}_k^\mathsf{T}\right) \\ &+ \left(\frac{\cos\theta}{\theta} - \frac{\sin\theta}{\theta^2}\right)(n_k[\mathbf{e}_l]_\times + n_l[\mathbf{e}_k]_\times)\end{aligned} \tag{C.10}$$

Since Eqs. (C.9) and (C.10) are valid only when $\theta > 0$, the derivatives of $\mathbf{R}(\boldsymbol{\theta})$ for $\theta = 0$ is calculated by utilizing the following relations:

$$\begin{aligned}\lim_{\theta\to0}\frac{1-\cos\theta}{\theta} &= 0 \\ \lim_{\theta\to0}\frac{\sin\theta}{\theta} &= 1 \\ \lim_{\theta\to0}\frac{1-\cos\theta}{\theta^2} &= \frac{1}{2} \\ \lim_{\theta\to0}\left(\frac{\cos\theta}{\theta} - \frac{\sin\theta}{\theta^2}\right) &= 0\end{aligned}$$

Hence, when $\theta = 0$ the first- and second-order derivatives of $\mathbf{R}(\boldsymbol{\theta})$ are calculated as follows:

$$\frac{\partial\mathbf{R}(\mathbf{0})}{\partial\theta_l} = [\mathbf{e}_l]_\times \tag{C.11}$$

$$\frac{\partial^2\mathbf{R}(\boldsymbol{\theta})}{\partial\theta_k\partial\theta_l} = -\delta_{kl}\mathbf{I}_3 + \frac{1}{2}\left(\mathbf{e}_k\mathbf{e}_l^\mathsf{T} + \mathbf{e}_l\mathbf{e}_k^\mathsf{T}\right) \tag{C.12}$$

Appendix D

Derivatives of incompatibility vector

This appendix shows the first- and second-order derivatives of the components of the incompatibility vector $\mathbf{G}(\mathbf{W})$ with respect to the components of the generalized displacement vector $\mathbf{W}$. It is assumed that the j-th end ($j = 1,2$) of member i ($= 1,\ldots,N_{\mathrm{M}}$) is connected to node k ($= 1,\ldots,N_{\mathrm{N}}$) rigidly or via hinge h ($= 1,\ldots,N_{\mathrm{H}}$) where N_{M}, N_{N}, and N_{H} are the number of nodes, members, and hinges of a frame model, respectively. According to Eq. (2.36), the non-zero first-order derivatives of the translational incompatibility vector $\Delta\mathbf{U}_{ij}$ at the j-th end of member i are calculated for $l = 1,2,3$ as follows:

$$\frac{\partial \Delta\mathbf{U}_{ij}}{\partial V_i^{(l)}} = -\mathbf{e}_l \tag{D.1}$$

$$\frac{\partial \Delta\mathbf{U}_{ij}}{\partial \Psi_i^{(l)}} = -\frac{\partial \mathbf{R}(\boldsymbol{\Psi}_i)}{\partial \Psi_i^{(l)}}\mathbf{r}_{ij} \tag{D.2}$$

$$\frac{\partial \Delta\mathbf{U}_{ij}}{\partial U_k^{(l)}} = \mathbf{e}_l \tag{D.3}$$

Note that the derivatives with respect to $\Theta_k^{(l)}$, φ_h are equal to zero for arbitrary $k = 1,\ldots,N_{\mathrm{N}}$, $h = 1,\ldots,N_{\mathrm{H}}$, and $l = 1,2,3$. In addition, the derivatives with respect to $V_{i'}^{(l)}$, $\Psi_{i'}^{(l)}$, $U_{k'}^{(l)}$ are also equal to zero when $i' \neq i$ and $k' \neq k$. Accordingly, the second-order derivative of $\Delta\mathbf{U}_{ij}$ is $\mathbf{0}$ except for the following term:

$$\frac{\partial^2 \Delta\mathbf{U}_{ij}}{\partial \Psi_i^{(l)} \partial \Psi_i^{(l')}} = -\frac{\partial^2 \mathbf{R}(\boldsymbol{\Psi}_i)}{\partial \Psi_i^{(l)} \partial \Psi_i^{(l')}}\mathbf{r}_{ij} \tag{D.4}$$

When j-th end of member i is rigidly connected to node k, the non-zero first-order derivatives of the rotational incompatibility vector $\Delta\boldsymbol{\Theta}_{ij}$ defined in the first equation of Eq. (2.37) are calculated as follows:

$$\frac{\partial \Delta\boldsymbol{\Theta}_{ij}}{\partial \Psi_i^{(l)}} = -\mathbf{e}_l \tag{D.5}$$

$$\frac{\partial \Delta\boldsymbol{\Theta}_{ij}}{\partial \Theta_k^{(l)}} = \mathbf{e}_l \tag{D.6}$$

Therefore, the second-order derivative of $\Delta\boldsymbol{\Theta}_{ij}$ with respect to any component of $\mathbf{W}$ is zero if the j-th end of member i is the rigid end. According to Eqs. (2.34), (2.35), and (2.37), when the j-th end of member i is connected to node k via hinge h, the non-zero first-order derivatives of $\Delta\boldsymbol{\Theta}_{ij} = \boldsymbol{\Phi}_{ij}(\boldsymbol{\Psi}_i, \boldsymbol{\Theta}_k, \varphi_h)$ are calculated as follows:

$$\frac{\partial \Phi_{ij}^{(1)}}{\partial \Psi_i^{(l)}} = \left(\frac{\partial \mathbf{R}(\boldsymbol{\Psi}_i)}{\partial \Psi_i^{(l)}} \boldsymbol{\tau}_h^{\langle 1\rangle}\right) \cdot \left(\mathbf{R}(\boldsymbol{\Theta}_k)\boldsymbol{\tau}_h^{\langle 2\rangle}\right) \tag{D.7}$$

$$\frac{\partial \Phi_{ij}^{(2)}}{\partial \Psi_i^{(l)}} = \left(\frac{\partial \mathbf{R}(\boldsymbol{\Psi}_i)}{\partial \Psi_i^{(l)}} \boldsymbol{\tau}_h^{\langle 1\rangle}\right) \cdot \left(\mathbf{R}(\boldsymbol{\Theta}_k)\boldsymbol{\tau}_h^{\langle 3\rangle}\right) \tag{D.8}$$

$$\frac{\partial \Phi_{ij}^{(3)}}{\partial \Psi_i^{(l)}} = \left(\frac{\partial \mathbf{R}(\boldsymbol{\Psi}_i)}{\partial \Psi_i^{(l)}} \boldsymbol{\tau}_h^{\langle 2\rangle}\right) \cdot \left\{\sin\varphi_h \left(\mathbf{R}(\boldsymbol{\Theta}_k)\boldsymbol{\tau}_h^{\langle 2\rangle}\right) + \cos\varphi_h \left(\mathbf{R}(\boldsymbol{\Theta}_k)\boldsymbol{\tau}_h^{\langle 3\rangle}\right)\right\} \tag{D.9}$$

$$\frac{\partial \Phi_{ij}^{(1)}}{\partial \Theta_k^{(l)}} = \left(\mathbf{R}(\boldsymbol{\Psi}_i)\boldsymbol{\tau}_h^{\langle 1\rangle}\right) \cdot \left(\frac{\partial \mathbf{R}(\boldsymbol{\Theta}_k)}{\partial \Theta_k^{(l)}} \boldsymbol{\tau}_h^{\langle 2\rangle}\right) \tag{D.10}$$

$$\frac{\partial \Phi_{ij}^{(2)}}{\partial \Theta_k^{(l)}} = \left(\mathbf{R}(\boldsymbol{\Psi}_i)\boldsymbol{\tau}_h^{\langle 1\rangle}\right) \cdot \left(\frac{\partial \mathbf{R}(\boldsymbol{\Theta}_k)}{\partial \Theta_k^{(l)}} \boldsymbol{\tau}_h^{\langle 3\rangle}\right) \tag{D.11}$$

$$\frac{\partial \Phi_{ij}^{(3)}}{\partial \Theta_k^{(l)}} = \left(\mathbf{R}(\boldsymbol{\Psi}_i)\boldsymbol{\tau}_h^{\langle 2\rangle}\right) \cdot \left\{\sin\varphi_h \left(\frac{\partial \mathbf{R}(\boldsymbol{\Theta}_k)}{\partial \Theta_k^{(l)}} \boldsymbol{\tau}_h^{\langle 2\rangle}\right) + \cos\varphi_h \left(\frac{\partial \mathbf{R}(\boldsymbol{\Theta}_k)}{\partial \Theta_k^{(l)}} \boldsymbol{\tau}_h^{\langle 3\rangle}\right)\right\} \tag{D.12}$$

$$\frac{\partial \Phi_{ij}^{(3)}}{\partial \varphi_{h_{ij}}} = \left(\mathbf{R}(\boldsymbol{\Psi}_i)\boldsymbol{\tau}_h^{\langle 2\rangle}\right) \cdot \left\{\cos\varphi_h \left(\mathbf{R}(\boldsymbol{\Theta}_k)\boldsymbol{\tau}_h^{\langle 2\rangle}\right) - \sin\varphi_h \left(\mathbf{R}(\boldsymbol{\Theta}_k)\boldsymbol{\tau}_h^{\langle 3\rangle}\right)\right\} \tag{D.13}$$

Therefore, the second-order derivatives of $\boldsymbol{\Phi}_{ij}$ are $\mathbf{0}$ except for the following terms:

$$\frac{\partial^2 \Phi_{ij}^{(1)}}{\partial \Psi_i^{(l)} \partial \Psi_i^{(l')}} = \left(\frac{\partial^2 \mathbf{R}(\boldsymbol{\Psi}_i)}{\partial \Psi_i^{(l)} \partial \Psi_i^{(l')}} \boldsymbol{\tau}_h^{\langle 1\rangle}\right) \cdot \left(\mathbf{R}(\boldsymbol{\Theta}_k)\boldsymbol{\tau}_h^{\langle 2\rangle}\right) \tag{D.14}$$

$$\frac{\partial^2 \Phi_{ij}^{(2)}}{\partial \Psi_i^{(l)} \partial \Psi_i^{(l')}} = \left(\frac{\partial^2 \mathbf{R}(\boldsymbol{\Psi}_i)}{\partial \Psi_i^{(l)} \partial \Psi_i^{(l')}} \boldsymbol{\tau}_h^{\langle 1\rangle}\right) \cdot \left(\mathbf{R}(\boldsymbol{\Theta}_k)\boldsymbol{\tau}_h^{\langle 3\rangle}\right) \tag{D.15}$$

$$\frac{\partial^2 \Phi_{ij}^{(3)}}{\partial \Psi_i^{(l)} \partial \Psi_i^{(l')}} = \left(\frac{\partial^2 \mathbf{R}(\boldsymbol{\Psi}_i)}{\partial \Psi_i^{(l)} \partial \Psi_i^{(l')}} \boldsymbol{\tau}_h^{\langle 2\rangle}\right) \cdot \left\{\sin\varphi_h \left(\mathbf{R}(\boldsymbol{\Theta}_k)\boldsymbol{\tau}_h^{\langle 2\rangle}\right) + \cos\varphi_h \left(\mathbf{R}(\boldsymbol{\Theta}_k)\boldsymbol{\tau}_h^{\langle 3\rangle}\right)\right\} \tag{D.16}$$

$$\frac{\partial^2 \Phi_{ij}^{(1)}}{\partial \Theta_k^{(l)} \partial \Theta_k^{(l')}} = \left(\mathbf{R}(\boldsymbol{\Psi}_i)\boldsymbol{\tau}_h^{\langle 1\rangle}\right) \cdot \left(\frac{\partial^2 \mathbf{R}(\boldsymbol{\Theta}_k)}{\partial \Theta_k^{(l)} \partial \Theta_k^{(l')}} \boldsymbol{\tau}_h^{\langle 2\rangle}\right) \tag{D.17}$$

$$\frac{\partial^2 \Phi_{ij}^{(2)}}{\partial \Theta_k^{(l)} \partial \Theta_k^{(l')}} = \left(\mathbf{R}(\boldsymbol{\Psi}_i)\boldsymbol{\tau}_h^{\langle 1\rangle}\right) \cdot \left(\frac{\partial^2 \mathbf{R}(\boldsymbol{\Theta}_k)}{\partial \Theta_k^{(l)} \partial \Theta_k^{(l')}} \boldsymbol{\tau}_h^{\langle 3\rangle}\right) \tag{D.18}$$

$$\frac{\partial^2 \Phi_{ij}^{(3)}}{\partial \Theta_k^{(l)} \partial \Theta_k^{(l')}} = \left(\mathbf{R}(\boldsymbol{\Psi}_i)\boldsymbol{\tau}_h^{\langle 2\rangle}\right) \cdot \left\{\sin\varphi_h \left(\frac{\partial^2 \mathbf{R}(\boldsymbol{\Theta}_k)}{\partial \Theta_k^{(l)} \partial \Theta_k^{(l')}} \boldsymbol{\tau}_h^{\langle 2\rangle}\right) + \cos\varphi_h \left(\frac{\partial^2 \mathbf{R}(\boldsymbol{\Theta}_k)}{\partial \Theta_k^{(l)} \partial \Theta_k^{(l')}} \boldsymbol{\tau}_h^{\langle 3\rangle}\right)\right\} \tag{D.19}$$

$$\frac{\partial^2 \Phi_{ij}^{(3)}}{\partial \varphi_h^2} = -\left(\mathbf{R}(\boldsymbol{\Psi}_i)\boldsymbol{\tau}_h^{\langle 2\rangle}\right) \cdot \left\{\sin\varphi_h \left(\mathbf{R}(\boldsymbol{\Theta}_k)\boldsymbol{\tau}_h^{\langle 2\rangle}\right) + \cos\varphi_h \left(\mathbf{R}(\boldsymbol{\Theta}_k)\boldsymbol{\tau}_h^{\langle 3\rangle}\right)\right\} = -\Phi_{ij}^{(3)} \tag{D.20}$$

$$\frac{\partial^2 \Phi_{ij}^{(1)}}{\partial \Psi_i^{(l)} \partial \Theta_k^{(l')}} = \left(\frac{\partial \mathbf{R}(\boldsymbol{\Psi}_i)}{\partial \Psi_i^{(l)}} \boldsymbol{\tau}_h^{\langle 1\rangle}\right) \cdot \left(\frac{\partial \mathbf{R}(\boldsymbol{\Theta}_k)}{\partial \Theta_k^{(l')}} \boldsymbol{\tau}_h^{\langle 2\rangle}\right) \tag{D.21}$$

$$\frac{\partial^2 \Phi_{ij}^{(2)}}{\partial \Psi_i^{(l)} \partial \Theta_k^{(l')}} = \left(\frac{\partial \mathbf{R}(\boldsymbol{\Psi}_i)}{\partial \Psi_i^{(l)}} \boldsymbol{\tau}_h^{\langle 1 \rangle} \right) \cdot \left(\frac{\partial \mathbf{R}(\boldsymbol{\Theta}_k)}{\partial \Theta_k^{(l')}} \boldsymbol{\tau}_h^{\langle 3 \rangle} \right) \tag{D.22}$$

$$\frac{\partial^2 \Phi_{ij}^{(3)}}{\partial \Psi_i^{(l)} \partial \Theta_k^{(l')}} = \left(\frac{\partial \mathbf{R}(\boldsymbol{\Psi}_i)}{\partial \Psi_i^{(l)}} \boldsymbol{\tau}_h^{\langle 2 \rangle} \right) \cdot \left\{ \sin \varphi_h \left(\frac{\partial \mathbf{R}(\boldsymbol{\Theta}_k)}{\partial \Theta_k^{(l')}} \boldsymbol{\tau}_h^{\langle 2 \rangle} \right) + \cos \varphi_h \left(\frac{\partial \mathbf{R}(\boldsymbol{\Theta}_k)}{\partial \Theta_k^{(l')}} \boldsymbol{\tau}_h^{\langle 3 \rangle} \right) \right\} \tag{D.23}$$

$$\frac{\partial^2 \Phi_{ij}^{(3)}}{\partial \Psi_i^{(l)} \partial \varphi_h} = \left(\frac{\partial \mathbf{R}(\boldsymbol{\Psi}_i)}{\partial \Psi_i^{(l)}} \boldsymbol{\tau}_h^{\langle 2 \rangle} \right) \cdot \left\{ \cos \varphi_h \left(\mathbf{R}(\boldsymbol{\Theta}_k) \boldsymbol{\tau}_h^{\langle 2 \rangle} \right) - \sin \varphi_h \left(\mathbf{R}(\boldsymbol{\Theta}_k) \boldsymbol{\tau}_h^{\langle 3 \rangle} \right) \right\} \tag{D.24}$$

$$\frac{\partial^2 \Phi_{ij}^{(3)}}{\partial \Theta_k^{(l)} \partial \varphi_h} = \left(\mathbf{R}(\boldsymbol{\Psi}_i) \boldsymbol{\tau}_h^{\langle 2 \rangle} \right) \cdot \left\{ \cos \varphi_h \left(\frac{\partial \mathbf{R}(\boldsymbol{\Theta}_k)}{\partial \Theta_k^{(l')}} \boldsymbol{\tau}_h^{\langle 2 \rangle} \right) - \sin \varphi_h \left(\frac{\partial \mathbf{R}(\boldsymbol{\Theta}_k)}{\partial \Theta_k^{(l')}} \boldsymbol{\tau}_h^{\langle 3 \rangle} \right) \right\} \tag{D.25}$$

Appendix E

Singular value decomposition for infinitesimal mechanism analysis

The number of components of the generalized displacement vector $\mathbf{W}$ and the incompatibility vector $\mathbf{G}(\mathbf{W})$ are denoted by N_{W} and N_{G}, respectively. As explained in Chapters 2 and 5, a first-order infinitesimal mechanism $\mathbf{W}' \in \mathbb{R}^{N_{\mathrm{W}}}$ and a second-order infinitesimal mechanism $\mathbf{W}'' \in \mathbb{R}^{N_{\mathrm{W}}}$ satisfy following equations [33, 40] when the displacement of the frame model is $\mathbf{W}$:

$$\boldsymbol{\Gamma}^{(1)}(\mathbf{W})\mathbf{W}' = \mathbf{0} \tag{E.1}$$

$$\boldsymbol{\Gamma}^{(1)}(\mathbf{W})\mathbf{W}'' + \left[\boldsymbol{\Gamma}^{(2)}(\bar{\mathbf{W}})\mathbf{W}'\right]\mathbf{W}' = \mathbf{0} \tag{E.2}$$

Here, $\boldsymbol{\Gamma}^{(1)}(\mathbf{W})$ and $\boldsymbol{\Gamma}^{(2)}(\mathbf{W})$ are the $N_{\mathrm{G}} \times N_{\mathrm{W}}$ matrix whose (i,j) component is $\partial G_i(\mathbf{W})/\partial W_j$ and the order-three tensor of size $N_{\mathrm{G}} \times N_{\mathrm{W}} \times N_{\mathrm{W}}$ whose (i,j,k) component is $\partial^2 G_i(\mathbf{W})/\partial W_j \partial W_k$, respectively, where $G_i(\mathbf{W})$ and W_j are the i-th component of $\mathbf{G}(\mathbf{W})$ and the j-th component $\mathbf{W}$, respectively. In the following, the argument $(\mathbf{W})$ is omitted for the simple expression.

When the rank of $\boldsymbol{\Gamma}^{(1)}$ is denoted by r_Γ and N_{D} and N_{S} are defined as $N_{\mathrm{D}} = N_{\mathrm{W}} - r_\Gamma$ and $N_{\mathrm{S}} = N_{\mathrm{G}} - r_\Gamma$, $\boldsymbol{\Gamma}^{(1)}$ is decomposed as follows by the singular value decomposition [63]:

$$\boldsymbol{\Gamma}^{(1)} = \begin{bmatrix} \boldsymbol{\upsilon}_1 & \cdots & \boldsymbol{\upsilon}_{N_{\mathrm{G}}} \end{bmatrix} \begin{bmatrix} \mathrm{diag}(\mu_1, \ldots, \mu_{r_\Gamma}) & \mathbf{O}_{r_\Gamma \times N_{\mathrm{D}}} \\ \mathbf{O}_{N_{\mathrm{S}} \times r_\Gamma} & \mathbf{O}_{N_{\mathrm{S}} \times N_{\mathrm{D}}} \end{bmatrix} \begin{bmatrix} \boldsymbol{\eta}_1^{\mathsf{T}} \\ \vdots \\ \boldsymbol{\eta}_{N_{\mathrm{W}}}^{\mathsf{T}} \end{bmatrix} \tag{E.3}$$

where $\mu_1, \ldots, \mu_{r_\Gamma}$ are the singular values ordered as $\mu_1 \geq \cdots \geq \mu_{r_\Gamma}$. The left singular vectors $\boldsymbol{\upsilon}_1, \ldots, \boldsymbol{\upsilon}_{N_{\mathrm{G}}} \in \mathbb{R}^{N_{\mathrm{G}}}$ and the right singular vectors $\boldsymbol{\eta}_1, \ldots, \boldsymbol{\eta}_{N_{\mathrm{W}}} \in \mathbb{R}^{N_{\mathrm{W}}}$ are the orthonormal bases of the N_{G} and N_{W} dimensional vector spaces, respectively. Then, they satisfy the following equations:

$$\boldsymbol{\Gamma}^{(1)}\boldsymbol{\eta}_j = \begin{cases} \mu_j \boldsymbol{\upsilon}_j & (j = 1, \ldots, r_\Gamma) \\ \mathbf{0} & (j = r_\Gamma + 1, \ldots, N_{\mathrm{W}}) \end{cases} \tag{E.4}$$

$$\boldsymbol{\Gamma}^{(1)\mathsf{T}}\boldsymbol{\upsilon}_i = \begin{cases} \mu_i \boldsymbol{\eta}_i & (i = 1, \ldots, r_\Gamma) \\ \mathbf{0} & (j = r_\Gamma + 1, \ldots, N_{\mathrm{G}}) \end{cases} \tag{E.5}$$

According to Eqs. (E.1) and (E.4), when $r_\Gamma < N_\mathrm{W}$, a first-order infinitesimal mechanism $\mathbf{W}'$ can be represented as the linear combination of the right singular vectors $\boldsymbol{\eta}_{r_\Gamma+1},\ldots,\boldsymbol{\eta}_{N_\mathrm{W}}$ corresponding to the zero singular values; i.e., $\mathbf{W}'$ is orthogonal to $\boldsymbol{\eta}_1,\ldots,\boldsymbol{\eta}_{r_\Gamma}$. In addition, if non-zero vectors $\mathbf{W}'$ and $\mathbf{W}''$ satisfying Eqs. (E.1) and (E.1) exist, $\left[\boldsymbol{\Gamma}^{(2)}(\bar{\mathbf{W}})\mathbf{W}'\right]\mathbf{W}'$ needs to be orthogonal to the left singular vectors $\boldsymbol{\upsilon}_{r_\Gamma+1},\ldots,\boldsymbol{\upsilon}_{N_\mathrm{G}}$ corresponding to the zero singular values since the non-zero vector $\boldsymbol{\Gamma}^{(1)}(\mathbf{W})\mathbf{W}''$ is orthogonal to them according to Eq. (E.4); i.e., $\boldsymbol{\upsilon}_i^\mathsf{T}\left[\boldsymbol{\Gamma}^{(2)}(\bar{\mathbf{W}})\mathbf{W}'\right]\mathbf{W}' = 0$ holds for all $i = r_\Gamma+1,\ldots,N_\mathrm{G}$. Conversely, if a non-zero $\mathbf{W}'$ satisfies Eq. (E.1) and $\boldsymbol{\upsilon}_i^\mathsf{T}\left[\boldsymbol{\Gamma}^{(2)}(\bar{\mathbf{W}})\mathbf{W}'\right]\mathbf{W}' = 0$ for all $i = r_\Gamma+1,\ldots,N_\mathrm{G}$, there exists a non-zero $\mathbf{W}''$ satisfying Eq. (E.2). Here, $\boldsymbol{\upsilon}_i^\mathsf{T}\left[\boldsymbol{\Gamma}^{(2)}(\bar{\mathbf{W}})\mathbf{W}'\right]\mathbf{W}'$ is equal to the quadratic form $\mathbf{W}'^\mathsf{T}\left[\boldsymbol{\upsilon}_i^\mathsf{T}\boldsymbol{\Gamma}^{(2)}\right]\mathbf{W}'$. Therefore, the necessary and sufficient condition for the existence of the first-order infinitesimal mechanism $\mathbf{W}'$ which can be extended to the second-order infinitesimal mechanism $\mathbf{W}''$ is that $\mathbf{W}'$ satisfies the following equations:

$$\mathbf{W}' \cdot \boldsymbol{\eta}_j = 0 \qquad (j = 1,\ldots,r_\Gamma) \tag{E.6}$$

$$\mathbf{W}'^\mathsf{T}\left[\boldsymbol{\upsilon}_i^\mathsf{T}\boldsymbol{\Gamma}^{(2)}\right]\mathbf{W}' = 0 \qquad (i = r_\Gamma+1,\ldots,N_\mathrm{G}) \tag{E.7}$$

Note that if $r_\Gamma < N_\mathrm{W}$ and $r_\Gamma = N_\mathrm{G}$, $\mathbf{W}'$ and $\mathbf{W}''$ satisfying Eqs. (E.1) and (E.2) always exist. In Chapters 2 and 5, the order of the singular vectors are reversed so that $\boldsymbol{\upsilon}_1,\ldots,\boldsymbol{\upsilon}_{N_\mathrm{G}}$ and $\boldsymbol{\eta}_1,\ldots,\boldsymbol{\eta}_{N_\mathrm{W}}$ in this appendix corresponds to $\boldsymbol{\upsilon}_{N_\mathrm{G}},\ldots,\boldsymbol{\upsilon}_1$ and $\boldsymbol{\eta}_{N_\mathrm{W}},\ldots,\boldsymbol{\eta}_1$ in Chapters 2 and 5, respectively.

Appendix F

Results for case studies of form generation

The tables of the DOFs and the values of the approximation error functions $F_{\text{dist}}(\mathbf{X})$, $F_{\text{area}}(\mathbf{X})$ are shown to compare the results obtained from different $(c_{\text{area}}, c_{\text{normal}})$ and from different choice of the design variables. In addition, the graphs of the DOFs and values of approximation error functions are shown for the examples of form generation in Chapter 4. The makers and the types of lines used in the following graphs are summarized in Table. F.1. In each graph, the DOFs or the values of the approximation error functions of the solutions with cut pattern C, E, or X obtained by setting $(c_{\text{area}}, c_{\text{normal}}) = (0, 0)$, $(0.2, 0.5)$, $(0.2, 1.0)$, $(0.4, 0.5)$, and $(0.4, 1.0)$ are plotted with those of the solutions without cut. The range of the vertical axes are defined so that the average values of the solution without cut are approximately centered.

Table F.1: Markers and lines in graphs of form generation results.

c_{area}	c_{normal}	Without cut	Cut pattern C	Cut pattern E	Cut pattern X
0.0	0.0				
0.2	0.5				
0.2	1.0				
0.4	0.5				
0.4	1.0				

F.1 Approximation of HP surface

The tables and graphs are shown for the solutions considered in Section 4.3 of Chapter 4, which approximate the HP surface in Fig. 4.5.

F.1.1 Tables comparing form generation results with respect to weight coefficients of approximation error functions

This section shows the tables arranged with respect to the weight coefficients c_{area} and c_{normal} in the approximation error function. The results of the approximation of the HP surface obtained in cases G1–R3 are summarized as follows:

- Case G1: Tables F.2–F.5
- Case G2: Tables F.6–F.9
- Case G3: Tables F.10–F.13
- Case R1: Tables F.14–F.17
- Case R2: Tables F.18–F.21
- Case R3: Tables F.22–F.25

Table F.2: Results for the approximation of the HP surface without cuts in Case G1 arranged with respect to c_{area} and c_{normal}.

c_{area}		0.0	0.2	0.2	0.4	0.4
c_{normal}		0.0	0.5	1.0	0.5	1.0
No. solutions		7	7	6	7	8
Min. DOF		3	1	5	1	1
$F_{\mathrm{dist}}(\mathbf{X})$	max.	4.95	3.80	1.90	2.23	4.64
	min.	1.79	1.51	1.82	1.87	1.98
	avg.	2.33	2.44	1.87	2.03	2.49
$F_{\mathrm{area}}(\mathbf{X})$	max.	6.73	9.20	3.43	3.65	3.45
	min.	5.17	2.94	2.93	2.37	2.31
	avg.	6.41	4.72	3.15	2.96	2.76
$F_{\mathrm{normal}}(\mathbf{X})$	max.	4.38	4.01	2.28	2.69	3.95
	min.	3.75	2.19	2.06	2.11	2.02
	avg.	4.22	2.88	2.16	2.38	2.39

Table F.3: Results for the approximation of the HP surface with cut pattern C in Case G1 arranged with respect to c_{area} and c_{normal}.

c_{area}		0.0	0.2	0.2	0.4	0.4
c_{normal}		0.0	0.5	1.0	0.5	1.0
No. solutions		10	8	6	7	8
Min. DOF		9	5	8	6	5
$F_{\mathrm{dist}}(\mathbf{X})$	max.	565.57	87.52	5.09	411.36	152.63
	min.	4.08	1.56	1.39	1.41	47.73
	avg.	232.89	18.86	3.01	133.13	132.30
$F_{\mathrm{area}}(\mathbf{X})$	max.	1598.92	111.47	16.80	128.03	439.98
	min.	13.69	3.20	2.51	2.30	63.01
	avg.	663.91	25.18	5.45	44.39	298.32
$F_{\mathrm{normal}}(\mathbf{X})$	max.	66.24	40.23	9.06	46.51	51.84
	min.	11.88	2.50	2.26	2.18	24.51
	avg.	40.42	12.23	4.02	17.79	42.34

Table F.4: Results for the approximation of the HP surface with cut pattern E in Case G1 arranged with respect to c_{area} and c_{normal}.

c_{area}		0.0	0.2	0.2	0.4	0.4
c_{normal}		0.0	0.5	1.0	0.5	1.0
No. solutions		7	8	10	7	7
Min. DOF		7	3	3	7	11
$F_{\text{dist}}(\mathbf{X})$	max.	1.79	2.91	8.77	2.09	0.67
	min.	0.18	0.20	0.35	0.36	0.28
	avg.	0.71	1.01	2.38	0.83	0.48
$F_{\text{area}}(\mathbf{X})$	max.	5.16	3.32	5.49	6.91	1.68
	min.	2.05	0.98	2.36	1.17	0.61
	avg.	3.19	2.00	3.45	2.13	1.16
$F_{\text{normal}}(\mathbf{X})$	max.	4.10	3.16	6.67	4.05	1.10
	min.	1.04	0.66	1.14	0.90	0.67
	avg.	2.17	1.73	2.75	1.57	0.89

Table F.5: Results for the approximation of the HP surface with cut pattern X in Case G1 arranged with respect to c_{area} and c_{normal}.

c_{area}		0.0	0.2	0.2	0.4	0.4
c_{normal}		0.0	0.5	1.0	0.5	1.0
No. solutions		11	8	11	10	8
Min. DOF		1	2	3	2	3
$F_{\text{dist}}(\mathbf{X})$	max.	12.08	8.28	209.47	34.56	175.03
	min.	1.10	1.27	1.58	1.89	1.43
	avg.	4.37	3.49	70.77	8.95	96.75
$F_{\text{area}}(\mathbf{X})$	max.	19.40	16.22	188.61	44.40	469.95
	min.	5.61	3.48	1.95	1.96	1.86
	avg.	10.89	8.21	56.53	10.71	245.46
$F_{\text{normal}}(\mathbf{X})$	max.	10.92	9.42	64.36	18.89	51.20
	min.	4.95	2.62	2.10	2.44	2.03
	avg.	6.48	5.29	21.82	5.91	30.46

Table F.6: Results for the approximation of the HP surface without cuts in Case G2 arranged with respect to c_{area} and c_{normal}.

c_{area}		0.0	0.2	0.2	0.4	0.4
c_{normal}		0.0	0.5	1.0	0.5	1.0
No. solutions		7	1	6	1	8
Min. DOF		1	21	1	21	3
$F_{\text{dist}}(\mathbf{X})$	max.	7.31	5.80	14.70	5.25	10.39
	min.	6.75	5.80	4.10	5.25	2.72
	avg.	7.15	5.80	7.37	5.25	5.69
$F_{\text{area}}(\mathbf{X})$	max.	16.41	0.00	4.61	0.00	5.85
	min.	3.48	0.00	0.00	0.00	0.00
	avg.	11.64	0.00	2.26	0.00	2.54
$F_{\text{normal}}(\mathbf{X})$	max.	7.02	2.31	5.36	1.99	3.55
	min.	3.58	2.31	1.89	1.99	1.85
	avg.	5.90	2.31	3.24	1.99	2.57

Table F.7: Results for the approximation of the HP surface with cut pattern C in Case G2 arranged with respect to c_{area} and c_{normal}.

c_{area}		0.0	0.2	0.2	0.4	0.4
c_{normal}		0.0	0.5	1.0	0.5	1.0
No. solutions		11	8	7	1	1
Min. DOF		5	8	5	26	26
$F_{\text{dist}}(\mathbf{X})$	max.	72.24	13.49	13.27	4.93	5.01
	min.	5.45	6.40	8.00	4.93	5.01
	avg.	23.22	9.83	10.48	4.93	5.01
$F_{\text{area}}(\mathbf{X})$	max.	62.02	4.25	3.48	0.00	0.00
	min.	2.07	0.00	1.33	0.00	0.00
	avg.	19.42	2.62	2.49	0.00	0.00
$F_{\text{normal}}(\mathbf{X})$	max.	19.39	2.89	3.68	1.95	1.91
	min.	4.52	2.24	2.09	1.95	1.91
	avg.	8.13	2.62	2.36	1.95	1.91

Table F.8: Results for the approximation of the HP surface with cut pattern E in Case G2 arranged with respect to c_{area} and c_{normal}.

c_{area}		0.0	0.2	0.2	0.4	0.4
c_{normal}		0.0	0.5	1.0	0.5	1.0
No. solutions		12	1	1	1	1
Min. DOF		5	29	29	29	29
$F_{\text{dist}}(\mathbf{X})$	max.	18.74	0.67	0.73	1.72	4.76
	min.	0.23	0.67	0.73	1.72	4.76
	avg.	6.49	0.67	0.73	1.72	4.76
$F_{\text{area}}(\mathbf{X})$	max.	5.63	0.00	0.00	0.00	0.00
	min.	1.56	0.00	0.00	0.00	0.00
	avg.	2.61	0.00	0.00	0.00	0.00
$F_{\text{normal}}(\mathbf{X})$	max.	5.61	0.73	0.71	1.03	0.89
	min.	0.75	0.73	0.71	1.03	0.89
	avg.	2.70	0.73	0.71	1.03	0.89

Table F.9: Results for the approximation of the HP surface with cut pattern X in Case G2 arranged with respect to c_{area} and c_{normal}.

c_{area}		0.0	0.2	0.2	0.4	0.4
c_{normal}		0.0	0.5	1.0	0.5	1.0
No. solutions		10	10	10	7	8
Min. DOF		4	4	2	4	1
$F_{\text{dist}}(\mathbf{X})$	max.	6.51	14.43	12.81	31.25	26.20
	min.	2.14	4.07	3.29	3.64	6.75
	avg.	3.82	7.05	8.37	10.71	10.27
$F_{\text{area}}(\mathbf{X})$	max.	11.18	8.83	6.41	28.16	6.98
	min.	6.22	0.00	0.00	0.00	0.35
	avg.	9.66	3.27	1.64	6.66	2.76
$F_{\text{normal}}(\mathbf{X})$	max.	6.65	4.49	3.84	15.82	6.22
	min.	3.49	1.81	1.81	1.96	2.34
	avg.	5.37	2.76	2.41	5.95	3.45

Table F.10: Results for the approximation of the HP surface without cuts in Case G3 arranged with respect to c_{area} and c_{normal}.

c_{area}		0.0	0.2	0.2	0.4	0.4
c_{normal}		0.0	0.5	1.0	0.5	1.0
No. solutions		7	10	9	9	7
Min. DOF		1	3	1	1	5
$F_{\text{dist}}(\mathbf{X})$	max.	66.07	46.56	17.72	73.57	14.41
	min.	3.92	3.53	7.11	2.48	3.98
	avg.	12.85	22.46	8.90	22.53	12.79
$F_{\text{area}}(\mathbf{X})$	max.	6.78	9.93	4.51	6.75	5.64
	min.	5.46	2.83	2.91	2.67	2.83
	avg.	5.96	4.76	3.30	3.60	3.28
$F_{\text{normal}}(\mathbf{X})$	max.	5.52	7.41	3.63	5.57	4.02
	min.	3.94	2.03	1.82	2.11	2.03
	avg.	4.26	3.52	2.13	2.65	2.32

Table F.11: Results for the approximation of the HP surface with cut pattern C in Case G3 arranged with respect to c_{area} and c_{normal}.

c_{area}		0.0	0.2	0.2	0.4	0.4
c_{normal}		0.0	0.5	1.0	0.5	1.0
No. solutions		12	9	9	7	10
Min. DOF		6	5	6	6	5
$F_{\text{dist}}(\mathbf{X})$	max.	21.37	42.14	20.46	19.36	113.01
	min.	2.01	18.72	7.06	18.10	4.51
	avg.	13.30	22.82	9.86	18.67	48.68
$F_{\text{area}}(\mathbf{X})$	max.	6.46	6.22	4.96	2.80	7.12
	min.	4.54	2.58	2.93	2.52	2.89
	avg.	5.82	3.37	3.24	2.67	4.49
$F_{\text{normal}}(\mathbf{X})$	max.	5.07	5.32	4.21	2.34	4.87
	min.	2.93	2.03	1.77	1.93	1.82
	avg.	4.25	2.80	2.17	2.04	3.68

Table F.12: Results for the approximation of the HP surface with cut pattern E in Case G3 arranged with respect to c_{area} and c_{normal}.

c_{area}		0.0	0.2	0.2	0.4	0.4
c_{normal}		0.0	0.5	1.0	0.5	1.0
No. solutions		12	8	8	8	9
Min. DOF		4	5	1	9	3
$F_{\text{dist}}(\mathbf{X})$	max.	21.83	33.20	5.87	7.80	23.17
	min.	0.18	0.31	0.40	0.23	0.65
	avg.	10.68	7.73	1.63	2.60	8.40
$F_{\text{area}}(\mathbf{X})$	max.	6.91	5.30	7.17	2.93	11.16
	min.	1.39	1.22	1.21	1.02	1.26
	avg.	4.22	2.68	2.69	1.75	3.60
$F_{\text{normal}}(\mathbf{X})$	max.	4.91	4.33	4.78	2.27	9.11
	min.	0.74	0.78	0.83	0.65	0.78
	avg.	2.86	2.02	1.76	1.17	2.66

Table F.13: Results for the approximation of the HP surface with cut pattern X in Case G3 arranged with respect to c_{area} and c_{normal}.

c_{area}		0.0	0.2	0.2	0.4	0.4
c_{normal}		0.0	0.5	1.0	0.5	1.0
No. solutions		10	11	10	9	10
Min. DOF		2	1	3	1	2
$F_{\text{dist}}(\mathbf{X})$	max.	9.54	37.17	71.35	52.51	35.60
	min.	1.97	3.30	3.42	3.28	2.52
	avg.	3.34	18.98	23.09	23.30	10.48
$F_{\text{area}}(\mathbf{X})$	max.	16.74	33.12	20.02	13.47	41.56
	min.	8.59	2.54	3.03	2.54	2.91
	avg.	11.11	6.60	7.40	4.65	7.67
$F_{\text{normal}}(\mathbf{X})$	max.	9.68	17.60	14.75	9.44	19.43
	min.	5.99	1.80	1.63	1.93	1.66
	avg.	7.09	4.07	5.44	3.35	4.16

Table F.14: Results for the approximation of the HP surface without cuts in Case R1 arranged with respect to c_{area} and c_{normal}.

c_{area}		0.0	0.2	0.2	0.4	0.4
c_{normal}		0.0	0.5	1.0	0.5	1.0
No. solutions		6	6	6	6	7
Min. DOF		1	1	1	1	1
$F_{\text{dist}}(\mathbf{X})$	max.	2.03	2.00	174.68	2.64	31.59
	min.	1.27	1.62	21.65	2.50	3.09
	avg.	1.59	1.71	70.05	2.54	7.20
$F_{\text{area}}(\mathbf{X})$	max.	10.65	5.11	82.03	3.25	24.54
	min.	9.13	4.01	35.48	2.95	2.60
	avg.	9.84	4.36	51.75	3.02	5.80
$F_{\text{normal}}(\mathbf{X})$	max.	7.26	3.83	33.40	3.05	11.16
	min.	6.83	3.37	24.82	2.98	2.82
	avg.	7.02	3.45	28.56	3.01	4.14

Table F.15: Results for the approximation of the HP surface with cut pattern C in Case R1 arranged with respect to c_{area} and c_{normal}.

c_{area}		0.0	0.2	0.2	0.4	0.4
c_{normal}		0.0	0.5	1.0	0.5	1.0
No. solutions		6	8	8	8	8
Min. DOF		12	4	1	3	1
$F_{\text{dist}}(\mathbf{X})$	max.	80.75	206.61	115.56	100.51	444.23
	min.	1.61	1.20	2.56	1.32	23.49
	avg.	30.46	39.78	17.71	17.56	105.10
$F_{\text{area}}(\mathbf{X})$	max.	202.06	80.02	73.83	213.65	215.32
	min.	8.19	3.11	3.40	2.19	33.90
	avg.	100.63	33.76	14.36	31.37	108.59
$F_{\text{normal}}(\mathbf{X})$	max.	55.74	41.20	29.34	49.73	50.14
	min.	6.35	2.66	3.04	2.46	24.56
	avg.	30.44	18.53	7.24	9.96	35.58

Table F.16: Results for the approximation of the HP surface with cut pattern E in Case R1 arranged with respect to c_{area} and c_{normal}.

c_{area}		0.0	0.2	0.2	0.4	0.4
c_{normal}		0.0	0.5	1.0	0.5	1.0
No. solutions		8	10	10	8	7
Min. DOF		1	5	5	5	7
$F_{\text{dist}}(\mathbf{X})$	max.	14.78	100.39	1.67	1.56	1.45
	min.	0.45	0.66	0.59	0.76	0.63
	avg.	2.62	11.82	1.27	1.22	0.86
$F_{\text{area}}(\mathbf{X})$	max.	36.48	15.99	2.81	2.65	3.22
	min.	2.40	1.72	1.37	1.06	1.34
	avg.	7.71	4.03	2.00	1.93	1.79
$F_{\text{normal}}(\mathbf{X})$	max.	29.37	8.17	2.41	2.30	1.80
	min.	2.06	1.22	0.99	1.10	1.12
	avg.	6.62	2.68	1.66	1.79	1.31

Table F.17: Results for the approximation of the HP surface with cut pattern X in Case R1 arranged with respect to c_{area} and c_{normal}.

c_{area}		0.0	0.2	0.2	0.4	0.4
c_{normal}		0.0	0.5	1.0	0.5	1.0
No. solutions		8	8	8	8	8
Min. DOF		1	1	1	1	1
$F_{\text{dist}}(\mathbf{X})$	max.	9.64	16.87	86.49	331.27	97.27
	min.	1.03	1.77	1.88	1.41	2.07
	avg.	3.26	5.98	28.36	117.13	20.18
$F_{\text{area}}(\mathbf{X})$	max.	28.11	29.67	89.11	533.68	128.06
	min.	6.35	3.56	2.87	2.79	2.48
	avg.	12.37	12.08	27.83	246.50	42.85
$F_{\text{normal}}(\mathbf{X})$	max.	18.28	18.52	34.58	66.65	46.62
	min.	5.39	2.33	2.88	2.56	2.81
	avg.	9.50	8.01	14.30	39.52	25.71

Table F.18: Results for the approximation of the HP surface without cuts in Case R2 arranged with respect to c_{area} and c_{normal}.

c_{area}		0.0	0.2	0.2	0.4	0.4
c_{normal}		0.0	0.5	1.0	0.5	1.0
No. solutions		6	1	6	1	1
Min. DOF		1	21	1	21	21
$F_{\text{dist}}(\mathbf{X})$	max.	7.31	8.71	11.44	7.65	7.41
	min.	5.79	8.71	7.38	7.65	7.41
	avg.	7.06	8.71	10.40	7.65	7.41
$F_{\text{area}}(\mathbf{X})$	max.	4.17	0.00	0.74	0.00	0.00
	min.	1.43	0.00	0.00	0.00	0.00
	avg.	1.89	0.00	0.59	0.00	0.00
$F_{\text{normal}}(\mathbf{X})$	max.	5.33	2.34	2.69	2.41	2.13
	min.	4.84	2.34	2.39	2.41	2.13
	avg.	4.94	2.34	2.56	2.41	2.13

Table F.19: Results for the approximation of the HP surface with cut pattern C in Case R2 arranged with respect to c_{area} and c_{normal}.

c_{area}		0.0	0.2	0.2	0.4	0.4
c_{normal}		0.0	0.5	1.0	0.5	1.0
No. solutions		9	8	8	8	9
Min. DOF		1	2	1	1	1
$F_{\text{dist}}(\mathbf{X})$	max.	78.00	33.34	15.07	72.00	78.34
	min.	4.40	8.73	7.00	5.55	7.59
	avg.	28.67	14.29	9.75	39.40	25.32
$F_{\text{area}}(\mathbf{X})$	max.	27.77	8.99	4.02	197.02	12.59
	min.	1.58	0.00	0.00	2.01	0.00
	avg.	8.91	1.77	0.89	77.81	3.31
$F_{\text{normal}}(\mathbf{X})$	max.	17.50	4.54	4.68	50.29	7.94
	min.	3.31	2.30	2.20	2.64	2.20
	avg.	7.08	2.71	3.31	27.53	3.28

Table F.20: Results for the approximation of the HP surface with cut pattern E in Case R2 arranged with respect to c_{area} and c_{normal}.

c_{area}		0.0	0.2	0.2	0.4	0.4
c_{normal}		0.0	0.5	1.0	0.5	1.0
No. solutions		10	1	1	1	1
Min. DOF		5	29	29	29	29
$F_{\text{dist}}(\mathbf{X})$	max.	8.58	1.97	2.20	1.77	1.82
	min.	2.35	1.97	2.20	1.77	1.82
	avg.	3.99	1.97	2.20	1.77	1.82
$F_{\text{area}}(\mathbf{X})$	max.	5.35	0.00	0.00	0.00	0.00
	min.	2.89	0.00	0.00	0.00	0.00
	avg.	4.05	0.00	0.00	0.00	0.00
$F_{\text{normal}}(\mathbf{X})$	max.	5.30	1.05	1.05	1.14	1.05
	min.	3.04	1.05	1.05	1.14	1.05
	avg.	4.39	1.05	1.05	1.14	1.05

Table F.21: Results for the approximation of the HP surface with cut pattern X in Case R2 arranged with respect to c_{area} and c_{normal}.

c_{area}		0.0	0.2	0.2	0.4	0.4
c_{normal}		0.0	0.5	1.0	0.5	1.0
No. solutions		8	9	8	9	8
Min. DOF		1	2	1	1	1
$F_{\text{dist}}(\mathbf{X})$	max.	5.30	97.50	13.59	17.47	13.48
	min.	4.38	5.81	4.32	5.59	5.39
	avg.	4.63	21.69	7.22	8.63	8.50
$F_{\text{area}}(\mathbf{X})$	max.	6.66	18.69	1.64	8.31	2.90
	min.	1.57	0.00	0.13	0.43	0.00
	avg.	2.93	4.77	0.98	2.87	1.05
$F_{\text{normal}}(\mathbf{X})$	max.	6.60	14.02	3.01	10.14	2.91
	min.	3.57	1.84	2.37	2.61	2.14
	avg.	4.37	4.63	2.56	3.56	2.60

Table F.22: Results for the approximation of the HP surface without cuts in Case R3 arranged with respect to c_{area} and c_{normal}.

c_{area}		0.0	0.2	0.2	0.4	0.4
c_{normal}		0.0	0.5	1.0	0.5	1.0
No. solutions		8	9	6	7	8
Min. DOF		1	1	1	1	1
$F_{\text{dist}}(\mathbf{X})$	max.	15.66	21.65	17.37	25.45	43.49
	min.	7.56	17.85	8.85	16.27	21.29
	avg.	9.38	20.05	11.69	23.07	24.42
$F_{\text{area}}(\mathbf{X})$	max.	22.30	4.70	3.10	5.07	3.82
	min.	4.52	2.61	2.88	2.36	2.56
	avg.	7.28	2.86	3.03	2.88	2.73
$F_{\text{normal}}(\mathbf{X})$	max.	15.54	5.23	1.92	3.95	4.32
	min.	4.59	1.96	1.85	2.60	1.97
	avg.	6.44	2.34	1.88	2.89	2.28

Table F.23: Results for the approximation of the HP surface with cut pattern C in Case R3 arranged with respect to c_{area} and c_{normal}.

c_{area}		0.0	0.2	0.2	0.4	0.4
c_{normal}		0.0	0.5	1.0	0.5	1.0
No. solutions		10	8	8	8	8
Min. DOF		1	3	5	2	1
$F_{\text{dist}}(\mathbf{X})$	max.	24.56	87.83	22.61	51.79	34.20
	min.	7.25	6.79	5.61	7.29	14.69
	avg.	12.82	22.39	9.88	15.21	18.07
$F_{\text{area}}(\mathbf{X})$	max.	27.62	8.01	3.60	17.38	5.36
	min.	4.58	2.67	2.88	2.77	2.68
	avg.	14.83	3.66	3.09	4.66	3.12
$F_{\text{normal}}(\mathbf{X})$	max.	20.87	8.12	3.58	11.51	4.67
	min.	4.18	1.91	2.22	2.73	2.12
	avg.	11.33	3.05	2.55	3.86	2.51

Table F.24: Results for the approximation of the HP surface with cut pattern E in Case R3 arranged with respect to c_{area} and c_{normal}.

c_{area}		0.0	0.2	0.2	0.4	0.4
c_{normal}		0.0	0.5	1.0	0.5	1.0
No. solutions		11	9	11	10	8
Min. DOF		5	5	1	5	5
$F_{\text{dist}}(\mathbf{X})$	max.	2.98	24.64	28.27	36.43	13.67
	min.	2.26	0.82	0.85	2.95	0.93
	avg.	2.68	9.02	11.37	13.83	7.17
$F_{\text{area}}(\mathbf{X})$	max.	6.12	5.62	3.93	2.24	1.53
	min.	3.84	1.25	1.45	1.28	1.25
	avg.	4.82	1.96	2.50	1.54	1.43
$F_{\text{normal}}(\mathbf{X})$	max.	5.17	3.53	3.52	3.00	1.60
	min.	3.11	0.98	1.12	1.10	0.98
	avg.	3.94	1.61	2.24	1.71	1.30

Table F.25: Results for the approximation of the HP surface with cut pattern X in Case R3 arranged with respect to c_{area} and c_{normal}.

c_{area}		0.0	0.2	0.2	0.4	0.4
c_{normal}		0.0	0.5	1.0	0.5	1.0
No. solutions		8	8	9	8	8
Min. DOF		1	3	1	1	1
$F_{\text{dist}}(\mathbf{X})$	max.	7.97	77.61	34.22	28.36	36.82
	min.	2.79	17.33	4.38	19.22	7.01
	avg.	7.26	39.59	13.80	21.18	22.55
$F_{\text{area}}(\mathbf{X})$	max.	8.16	141.10	27.79	4.57	7.70
	min.	4.24	2.50	2.45	2.20	2.86
	avg.	5.09	68.25	7.32	2.64	4.19
$F_{\text{normal}}(\mathbf{X})$	max.	5.98	45.66	12.89	4.58	6.20
	min.	4.06	2.24	2.20	2.43	2.14
	avg.	4.58	26.48	4.39	2.78	3.47

F.1.2 Tables comparing form generation results with respect to choice of design variables

This section shows the tables arranged with respect to the design variables of the optimization problems (3.50) and (3.51), which are the nodal coordinates of the frame model or the pairs of (s,t) parameters of the target Bézier surface and the offsets. The results of the approximation of the HP surface obtained by setting $(c_{\text{area}}, c_{\text{normal}})$ to $(0.0, 0.0)$, $(0.2, 0.5)$, $(0.2, 1.0)$, $(0.4, 0.5)$, and $(0.4, 1.0)$ are summarized as follows:

- $(c_{\text{area}}, c_{\text{normal}}) = (0.0, 0.0)$: Tables F.26–F.29
- $(c_{\text{area}}, c_{\text{normal}}) = (0.2, 0.5)$: Tables F.30–F.33
- $(c_{\text{area}}, c_{\text{normal}}) = (0.2, 1.0)$: Tables F.34–F.37
- $(c_{\text{area}}, c_{\text{normal}}) = (0.4, 0.5)$: Tables F.38–F.41
- $(c_{\text{area}}, c_{\text{normal}}) = (0.4, 1.0)$: Tables F.42–F.45

Table F.26: Results for the approximation of the HP surface without cuts and with $(c_{\text{area}}, c_{\text{normal}}) = (0.0, 0.0)$ arranged with respect to the choice of design variables.

Cases		G1	G2	G3	R1	R2	R3
No. solutions		7	7	7	6	6	8
Min. DOF		3	1	1	1	1	1
$F_{\text{dist}}(\mathbf{X})$	max.	4.95	7.31	66.07	2.03	7.31	15.66
	min.	1.79	6.75	3.92	1.27	5.79	7.56
	avg.	2.33	7.15	12.85	1.59	7.06	9.38
$F_{\text{area}}(\mathbf{X})$	max.	6.73	16.41	6.78	10.65	4.17	22.30
	min.	5.17	3.48	5.46	9.13	1.43	4.52
	avg.	6.41	11.64	5.96	9.84	1.89	7.28
$F_{\text{normal}}(\mathbf{X})$	max.	4.38	7.02	5.52	7.26	5.33	15.54
	min.	3.75	3.58	3.94	6.83	4.84	4.59
	avg.	4.22	5.90	4.26	7.02	4.94	6.44

Table F.27: Results for the approximation of the HP surface with cut pattern C and $(c_{\text{area}}, c_{\text{normal}}) = (0.0, 0.0)$ arranged with respect to the choice of design variables.

Cases		G1	G2	G3	R1	R2	R3
No. solutions		10	11	12	6	9	10
Min. DOF		9	5	6	12	1	1
$F_{\text{dist}}(\mathbf{X})$	max.	565.57	72.24	21.37	80.75	78.00	24.56
	min.	4.08	5.45	2.01	1.61	4.40	7.25
	avg.	232.89	23.22	13.30	30.46	28.67	12.82
$F_{\text{area}}(\mathbf{X})$	max.	1598.92	62.02	6.46	202.06	27.77	27.62
	min.	13.69	2.07	4.54	8.19	1.58	4.58
	avg.	663.91	19.42	5.82	100.63	8.91	14.83
$F_{\text{normal}}(\mathbf{X})$	max.	66.24	19.39	5.07	55.74	17.50	20.87
	min.	11.88	4.52	2.93	6.35	3.31	4.18
	avg.	40.42	8.13	4.25	30.44	7.08	11.33

Table F.28: Results for the approximation of the HP surface with cut pattern E and $(c_{\text{area}}, c_{\text{normal}}) = (0.0, 0.0)$ arranged with respect to the choice of design variables.

Cases		G1	G2	G3	R1	R2	R3
No. solutions		7	12	12	8	10	11
Min. DOF		7	5	4	1	5	5
$F_{\text{dist}}(\mathbf{X})$	max.	1.79	18.74	21.83	14.78	8.58	2.98
	min.	0.18	0.23	0.18	0.45	2.35	2.26
	avg.	0.71	6.49	10.68	2.62	3.99	2.68
$F_{\text{area}}(\mathbf{X})$	max.	5.16	5.63	6.91	36.48	5.35	6.12
	min.	2.05	1.56	1.39	2.40	2.89	3.84
	avg.	3.19	2.61	4.22	7.71	4.05	4.82
$F_{\text{normal}}(\mathbf{X})$	max.	4.10	5.61	4.91	29.37	5.30	5.17
	min.	1.04	0.75	0.74	2.06	3.04	3.11
	avg.	2.17	2.70	2.86	6.62	4.39	3.94

Table F.29: Results for the approximation of the HP surface with cut pattern X and $(c_{\text{area}}, c_{\text{normal}}) = (0.0, 0.0)$ arranged with respect to the choice of design variables.

Cases		G1	G2	G3	R1	R2	R3
No. solutions		11	10	10	8	8	8
Min. DOF		1	4	2	1	1	1
$F_{\text{dist}}(\mathbf{X})$	max.	12.08	6.51	9.54	9.64	5.30	7.97
	min.	1.10	2.14	1.97	1.03	4.38	2.79
	avg.	4.37	3.82	3.34	3.26	4.63	7.26
$F_{\text{area}}(\mathbf{X})$	max.	19.40	11.18	16.74	28.11	6.66	8.16
	min.	5.61	6.22	8.59	6.35	1.57	4.24
	avg.	10.89	9.66	11.11	12.37	2.93	5.09
$F_{\text{normal}}(\mathbf{X})$	max.	10.92	6.65	9.68	18.28	6.60	5.98
	min.	4.95	3.49	5.99	5.39	3.57	4.06
	avg.	6.48	5.37	7.09	9.50	4.37	4.58

Table F.30: Results for the approximation of the HP surface without cuts and with $(c_{\text{area}}, c_{\text{normal}}) = (0.2, 0.5)$ arranged with respect to the choice of design variables.

Cases		G1	G2	G3	R1	R2	R3
No. solutions		7	1	10	6	1	9
Min. DOF		1	21	3	1	21	1
$F_{\text{dist}}(\mathbf{X})$	max.	3.80	5.80	46.56	2.00	8.71	21.65
	min.	1.51	5.80	3.53	1.62	8.71	17.85
	avg.	2.44	5.80	22.46	1.71	8.71	20.05
$F_{\text{area}}(\mathbf{X})$	max.	9.20	0.00	9.93	5.11	0.00	4.70
	min.	2.94	0.00	2.83	4.01	0.00	2.61
	avg.	4.72	0.00	4.76	4.36	0.00	2.86
$F_{\text{normal}}(\mathbf{X})$	max.	4.01	2.31	7.41	3.83	2.34	5.23
	min.	2.19	2.31	2.03	3.37	2.34	1.96
	avg.	2.88	2.31	3.52	3.45	2.34	2.34

Table F.31: Results for the approximation of the HP surface with cut pattern C and $(c_{\text{area}}, c_{\text{normal}}) = (0.2, 0.5)$ arranged with respect to the choice of design variables.

Cases		G1	G2	G3	R1	R2	R3
No. solutions		8	8	9	8	8	8
Min. DOF		5	8	5	4	2	3
$F_{\text{dist}}(\mathbf{X})$	max.	87.52	13.49	42.14	206.61	33.34	87.83
	min.	1.56	6.40	18.72	1.20	8.73	6.79
	avg.	18.86	9.83	22.82	39.78	14.29	22.39
$F_{\text{area}}(\mathbf{X})$	max.	111.47	4.25	6.22	80.02	8.99	8.01
	min.	3.20	0.00	2.58	3.11	0.00	2.67
	avg.	25.18	2.62	3.37	33.76	1.77	3.66
$F_{\text{normal}}(\mathbf{X})$	max.	40.23	2.89	5.32	41.20	4.54	8.12
	min.	2.50	2.24	2.03	2.66	2.30	1.91
	avg.	12.23	2.62	2.80	18.53	2.71	3.05

Table F.32: Results for the approximation of the HP surface with cut pattern E and $(c_{\text{area}}, c_{\text{normal}}) = (0.2, 0.5)$ arranged with respect to the choice of design variables.

Cases		G1	G2	G3	R1	R2	R3
No. solutions		8	1	8	10	1	9
Min. DOF		3	29	5	5	29	5
$F_{\text{dist}}(\mathbf{X})$	max.	2.91	0.67	33.20	100.39	1.97	24.64
	min.	0.20	0.67	0.31	0.66	1.97	0.82
	avg.	1.01	0.67	7.73	11.82	1.97	9.02
$F_{\text{area}}(\mathbf{X})$	max.	3.32	0.00	5.30	15.99	0.00	5.62
	min.	0.98	0.00	1.22	1.72	0.00	1.25
	avg.	2.00	0.00	2.68	4.03	0.00	1.96
$F_{\text{normal}}(\mathbf{X})$	max.	3.16	0.73	4.33	8.17	1.05	3.53
	min.	0.66	0.73	0.78	1.22	1.05	0.98
	avg.	1.73	0.73	2.02	2.68	1.05	1.61

Table F.33: Results for the approximation of the HP surface with cut pattern X and $(c_{\text{area}}, c_{\text{normal}}) = (0.2, 0.5)$ arranged with respect to the choice of design variables.

Cases		G1	G2	G3	R1	R2	R3
No. solutions		8	10	11	8	9	8
Min. DOF		2	4	1	1	2	3
$F_{\text{dist}}(\mathbf{X})$	max.	8.28	14.43	37.17	16.87	97.50	77.61
	min.	1.27	4.07	3.30	1.77	5.81	17.33
	avg.	3.49	7.05	18.98	5.98	21.69	39.59
$F_{\text{area}}(\mathbf{X})$	max.	16.22	8.83	33.12	29.67	18.69	141.10
	min.	3.48	0.00	2.54	3.56	0.00	2.50
	avg.	8.21	3.27	6.60	12.08	4.77	68.25
$F_{\text{normal}}(\mathbf{X})$	max.	9.42	4.49	17.60	18.52	14.02	45.66
	min.	2.62	1.81	1.80	2.33	1.84	2.24
	avg.	5.29	2.76	4.07	8.01	4.63	26.48

Table F.34: Results for the approximation of the HP surface without cuts and with $(c_{\text{area}}, c_{\text{normal}}) = (0.2, 1.0)$ arranged with respect to the choice of design variables.

Cases		G1	G2	G3	R1	R2	R3
No. solutions		6	6	9	6	6	6
Min. DOF		5	1	1	1	1	1
$F_{\text{dist}}(\mathbf{X})$	max.	1.90	14.70	17.72	174.68	11.44	17.37
	min.	1.82	4.10	7.11	21.65	7.38	8.85
	avg.	1.87	7.37	8.90	70.05	10.40	11.69
$F_{\text{area}}(\mathbf{X})$	max.	3.43	4.61	4.51	82.03	0.74	3.10
	min.	2.93	0.00	2.91	35.48	0.00	2.88
	avg.	3.15	2.26	3.30	51.75	0.59	3.03
$F_{\text{normal}}(\mathbf{X})$	max.	2.28	5.36	3.63	33.40	2.69	1.92
	min.	2.06	1.89	1.82	24.82	2.39	1.85
	avg.	2.16	3.24	2.13	28.56	2.56	1.88

Table F.35: Results for the approximation of the HP surface with cut pattern C and $(c_{\text{area}}, c_{\text{normal}}) = (0.2, 1.0)$ arranged with respect to the choice of design variables.

Cases		G1	G2	G3	R1	R2	R3
No. solutions		6	7	9	8	8	8
Min. DOF		8	5	6	1	1	5
$F_{\text{dist}}(\mathbf{X})$	max.	5.09	13.27	20.46	115.56	15.07	22.61
	min.	1.39	8.00	7.06	2.56	7.00	5.61
	avg.	3.01	10.48	9.86	17.71	9.75	9.88
$F_{\text{area}}(\mathbf{X})$	max.	16.80	3.48	4.96	73.83	4.02	3.60
	min.	2.51	1.33	2.93	3.40	0.00	2.88
	avg.	5.45	2.49	3.24	14.36	0.89	3.09
$F_{\text{normal}}(\mathbf{X})$	max.	9.06	3.68	4.21	29.34	4.68	3.58
	min.	2.26	2.09	1.77	3.04	2.20	2.22
	avg.	4.02	2.36	2.17	7.24	3.31	2.55

Table F.36: Results for the approximation of the HP surface with cut pattern E and $(c_{\text{area}}, c_{\text{normal}}) = (0.2, 1.0)$ arranged with respect to the choice of design variables.

Cases		G1	G2	G3	R1	R2	R3
No. solutions		10	1	8	10	1	11
Min. DOF		3	29	1	5	29	1
$F_{\text{dist}}(\mathbf{X})$	max.	8.77	0.73	5.87	1.67	2.20	28.27
	min.	0.35	0.73	0.40	0.59	2.20	0.85
	avg.	2.38	0.73	1.63	1.27	2.20	11.37
$F_{\text{area}}(\mathbf{X})$	max.	5.49	0.00	7.17	2.81	0.00	3.93
	min.	2.36	0.00	1.21	1.37	0.00	1.45
	avg.	3.45	0.00	2.69	2.00	0.00	2.50
$F_{\text{normal}}(\mathbf{X})$	max.	6.67	0.71	4.78	2.41	1.05	3.52
	min.	1.14	0.71	0.83	0.99	1.05	1.12
	avg.	2.75	0.71	1.76	1.66	1.05	2.24

Table F.37: Results for the approximation of the HP surface with cut pattern X and $(c_{\text{area}}, c_{\text{normal}}) = (0.2, 1.0)$ arranged with respect to the choice of design variables.

Cases		G1	G2	G3	R1	R2	R3
No. solutions		11	10	10	8	8	9
Min. DOF		3	2	3	1	1	1
$F_{\text{dist}}(\mathbf{X})$	max.	209.47	12.81	71.35	86.49	13.59	34.22
	min.	1.58	3.29	3.42	1.88	4.32	4.38
	avg.	70.77	8.37	23.09	28.36	7.22	13.80
$F_{\text{area}}(\mathbf{X})$	max.	188.61	6.41	20.02	89.11	1.64	27.79
	min.	1.95	0.00	3.03	2.87	0.13	2.45
	avg.	56.53	1.64	7.40	27.83	0.98	7.32
$F_{\text{normal}}(\mathbf{X})$	max.	64.36	3.84	14.75	34.58	3.01	12.89
	min.	2.10	1.81	1.63	2.88	2.37	2.20
	avg.	21.82	2.41	5.44	14.30	2.56	4.39

Table F.38: Results for the approximation of the HP surface without cuts and with $(c_{\text{area}}, c_{\text{normal}}) = (0.4, 0.5)$ arranged with respect to the choice of design variables.

Cases		G1	G2	G3	R1	R2	R3
No. solutions		7	1	9	6	1	7
Min. DOF		1	21	1	1	21	1
$F_{\text{dist}}(\mathbf{X})$	max.	2.23	5.25	73.57	2.64	7.65	25.45
	min.	1.87	5.25	2.48	2.50	7.65	16.27
	avg.	2.03	5.25	22.53	2.54	7.65	23.07
$F_{\text{area}}(\mathbf{X})$	max.	3.65	0.00	6.75	3.25	0.00	5.07
	min.	2.37	0.00	2.67	2.95	0.00	2.36
	avg.	2.96	0.00	3.60	3.02	0.00	2.88
$F_{\text{normal}}(\mathbf{X})$	max.	2.69	1.99	5.57	3.05	2.41	3.95
	min.	2.11	1.99	2.11	2.98	2.41	2.60
	avg.	2.38	1.99	2.65	3.01	2.41	2.89

Table F.39: Results for the approximation of the HP surface with cut pattern C and $(c_{\text{area}}, c_{\text{normal}}) = (0.4, 0.5)$ arranged with respect to the choice of design variables.

Cases		G1	G2	G3	R1	R2	R3
No. solutions		7	1	7	8	8	8
Min. DOF		6	26	6	3	1	2
$F_{\text{dist}}(\mathbf{X})$	max.	411.36	4.93	19.36	100.51	72.00	51.79
	min.	1.41	4.93	18.10	1.32	5.55	7.29
	avg.	133.13	4.93	18.67	17.56	39.40	15.21
$F_{\text{area}}(\mathbf{X})$	max.	128.03	0.00	2.80	213.65	197.02	17.38
	min.	2.30	0.00	2.52	2.19	2.01	2.77
	avg.	44.39	0.00	2.67	31.37	77.81	4.66
$F_{\text{normal}}(\mathbf{X})$	max.	46.51	1.95	2.34	49.73	50.29	11.51
	min.	2.18	1.95	1.93	2.46	2.64	2.73
	avg.	17.79	1.95	2.04	9.96	27.53	3.86

Table F.40: Results for the approximation of the HP surface with cut pattern E and $(c_{\text{area}}, c_{\text{normal}}) = (0.4, 0.5)$ arranged with respect to the choice of design variables.

Cases		G1	G2	G3	R1	R2	R3
No. solutions		7	1	8	8	1	10
Min. DOF		7	29	9	5	29	5
$F_{\text{dist}}(\mathbf{X})$	max.	2.09	1.72	7.80	1.56	1.77	36.43
	min.	0.36	1.72	0.23	0.76	1.77	2.95
	avg.	0.83	1.72	2.60	1.22	1.77	13.83
$F_{\text{area}}(\mathbf{X})$	max.	6.91	0.00	2.93	2.65	0.00	2.24
	min.	1.17	0.00	1.02	1.06	0.00	1.28
	avg.	2.13	0.00	1.75	1.93	0.00	1.54
$F_{\text{normal}}(\mathbf{X})$	max.	4.05	1.03	2.27	2.30	1.14	3.00
	min.	0.90	1.03	0.65	1.10	1.14	1.10
	avg.	1.57	1.03	1.17	1.79	1.14	1.71

Table F.41: Results for the approximation of the HP surface with cut pattern X and $(c_{\text{area}}, c_{\text{normal}}) = (0.4, 0.5)$ arranged with respect to the choice of design variables.

Cases		G1	G2	G3	R1	R2	R3
No. solutions		10	7	9	8	9	8
Min. DOF		2	4	1	1	1	1
$F_{\text{dist}}(\mathbf{X})$	max.	34.56	31.25	52.51	331.27	17.47	28.36
	min.	1.89	3.64	3.28	1.41	5.59	19.22
	avg.	8.95	10.71	23.30	117.13	8.63	21.18
$F_{\text{area}}(\mathbf{X})$	max.	44.40	28.16	13.47	533.68	8.31	4.57
	min.	1.96	0.00	2.54	2.79	0.43	2.20
	avg.	10.71	6.66	4.65	246.50	2.87	2.64
$F_{\text{normal}}(\mathbf{X})$	max.	18.89	15.82	9.44	66.65	10.14	4.58
	min.	2.44	1.96	1.93	2.56	2.61	2.43
	avg.	5.91	5.95	3.35	39.52	3.56	2.78

Table F.42: Results for the approximation of the HP surface without cuts and with $(c_{\text{area}}, c_{\text{normal}}) = (0.4, 1.0)$ arranged with respect to the choice of design variables.

Cases		G1	G2	G3	R1	R2	R3
No. solutions		8	8	7	7	1	8
Min. DOF		1	3	5	1	21	1
$F_{\text{dist}}(\mathbf{X})$	max.	4.64	10.39	14.41	31.59	7.41	43.49
	min.	1.98	2.72	3.98	3.09	7.41	21.29
	avg.	2.49	5.69	12.79	7.20	7.41	24.42
$F_{\text{area}}(\mathbf{X})$	max.	3.45	5.85	5.64	24.54	0.00	3.82
	min.	2.31	0.00	2.83	2.60	0.00	2.56
	avg.	2.76	2.54	3.28	5.80	0.00	2.73
$F_{\text{normal}}(\mathbf{X})$	max.	3.95	3.55	4.02	11.16	2.13	4.32
	min.	2.02	1.85	2.03	2.82	2.13	1.97
	avg.	2.39	2.57	2.32	4.14	2.13	2.28

Table F.43: Results for the approximation of the HP surface with cut pattern C and $(c_{\text{area}}, c_{\text{normal}}) = (0.4, 1.0)$ arranged with respect to the choice of design variables.

Cases		G1	G2	G3	R1	R2	R3
No. solutions		8	1	10	8	9	8
Min. DOF		5	26	5	1	1	1
$F_{\text{dist}}(\mathbf{X})$	max.	152.63	5.01	113.01	444.23	78.34	34.20
	min.	47.73	5.01	4.51	23.49	7.59	14.69
	avg.	132.30	5.01	48.68	105.10	25.32	18.07
$F_{\text{area}}(\mathbf{X})$	max.	439.98	0.00	7.12	215.32	12.59	5.36
	min.	63.01	0.00	2.89	33.90	0.00	2.68
	avg.	298.32	0.00	4.49	108.59	3.31	3.12
$F_{\text{normal}}(\mathbf{X})$	max.	51.84	1.91	4.87	50.14	7.94	4.67
	min.	24.51	1.91	1.82	24.56	2.20	2.12
	avg.	42.34	1.91	3.68	35.58	3.28	2.51

Table F.44: Results for the approximation of the HP surface with cut pattern E and $(c_{\text{area}}, c_{\text{normal}}) = (0.4, 1.0)$ arranged with respect to the choice of design variables.

Cases		G1	G2	G3	R1	R2	R3
No. solutions		7	1	9	7	1	8
Min. DOF		11	29	3	7	29	5
$F_{\text{dist}}(\mathbf{X})$	max.	0.67	4.76	23.17	1.45	1.82	13.67
	min.	0.28	4.76	0.65	0.63	1.82	0.93
	avg.	0.48	4.76	8.40	0.86	1.82	7.17
$F_{\text{area}}(\mathbf{X})$	max.	1.68	0.00	11.16	3.22	0.00	1.53
	min.	0.61	0.00	1.26	1.34	0.00	1.25
	avg.	1.16	0.00	3.60	1.79	0.00	1.43
$F_{\text{normal}}(\mathbf{X})$	max.	1.10	0.89	9.11	1.80	1.05	1.60
	min.	0.67	0.89	0.78	1.12	1.05	0.98
	avg.	0.89	0.89	2.66	1.31	1.05	1.30

Table F.45: Results for the approximation of the HP surface with cut pattern X and $(c_{\text{area}}, c_{\text{normal}}) = (0.4, 1.0)$ arranged with respect to the choice of design variables.

Cases		G1	G2	G3	R1	R2	R3
No. solutions		8	8	10	8	8	8
Min. DOF		3	1	2	1	1	1
$F_{\text{dist}}(\mathbf{X})$	max.	175.03	26.20	35.60	97.27	13.48	36.82
	min.	1.43	6.75	2.52	2.07	5.39	7.01
	avg.	96.75	10.27	10.48	20.18	8.50	22.55
$F_{\text{area}}(\mathbf{X})$	max.	469.95	6.98	41.56	128.06	2.90	7.70
	min.	1.86	0.35	2.91	2.48	0.00	2.86
	avg.	245.46	2.76	7.67	42.85	1.05	4.19
$F_{\text{normal}}(\mathbf{X})$	max.	51.20	6.22	19.43	46.62	2.91	6.20
	min.	2.03	2.34	1.66	2.81	2.14	2.14
	avg.	30.46	3.45	4.16	25.71	2.60	3.47

F.1.3 Graphs of solutions approximating HP surface

The graphs plotting the DOFs and values of approximation error functions with respect to the number of fixed crease lines are shown for the examples of the approximation of the HP surface. The correspondence between the cases of examples and the indices of graphs are as follows:

- Case G1: Figs. F.1–F.4
- Case G2: Figs. F.5–F.8
- Case G3: Figs. F.9–F.12
- Case R1: Figs. F.13–F.16
- Case R2: Figs. F.17–F.20
- Case R3: Figs. F.21–F.24

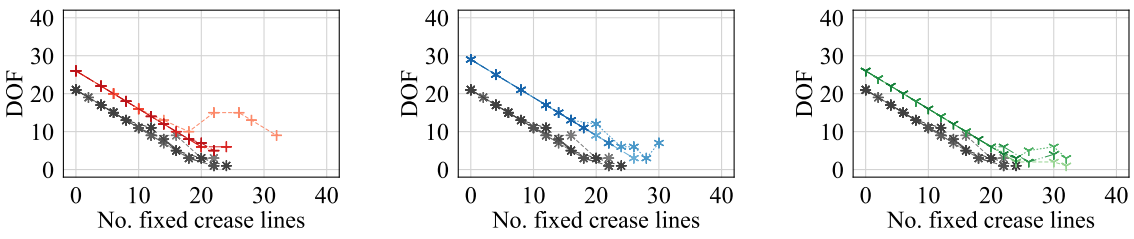

(a) Cut pattern C **(b)** Cut pattern E **(c)** Cut pattern X

Figure F.1: DOFs in Case G1 with the HP surface.

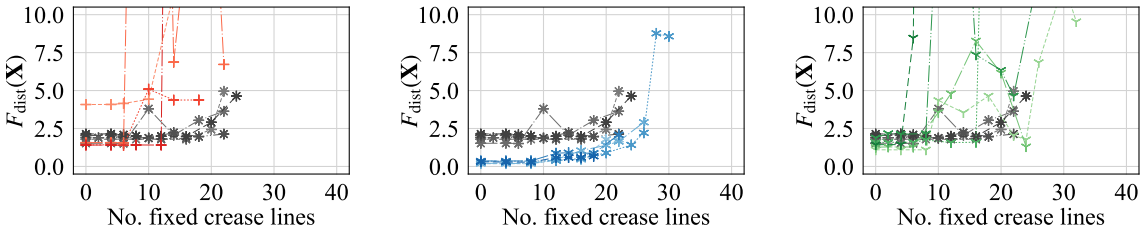

(a) Cut pattern C **(b)** Cut pattern E **(c)** Cut pattern X

Figure F.2: Values of $F_{\text{dist}}(\mathbf{X})$ in Case G1 with the HP surface.

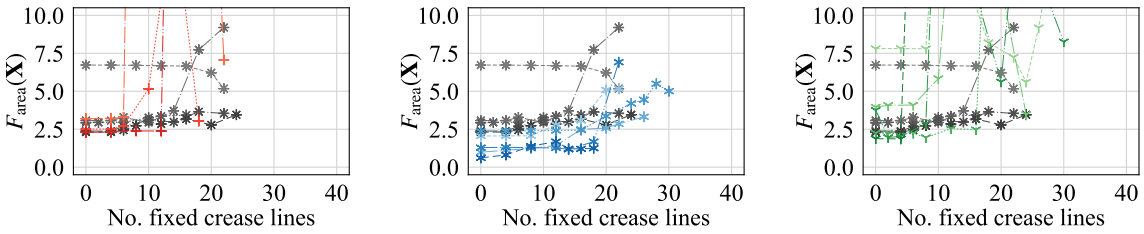

(a) Cut pattern C **(b)** Cut pattern E **(c)** Cut pattern X

Figure F.3: Values of $F_{\text{area}}(\mathbf{X})$ in Case G1 with the HP surface.

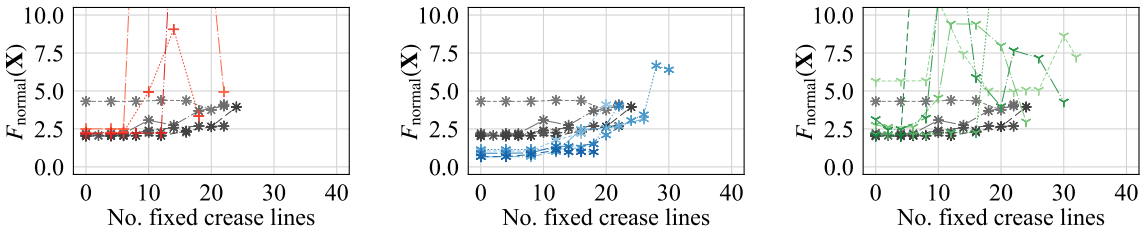

(a) Cut pattern C **(b)** Cut pattern E **(c)** Cut pattern X

Figure F.4: Values of $F_{\text{normal}}(\mathbf{X})$ in Case G1 with the HP surface.

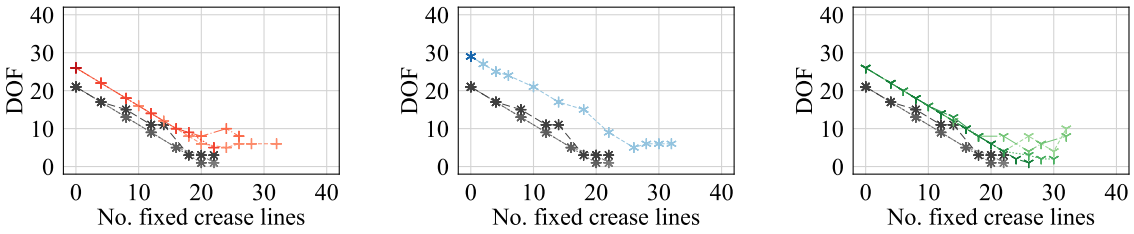

(a) Cut pattern C **(b)** Cut pattern E **(c)** Cut pattern X

Figure F.5: DOFs in Case G2 with the HP surface.

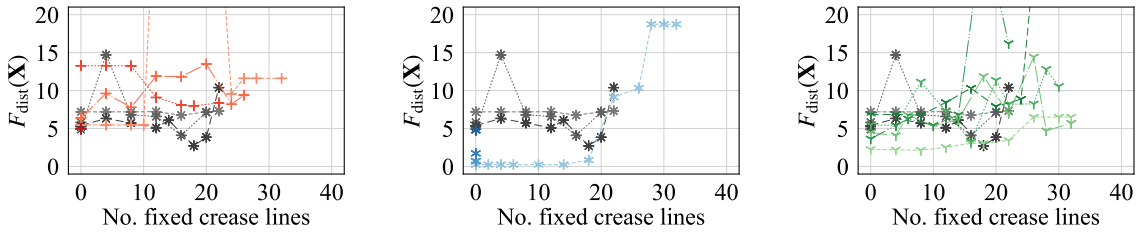

(a) Cut pattern C **(b)** Cut pattern E **(c)** Cut pattern X

Figure F.6: Values of $F_{\text{dist}}(\mathbf{X})$ in Case G2 with the HP surface.

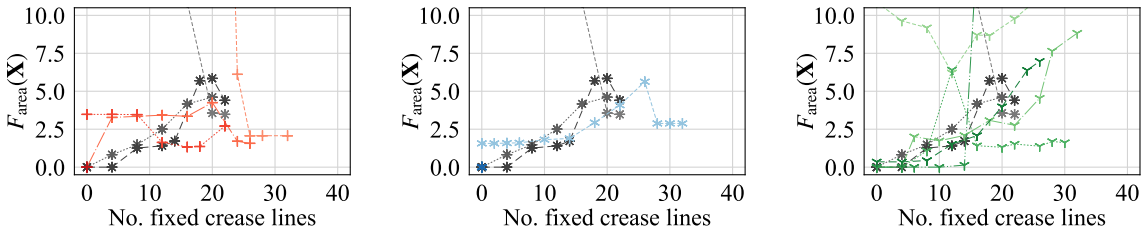

(a) Cut pattern C **(b)** Cut pattern E **(c)** Cut pattern X

Figure F.7: Values of $F_{\text{area}}(\mathbf{X})$ in Case G2 with the HP surface.

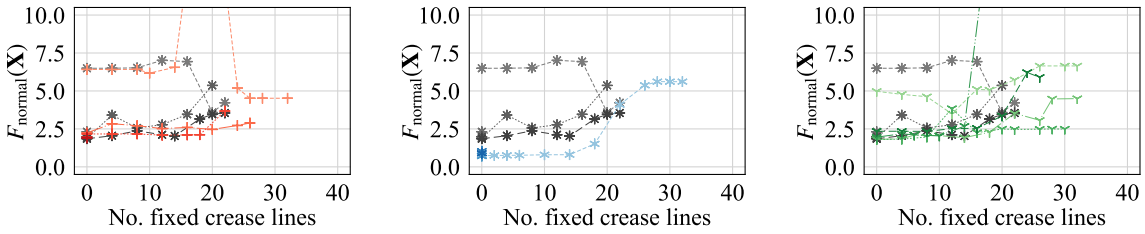

(a) Cut pattern C **(b)** Cut pattern E **(c)** Cut pattern X

Figure F.8: Values of $F_{\text{normal}}(\mathbf{X})$ in Case G2 with the HP surface.

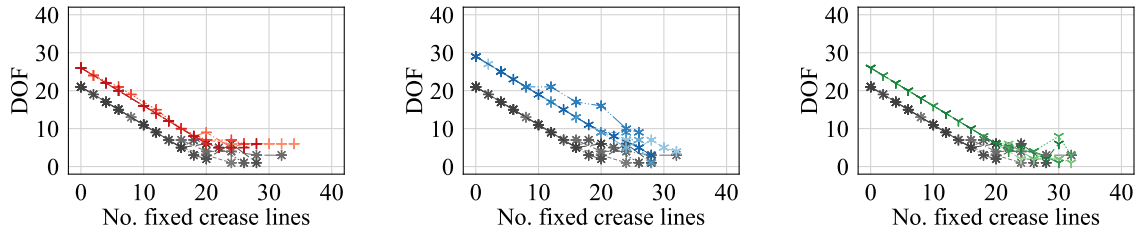

(a) Cut pattern C **(b)** Cut pattern E **(c)** Cut pattern X

Figure F.9: DOFs in Case G3 with the HP surface.

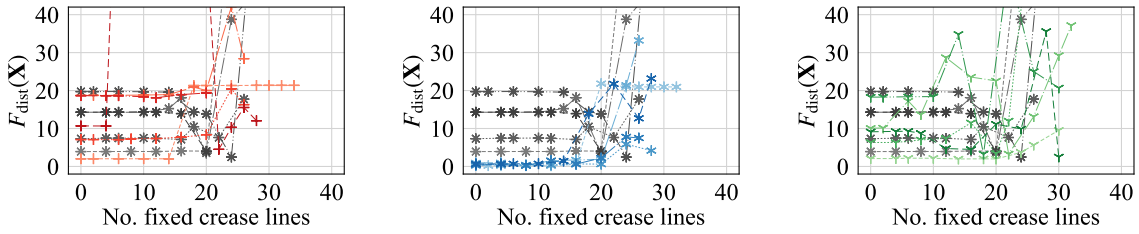

(a) Cut pattern C **(b)** Cut pattern E **(c)** Cut pattern X

Figure F.10: Values of $F_{\text{dist}}(\mathbf{X})$ in Case G3 with the HP surface.

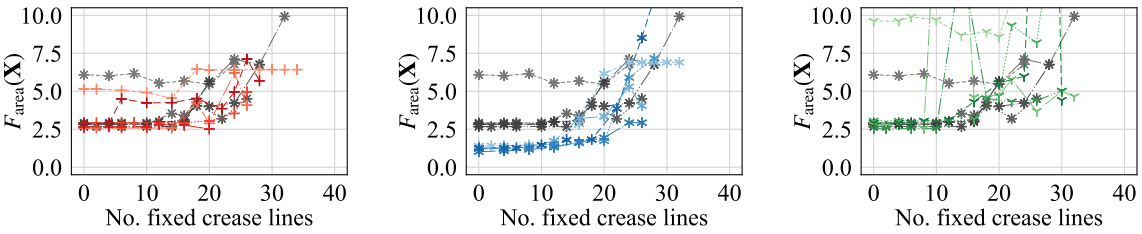

(a) Cut pattern C **(b)** Cut pattern E **(c)** Cut pattern X

Figure F.11: Values of $F_{\text{area}}(\mathbf{X})$ in Case G3 with the HP surface.

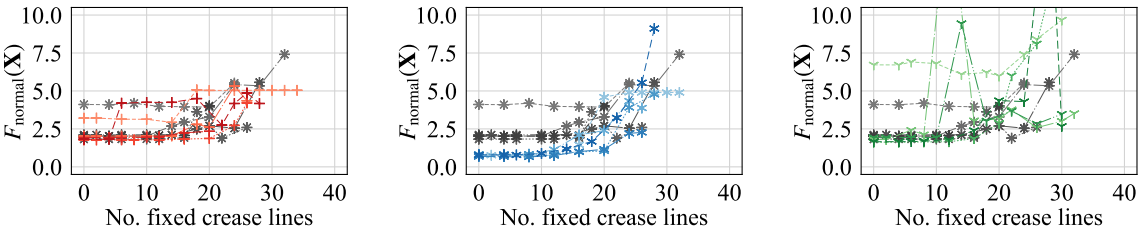

(a) Cut pattern C **(b)** Cut pattern E **(c)** Cut pattern X

Figure F.12: Values of $F_{\text{normal}}(\mathbf{X})$ in Case G3 with the HP surface.

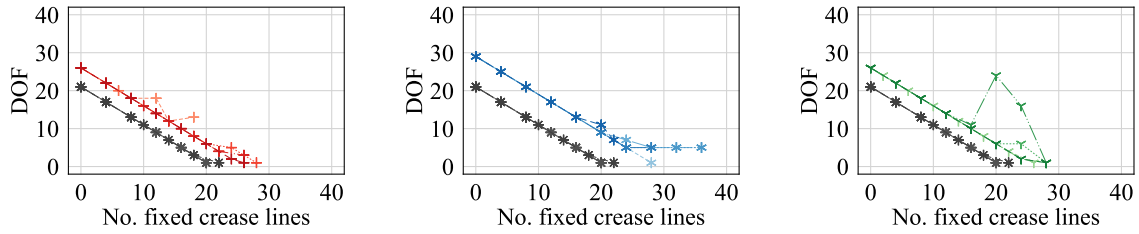

(a) Cut pattern C **(b)** Cut pattern E **(c)** Cut pattern X

Figure F.13: DOFs in Case R1 with the HP surface.

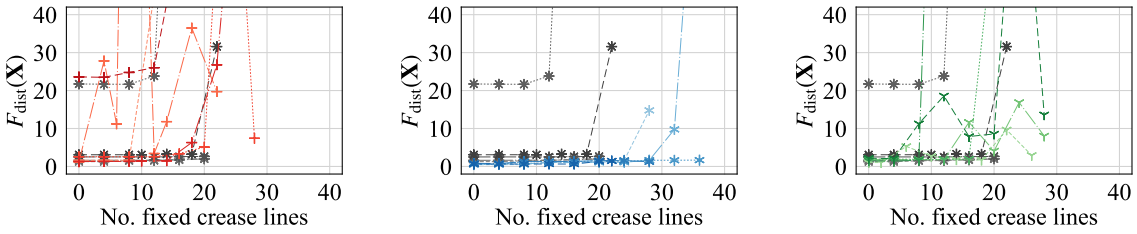

(a) Cut pattern C **(b)** Cut pattern E **(c)** Cut pattern X

Figure F.14: Values of $F_{\text{dist}}(\mathbf{X})$ in Case R1 with the HP surface.

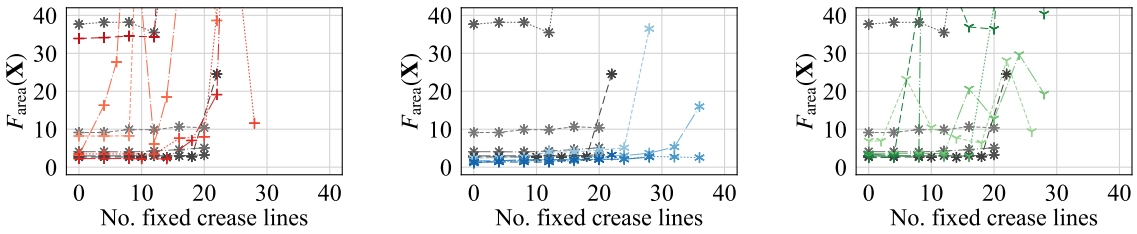

(a) Cut pattern C **(b)** Cut pattern E **(c)** Cut pattern X

Figure F.15: Values of $F_{\text{area}}(\mathbf{X})$ in Case R1 with the HP surface.

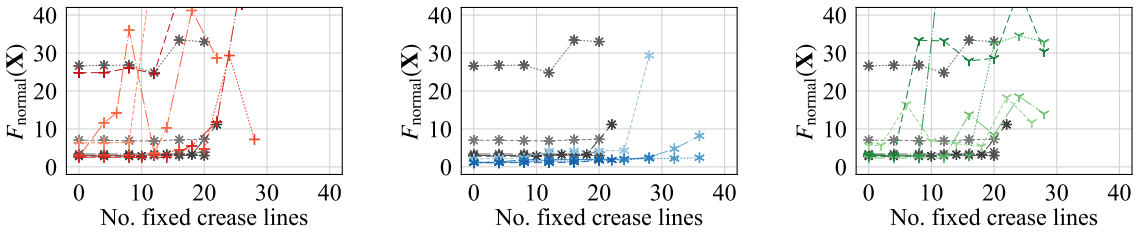

(a) Cut pattern C **(b)** Cut pattern E **(c)** Cut pattern X

Figure F.16: Values of $F_{\text{normal}}(\mathbf{X})$ in Case R1 with the HP surface.

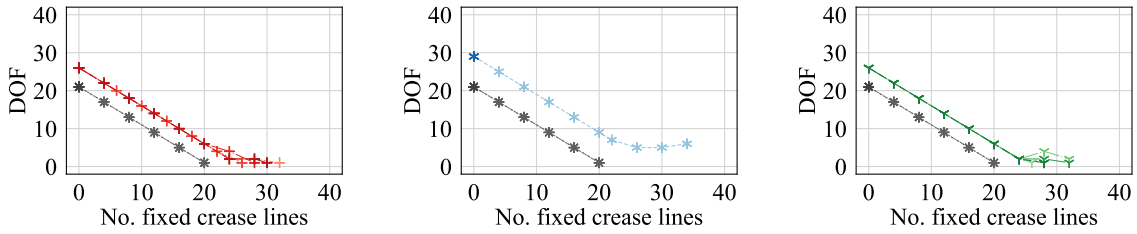

(a) Cut pattern C **(b)** Cut pattern E **(c)** Cut pattern X

Figure F.17: DOFs in Case R2 with the HP surface.

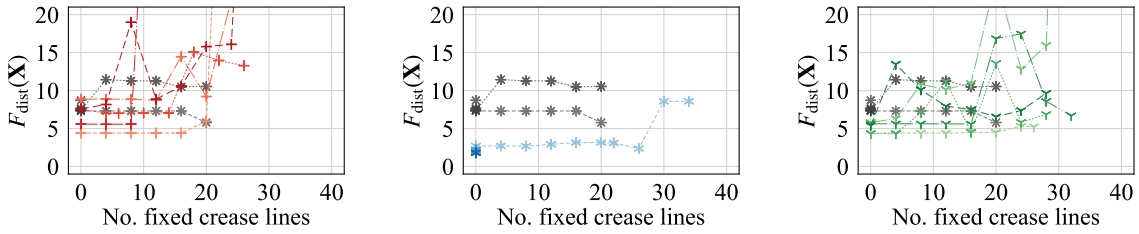

(a) Cut pattern C **(b)** Cut pattern E **(c)** Cut pattern X

Figure F.18: Values of $F_{\text{dist}}(\mathbf{X})$ in Case R2 with the HP surface.

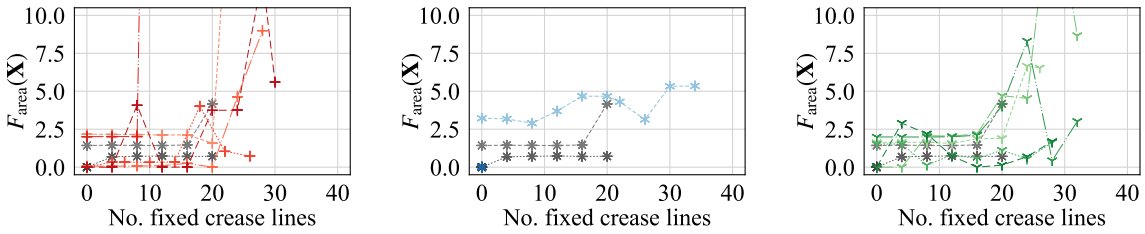

(a) Cut pattern C **(b)** Cut pattern E **(c)** Cut pattern X

Figure F.19: Values of $F_{\text{area}}(\mathbf{X})$ in Case R2 with the HP surface.

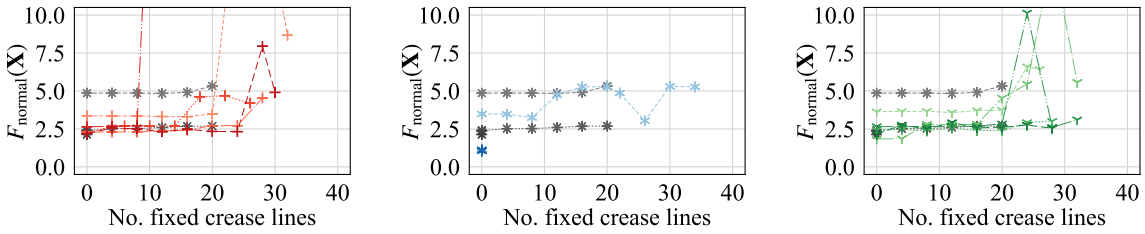

(a) Cut pattern C **(b)** Cut pattern E **(c)** Cut pattern X

Figure F.20: Values of $F_{\text{normal}}(\mathbf{X})$ in Case R2 with the HP surface.

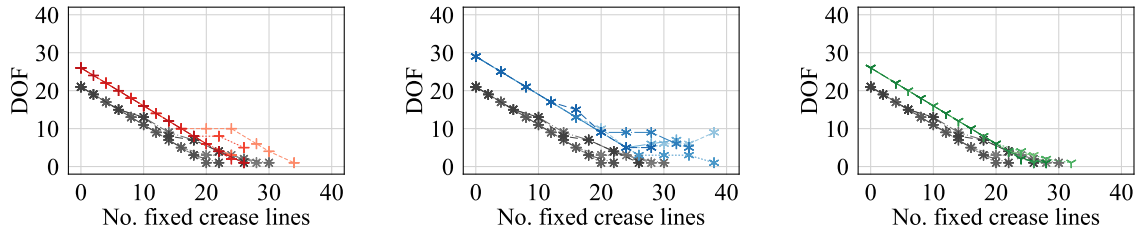

(a) Cut pattern C **(b)** Cut pattern E **(c)** Cut pattern X

Figure F.21: DOFs in Case R3 with the HP surface.

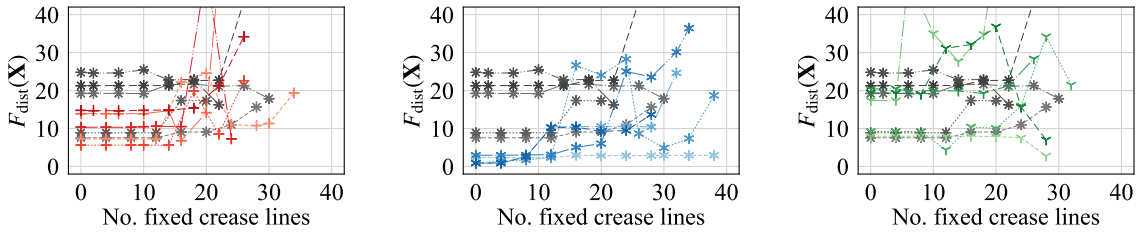

(a) Cut pattern C **(b)** Cut pattern E **(c)** Cut pattern X

Figure F.22: Values of $F_{\text{dist}}(\mathbf{X})$ in Case R3 with the HP surface.

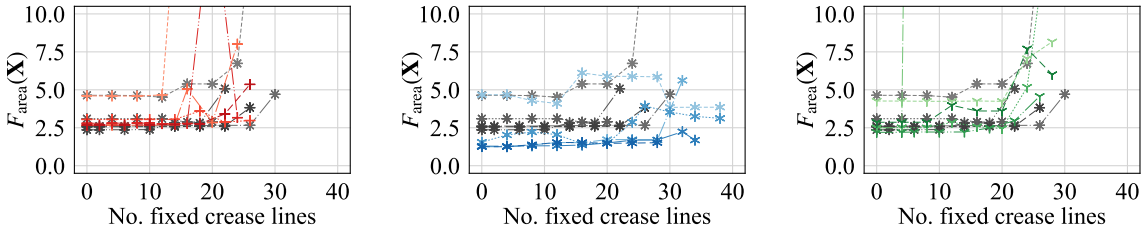

(a) Cut pattern C **(b)** Cut pattern E **(c)** Cut pattern X

Figure F.23: Values of $F_{\text{area}}(\mathbf{X})$ in Case R3 with the HP surface.

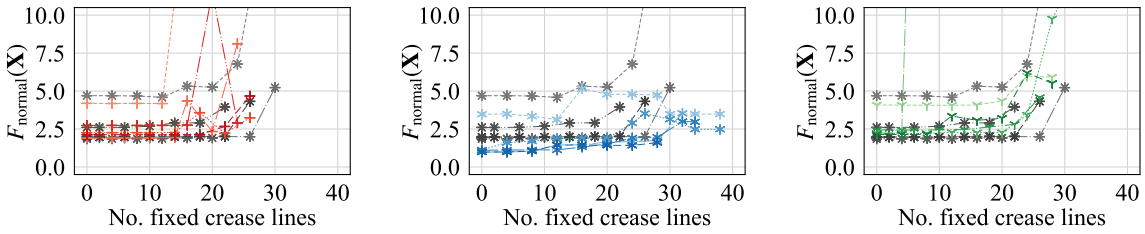

(a) Cut pattern C **(b)** Cut pattern E **(c)** Cut pattern X

Figure F.24: Values of $F_{\text{normal}}(\mathbf{X})$ in Case R3 with the HP surface.

F.2 Approximation of dome surface

The tables and graphs are shown for the solutions considered in Section 4.3 of Chapter 4, which approximate the dome surface in Fig. 4.6.

F.2.1 Tables comparing form generation results with respect to weight coefficients of approximation error functions

This section shows the tables arranged with respect to the weight coefficients c_{area} and c_{normal} in the approximation error function. The results of the approximation of the HP

surface obtained in cases G1–R3 are summarized as follows:

- Case G1: Tables F.46–F.49
- Case G2: Tables F.50–F.53
- Case G3: Tables F.54–F.57
- Case R1: Tables F.58–F.61
- Case R2: Tables F.62–F.65
- Case R3: Tables F.66–F.69

Table F.46: Results for the approximation of the dome surface without cuts in Case G1 arranged with respect to c_{area} and c_{normal}.

c_{area}		0.0	0.2	0.2	0.4	0.4
c_{normal}		0.0	0.5	1.0	0.5	1.0
No. solutions		7	7	7	7	1
Min. DOF		3	1	1	3	21
$F_{\text{dist}}(\mathbf{X})$	max.	2.50	33.22	5.93	18.33	2.32
	min.	2.06	2.24	2.61	2.18	2.32
	avg.	2.30	11.40	4.17	9.82	2.32
$F_{\text{area}}(\mathbf{X})$	max.	1.25	8.82	3.35	4.31	0.00
	min.	0.00	0.00	0.00	0.00	0.00
	avg.	0.56	2.25	0.56	0.62	0.00
$F_{\text{normal}}(\mathbf{X})$	max.	4.43	15.83	8.11	13.44	2.31
	min.	4.12	3.21	2.70	3.35	2.31
	avg.	4.21	8.43	4.14	8.58	2.31

Table F.47: Results for the approximation of the dime surface with cut pattern C in Case G1 arranged with respect to c_{area} and c_{normal}.

c_{area}		0.0	0.2	0.2	0.4	0.4
c_{normal}		0.0	0.5	1.0	0.5	1.0
No. solutions		6	7	7	7	8
Min. DOF		15	9	6	10	3
$F_{\text{dist}}(\mathbf{X})$	max.	305.62	172.42	49.93	567.64	449.52
	min.	2.11	2.09	3.37	177.68	2.91
	avg.	59.50	60.02	20.38	500.97	80.46
$F_{\text{area}}(\mathbf{X})$	max.	173.35	127.53	35.83	1493.76	68.12
	min.	2.07	0.00	0.00	621.89	0.00
	avg.	49.97	51.45	12.91	1265.15	30.56
$F_{\text{normal}}(\mathbf{X})$	max.	37.06	40.39	24.80	58.19	44.10
	min.	7.44	3.77	3.01	56.58	3.53
	avg.	20.63	19.81	12.16	57.12	27.13

Table F.48: Results for the approximation of the dome surface with cut pattern E in Case G1 arranged with respect to c_{area} and c_{normal}.

c_{area}		0.0	0.2	0.2	0.4	0.4
c_{normal}		0.0	0.5	1.0	0.5	1.0
No. solutions		5	4	3	7	2
Min. DOF		13	17	21	9	25
$F_{\text{dist}}(\mathbf{X})$	max.	0.66	0.71	0.55	1.25	0.72
	min.	0.42	0.44	0.54	0.54	0.72
	avg.	0.52	0.58	0.55	0.77	0.72
$F_{\text{area}}(\mathbf{X})$	max.	0.34	0.00	0.00	0.03	0.00
	min.	0.02	0.00	0.00	0.00	0.00
	avg.	0.21	0.00	0.00	0.00	0.00
$F_{\text{normal}}(\mathbf{X})$	max.	1.39	1.34	1.56	1.78	1.66
	min.	1.16	1.01	1.04	1.19	1.60
	avg.	1.28	1.15	1.22	1.58	1.63

Table F.49: Results for the approximation of the dome surface with cut pattern X in Case G1 arranged with respect to c_{area} and c_{normal}.

c_{area}		0.0	0.2	0.2	0.4	0.4
c_{normal}		0.0	0.5	1.0	0.5	1.0
No. solutions		7	7	9	8	8
Min. DOF		2	6	3	1	1
$F_{\text{dist}}(\mathbf{X})$	max.	151.42	311.04	196.32	36.12	560.27
	min.	1.94	2.07	2.63	2.53	3.68
	avg.	27.28	95.87	147.06	16.21	305.95
$F_{\text{area}}(\mathbf{X})$	max.	25.76	205.25	503.27	16.57	252.53
	min.	0.45	0.00	0.00	0.00	0.00
	avg.	7.45	66.51	372.35	4.53	133.27
$F_{\text{normal}}(\mathbf{X})$	max.	14.86	46.79	63.35	8.30	46.31
	min.	3.70	2.52	2.71	3.06	3.58
	avg.	6.56	26.99	49.65	6.06	30.76

Table F.50: Results for the approximation of the dome surface without cuts in Case G2 arranged with respect to c_{area} and c_{normal}.

c_{area}		0.0	0.2	0.2	0.4	0.4
c_{normal}		0.0	0.5	1.0	0.5	1.0
No. solutions		8	5	7	1	6
Min. DOF		1	5	1	21	3
$F_{\text{dist}}(\mathbf{X})$	max.	77.97	23.34	57.22	6.15	41.21
	min.	6.13	8.56	3.94	6.15	3.57
	avg.	20.83	16.52	16.89	6.15	13.08
$F_{\text{area}}(\mathbf{X})$	max.	37.36	0.00	1.02	0.00	0.00
	min.	3.44	0.00	0.00	0.00	0.00
	avg.	17.89	0.00	0.15	0.00	0.00
$F_{\text{normal}}(\mathbf{X})$	max.	13.04	3.60	5.17	3.03	6.53
	min.	3.31	2.61	2.05	3.03	2.10
	avg.	7.54	3.14	3.02	3.03	3.48

Table F.51: Results for the approximation of the dime surface with cut pattern C in Case G2 arranged with respect to c_{area} and c_{normal}.

c_{area}		0.0	0.2	0.2	0.4	0.4
c_{normal}		0.0	0.5	1.0	0.5	1.0
No. solutions		8	8	1	6	6
Min. DOF		6	1	26	10	7
$F_{\text{dist}}(\mathbf{X})$	max.	71.73	79.30	5.13	45.90	81.56
	min.	52.11	5.00	5.13	7.28	29.78
	avg.	61.35	32.55	5.13	22.97	46.16
$F_{\text{area}}(\mathbf{X})$	max.	103.57	0.00	0.00	0.00	0.43
	min.	75.26	0.00	0.00	0.00	0.00
	avg.	95.80	0.00	0.00	0.00	0.07
$F_{\text{normal}}(\mathbf{X})$	max.	35.08	7.35	2.01	7.78	12.06
	min.	30.31	2.40	2.01	2.66	2.78
	avg.	31.43	5.33	2.01	4.51	5.22

Table F.52: Results for the approximation of the dome surface with cut pattern E in Case G2 arranged with respect to c_{area} and c_{normal}.

c_{area}		0.0	0.2	0.2	0.4	0.4
c_{normal}		0.0	0.5	1.0	0.5	1.0
No. solutions		8	1	1	1	1
Min. DOF		3	29	29	29	29
$F_{\text{dist}}(\mathbf{X})$	max.	4.39	0.57	0.81	0.54	1.45
	min.	0.83	0.57	0.81	0.54	1.45
	avg.	1.51	0.57	0.81	0.54	1.45
$F_{\text{area}}(\mathbf{X})$	max.	2.49	0.00	0.00	0.00	0.00
	min.	0.97	0.00	0.00	0.00	0.00
	avg.	1.60	0.00	0.00	0.00	0.00
$F_{\text{normal}}(\mathbf{X})$	max.	3.18	0.78	0.78	0.73	0.78
	min.	1.69	0.78	0.78	0.73	0.78
	avg.	2.03	0.78	0.78	0.73	0.78

Table F.53: Results for the approximation of the dome surface with cut pattern X in Case G2 arranged with respect to c_{area} and c_{normal}.

c_{area}		0.0	0.2	0.2	0.4	0.4
c_{normal}		0.0	0.5	1.0	0.5	1.0
No. solutions		9	8	9	8	8
Min. DOF		1	1	3	1	2
$F_{\text{dist}}(\mathbf{X})$	max.	99.53	39.47	48.31	85.04	78.44
	min.	6.55	4.04	5.71	6.17	5.48
	avg.	21.68	11.03	29.00	36.61	23.49
$F_{\text{area}}(\mathbf{X})$	max.	16.52	0.07	4.29	0.00	0.00
	min.	1.43	0.00	0.00	0.00	0.00
	avg.	8.73	0.01	0.76	0.00	0.00
$F_{\text{normal}}(\mathbf{X})$	max.	13.22	6.74	8.31	8.87	9.79
	min.	4.08	2.22	2.21	2.44	2.23
	avg.	6.95	3.86	4.59	5.08	6.37

Table F.54: Results for the approximation of the dome surface without cuts in Case G3 arranged with respect to c_{area} and c_{normal}.

c_{area}		0.0	0.2	0.2	0.4	0.4
c_{normal}		0.0	0.5	1.0	0.5	1.0
No. solutions		7	9	8	2	1
Min. DOF		1	1	1	17	21
$F_{\text{dist}}(\mathbf{X})$	max.	12.30	17.28	13.08	5.00	8.60
	min.	12.23	6.12	3.45	4.87	8.60
	avg.	12.26	9.53	7.83	4.94	8.60
$F_{\text{area}}(\mathbf{X})$	max.	1.64	0.03	25.24	0.00	0.00
	min.	1.17	0.00	0.00	0.00	0.00
	avg.	1.49	0.01	3.16	0.00	0.00
$F_{\text{normal}}(\mathbf{X})$	max.	6.27	11.10	12.85	4.04	4.52
	min.	5.82	4.16	2.33	3.28	4.52
	avg.	5.97	5.88	5.03	3.66	4.52

Table F.55: Results for the approximation of the dime surface with cut pattern C in Case G3 arranged with respect to c_{area} and c_{normal}.

c_{area}		0.0	0.2	0.2	0.4	0.4
c_{normal}		0.0	0.5	1.0	0.5	1.0
No. solutions		8	9	5	9	8
Min. DOF		3	2	12	2	1
$F_{\text{dist}}(\mathbf{X})$	max.	82.40	21.80	7.12	11.33	23.64
	min.	9.46	3.60	5.14	4.69	7.36
	avg.	42.29	10.97	6.37	6.73	13.72
$F_{\text{area}}(\mathbf{X})$	max.	209.27	0.00	0.02	0.05	0.02
	min.	8.12	0.00	0.00	0.00	0.00
	avg.	96.07	0.00	0.00	0.01	0.00
$F_{\text{normal}}(\mathbf{X})$	max.	36.46	8.08	2.84	5.57	11.77
	min.	5.65	2.00	1.88	2.23	2.38
	avg.	19.01	4.72	2.60	3.81	5.79

Table F.56: Results for the approximation of the dome surface with cut pattern E in Case G3 arranged with respect to c_{area} and c_{normal}.

c_{area}		0.0	0.2	0.2	0.4	0.4
c_{normal}		0.0	0.5	1.0	0.5	1.0
No. solutions		8	1	5	1	1
Min. DOF		1	29	13	29	29
$F_{\text{dist}}(\mathbf{X})$	max.	9.21	0.91	1.22	0.57	0.94
	min.	0.58	0.91	0.75	0.57	0.94
	avg.	1.82	0.91	1.05	0.57	0.94
$F_{\text{area}}(\mathbf{X})$	max.	1.87	0.00	0.00	0.00	0.00
	min.	0.09	0.00	0.00	0.00	0.00
	avg.	1.01	0.00	0.00	0.00	0.00
$F_{\text{normal}}(\mathbf{X})$	max.	4.95	1.45	1.60	0.78	1.46
	min.	1.07	1.45	0.90	0.78	1.46
	avg.	1.69	1.45	1.44	0.78	1.46

Table F.57: Results for the approximation of the dome surface with cut pattern X in Case G3 arranged with respect to c_{area} and c_{normal}.

c_{area}		0.0	0.2	0.2	0.4	0.4
c_{normal}		0.0	0.5	1.0	0.5	1.0
No. solutions		9	8	8	8	5
Min. DOF		1	1	2	1	10
$F_{\text{dist}}(\mathbf{X})$	max.	81.21	19.93	35.46	56.90	76.52
	min.	7.44	2.98	3.11	3.36	3.30
	avg.	30.59	7.52	12.61	20.99	44.78
$F_{\text{area}}(\mathbf{X})$	max.	72.29	3.14	4.57	0.14	203.02
	min.	0.07	0.00	0.00	0.00	0.00
	avg.	27.86	0.69	0.57	0.02	110.18
$F_{\text{normal}}(\mathbf{X})$	max.	24.26	8.46	6.95	18.38	40.93
	min.	5.84	2.48	2.26	2.45	2.37
	avg.	12.53	4.37	4.34	8.85	24.45

Table F.58: Results for the approximation of the dome surface without cuts in Case R1 arranged with respect to c_{area} and c_{normal}.

c_{area}		0.0	0.2	0.2	0.4	0.4
c_{normal}		0.0	0.5	1.0	0.5	1.0
No. solutions		8	2	3	3	5
Min. DOF		1	19	13	17	7
$F_{\text{dist}}(\mathbf{X})$	max.	5.62	2.95	2.69	4.17	3.42
	min.	1.84	2.25	2.45	2.22	2.43
	avg.	3.25	2.60	2.57	3.04	2.90
$F_{\text{area}}(\mathbf{X})$	max.	4.66	0.00	0.00	0.00	0.00
	min.	0.08	0.00	0.00	0.00	0.00
	avg.	2.88	0.00	0.00	0.00	0.00
$F_{\text{normal}}(\mathbf{X})$	max.	10.17	4.49	2.88	4.31	3.45
	min.	3.82	2.75	2.62	2.89	2.65
	avg.	5.93	3.62	2.74	3.55	3.23

Table F.59: Results for the approximation of the dime surface with cut pattern C in Case R1 arranged with respect to c_{area} and c_{normal}.

c_{area}		0.0	0.2	0.2	0.4	0.4
c_{normal}		0.0	0.5	1.0	0.5	1.0
No. solutions		9	0	8	8	0
Min. DOF		5	-	2	5	-
$F_{\text{dist}}(\mathbf{X})$	max.	502.45	-	17.45	90.81	-
	min.	1.89	-	2.67	2.23	-
	avg.	129.36	-	4.95	22.46	-
$F_{\text{area}}(\mathbf{X})$	max.	78.91	-	4.44	54.44	-
	min.	1.49	-	0.00	0.00	-
	avg.	22.06	-	1.23	12.42	-
$F_{\text{normal}}(\mathbf{X})$	max.	53.05	-	7.93	36.70	-
	min.	4.53	-	3.37	2.79	-
	avg.	23.17	-	4.92	14.41	-

Table F.60: Results for the approximation of the dome surface with cut pattern E in Case R1 arranged with respect to c_{area} and c_{normal}.

c_{area}		0.0	0.2	0.2	0.4	0.4
c_{normal}		0.0	0.5	1.0	0.5	1.0
No. solutions		7	1	1	1	1
Min. DOF		7	29	29	29	29
$F_{\text{dist}}(\mathbf{X})$	max.	2.10	0.39	0.72	0.39	0.41
	min.	0.57	0.39	0.72	0.39	0.41
	avg.	0.99	0.39	0.72	0.39	0.41
$F_{\text{area}}(\mathbf{X})$	max.	3.64	0.00	0.00	0.00	0.00
	min.	0.36	0.00	0.00	0.00	0.00
	avg.	1.73	0.00	0.00	0.00	0.00
$F_{\text{normal}}(\mathbf{X})$	max.	3.15	0.92	1.46	0.92	0.93
	min.	2.07	0.92	1.46	0.92	0.93
	avg.	2.46	0.92	1.46	0.92	0.93

Table F.61: Results for the approximation of the dome surface with cut pattern X in Case R1 arranged with respect to c_{area} and c_{normal}.

c_{area}		0.0	0.2	0.2	0.4	0.4
c_{normal}		0.0	0.5	1.0	0.5	1.0
No. solutions		9	8	8	8	10
Min. DOF		5	6	1	1	1
$F_{\text{dist}}(\mathbf{X})$	max.	530.93	156.08	68.35	52.46	73.42
	min.	1.64	3.22	7.78	4.15	3.05
	avg.	204.30	64.69	43.99	16.10	29.23
$F_{\text{area}}(\mathbf{X})$	max.	829.51	308.72	163.19	32.41	28.72
	min.	1.38	0.00	27.17	0.00	0.00
	avg.	318.11	156.37	107.91	11.46	8.46
$F_{\text{normal}}(\mathbf{X})$	max.	70.26	60.42	57.53	21.23	34.36
	min.	7.15	4.37	17.95	5.30	3.86
	avg.	46.02	45.00	45.51	11.46	11.53

Table F.62: Results for the approximation of the dome surface without cuts in Case R2 arranged with respect to c_{area} and c_{normal}.

c_{area}		0.0	0.2	0.2	0.4	0.4
c_{normal}		0.0	0.5	1.0	0.5	1.0
No. solutions		8	1	6	1	7
Min. DOF		1	21	1	21	1
$F_{\text{dist}}(\mathbf{X})$	max.	6.97	3.36	11.90	3.96	12.19
	min.	4.11	3.36	3.71	3.96	2.88
	avg.	4.76	3.36	9.33	3.96	8.52
$F_{\text{area}}(\mathbf{X})$	max.	8.17	0.00	0.14	0.00	0.00
	min.	2.30	0.00	0.00	0.00	0.00
	avg.	4.84	0.00	0.02	0.00	0.00
$F_{\text{normal}}(\mathbf{X})$	max.	5.75	2.85	3.15	2.80	5.30
	min.	2.90	2.85	2.32	2.80	2.50
	avg.	4.05	2.85	2.82	2.80	3.69

Table F.63: Results for the approximation of the dime surface with cut pattern C in Case R2 arranged with respect to c_{area} and c_{normal}.

c_{area}		0.0	0.2	0.2	0.4	0.4
c_{normal}		0.0	0.5	1.0	0.5	1.0
No. solutions		7	9	8	10	9
Min. DOF		2	3	1	2	2
$F_{\text{dist}}(\mathbf{X})$	max.	52.36	82.72	54.43	43.91	91.17
	min.	42.47	4.72	9.03	4.49	3.39
	avg.	44.71	46.21	19.09	15.91	23.15
$F_{\text{area}}(\mathbf{X})$	max.	95.23	12.09	13.42	8.29	0.04
	min.	78.84	0.00	0.00	0.00	0.00
	avg.	83.15	2.67	1.68	1.32	0.01
$F_{\text{normal}}(\mathbf{X})$	max.	43.21	18.99	18.57	9.30	9.24
	min.	40.14	3.21	2.70	3.17	2.51
	avg.	41.88	11.87	5.03	4.93	4.78

Table F.64: Results for the approximation of the dome surface with cut pattern E in Case R2 arranged with respect to c_{area} and c_{normal}.

c_{area}		0.0	0.2	0.2	0.4	0.4
c_{normal}		0.0	0.5	1.0	0.5	1.0
No. solutions		11	1	7	1	1
Min. DOF		9	29	7	29	29
$F_{\text{dist}}(\mathbf{X})$	max.	10.90	0.56	11.06	0.45	0.50
	min.	1.73	0.56	0.49	0.45	0.50
	avg.	4.50	0.56	3.86	0.45	0.50
$F_{\text{area}}(\mathbf{X})$	max.	5.15	0.00	0.00	0.00	0.00
	min.	3.15	0.00	0.00	0.00	0.00
	avg.	3.81	0.00	0.00	0.00	0.00
$F_{\text{normal}}(\mathbf{X})$	max.	4.32	0.90	1.98	0.90	0.89
	min.	1.58	0.90	0.89	0.90	0.89
	avg.	2.58	0.90	1.46	0.90	0.89

Table F.65: Results for the approximation of the dome surface with cut pattern X in Case R2 arranged with respect to c_{area} and c_{normal}.

c_{area}		0.0	0.2	0.2	0.4	0.4
c_{normal}		0.0	0.5	1.0	0.5	1.0
No. solutions		9	8	9	9	8
Min. DOF		1	2	2	2	7
$F_{\text{dist}}(\mathbf{X})$	max.	85.75	34.97	56.99	89.29	116.79
	min.	8.03	7.03	6.23	23.43	61.49
	avg.	27.29	19.29	17.73	53.89	85.98
$F_{\text{area}}(\mathbf{X})$	max.	44.86	0.00	15.43	16.14	367.36
	min.	5.85	0.00	0.00	0.00	216.71
	avg.	16.38	0.00	2.21	1.79	283.89
$F_{\text{normal}}(\mathbf{X})$	max.	22.29	6.00	11.27	12.93	49.83
	min.	5.23	2.68	2.53	5.43	43.15
	avg.	10.50	4.12	5.18	8.80	47.46

Table F.66: Results for the approximation of the dome surface without cuts in Case R3 arranged with respect to c_{area} and c_{normal}.

c_{area}		0.0	0.2	0.2	0.4	0.4
c_{normal}		0.0	0.5	1.0	0.5	1.0
No. solutions		7	1	7	1	1
Min. DOF		1	21	1	21	21
$F_{\text{dist}}(\mathbf{X})$	max.	4.72	4.66	26.37	5.57	5.03
	min.	4.40	4.66	3.13	5.57	5.03
	avg.	4.54	4.66	10.93	5.57	5.03
$F_{\text{area}}(\mathbf{X})$	max.	4.49	0.00	0.01	0.00	0.00
	min.	2.40	0.00	0.00	0.00	0.00
	avg.	3.28	0.00	0.00	0.00	0.00
$F_{\text{normal}}(\mathbf{X})$	max.	4.63	2.89	5.54	3.06	2.99
	min.	3.56	2.89	2.47	3.06	2.99
	avg.	4.13	2.89	3.58	3.06	2.99

Table F.67: Results for the approximation of the dime surface with cut pattern C in Case R3 arranged with respect to c_{area} and c_{normal}.

c_{area}		0.0	0.2	0.2	0.4	0.4
c_{normal}		0.0	0.5	1.0	0.5	1.0
No. solutions		8	8	8	6	9
Min. DOF		3	1	1	10	2
$F_{\text{dist}}(\mathbf{X})$	max.	64.85	20.52	20.24	75.23	62.47
	min.	59.17	3.03	6.18	9.83	5.46
	avg.	62.56	8.86	8.89	61.07	16.33
$F_{\text{area}}(\mathbf{X})$	max.	186.15	0.00	16.45	145.12	3.72
	min.	50.12	0.00	0.00	0.00	0.00
	avg.	137.67	0.00	2.06	30.32	0.42
$F_{\text{normal}}(\mathbf{X})$	max.	42.05	7.10	11.35	48.51	22.85
	min.	40.23	2.81	3.40	5.80	2.72
	avg.	40.87	4.54	5.28	28.66	8.31

Table F.68: Results for the approximation of the dome surface with cut pattern E in Case R3 arranged with respect to c_{area} and c_{normal}.

c_{area}		0.0	0.2	0.2	0.4	0.4
c_{normal}		0.0	0.5	1.0	0.5	1.0
No. solutions		10	1	1	1	1
Min. DOF		11	29	29	29	29
$F_{\text{dist}}(\mathbf{X})$	max.	2.44	0.46	0.45	0.44	0.46
	min.	1.32	0.46	0.45	0.44	0.46
	avg.	1.80	0.46	0.45	0.44	0.46
$F_{\text{area}}(\mathbf{X})$	max.	2.61	0.00	0.00	0.00	0.00
	min.	1.50	0.00	0.00	0.00	0.00
	avg.	2.03	0.00	0.00	0.00	0.00
$F_{\text{normal}}(\mathbf{X})$	max.	3.81	0.87	0.87	0.87	0.87
	min.	1.72	0.87	0.87	0.87	0.87
	avg.	2.60	0.87	0.87	0.87	0.87

Table F.69: Results for the approximation of the dome surface with cut pattern X in Case R3 arranged with respect to c_{area} and c_{normal}.

c_{area}		0.0	0.2	0.2	0.4	0.4
c_{normal}		0.0	0.5	1.0	0.5	1.0
No. solutions		12	9	2	8	8
Min. DOF		1	1	24	2	3
$F_{\text{dist}}(\mathbf{X})$	max.	70.98	32.82	11.70	74.86	94.06
	min.	7.05	5.23	4.85	18.60	5.10
	avg.	53.42	13.81	8.28	48.67	45.09
$F_{\text{area}}(\mathbf{X})$	max.	87.18	0.00	0.00	160.34	115.09
	min.	4.47	0.00	0.00	0.00	0.00
	avg.	58.96	0.00	0.00	30.50	14.39
$F_{\text{normal}}(\mathbf{X})$	max.	17.14	9.23	3.85	48.12	42.64
	min.	4.62	3.74	3.36	16.26	3.50
	avg.	14.10	5.65	3.61	32.60	23.14

F.2.2 Tables comparing form generation results with respect to choice of design variables

This section shows the tables arranged with respect to the design variables of the optimization problems (3.50) and (3.51). The results of the approximation of the dome surface obtained by setting $(c_{\text{area}}, c_{\text{normal}})$ to $(0.0, 0.0)$, $(0.2, 0.5)$, $(0.2, 1.0)$, $(0.4, 0.5)$, and $(0.4, 1.0)$ are summarized as follows:

- $(c_{\text{area}}, c_{\text{normal}}) = (0.0, 0.0)$: Tables F.70–F.73
- $(c_{\text{area}}, c_{\text{normal}}) = (0.2, 0.5)$: Tables F.74–F.77
- $(c_{\text{area}}, c_{\text{normal}}) = (0.2, 1.0)$: Tables F.78–F.81
- $(c_{\text{area}}, c_{\text{normal}}) = (0.4, 0.5)$: Tables F.82–F.85
- $(c_{\text{area}}, c_{\text{normal}}) = (0.4, 1.0)$: Tables F.86–F.89

Table F.70: Results for the approximation of the dome surface without cuts and with $(c_{\text{area}}, c_{\text{normal}}) = (0.0, 0.0)$ arranged with respect to the choice of design variables.

Cases		G1	G2	G3	R1	R2	R3
No. solutions		7	8	7	8	8	7
Min. DOF		3	1	1	1	1	1
$F_{\text{dist}}(\mathbf{X})$	max.	2.50	77.97	12.30	5.62	6.97	4.72
	min.	2.06	6.13	12.23	1.84	4.11	4.40
	avg.	2.30	20.83	12.26	3.25	4.76	4.54
$F_{\text{area}}(\mathbf{X})$	max.	1.25	37.36	1.64	4.66	8.17	4.49
	min.	0.00	3.44	1.17	0.08	2.30	2.40
	avg.	0.56	17.89	1.49	2.88	4.84	3.28
$F_{\text{normal}}(\mathbf{X})$	max.	4.43	13.04	6.27	10.17	5.75	4.63
	min.	4.12	3.31	5.82	3.82	2.90	3.56
	avg.	4.21	7.54	5.97	5.93	4.05	4.13

Table F.71: Results for the approximation of the dome surface with cut pattern C and $(c_{\text{area}}, c_{\text{normal}}) = (0.0, 0.0)$ arranged with respect to the choice of design variables.

Cases		G1	G2	G3	R1	R2	R3
No. solutions		6	8	8	9	7	8
Min. DOF		15	6	3	5	2	3
$F_{\text{dist}}(\mathbf{X})$	max.	305.62	71.73	82.40	502.45	52.36	64.85
	min.	2.11	52.11	9.46	1.89	42.47	59.17
	avg.	59.50	61.35	42.29	129.36	44.71	62.56
$F_{\text{area}}(\mathbf{X})$	max.	173.35	103.57	209.27	78.91	95.23	186.15
	min.	2.07	75.26	8.12	1.49	78.84	50.12
	avg.	49.97	95.80	96.07	22.06	83.15	137.67
$F_{\text{normal}}(\mathbf{X})$	max.	37.06	35.08	36.46	53.05	43.21	42.05
	min.	7.44	30.31	5.65	4.53	40.14	40.23
	avg.	20.63	31.43	19.01	23.17	41.88	40.87

Table F.72: Results for the approximation of the dome surface with cut pattern E and $(c_{\text{area}}, c_{\text{normal}}) = (0.0, 0.0)$ arranged with respect to the choice of design variables.

Cases		G1	G2	G3	R1	R2	R3
No. solutions		5	8	8	7	11	10
Min. DOF		13	3	1	7	9	11
$F_{\text{dist}}(\mathbf{X})$	max.	0.66	4.39	9.21	2.10	10.90	2.44
	min.	0.42	0.83	0.58	0.57	1.73	1.32
	avg.	0.52	1.51	1.82	0.99	4.50	1.80
$F_{\text{area}}(\mathbf{X})$	max.	0.34	2.49	1.87	3.64	5.15	2.61
	min.	0.02	0.97	0.09	0.36	3.15	1.50
	avg.	0.21	1.60	1.01	1.73	3.81	2.03
$F_{\text{normal}}(\mathbf{X})$	max.	1.39	3.18	4.95	3.15	4.32	3.81
	min.	1.16	1.69	1.07	2.07	1.58	1.72
	avg.	1.28	2.03	1.69	2.46	2.58	2.60

Table F.73: Results for the approximation of the dome surface with cut pattern X and $(c_{\text{area}}, c_{\text{normal}}) = (0.0, 0.0)$ arranged with respect to the choice of design variables.

Cases		G1	G2	G3	R1	R2	R3
No. solutions		7	9	9	9	9	12
Min. DOF		2	1	1	5	1	1
$F_{\text{dist}}(\mathbf{X})$	max.	151.42	99.53	81.21	530.93	85.75	70.98
	min.	1.94	6.55	7.44	1.64	8.03	7.05
	avg.	27.28	21.68	30.59	204.30	27.29	53.42
$F_{\text{area}}(\mathbf{X})$	max.	25.76	16.52	72.29	829.51	44.86	87.18
	min.	0.45	1.43	0.07	1.38	5.85	4.47
	avg.	7.45	8.73	27.86	318.11	16.38	58.96
$F_{\text{normal}}(\mathbf{X})$	max.	14.86	13.22	24.26	70.26	22.29	17.14
	min.	3.70	4.08	5.84	7.15	5.23	4.62
	avg.	6.56	6.95	12.53	46.02	10.50	14.10

Table F.74: Results for the approximation of the dome surface without cuts and with $(c_{\text{area}}, c_{\text{normal}}) = (0.2, 0.5)$ arranged with respect to the choice of design variables.

Cases		G1	G2	G3	R1	R2	R3
No. solutions		7	5	9	2	1	1
Min. DOF		1	5	1	19	21	21
$F_{\text{dist}}(\mathbf{X})$	max.	33.22	23.34	17.28	2.95	3.36	4.66
	min.	2.24	8.56	6.12	2.25	3.36	4.66
	avg.	11.40	16.52	9.53	2.60	3.36	4.66
$F_{\text{area}}(\mathbf{X})$	max.	8.82	0.00	0.03	0.00	0.00	0.00
	min.	0.00	0.00	0.00	0.00	0.00	0.00
	avg.	2.25	0.00	0.01	0.00	0.00	0.00
$F_{\text{normal}}(\mathbf{X})$	max.	15.83	3.60	11.10	4.49	2.85	2.89
	min.	3.21	2.61	4.16	2.75	2.85	2.89
	avg.	8.43	3.14	5.88	3.62	2.85	2.89

Table F.75: Results for the approximation of the dome surface with cut pattern C and $(c_{\text{area}}, c_{\text{normal}}) = (0.2, 0.5)$ arranged with respect to the choice of design variables.

Cases		G1	G2	G3	R1	R2	R3
No. solutions		7	8	9	0	9	8
Min. DOF		9	1	2	-	3	1
$F_{\text{dist}}(\mathbf{X})$	max.	172.42	79.30	21.80	-	82.72	20.52
	min.	2.09	5.00	3.60	-	4.72	3.03
	avg.	60.02	32.55	10.97	-	46.21	8.86
$F_{\text{area}}(\mathbf{X})$	max.	127.53	0.00	0.00	-	12.09	0.00
	min.	0.00	0.00	0.00	-	0.00	0.00
	avg.	51.45	0.00	0.00	-	2.67	0.00
$F_{\text{normal}}(\mathbf{X})$	max.	40.39	7.35	8.08	-	18.99	7.10
	min.	3.77	2.40	2.00	-	3.21	2.81
	avg.	19.81	5.33	4.72	-	11.87	4.54

Table F.76: Results for the approximation of the dome surface with cut pattern E and $(c_{\text{area}}, c_{\text{normal}}) = (0.2, 0.5)$ arranged with respect to the choice of design variables.

Cases		G1	G2	G3	R1	R2	R3
No. solutions		4	1	1	1	1	1
Min. DOF		17	29	29	29	29	29
$F_{\text{dist}}(\mathbf{X})$	max.	0.71	0.57	0.91	0.39	0.56	0.46
	min.	0.44	0.57	0.91	0.39	0.56	0.46
	avg.	0.58	0.57	0.91	0.39	0.56	0.46
$F_{\text{area}}(\mathbf{X})$	max.	0.00	0.00	0.00	0.00	0.00	0.00
	min.	0.00	0.00	0.00	0.00	0.00	0.00
	avg.	0.00	0.00	0.00	0.00	0.00	0.00
$F_{\text{normal}}(\mathbf{X})$	max.	1.34	0.78	1.45	0.92	0.90	0.87
	min.	1.01	0.78	1.45	0.92	0.90	0.87
	avg.	1.15	0.78	1.45	0.92	0.90	0.87

Table F.77: Results for the approximation of the dome surface with cut pattern X and $(c_{\text{area}}, c_{\text{normal}}) = (0.2, 0.5)$ arranged with respect to the choice of design variables.

Cases		G1	G2	G3	R1	R2	R3
No. solutions		7	8	8	8	8	9
Min. DOF		6	1	1	6	2	1
$F_{\text{dist}}(\mathbf{X})$	max.	311.04	39.47	19.93	156.08	34.97	32.82
	min.	2.07	4.04	2.98	3.22	7.03	5.23
	avg.	95.87	11.03	7.52	64.69	19.29	13.81
$F_{\text{area}}(\mathbf{X})$	max.	205.25	0.07	3.14	308.72	0.00	0.00
	min.	0.00	0.00	0.00	0.00	0.00	0.00
	avg.	66.51	0.01	0.69	156.37	0.00	0.00
$F_{\text{normal}}(\mathbf{X})$	max.	46.79	6.74	8.46	60.42	6.00	9.23
	min.	2.52	2.22	2.48	4.37	2.68	3.74
	avg.	26.99	3.86	4.37	45.00	4.12	5.65

Table F.78: Results for the approximation of the dome surface without cuts and with $(c_{\text{area}}, c_{\text{normal}}) = (0.2, 1.0)$ arranged with respect to the choice of design variables.

Cases		G1	G2	G3	R1	R2	R3
No. solutions		7	7	8	3	6	7
Min. DOF		1	1	1	13	1	1
$F_{\text{dist}}(\mathbf{X})$	max.	5.93	57.22	13.08	2.69	11.90	26.37
	min.	2.61	3.94	3.45	2.45	3.71	3.13
	avg.	4.17	16.89	7.83	2.57	9.33	10.93
$F_{\text{area}}(\mathbf{X})$	max.	3.35	1.02	25.24	0.00	0.14	0.01
	min.	0.00	0.00	0.00	0.00	0.00	0.00
	avg.	0.56	0.15	3.16	0.00	0.02	0.00
$F_{\text{normal}}(\mathbf{X})$	max.	8.11	5.17	12.85	2.88	3.15	5.54
	min.	2.70	2.05	2.33	2.62	2.32	2.47
	avg.	4.14	3.02	5.03	2.74	2.82	3.58

Table F.79: Results for the approximation of the dome surface with cut pattern C and $(c_{\text{area}}, c_{\text{normal}}) = (0.2, 1.0)$ arranged with respect to the choice of design variables.

Cases		G1	G2	G3	R1	R2	R3
No. solutions		7	1	5	8	8	8
Min. DOF		6	26	12	2	1	1
$F_{\text{dist}}(\mathbf{X})$	max.	49.93	5.13	7.12	17.45	54.43	20.24
	min.	3.37	5.13	5.14	2.67	9.03	6.18
	avg.	20.38	5.13	6.37	4.95	19.09	8.89
$F_{\text{area}}(\mathbf{X})$	max.	35.83	0.00	0.02	4.44	13.42	16.45
	min.	0.00	0.00	0.00	0.00	0.00	0.00
	avg.	12.91	0.00	0.00	1.23	1.68	2.06
$F_{\text{normal}}(\mathbf{X})$	max.	24.80	2.01	2.84	7.93	18.57	11.35
	min.	3.01	2.01	1.88	3.37	2.70	3.40
	avg.	12.16	2.01	2.60	4.92	5.03	5.28

Table F.80: Results for the approximation of the dome surface with cut pattern E and $(c_{\text{area}}, c_{\text{normal}}) = (0.2, 1.0)$ arranged with respect to the choice of design variables.

Cases		G1	G2	G3	R1	R2	R3
No. solutions		3	1	5	1	7	1
Min. DOF		21	29	13	29	7	29
$F_{\text{dist}}(\mathbf{X})$	max.	0.55	0.81	1.22	0.72	11.06	0.45
	min.	0.54	0.81	0.75	0.72	0.49	0.45
	avg.	0.55	0.81	1.05	0.72	3.86	0.45
$F_{\text{area}}(\mathbf{X})$	max.	0.00	0.00	0.00	0.00	0.00	0.00
	min.	0.00	0.00	0.00	0.00	0.00	0.00
	avg.	0.00	0.00	0.00	0.00	0.00	0.00
$F_{\text{normal}}(\mathbf{X})$	max.	1.56	0.78	1.60	1.46	1.98	0.87
	min.	1.04	0.78	0.90	1.46	0.89	0.87
	avg.	1.22	0.78	1.44	1.46	1.46	0.87

Table F.81: Results for the approximation of the dome surface with cut pattern X and $(c_{\text{area}}, c_{\text{normal}}) = (0.2, 1.0)$ arranged with respect to the choice of design variables.

Cases		G1	G2	G3	R1	R2	R3
No. solutions		9	9	8	8	9	2
Min. DOF		3	3	2	1	2	24
$F_{\text{dist}}(\mathbf{X})$	max.	196.32	48.31	35.46	68.35	56.99	11.70
	min.	2.63	5.71	3.11	7.78	6.23	4.85
	avg.	147.06	29.00	12.61	43.99	17.73	8.28
$F_{\text{area}}(\mathbf{X})$	max.	503.27	4.29	4.57	163.19	15.43	0.00
	min.	0.00	0.00	0.00	27.17	0.00	0.00
	avg.	372.35	0.76	0.57	107.91	2.21	0.00
$F_{\text{normal}}(\mathbf{X})$	max.	63.35	8.31	6.95	57.53	11.27	3.85
	min.	2.71	2.21	2.26	17.95	2.53	3.36
	avg.	49.65	4.59	4.34	45.51	5.18	3.61

Table F.82: Results for the approximation of the dome surface without cuts and with $(c_{\text{area}}, c_{\text{normal}}) = (0.4, 0.5)$ arranged with respect to the choice of design variables.

Cases		G1	G2	G3	R1	R2	R3
No. solutions		7	1	2	3	1	1
Min. DOF		3	21	17	17	21	21
$F_{\text{dist}}(\mathbf{X})$	max.	18.33	6.15	5.00	4.17	3.96	5.57
	min.	2.18	6.15	4.87	2.22	3.96	5.57
	avg.	9.82	6.15	4.94	3.04	3.96	5.57
$F_{\text{area}}(\mathbf{X})$	max.	4.31	0.00	0.00	0.00	0.00	0.00
	min.	0.00	0.00	0.00	0.00	0.00	0.00
	avg.	0.62	0.00	0.00	0.00	0.00	0.00
$F_{\text{normal}}(\mathbf{X})$	max.	13.44	3.03	4.04	4.31	2.80	3.06
	min.	3.35	3.03	3.28	2.89	2.80	3.06
	avg.	8.58	3.03	3.66	3.55	2.80	3.06

Table F.83: Results for the approximation of the dome surface with cut pattern C and $(c_{\text{area}}, c_{\text{normal}}) = (0.4, 0.5)$ arranged with respect to the choice of design variables.

Cases		G1	G2	G3	R1	R2	R3
No. solutions		7	6	9	8	10	6
Min. DOF		10	10	2	5	2	10
$F_{\text{dist}}(\mathbf{X})$	max.	567.64	45.90	11.33	90.81	43.91	75.23
	min.	177.68	7.28	4.69	2.23	4.49	9.83
	avg.	500.97	22.97	6.73	22.46	15.91	61.07
$F_{\text{area}}(\mathbf{X})$	max.	1493.76	0.00	0.05	54.44	8.29	145.12
	min.	621.89	0.00	0.00	0.00	0.00	0.00
	avg.	1265.15	0.00	0.01	12.42	1.32	30.32
$F_{\text{normal}}(\mathbf{X})$	max.	58.19	7.78	5.57	36.70	9.30	48.51
	min.	56.58	2.66	2.23	2.79	3.17	5.80
	avg.	57.12	4.51	3.81	14.41	4.93	28.66

Table F.84: Results for the approximation of the dome surface with cut pattern E and $(c_{\text{area}}, c_{\text{normal}}) = (0.4, 0.5)$ arranged with respect to the choice of design variables.

Cases		G1	G2	G3	R1	R2	R3
No. solutions		7	1	1	1	1	1
Min. DOF		9	29	29	29	29	29
$F_{\text{dist}}(\mathbf{X})$	max.	1.25	0.54	0.57	0.39	0.45	0.44
	min.	0.54	0.54	0.57	0.39	0.45	0.44
	avg.	0.77	0.54	0.57	0.39	0.45	0.44
$F_{\text{area}}(\mathbf{X})$	max.	0.03	0.00	0.00	0.00	0.00	0.00
	min.	0.00	0.00	0.00	0.00	0.00	0.00
	avg.	0.00	0.00	0.00	0.00	0.00	0.00
$F_{\text{normal}}(\mathbf{X})$	max.	1.78	0.73	0.78	0.92	0.90	0.87
	min.	1.19	0.73	0.78	0.92	0.90	0.87
	avg.	1.58	0.73	0.78	0.92	0.90	0.87

Table F.85: Results for the approximation of the dome surface with cut pattern X and $(c_{\text{area}}, c_{\text{normal}}) = (0.4, 0.5)$ arranged with respect to the choice of design variables.

Cases		G1	G2	G3	R1	R2	R3
No. solutions		8	8	8	8	9	8
Min. DOF		1	1	1	1	2	2
$F_{\text{dist}}(\mathbf{X})$	max.	36.12	85.04	56.90	52.46	89.29	74.86
	min.	2.53	6.17	3.36	4.15	23.43	18.60
	avg.	16.21	36.61	20.99	16.10	53.89	48.67
$F_{\text{area}}(\mathbf{X})$	max.	16.57	0.00	0.14	32.41	16.14	160.34
	min.	0.00	0.00	0.00	0.00	0.00	0.00
	avg.	4.53	0.00	0.02	11.46	1.79	30.50
$F_{\text{normal}}(\mathbf{X})$	max.	8.30	8.87	18.38	21.23	12.93	48.12
	min.	3.06	2.44	2.45	5.30	5.43	16.26
	avg.	6.06	5.08	8.85	11.46	8.80	32.60

Table F.86: Results for the approximation of the dome surface without cuts and with $(c_{\text{area}}, c_{\text{normal}}) = (0.4, 1.0)$ arranged with respect to the choice of design variables.

Cases		G1	G2	G3	R1	R2	R3
No. solutions		1	6	1	5	7	1
Min. DOF		21	3	21	7	1	21
$F_{\text{dist}}(\mathbf{X})$	max.	2.32	41.21	8.60	3.42	12.19	5.03
	min.	2.32	3.57	8.60	2.43	2.88	5.03
	avg.	2.32	13.08	8.60	2.90	8.52	5.03
$F_{\text{area}}(\mathbf{X})$	max.	0.00	0.00	0.00	0.00	0.00	0.00
	min.	0.00	0.00	0.00	0.00	0.00	0.00
	avg.	0.00	0.00	0.00	0.00	0.00	0.00
$F_{\text{normal}}(\mathbf{X})$	max.	2.31	6.53	4.52	3.45	5.30	2.99
	min.	2.31	2.10	4.52	2.65	2.50	2.99
	avg.	2.31	3.48	4.52	3.23	3.69	2.99

Table F.87: Results for the approximation of the dome surface with cut pattern C and $(c_{\text{area}}, c_{\text{normal}}) = (0.4, 1.0)$ arranged with respect to the choice of design variables.

Cases		G1	G2	G3	R1	R2	R3
No. solutions		8	6	8	0	9	9
Min. DOF		3	7	1	-	2	2
$F_{\text{dist}}(\mathbf{X})$	max.	449.52	81.56	23.64	-	91.17	62.47
	min.	2.91	29.78	7.36	-	3.39	5.46
	avg.	80.46	46.16	13.72	-	23.15	16.33
$F_{\text{area}}(\mathbf{X})$	max.	68.12	0.43	0.02	-	0.04	3.72
	min.	0.00	0.00	0.00	-	0.00	0.00
	avg.	30.56	0.07	0.00	-	0.01	0.42
$F_{\text{normal}}(\mathbf{X})$	max.	44.10	12.06	11.77	-	9.24	22.85
	min.	3.53	2.78	2.38	-	2.51	2.72
	avg.	27.13	5.22	5.79	-	4.78	8.31

Table F.88: Results for the approximation of the dome surface with cut pattern E and $(c_{\text{area}}, c_{\text{normal}}) = (0.4, 1.0)$ arranged with respect to the choice of design variables.

Cases		G1	G2	G3	R1	R2	R3
No. solutions		2	1	1	1	1	1
Min. DOF		25	29	29	29	29	29
$F_{\text{dist}}(\mathbf{X})$	max.	0.72	1.45	0.94	0.41	0.50	0.46
	min.	0.72	1.45	0.94	0.41	0.50	0.46
	avg.	0.72	1.45	0.94	0.41	0.50	0.46
$F_{\text{area}}(\mathbf{X})$	max.	0.00	0.00	0.00	0.00	0.00	0.00
	min.	0.00	0.00	0.00	0.00	0.00	0.00
	avg.	0.00	0.00	0.00	0.00	0.00	0.00
$F_{\text{normal}}(\mathbf{X})$	max.	1.66	0.78	1.46	0.93	0.89	0.87
	min.	1.60	0.78	1.46	0.93	0.89	0.87
	avg.	1.63	0.78	1.46	0.93	0.89	0.87

Table F.89: Results for the approximation of the dome surface with cut pattern X and $(c_{\text{area}}, c_{\text{normal}}) = (0.4, 1.0)$ arranged with respect to the choice of design variables.

Cases		G1	G2	G3	R1	R2	R3
No. solutions		8	8	5	10	8	8
Min. DOF		1	2	10	1	7	3
$F_{\text{dist}}(\mathbf{X})$	max.	560.27	78.44	76.52	73.42	116.79	94.06
	min.	3.68	5.48	3.30	3.05	61.49	5.10
	avg.	305.95	23.49	44.78	29.23	85.98	45.09
$F_{\text{area}}(\mathbf{X})$	max.	252.53	0.00	203.02	28.72	367.36	115.09
	min.	0.00	0.00	0.00	0.00	216.71	0.00
	avg.	133.27	0.00	110.18	8.46	283.89	14.39
$F_{\text{normal}}(\mathbf{X})$	max.	46.31	9.79	40.93	34.36	49.83	42.64
	min.	3.58	2.23	2.37	3.86	43.15	3.50
	avg.	30.76	6.37	24.45	11.53	47.46	23.14

F.2.3 Graphs of solutions approximating dome surface

The graphs plotting the DOFs and values of approximation error functions with respect to the number of fixed crease lines are shown for the examples of the approximation of the dome surface. The correspondence between the cases of examples and the indices of graphs are as follows:

- Case G1: Figs. F.25–F.28
- Case G2: Figs. F.29–F.32
- Case G3: Figs. F.33–F.36
- Case R1: Figs. F.37–F.40
- Case R2: Figs. F.41–F.44
- Case R3: Figs. F.45–F.48

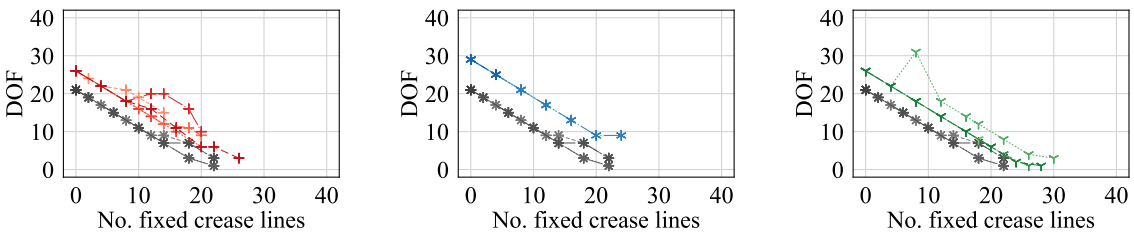

(a) Cut pattern C **(b)** Cut pattern E **(c)** Cut pattern X

Figure F.25: DOFs in Case G1 with the dome surface.

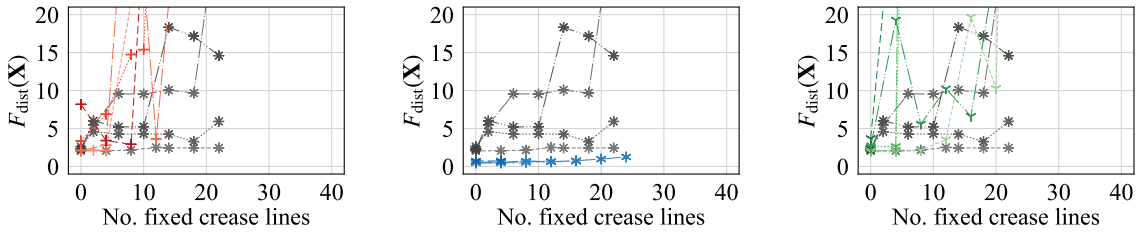

(a) Cut pattern C **(b)** Cut pattern E **(c)** Cut pattern X

Figure F.26: Values of $F_{\text{dist}}(\mathbf{X})$ in Case G1 with the dome surface.

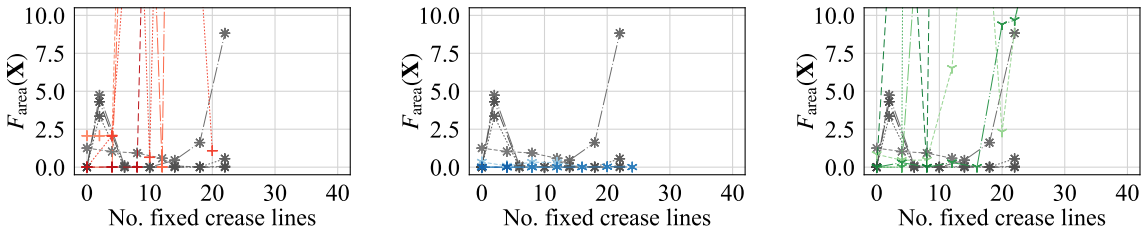

(a) Cut pattern C **(b)** Cut pattern E **(c)** Cut pattern X

Figure F.27: Values of $F_{\text{area}}(\mathbf{X})$ in Case G1 with the dome surface.

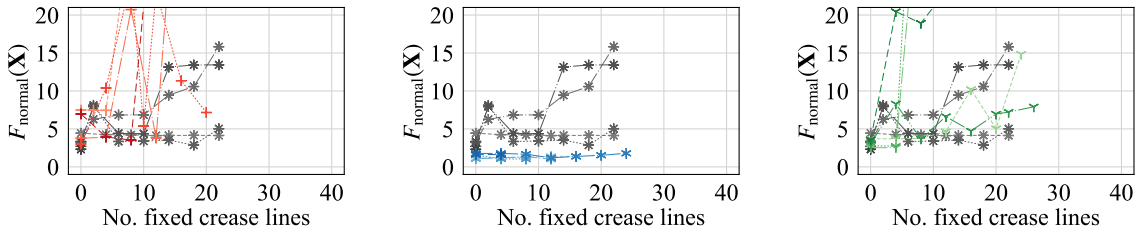

(a) Cut pattern C **(b)** Cut pattern E **(c)** Cut pattern X

Figure F.28: Values of $F_{\text{normal}}(\mathbf{X})$ in Case G1 with the dome surface.

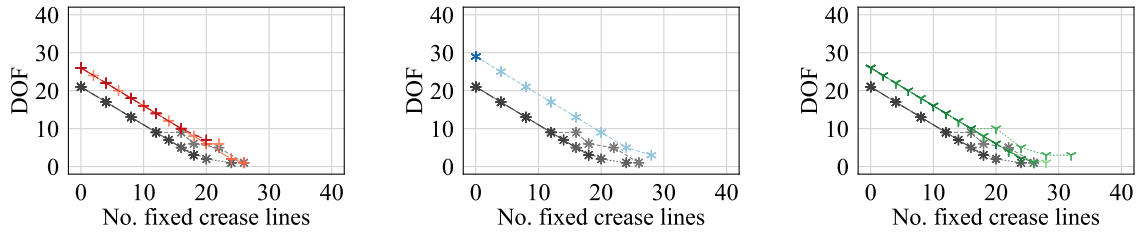

(a) Cut pattern C **(b)** Cut pattern E **(c)** Cut pattern X

Figure F.29: DOFs in Case G2 with the dome surface.

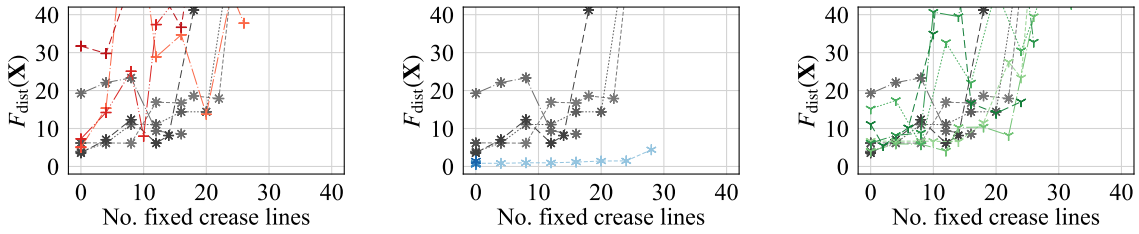

(a) Cut pattern C **(b)** Cut pattern E **(c)** Cut pattern X

Figure F.30: Values of $F_{\text{dist}}(\mathbf{X})$ in Case G2 with the dome surface.

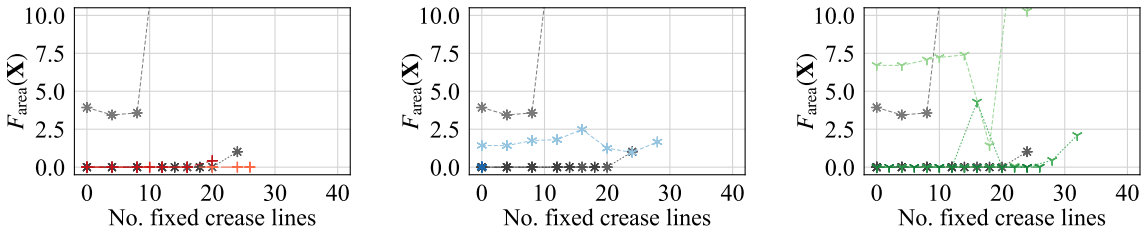

(a) Cut pattern C **(b)** Cut pattern E **(c)** Cut pattern X

Figure F.31: Values of $F_{\text{area}}(\mathbf{X})$ in Case G2 with the dome surface.

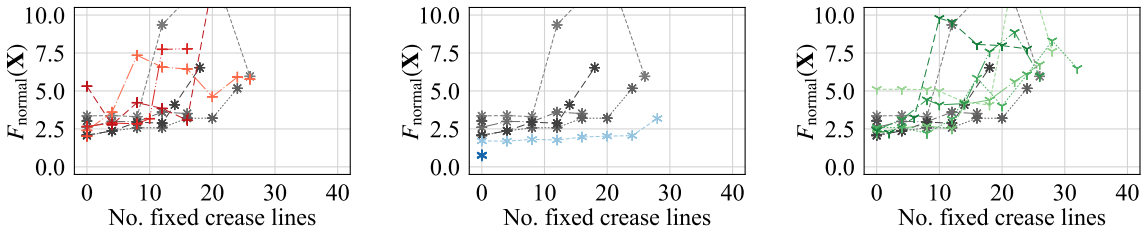

(a) Cut pattern C **(b)** Cut pattern E **(c)** Cut pattern X

Figure F.32: Values of $F_{\text{normal}}(\mathbf{X})$ in Case G2 with the dome surface.

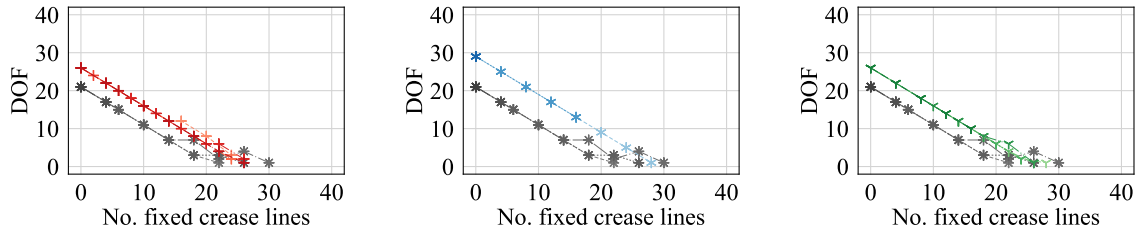

(a) Cut pattern C **(b)** Cut pattern E **(c)** Cut pattern X

Figure F.33: DOFs in Case G3 with the dome surface.

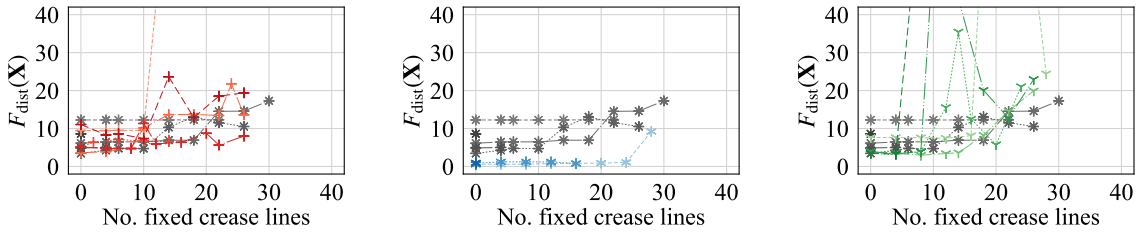

(a) Cut pattern C **(b)** Cut pattern E **(c)** Cut pattern X

Figure F.34: Values of $F_{\text{dist}}(\mathbf{X})$ in Case G3 with the dome surface.

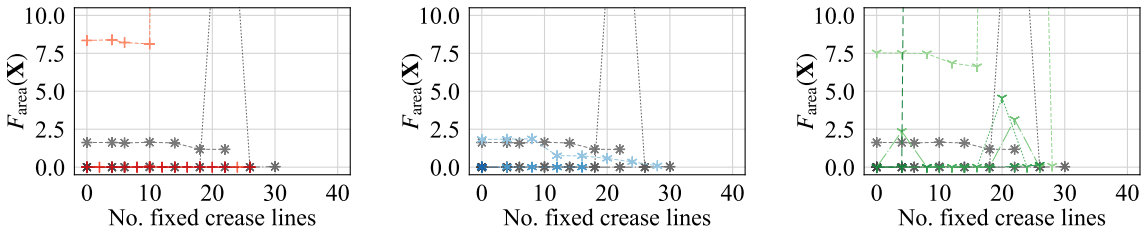

(a) Cut pattern C **(b)** Cut pattern E **(c)** Cut pattern X

Figure F.35: Values of $F_{\text{area}}(\mathbf{X})$ in Case G3 with the dome surface.

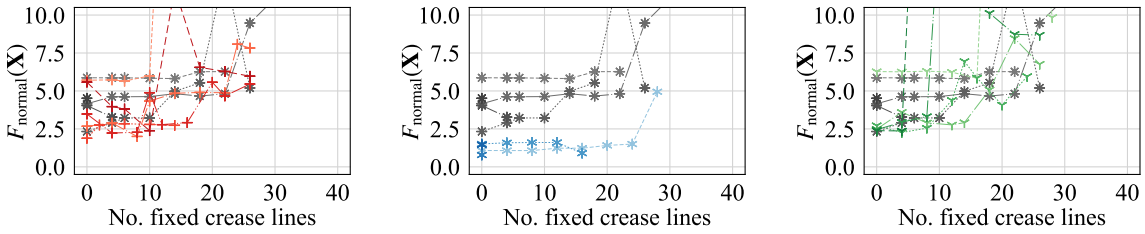

(a) Cut pattern C **(b)** Cut pattern E **(c)** Cut pattern X

Figure F.36: Values of $F_{\text{normal}}(\mathbf{X})$ in Case G3 with the dome surface.

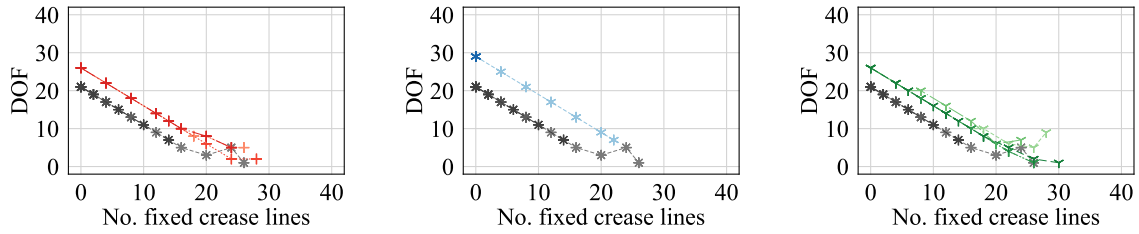

(a) Cut pattern C **(b)** Cut pattern E **(c)** Cut pattern X

Figure F.37: DOFs in Case R1 with the dome surface.

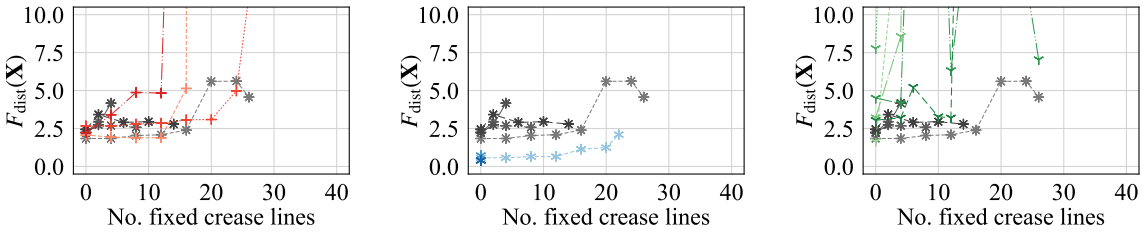

(a) Cut pattern C **(b)** Cut pattern E **(c)** Cut pattern X

Figure F.38: Values of $F_{\text{dist}}(\mathbf{X})$ in Case R1 with the dome surface.

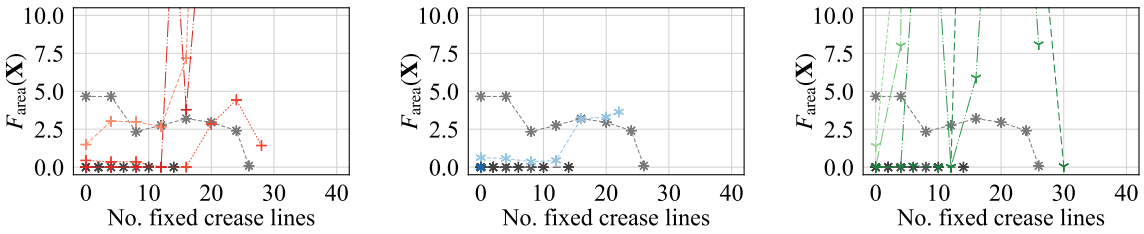

(a) Cut pattern C **(b)** Cut pattern E **(c)** Cut pattern X

Figure F.39: Values of $F_{\text{area}}(\mathbf{X})$ in Case R1 with the dome surface.

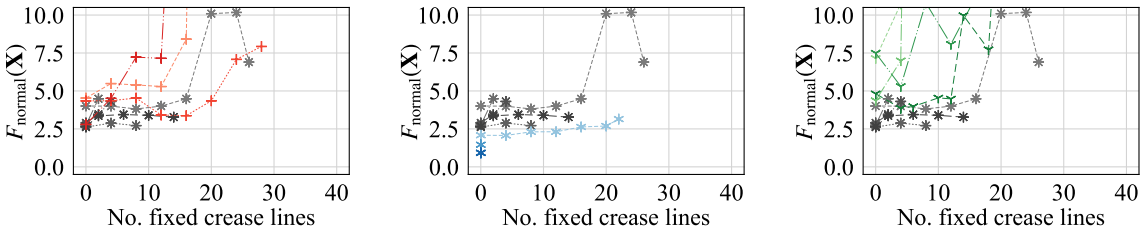

(a) Cut pattern C **(b)** Cut pattern E **(c)** Cut pattern X

Figure F.40: Values of $F_{\text{normal}}(\mathbf{X})$ in Case R1 with the dome surface.

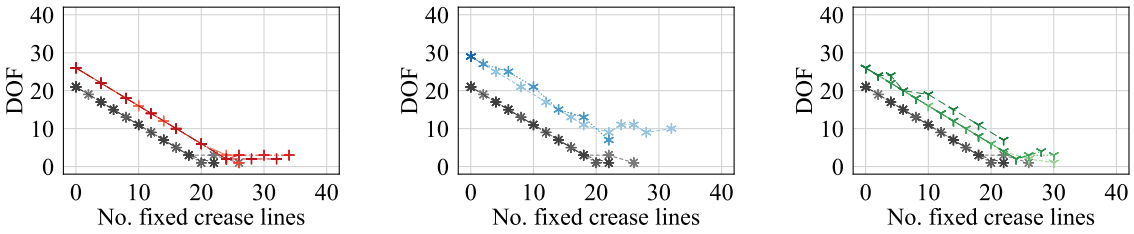

(a) Cut pattern C **(b)** Cut pattern E **(c)** Cut pattern X

Figure F.41: DOFs in Case R2 with the dome surface.

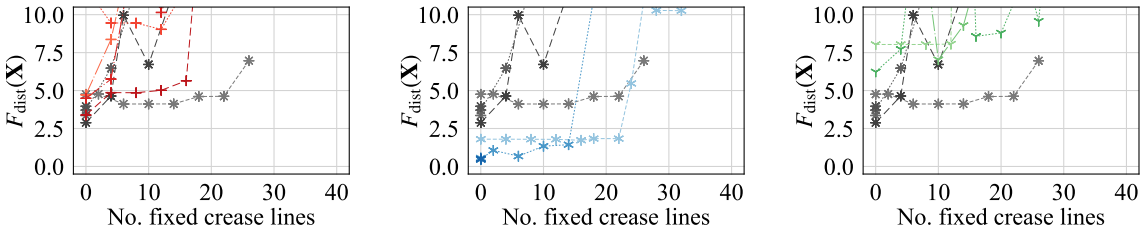

(a) Cut pattern C **(b)** Cut pattern E **(c)** Cut pattern X

Figure F.42: Values of $F_{\text{dist}}(\mathbf{X})$ in Case R2 with the dome surface.

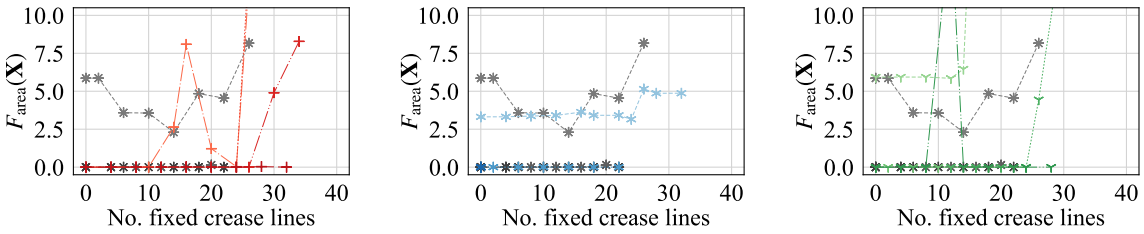

(a) Cut pattern C **(b)** Cut pattern E **(c)** Cut pattern X

Figure F.43: Values of $F_{\text{area}}(\mathbf{X})$ in Case R2 with the dome surface.

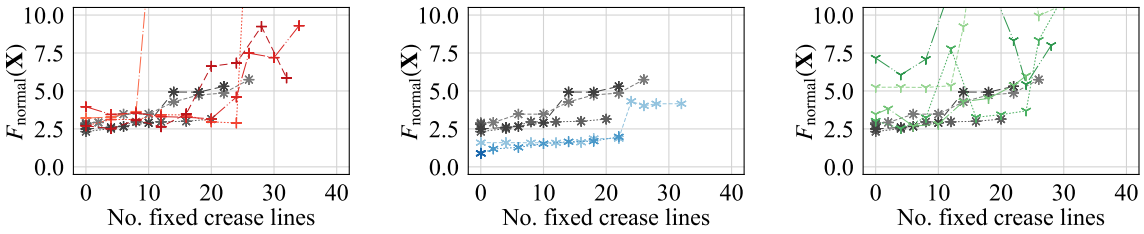

(a) Cut pattern C **(b)** Cut pattern E **(c)** Cut pattern X

Figure F.44: Values of $F_{\text{normal}}(\mathbf{X})$ in Case R2 with the dome surface.

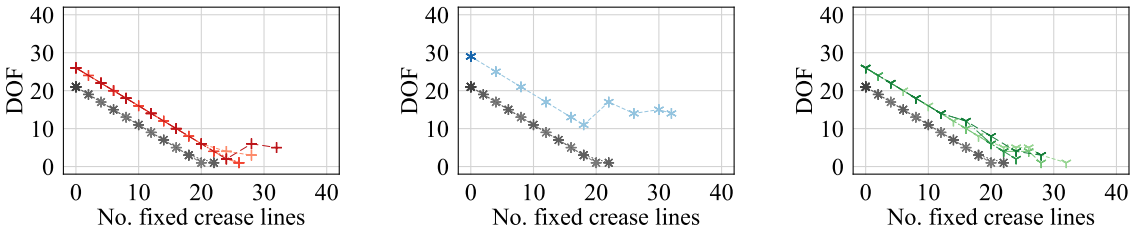

(a) Cut pattern C **(b)** Cut pattern E **(c)** Cut pattern X

Figure F.45: DOFs in Case R3 with the dome surface.

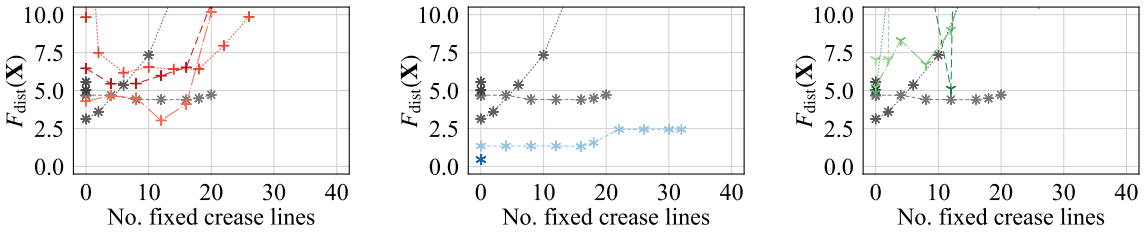

(a) Cut pattern C **(b)** Cut pattern E **(c)** Cut pattern X

Figure F.46: Values of $F_{\text{dist}}(\mathbf{X})$ in Case R3 with the dome surface.

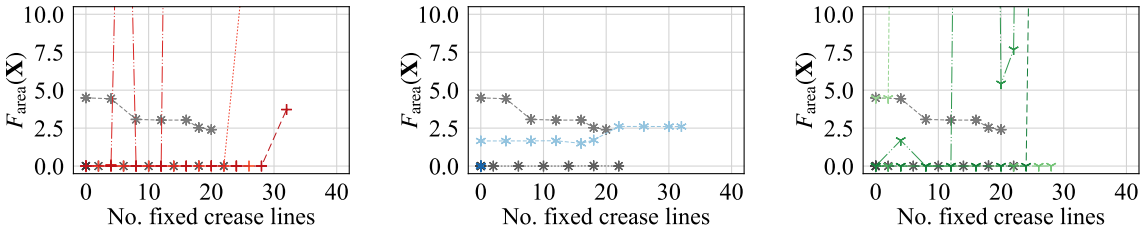

(a) Cut pattern C **(b)** Cut pattern E **(c)** Cut pattern X

Figure F.47: Values of $F_{\text{area}}(\mathbf{X})$ in Case R3 with the dome surface.

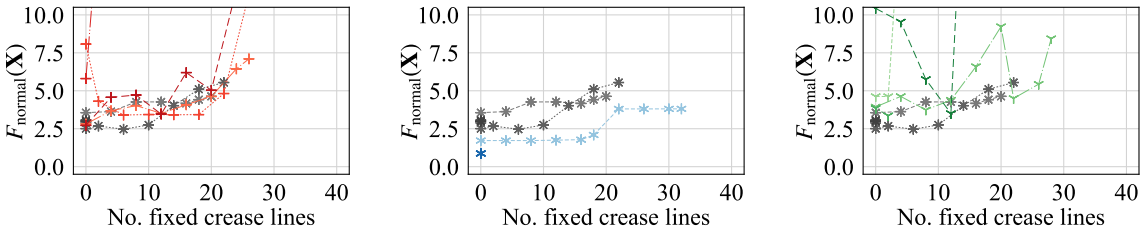

(a) Cut pattern C **(b)** Cut pattern E **(c)** Cut pattern X

Figure F.48: Values of $F_{\text{normal}}(\mathbf{X})$ in Case R3 with the dome surface.

References

[1] T. Ida. *An Introduction to Computational Origami*. Springer, Gewerbestrasse, Switzerland, 2020.

[2] R. J. Lang. *Origami Design Secrets: Mathematical Methods for an Ancient Art, Second Edition*. CRC Press, Boca Raton, FL, United States of America, 2011.

[3] E. D. Demaine and J. O'Rourke. *Geometric folding algorithms: linkages, origami, polyhedra*. Cambridge University Press, Cambridge, United Kingdom, 2007.

[4] R. Uehara. *Introduction to Computational Origami*. Springer, Gewerbestrasse, Switzerland, 2020.

[5] T. Tachi. Introduction to structural origami. *Journal of the International Association for Shell and Spatial Structures*, Vol. 60, No. 1, pp. 7–18, Mar. 2019.

[6] M. Meloni, J. Cai, Q. Zhang, D. S. Lee, M. Li, R. Ma, T. E. Parashkevov, and J. Feng. Engineering origami: A comprehensive review of recent applications, design methods, and tools. *Advanced Science*, Vol. 8, pp. 2000636, July 2021.

[7] K. Miura. Method of packaging and deployment of large membranes in space. *The Institute of Space and Astronautical Science report*, Vol. 618, pp. 1–9, Dec. 1985.

[8] N. De Temmerman, M. Mollaert, T. Van Mele, and L. De Laet. Design and analysis of a foldable mobile shelter system. *International Journal of Space Structures*, Vol. 22, No. 3, pp. 161–168, Sep. 2007.

[9] T.-U. Lee and J. M. Gattas. Geometric design and construction of structurally stabilized accordion shelters. *Journal of Mechanisms and Robotics*, Vol. 8, No. 3, pp. 031009–1–031009–8, Mar. 2016.

[10] J. Ma and Z. You. Energy absorption of thin-walled square tubes with a prefolded origami pattern-part I: Geometry and numerical simulation. *Journal of Applied Mechanics*, Vol. 81, No. 1, pp. 011003, Aug. 2013.

[11] C. Zhou, Y. Zhou, and B. Wang. Crashworthiness design for trapezoid origami crash boxes. *Thin-Walled Structures*, Vol. 117, pp. 257–267, Aug. 2017.

[12] K. Kuribayashi, K. Tsuchiya, Z. You, D. Tomus, M. Umemoto, T. Ito, and M. Sasaki. Self-deployable origami stent grafts as a biomedical application of ni-rich tini shape memory alloy foil. *Materials Science and Engineering: A*, Vol. 419, No. 1, pp. 131–137, Mar. 2006.

[13] J. L. Silverberg, A. A. Evans, L. McLeod, R. C. Hayward, T. Hull, C. D. Santangelo, and I. Cohen. Applied origami. Using origami design principles to fold reprogrammable mechanical metamaterials. *Science*, Vol. 345, No. 6197, pp. 647–650, Aug. 2014.

[14] P. P. Pratapa, K. Liu, and G. H. Paulino. Geometric mechanics of origami patterns exhibiting poisson's ratio switch by breaking mountain and valley assignment. *Physical Review Letters*, Vol. 122, pp. 155501, Apr. 2019.

[15] S. A. Rogers. Origami-Inspired Architecture: 14 Geometric Structures | Urbanist. `https://weburbanist.com/2013/11/11/origami-inspired-architecture-14-geometric-structures/`, (Accessed Oct. 2022).

[16] International association for shell and spatial structures. IASS - International Association for Shell and Spatial Structures - Working Groups. `https://iass-structures.org/Working-Groups`, (Accessed Oct. 2022).

[17] J. Mitani. *Curved-folding Origami Design*. CRC Press, Boca Raton, FL, United States of America, 2019.

[18] S. A. Zirbel, R. J. Lang, M. W. Thomson, D. A. Sigel, P. E. Walkemeyer, B. P. Trease, S. P. Magleby, and L. L. Howell. Accommodating thickness in origami-based deployable arrays. *Journal of Mechanical Design*, Vol. 135, No. 11, pp. 111005, Oct. 2013.

[19] C. H. Belke and J. Paik. Mori: A modular origami robot. *IEEE/ASME Transactions on Mechatronics*, Vol. 22, No. 5, pp. 2153–2164, Oct. 2017.

[20] P. M. Reis, F. L. Jiménez, and J. Marthelot. Transforming architectures inspired by origami. *Proceedings of the National Academy of Sciences of the United States of America*, Vol. 112, No. 40, pp. 12234–12235, Oct. 2015.

[21] M. Kawaguchi. Design problems of long span spatial structures. *Engineering Structures*, Vol. 13, No. 2, pp. 144–163, Apr. 1991.

[22] W. K. Schief, A. I. Bobenko, and T. Hoffmann. On the integrability of infinitesimal and finite deformations of polyhedral surfaces. In A. I. Bobenko, J. M. Sullivan, P. Schröder, and P. M. Ziegler, editors, *Discrete Differential Geometry. Oberwolfach Seminars*, volume 38, pp. 67–93. Birkhäuser Verlag, Basel, Switzerland, 2008.

[23] T. Tachi. Generalization of rigid foldable quadrilateral mesh origami. *Journal of the International Association for Shell and Spatial Structures*, Vol. 50, No. 162, pp. 173–179, Dec. 2009.

[24] T. Tachi. Simulation of rigid origami. In R. J. Lang, editor, *Proceedings of the 4th International Meeting of Origami Science, Mathematics, and Education (Origami4)*, pp. 175–187. AK Peters, Natick, MA, United States of America, 2009.

[25] S. Shende, A. Gillman, D. Yoo, P. Buskoh, and K. Vemaganti. Bayesian topology optimization for efficient design of origami folding structures. *Structural and Multidisciplinary Optimization*, Vol. 63, pp. 1907–1926, Jan. 2021.

[26] N. Katoh and S. Tanigawa. A proof of the molecular conjecture. *Discrete and Computational Geometry*, Vol. 45, pp. 647–700, Mar. 2011.

[27] Y. Chen, L. Fan, Y. Bai, J. Feng, and P. Sareh. Assigning mountain-valley fold lines of flat-foldable origami patterns based on graph theory and mixed-integer linear programming. *Computers and Structures*, Vol. 239, pp. 106328, Oct. 2020.

[28] K. Hayakawa and M. Ohsaki. Form generation of rigid-foldable origami structure using frame model. *Journal of Environmental Engineering (Transactions of AIJ)*, Vol. 84, No. 760, pp. 597–605, June 2019. (in Japanese).

[29] K. Hayakawa and M. Ohsaki. Frame model for analysis and form generation of rigid origami for deployable roof structure. In *Proceedings of the IASS Annual Symposium 2019*, pp. 1080–1087, Barcelona, Spain, 2019.

[30] K. Hayakawa and M. Ohsaki. Form generation of rigid origami for approximation of a curved surface based on mechanical property of partially rigid frames. *International Journal of Solids and Structures*, Vol. 216, pp. 182–199, May 2021.

[31] K. Hayakawa and M. Ohsaki. Equilibrium path and stability analysis of rigid origami using energy minimization of frame model. *Frontiers in Built Environment*, Vol. 8, Aug. 2022.

[32] N. Watanabe. Foldable condition in a singular state of a rigid origami model. *Transactions of the Japan Society for Industrial and Applied Mathematics*, Vol. 28, No. 1, pp. 54–71, Jan. 2018. (in Japanese).

[33] Z. He and S. D. Guest. On rigid origami III: local rigidity analysis. *Proceedings of the Royal Society A: Mathematical, Physical and Engineering Sciences*, Vol. 478, No. 2258, pp. 20210589, 2022.

[34] M. Schenk and S. D. Guest. Origami folding: A structural engineering approach. In P. Wang-Iverson, R. J. Lang, and M. Yim, editors, *Proceedings of the 5th International Meeting of Origami Science, Mathematics, and Education (Origami5)*, pp. 291–303. CRC Press, Boca Raton, FL, United States of America, 2011.

[35] E. T. Filipov, K. Liu, T. Tachi, M. Schenk, and G. H. Paulino. Bar and hinge models for scalable analysis of origami. *International Journal of Solids and Structures*, Vol. 124, pp. 26–45, 2017.

[36] K. Saito, A. Tsukahara, and Y. Okabe. New deployable structures based on an elastic origami model. *Journal of mechanical design*, Vol. 137, No. 2, pp. 021402, Feb. 2015.

[37] T. Zhang, K. Kawaguchi, and M. Wu. A folding analysis method for origami based on the frame with kinematic indeterminacy. *International Journal of Mechanical Sciences*, Vol. 146-147, pp. 234–248, Oct. 2018.

[38] S. Tsuda, M. Ohsaki, S. Kikugawa, and Y. Kanno. Analysis of stability and mechanism of frames with partially rigid connections. *Journal of Structural and Construction Engineering (Transactions of AIJ)*, Vol. 78, No. 686, pp. 791–798, Apr. 2013. (in Japanese).

[39] M. Ohsaki, S. Tsuda, and Y. Miyazu. Design of linkage mechanisms of partially rigid frames using limit analysis with quadratic yield functions. *International Journal of Solids and Structures*, Vol. 88-89, pp. 68–78, June 2016.

[40] R. Watada and M. Ohsaki. Series expansion method for determination of order of 3-dimensional bar-joint mechanism with arbitrarily inclined hinges. *International Journal of Solids and Structures*, Vol. 141-142, pp. 78–85, June 2018.

[41] L. H. Dudte, E. Vouga, T. Tachi, and L. Mahadevan. Programming curvature using origami tessellations. *Nature Materials*, Vol. 15, pp. 583–588, Jan. 2016.

[42] K. Song, X. Zhou, S. Zang, H. Wang, and Z. You. Design of rigid-foldable doubly curved origami tessellations based on trapezoidal crease patterns. *Proceedings of the Royal Society A: Mathematical, Physical and Engineering Sciences*, Vol. 473, No. 2200, pp. 20170016, Apr. 2017.

[43] T. Tachi. Designing freeform origami tessellations by generalizing resch's patterns. *Journal of Mechanical Design*, Vol. 135, No. 11, pp. 111066–1–111006–10, Nov. 2013.

[44] Y. Zhao, Y. Endo, Y. Kanamori, and J. Mitani. Approximating 3d surfaces using generalized waterbomb tessellations. *Journal of Computational Design and Engineering*, Vol. 5, pp. 442–448, Jan. 2018.

[45] J. Wu. Folding yoshimura pattern into large-scale art installation. In R. J. Lang, M. Bolitho, and Z. You, editors, *The proceedings from the 7th International Meeting of Origami Science, Mathematics, and Education (Origami7)*, pp. 1–13. Tarquin, St Albans, United Kingdom, 2018.

[46] T. Tachi. Geometric considerations for the design of rigid origami structures. In *Proceedings of the IASS Annual Symposium 2010*, pp. 8–12, Shanghai, China, 2010.

[47] Z. He and S. D. Guest. Design of novel origami shell structures. In *Proceedings of the IASS Annual Symposium 2019*, pp. 1055–1062, Barcelona, Spain, 2019.

[48] Z. He and S. D. Guest. On rigid origami II: quadrilateral creased papers. *Proceedings of the Royal Society A: Mathematical, Physical and Engineering Sciences*, Vol. 476, No. 2237, pp. 20200020, May 2020.

[49] K. Fuchi and A. R. Diaz. Origami design by topology optimization. *Journal of Mechanical Design*, Vol. 135, No. 11, pp. 111003:1–111003:7, Nov. 2013.

[50] A. S. Gillman, K. Fuchi, and P. R. Buskohl. Discovering sequenced origami folding through nonlinear mechanics and topology optimization. *Journal of Mechanical Design*, Vol. 141, No. 4, pp. 041401:1–041401:11, Apr. 2019.

[51] G. Farin. *Curves and Surfaces for CAGD: A Practical Guide*. Morgan Kaufmann Publishers Inc., San Francisco, CA, Unitesd State of America, 5th edition, 2001.

[52] K. Hayakawa, Y. Maruyama, A. Adachi, and M. Ohsaki. Approximation of curved surface by rigid origami with cutting lines. *Journal of Architecture and Planning (Transactions of AIJ)*, Vol. 87, No. 801, pp. 2288–2297, Nov. 2022. (in Japanese).

[53] K. Liu and G. H. Paulino. Highly efficient nonlinear structural analysis of origami assemblages using the merlin2 software. In R. J. Lang, M. Bolitho, and Z. You, editors, *Proceedings of the 7th International Meeting of Origami Science, Mathematics, and Education (Origami7)*, pp. 1197–1182. Tarquin, St Albans, United Kingdom, 2018.

[54] A. Ghassaei, E. D. Demaine, and N. Gershenfeld. Fast, interactive origami simulation using GPU computation. In R. J. Lang, M. Bolitho, and Z. You, editors, *Proceedings of the 7th International Meeting of Origami Science, Mathematics, and Education (Origami7)*, pp. 1151–1156. Tarquin, St Albans, United Kingdom, 2018.

[55] T. Tachi and T. C. Hull. Self-foldability of rigid origami. *Journal of Mechanisms and Robotics*, Vol. 9, No. 2, pp. 021008, Mar. 2017.

[56] J. Denavit and R. S. Hartenberg. A kinematic notation for lower-pair mechanisms based on matrices. *Journal of Applied Mechanics*, Vol. 22, No. 2, pp. 215–221, June 1995.

[57] Y. Chen, Z. You, and T. Tarnai. Threefold-symmetric Bricard linkages for deployable structures. *International Journal of Solids and Structures*, Vol. 42, No. 8, pp. 2287–2301, Apr. 2005.

[58] T. Tachi. Rigid Origami Simulator. `http://www.tsg.ne.jp/TT/software/`, (Accessed Oct. 2022).

[59] G. H. Paulino. MERLIN2. `http://paulino.princeton.edu/software.html`, (Accessed Oct. 2022).

[60] A. Ghassaei. Origami Simulator. `https://origamisimulator.org/`, (Accessed Oct. 2022).

[61] B. H. Hanna, J. M. Lund, R. J. Lang, S. P. Magleby, and L. L. Howell. Waterbomb base: a symmetric single-vertex bistable origami mechanism. *Smart Materials and Structures*, Vol. 23, No. 9, pp. 094009, Aug. 2014.

[62] G. J. Borse. *Numerical Methods with MATLAB: A Resource for Scientists and Engineers*. International Thomson Publishing, London, United Kingdom, 1996.

[63] C. D. Meyer. *Matrix Analysis and Applied Linear Algebra*. SIAM, Philadelphia, PA, United States of America, 2000.

[64] M. Géradin and A. Cardona. *Flexible Multibody Dynamics: A Finite Element Approach*. Wiley, London, United Kingdom, 2007.

[65] M. Konaković-Luković, J. Panetta, K. Crane, and M. Pauly. Rapid deployment of curved surfaces via programmable auxetics. *ACM Transactions on Graphics*, Vol. 37, No. 4, pp. 106:1–106:13, Jul. 2018.

[66] G. P. T. Choi, L. H. Dudte, and L. Mahadevan. Programming shape using kirigami tessellations. *Nature Materials*, Vol. 18, pp. 999–1004, Aug. 2019.

[67] K. Takahashi, T. Tachi, and Y. Yamaguchi. An approximation method of triangular mesh models for generating development diagrams with creases and slits. *IPSJ SIG Technical Report*, Vol. 2013-CG-153, No. 10, pp. 1–6, Nov. 2013. (in Japanese).

[68] J. Mitani and H. Suzuki. Making papercraft toys from meshes using strip-based approximate unfolding. *ACM Transactions on Graphics*, Vol. 23, No. 3, pp. 259–263, Aug. 2004.

[69] J. M. Sullivan. Curvatures of smooth and discrete surfaces. In A. I. Bobenko, J. M. Sullivan, P. Schröder, and P. M. Ziegler, editors, *Discrete Differential Geometry. Oberwolfach Seminars*, volume 38, pp. 175–188. Birkhäuser Verlag, Basel, Switzerland, 2008.

[70] C. C. L. Wang, S. S.-F. Smith, and M. M. F. Yuen. Surface flattening based on energy model. *Computer-Aided Design*, Vol. 34, No. 11, pp. 823–833, Sep. 2002.

[71] Y. Yamaguchi. Normal cones and visibility cones of bézier type surfaces. In *Proceedings of the 15th National Convention of IPSJ*, pp. 2–277–2–278, Toyama, Japan, 1995. (in Japanese).

[72] S.-M. Hu and J. Wallner. A second order algorithm for orthogonal projection onto curves and surfaces. *Computer Aided Geometric Design*, Vol. 22, No. 3, pp. 251–260, Mar. 2005.

[73] R. B. Nelson. Simplified calculation of eigenvector derivatives. *AIAA Journal*, Vol. 14, No. 9, pp. 1201–1205, Sep. 1976.

[74] P. E. Gill, W. Murray, and M. A. Saunders. SNOPT: An SQP algorithm for large-scale constrained optimization. *SIAM Journal on Optimization*, Vol. 12, No. 4, pp. 979–1006, Apr. 2002.

[75] R. E. Perez, P. W. Jansen, and J. R. R. A. Martins. pyOpt: A Python-based object-oriented framework for nonlinear constrained optimization. *Structures and Multidisciplinary Optimization*, Vol. 45, No. 1, pp. 101–118, Jan. 2012.

[76] R. E. Perez, P. W. Jansen, and J. R. R. A. Martins. pyOpt Documentation, Release 1.2. `http://www.pyopt.org/`, (Accessed Oct. 2022).

[77] NumPy Developers. numpy.linalg.svd — NumPy v1.23 Manual. `https://numpy.org/doc/stable/reference/generated/numpy.linalg.svd.html`, (Accessed Oct. 2022).

[78] Dassault Systèmes. Abaqus 2020 documentation, 2019.

[79] K. Miura and S. Pellegrino. *Forms and Concepts for Lightweight Structures*. Cambridge University Press, Cambridge, United Kingdom, 2020.

[80] W. McGuire, R. H. Gallagher, and R. D. Ziemian. *Matrix Structural Analysis, 2nd Edition*. CreateSpace Independent Publishing Platform, North Charleston, SC, United States of America, 2015.

[81] G. Salerno. How to recognize the order of infinitesimal mechanisms: A numerical approach. *International Journal for Numerical Methods in Engineering*, Vol. 35, pp. 1351–1395, Oct. 1992.

[82] P. Kumar and S. Pellegrino. Computation of kinematic paths and bifurcation points. *International Journal of Solids and Structures*, Vol. 37, No. 46-47, pp. 7003–7027, Nov. 2000.

[83] E. D. Demaine, M. D. Demaine, D. A. Huffman, T. C. Hull, D. Koschitz, and T. Tachi. Zero-area reciprocal diagram of origami. In *Proceedings of the IASS Annual Symposium 2016*, Tokyo, Japan, 2016.

[84] J. M. T. Thompson and G. W. Hunt. *A General Theory of Elastic Stability*. Wiley-Interscience publication. Wiley, 1973.

[85] A. Gillman, K. Fuchi, and P. R. Buskohl. Truss-based nonlinear mechanical analysis for origami structures exhibiting bifurcation and limit point instabilities. *International Journal of Solids and Structures*, Vol. 147, No. 15, pp. 80–93, Aug. 2018.

[86] Y. Li. Motion paths finding for multi-degree-of-freedom mechanisms. *International Journal of Mechanical Sciences*, Vol. 185, pp. 105709, Nov. 2020.

[87] M. Ohsaki and K. Ikeda. Imperfection sensitivity analysis of hill-top branching with many symmetric bifurcation points. *International Journal of Solids and Structures*, Vol. 43, pp. 4704–4719, Aug. 2006.

[88] M. Ohsaki and K. Ikeda. *Stability and Optimization of Structures: Generalized Sensitivity Analysis*. Springer, 2007.

[89] M. R. Hestenes. Multiplier and gradient methods. *Journal of optimization theory and applications*, Vol. 4, No. 5, pp. 303–320, Nov. 1969.

[90] E. G. Birgin and J. M. Martínez. Augmented Lagrangian method with nonmonotone penalty parameters for constrained optimization. *Computational Optimization and Applications*, Vol. 51, No. 3, pp. 941–965, Apr. 2012.

[91] T. Tachi. Design of infinitesimally and finitely flexible origami based on reciprocal figures. *Journal for Geometry and Graphics*, Vol. 16, No. 2, pp. 223–234, Dec. 2012.

[92] B. G. Chen and C. D. Santangelo. Branches of triangulated origami near the unfolded state. *Physical Review X*, Vol. 8, pp. 011034, Feb. 2018.

[93] A. F. Izmailov and M. V. Solodov. Critical Lagrange multipliers: what we currently know about them, how they spoil our lives, and what we can do about it. *TOP*, Vol. 23, pp. 1–26, Feb. 2015.

[94] Z. P. Bažant and L. Cedolin. *Stability of Structures: Elastic, Inelastic, Fracture and Damage Theories*. World Scientific Publishing Co. Pte. Ltd., 2010.

[95] W. Forst and D. Hoffmann. *Optimization: Theory and Practice*. Springer, 2010.

[96] J. L. Morales and J. Nocedal. Remark on "algorithm 778: L-BFGS-B: Fortran subroutines for large-scale bound constrained optimization". *ACM Transactions on Mathematical Software*, Vol. 38, No. 1, Nov. 2011.

[97] J. Zhang, M. Ohsaki, and Y. Kanno. A direct approach to design of geometry and forces of tensegrity systems. *International Journal of Solids and Structures*, Vol. 43, No. 7, pp. 2260–2278, Apr. 2006.

[98] K. Hayakawa and M. Ohsaki. Shape design of membrane structure using geometric invariants of discrete surface. *Journal of Structural and Construction Engineering (Transactions of AIJ)*, Vol. 86, No. 783, pp. 772–782, May 2021. (in Japanese).

List of papers and presentations

Papers and presentations related to this study

Peer-reviewed journal papers

1. K. Hayakawa and M. Ohsaki, Form generation of rigid origami for approximation of a curved surface based on mechanical property of partially rigid frames, *International Journal of Solids and Structures*, Vol. 216, pp.182–199, May 2021.

2. K. Hayakawa, Y. Maruyama, A. Adachi, and M. Ohsaki, Approximation of curved surface by rigid origami with cutting lines, *Journal of Architecture and Planning (Transactions of AIJ)*, Vol. 87, No. 801, pp. 2288–2297, Nov. 2022 (in Japanese).

3. K. Hayakawa and M. Ohsaki, Equilibrium path and stability analysis of rigid origami using energy minimization of frame model, *Frontiers in Built Environment*, Vol. 8, Aug. 2022.

4. K. Hayakawa and M. Ohsaki, Form generation of rigid-foldable origami structure using frame model, *Journal of Environmental Engineering (Transactions of AIJ)*, Vol. 84, No. 760, pp. 597–605, June. 2019 (in Japanese).

International conferences with full papers

1. K. Hayakawa and M. Ohsaki, Form generation of rigid origami by multiobjective optimization for approximating curved surface, in *Proceedings of the IASS symposium 2020/21*, Guilford, UK (online), pp. 2743–2754, Aug. 2021.

2. K. Hayakawa and M. Ohsaki, Form generation of rigid origami reflecting the mean curvature and feature lines of target surface, in *Proceedings of the IASS symposium 2022*, Beijing, China (online), pp. 2382–2393, Sept. 2022.

Other oral presentations

1. ○ K. Hayakawa and M. Ohsaki, Improvement of efficiency of form generation of rigid origami based on mechanical theory of partially rigid frame, in *Summaries of Technical Papers of Annual Meeting, Architectural Institute of Japan*, Structures-1, pp. 919—920, July 2020. (in Japanese)

2. ○ K. Hayakawa and M. Ohsaki, Optimization of crease pattern and form generation of rigid origami, in *Proceedings of Annual Meeting of JSIAM 2020*, pp.86-87, Sept. 2020.

3. ○ K. Hayakawa and M. Ohsaki, Equilibrium path analysis of rigid origami with multiple degrees of freedom by using partially rigid frame, in *Summaries of Technical Papers of Annual Meeting, Architectural Institute of Japan*, Structures-1, pp. 177—178, July 2021. (in Japanese)

4. ○ K. Hayakawa and M. Ohsaki, Arrangement optimization of crease lines of rigid origami with cut for approximating curved surface, in *Proceedings of Annual Meeting of JSIAM 2021*, Sept. 2021.

5. ○ K. Hayakawa and M. Ohsaki, Energy minimization approach to equilibrium path analysis of rigid origami using frame model, in *Summaries of Technical Papers of Annual Meeting, Architectural Institute of Japan*, Structures-1, pp. 163—164, July 2022. (in Japanese)

Other Papers and presentations

Peer-reviewed journal papers

1. K. Hayakawa and M. Ohsaki, Shape design of membrane structure using geometric invariants of discrete surface, *Journal of Structural and Construction Engineering (Transactions of AIJ)*, Vol. 86, No. 783, pp. 772–782, May. 2021 (in Japanese)

2. M. Ohsaki and K. Hayakawa, Non-parametric shape design of free-form shells using fairness measures and discrete differential geometry, *Journal of the International Association of Shell and Spatial Structures*, Vol. 62, No. 2, pp. 93-101, June 2021

3. K. Hayakawa, M. Ohsaki, and J. Zhang, Meshless non-parametric shape design of piecewise approximately developable surfaces using discretized local Gauss map, *Journal of the International Association for Shell and Spatial Structures* (accepted for publication)

International conferences with full papers

1. M. Ohsaki and K. Hayakawa, Non-parametric shape design of free-form shells using extended Gauss map and discrete differential geometry, in *Proceedings of the IASS symposium 2020/21*, Guilford, UK (online), pp. 2743–2754, Aug. 2021.

Other oral presentations

1. ○ M. Ohsaki and K. Hayakawa, Design of membrane grid using developable surface and minimal surface, in *Proc. Asian Congress of Structural and Multidisciplinary Optimization (ACSMO 2020)*, Seoul, Korea (online), Paper W3B-3, p. 226, Nov. 2020.

2. ○ R. Uemura, M. Ohsaki, and K. Hayakawa, Shape optimization of curved structures using discrete developable surfaces, in *Summaries of Technical Papers of Annual Meeting, Architectural Institute of Japan*, Structures-1, pp. 923—924, July 2020. (in Japanese)

3. ○ K. Hayakawa and M. Ohsaki, A basic study on segmentation of discrete surface using geometrical invariants of triangular mesh, in *Proceedings of the 43rd Symposium on Computer Technology of Information, Systems and Applications*, pp.104–107, Dec. 2020.

4. ○ A. Adachi, J. Zhang, K. Hayakawa, and M. Ohsaki, Equilibrium of forces on discrete CMC surface, in *Summaries of Technical Papers of Annual Meeting, Architectural Institute of Japan*, Structures-1, pp. 747—748, July 2022. (in Japanese)

Other publications

1. K. Hayakawa, Y. Jikumaru, Y. Yokosuka, T. Kagaya, K. Hayashi, and Y. Sakai, Differential geometric approaches to shell membrane theory and their applications to architectural surface design, MI Lecture Note Vol. 83, Institute of Mathematics for Industry, Kyusyu University, July 2021.

Acknowledgment

This research was supported by Grant-in-Aid for JSPS Research Fellow No. JP20J21650, JST CREST Grant No. JPMJCR1911, and JSPS KAKENHI Grant No. JP19K04714. I would like to express my gratitude to my supervisor, Professor Makoto Ohsaki, whose expertise in structural optimization has been invaluable in formulating the research questions and constructing the methodology. He has taught me countless things about how to behave in the academic field and has always respected my interests and intentions. I would like to thank the co-chairs of my dissertation committee, Professor Izuru Takewaki and Associate Professor Yuji Koetaka. Their expertise, guidance, and encouragement were crucial to the completion of this thesis. I am also grateful to Associate Professor Jingyao Zhang and Dr. Akito Adachi for their insightful feedback in the seminars and meetings that brought my work to a higher level. I would also like to express my gratitude to the members of the laboratory for their help at every stage of the research. I am very grateful to Safumi Saiki for her administrative support that has accelerated my efforts over the years. The valuable experience at the University of Cambridge has also greatly improved my research. My sincere thanks go to Professor Simon D. Guest for welcoming me as a visiting student in his laboratory. Discussions with him and Dr. Zeyuan He at the University of Cambridge have greatly broadened my knowledge and research perspectives. Finally, I cannot forget to thank my family for their love and unwavering faith in me. I am grateful for everything they have done for me and for making my life so amazing.